UNIVERSITY OF LONDON THESIS

Degree PhD Year 2006 Name of Author SOFRONIOU Anastasia

The Parametrically Excited Pendulum System and Applications to Ship Dynamics

Anastasia Sofroniou

Department of Mathematics
University College London

University of London

A thesis submitted for the degree of

Doctor of Philosophy

Supervisor: Prof. S.R. Bishop

November 2006

ProQuest LLC
789 East Eisenhower Parkway
P.O. Box 1346
Ann Arbor, MI 48106-1346

Dedicated to my family

Acknowledgements

I wish to express my greatest thanks to my supervisor, Professor Steven Bishop for his continuous support and guidance throughout this project. I am grateful for his kindness and endless encouragement and most importantly for his example of positive attitude towards serious research in Nonlinear Dynamics. I am indebted to him for his unlimited assistance and the illuminating discussions we have shared. It has been a unique experience to work with such an outstanding researcher and teacher and to know that I could constantly trust his scientific judgements.

I would also like to thank Professor Kostas Spyrou and his colleagues from the School of Naval Architecture and Marine Engineering at the National Technical University of Athens, for giving me the opportunity to conduct within their department my experimental testing that contribute to the significant and practical application of my research. I am grateful for the valuable conversations and the overall help they provided me during my visit.

I want to especially thank Professor Simon Rusling and fellow researcher Thomas Grafton from the Naval Architecture and Marine Engineering Research Group of the Mechanical Engineering Department at University College London, for their collaboration on the final section of my project. The valuable access they granted me to their experimental data allowed for the constructive progress of my project.

Thanks are also due to Dr. Pengliang Shi, a former research assistant with whom I closely worked with during my first year and with whom I jointly published a paper. I shall always treasure our social and academic discussions and look forward to one day visiting him and his wife in China.

I also wish to express my gratefulness to Dr. Gert Van der Heijden for his impor-

tant suggestions and beneficial talks as well as Dr. Maria Prodromou for her kind assistance throughout my research studies.

I would also like to extend my appreciation to Professor Knaust Helmut from the Mathematics Department at the University of Texas at El Paso for his cooperation even from such a distance.

In addition, I would like to thank the Department of Mathematics here at University College London for awarding me, for two consecutive years, the Lighthill Scholarship Award as well as offering me Research Funding for my research trips abroad.

Finally, my deepest gratitude goes towards my family for their endless love, patience and support. Their confidence in me has been tremendously encouraging and provided me with the strength to accomplish my tasks and goals.

Abstract

The parametrically excited pendulum system is a dynamical system that can exhibit many nonlinear phenomena including that of chaos. Initially in this work, an examination of the symmetric parametrically driven system is undertaken and its bifurcational nature is highlighted in detail.

In any physical representation of a mathematical model, perfect symmetry can never quite be achieved even with elaborate and detailed experimental arrangements. So, it is necessary to gain a deeper understanding on how breaking the symmetry of this specific system can affect its bifurcational and nonlinear behaviour. This work continues to examine this asymmetric case and perform a comparison with its symmetric counterpart, with the aim of providing a better physical realisation of the model. The experimental importance of undergoing such an alteration in a system is discussed and applications to field of ship dynamics are investigated.

In addition, an examination of another form of the parametrically excited pendulum is considered where an extra harmonic forcing is incorporated within the equation of motion. The relevance of such an extension as well as of the study of the single parametrically excited system is shown by their proposed application to ship dynamics. Experimental roll decay tests are performed at the National Technical University of Athens, Greece, on a newly designed monohull model. Results are compared with corresponding adopted trimaran tests recently conducted by the Naval Architecture and Marine Engineering Research Group of UCL in conjunction with QinetiQ Haslar. The intention is to convey that by implementing equations of single and double forcing in the numerical simulations, better characterisation of the behaviour of roll damping assessment for these models is achieved, since adapting existing theoretical methods do not yield accurate roll damping predictions.

Consequently, this attempt may develop a validated theory for the prediction of monohull and trimaran roll motion and furthermore results from this nonlinear study may provide a more useful approach for future analysis of multihull vessels.

Contents

List of Figures

List of Tables

Chapter 1

Introduction

This work is an application of the conceptual framework and methods of nonlinear dynamics to the problem of the parametrically excited pendulum and its applicability to the field of ship stability and capsize. Both subjects, nonlinear dynamics and ship dynamics, are today vast disciplines.

No attempt can therefore be made here to provide a complete account of any of those areas. Far from that, we shall just be selecting a few tools available from the already considerable repertoire of nonlinear dynamics, so that we may provide from the resulting set of equations, amenable mathematical analysis. At the same time, we shall try to emphasise the significance of the problem and our results from a practical point of view.

In this Introduction we set the stage and lay the foundations for the subsequent Chapters by reviewing concepts on dynamical systems. The aim is to provide a motivating overview in preparation for the more detailed treatments to be pursued in the Chapters that follow within the thesis.

1.1 Dynamical Systems

A dynamical system may be defined as a deterministic mathematical prescription for evolving the state of a system forward in time. Time may either be a continuous variable or a discrete integer-valued variable. In the case where time, denoted as t, is a continuous variable, a dynamical system may be modelled by ordinary differential equations. As an example, we consider the general N-dimensional

$$\frac{d\underline{x}}{dt} = f(\underline{x}(t), \alpha) \tag{1.1.1}$$

where $\underline{x} \subset \mathbb{R}^N$, is an N-dimensional state space vector whose components are scalar properties of the dynamical system and the independent term $\alpha \subset \mathbb{R}^M$ is an M-dimensional vector of parameters of the dynamical system. This is a dynamical system because, for any initial state of the system $\underline{x}(0)$, we can in principle solve the equations to obtain the future system state $\underline{x}(t)$ for $t > 0$.

In the case when $N = 3$, the system state evolves with time, onto a space $(x^{(1)}, x^{(2)}, x^{(3)})$, representing a three dimensional coordinate axes, referred to as the phase space (Ott, 1993). The path in phase space followed by the system as it evolves in time is called an orbit or a trajectory.

A continuous time dynamical system is often called a flow. Considering nonlinear ordinary differential equations, they are usually very hard to solve analytically, if not impossible. Poincaré (1892), was the first to recognise the difficulty of solving such problems. He derived geometric methods which give qualitative insight into the problem at hand without the need of getting the actual analytic solution. Poincaré's geometric methods were motivated by the three body problem, that is, the problem of three celestial bodies experiencing mutual gravitational attraction, for example

the moon and two planets (Ott, 1993).

In the discrete, integer-valued time case, with n denoting the time variable, $n = 0, 1, 2..$, an example of a dynamical system is a map, which may be written in vector form as

$$\underline{x}_{n+1} = M(\underline{x}_n) \tag{1.1.2}$$

where $\underline{x}_n$ is N-dimensional, $\underline{x}_n = (x_n^{(1)}, x_n^{(2)}, x_n^{(3)}.., x_n^{(N)})$. Given an initial state, $\underline{x}_0$, the state at time $n = 1$, $\underline{x}_1$, may be obtained by $\underline{x}_1 = M(\underline{x}_0)$ and having determined $\underline{x}_1$, the state at $n = 2$ may be determined, and so on. Hence, given an initial condition $\underline{x}_0$, an orbit of the discrete time system, $\underline{x}_0$, $\underline{x}_1$, $\underline{x}_2$, ... may be generated.

A continuous time system, flow, may be reduced for sake of usefulness to a discrete time map by a technique called the Poincaré surface of section method (Arrowsmith and Place, 1990, Ott, 1993). The Poincaré map represents a reduction of an N-dimensional flow to an $(N-1)$-dimensional map. Consider a solution of a system of N first order, autonomous, ordinary differential equations that may be written as equation (1.1.1). An appropriate $(N-1)$-dimensional surface section in the N-dimensional phase space is constructed and the intersections of the orbit with the surface are observed. The points that represent the successive crossings of the surface of section are uniquely determined by each other. In other words, one of the points may be used as an initial condition in order to determine the next successive crossing point. The vice versa case, would imply reversing time in the systems ordinary differential equation. Thus, for example, for $N = 3$, the Poincaré map represents an invertible two-dimensional map, transforming coordinates $(x_n^{(1)}, x_n^{(2)})$ of the nth piercing of the surface of section to the coordinates $(x_{n+1}^{(1)}, x_{n+1}^{(2)})$ at piercing

$(n+1)$.

We provide here a few rules of thumb about properties of the dynamical response for a system modelled by equation (1.1.1).

(i) Suppose $\underline{x}(t)$ comes to rest at some point $\underline{x}^*$, then the velocity must be zero, so we call $\underline{x}^*$ a fixed point. It corresponds to an equilibrium state of the physical system modelled by equation (1.1.1). If all small disturbances away from $\underline{x}^*$ damp out, ($\underline{x}(t) \rightarrow \underline{x}^*$ as $t \rightarrow \infty$), then $\underline{x}^*$ is called a stable fixed point. It acts as an attractor for states in its vicinity. Or in other words, as an attractor where regions of initial condition of non-zero phase space asymptote to it as time increases. A classic example of a fixed point is the hanging solution of a simple damped pendulum. Any initial condition will produce an orbit that decays to this hanging solution as time increases. The rate at which the oscillations die away depends on the damping term.

(ii) Another possibility is that $\underline{x}^*$ flows towards a closed loop and eventually circulates around it forever. Such loop is called a limit cycle. An initial condition outside the limit cycle yields an orbit which, with time, spirals into the limit cycle on which it circulates in periodic motion in the $t \rightarrow \infty$ limit. Similarly an initial condition inside the limit cycle yields an orbit which spirals outward, asymptotically approaching the closed loop. Hence in this case, the closed loop is the attractor. It represents a pendulum oscillating periodically.

(iii) Another example, is that $\underline{x}(t)$ may not settle to a fixed point or a limit cycle, and an asymptotic steady state attractor that does this, is often called chaotic. One might consider this term unspecific, but it is still useful for categorising the behaviour of many nonlinear systems. Chaotic trajectories may be distinguished by considering two nearby initial conditions. The solutions do not converge as integration proceeds but on the contrary, the trajectories diverge exponentially and soon become entirely

uncorrelated.

From the engineering prospective, the result of chaos in a system, is that any measurement error in specifying the initial states of a chaotic system will be magnified with time.

1.2 Bifurcational Behaviour

We mentioned earlier that a nonlinear dynamical system may be modelled in terms of N-dimensional ordinary differential equations. Typically three dimensions are enough to characterise a numerous amount of behaviour found in a higher dimensional dynamical system.

Often what concerns researchers is the qualitative effects of behaviour in a system due to changes of control parameter(s) and this may be accomplished by the study of bifurcational behaviour (Guckenheimer and Holmes, 1983). By bifurcation we refer to the branching of one path of equilibrium to a qualitatively alternative path or paths whilst varying a control parameter. Hence, bifurcation theory is important to the understanding of nonlinear dynamical systems.

The type of bifurcation produced depends on the eigenvalues or characteristic multipliers of the solutions to the equation of a system by assessing the stability of a particular solution (Seydel, 1991, Glendinning, 1994). As a control parameter is varied, the eigenvalues change and one may leave the unit circle at a bifurcation.

A few examples of different types of bifurcations are described below. The Chapters that follow also include descriptions of other typical bifurcations that occur in our interested system of the parametrically excited pendulum.

Period doubling Bifurcation

The period doubling bifurcation (or otherwise referred to as a flip bifurcation) occurs when a stable limit cycle with period T becomes unstable giving rise to a stable limit cycle of period $2T$. At this bifurcation, an eigenvalue leaves the unit circle through -1. A period doubling bifurcation of period T to a period $2T$ solution, may be followed by another period doubling to a period $4T$ limit cycle and so on. This

cascade of bifurcations occurs often in nonlinear systems, as we shall see in this research study.

Saddle node Bifurcation

In a saddle node bifurcation (also called the fold bifurcation), a pair of periodic steady state solutions are created, one of which is always unstable (saddle) and the other is always stable (node). They collide and annihilate each other. The saddle node bifurcation is fundamental to the study of nonlinear systems since it is one of the most basic processes by which periodic orbits are created. At the bifurcation, one characteristic multiplier for both the stable and unstable limit cycle reaches $+1$. Saddle node bifurcations may be associated with hysterisis and catastrophes, where evidence of this is encountered within the later Chapters of the thesis.

Hopf Bifurcation

In both the above examples, we have only considered cases where one of the characteristic multipliers leaves the unit circle along the real axis. If one of the characteristic multipliers is imaginary, then the other will be its complex conjugate, so that a pair of characteristic multipliers may leave the unit circle as a complex conjugate pair. This occurs when a fixed point bifurcates into a stable limit cycle at a Hopf bifurcation (Thompson and Stewart, 1986).

In our parametrically excited pendulum model however, it is important to accentuate the special nature of this system; since there will always be a periodic forcing term, fixed point solutions are precluded and so Hopf bifurcations will not be experienced within this system. This will become clearer within Chapter 3.

Moreover, these examples consider only local bifurcations that occur due to periodic orbits colliding and losing stability. We are interested in these types of bifurcations that only affect trajectories in the neighbourhood of the attractors.

1.3 Brief Literature Overview

An important class of dynamical systems exhibiting chaotic phenomenon is one which model oscillating physical systems, which are often called oscillators. Oscillators are self-excited, parametrically excited (that is, that one of the parameters in the ordinary differential equation oscillates) or externally excited, where the latter can often be called forced oscillators.

In this thesis, we begin our study by focusing on oscillators that are parametrically excited, noting also that the majority of exhibited behaviour may in fact be experienced by many other nonlinear systems.

An ordinary simple planar pendulum whose axis is driven periodically in the vertical direction is therefore a paradigm of contemporary nonlinear dynamics. This mechanical system is interesting since the differential equation of the pendulum is often encountered in various problems of modern physics. There is a strong interest to study this system within the engineering field, ranging from the behaviour of offshore structures (Bishop, 2000), buildings in earthquakes (Housner, 1963) to the response of a ship in a seaway (Féat and Jones, 1981, Thompson *et al*, 1992, Francescutto and Contento, 1999, Spyrou 2000a, 2000b, France *et al*, 2003, Bulian, 2005). In all these applications, despite the obvious simplifications in the modelling process, much of the behaviour of the system may be characterised at least qualitatively by the parametrically excited pendulum.

Mechanical analogies of physical systems allow a direct visualization of motion and thus can be very useful in gaining an intuitive understanding of complex phenomena. Depending on the frequency and amplitude of forced oscillations of the pivot point, this mechanical system exhibits an array of nonlinear behaviour characterised by

different types of motion. A wide range of possible solutions and bifurcational behaviour may be realised over a range of operating parameters, including nonlinear phenomena such as chaos (Miles, 1989, Bryant and Miles, 1990a, 1990b, 1990c, Bishop and Clifford, 1994a, 1994b, Clifford and Bishop, 1996, Szemplińska-Stupnicka *et al*, 2000, Bishop, Sofroniou and Shi, 2005).

When the external excitation frequency is approximately twice the natural frequency of the pendulum, the hanging state becomes unstable and the system is often left executing oscillations whose amplitude increases progressively. It is this phenomena that is known as parametric resonance.

Another interesting feature in the behaviour of a pendulum whose suspension is forced to vibrate with a high frequency along the vertical line is the dynamic stabilization of its inverted position. When the frequency and amplitude of these vibrations are large enough, the inverted pendulum shows no tendency to turn down to the hanging position (Kalmus, 1970, Michaelis, 1985, Blackburn *et al*, 1992, Sudor and Bishop, 1999). Moreover, at small and moderate deviations from the vertical inverted state, the pendulum tends to return at the upright position (Bishop and Sudor, 1999). Other pendulum models have also been studied and they include the horizontal pendulum (Bryant and Miles, 1990b, Van Dooren, 1996, Koplow and Mann, 2005) and the spherical pendulum (Tritton, 1986, Miles and Zou, 1993).

Nevertheless, more and more new features in the behaviour of the vertically parametrically driven pendulum of this apparently "simple" system are reported regularly. One such extension is the issue of breaking the symmetry of the parametrically excited pendulum model (Sofroniou and Bishop, 2006). In any physical realisation of a mathematical model, perfect symmetry can never quite be achieved, even with elaborate and precise experimental arrangements and so, it only seems wise, to examine

the effects of such a scenario under this system.

The growing interest in the application on nonlinear dynamics to the field of ship dynamics has attracted considerable attention over recent years (Blocki, 1980, Kan *et al*, 1991, 1993, Francescutto and Contento, 1999, Spyrou, 2000a, 2000b, Spyrou and Thompson, 2000, Spyrou *et al*, 2002, Wu *et al*, 2004). Research conducted since the late 80's at University College London by J.M.T. Thompson and co-workers on the application of the conceptual framework of nonlinear dynamics to the problem of ship capsize has resulted in significant improvement of the basic understanding of the complex dynamics involved, revealing new phenomena and patterns of behaviour. These results allowed for a more comprehensive picture of the problem and pointed to novel methods of evaluating ship stability (Thompson *et al*, 1990, 1992, Spyrou and Thompson, 2000).

In Japan, research conducted by M. Kan and colleagues has approached many aspects of ship dynamics and capsize using the modern tools of nonlinear dynamics, supported by analytical, numerical and experimental investigations (Kan *et al*, 1990, Kan and Taguchi, 1991, Kan *et al*, 1993).

In the USA, at the Virginia Polytechnic Institute and State University, A. Nayfeh and colleagues have been exploring modern concepts of nonlinear dynamics and their work include extensive analytical investigations through the use of perturbation methods, and also numerical studies (Nayfeh and Sanchez, 1988, 1990, Bikdash *et al*, 1994).

To date, there has been only very limited research into the roll motion of a specific type of ship, called trimaran (Pattison and Zhang, 1994, Zhang and Andrews, 1999, Francescutto, 2001, Grafton *et al*, 2003, 2004). Zhang and Andrews (Zhang and Andrews, 1999) showed via their conducted experiments that a large proportion of

the roll damping for their particular trimaran model was provided by appendages. An area however where further research is needed and clearly be beneficial to Naval Architects and Marine Engineers, is to ensure that the existing theoretical roll damping prediction methods give accurate roll motion estimates for a trimaran without roll damping appendages. It is in this thesis where we apply the equation of motion of the parametrically excited pendulum system, studied in detail here within, and show a different application of the equation to the field of ship dynamics assuming another approach to roll damping assessment.

1.4 Aims and Objectives

The aim of this thesis is to examine the parametrically excited pendulum system and to investigate the nonlinear dynamical behaviour entailed for this problem as well as exploring the effects once symmetry is broken, both with respect to the response and to the actual model. The intent of this thesis is to further apply the model to the field of ship dynamics with the purpose of providing an alternative theoretical approach to the prediction of roll damping assessment for vessels.

Given these aims, it is helpful to write down some of the basic issues to be confronted.

(i) What are the dynamics involved with the parametrically excited pendulum and what analytical and numerical methods may be used to produce a complete picture of the bifurcational behaviour of the model?

(ii) What is symmetry breaking in the response of the parametrically excited pendulum?

(iii) How can symmetry of the model be broken? What is the importance of acknowledging effects of non-symmetry in a model? What combinations of forcing amplitude and frequency cause the system to escape the confines of the local potential energy well? How does the bifurcation scenario change due to the asymmetry?

(iv) How can breaking the symmetry of a model be justified in view of ship dynamics? What is the effect on ship stability? How can asymmetry be quantified and measured?

(v) What happens when a double parametric forcing is considered for the pendulum system? What is the form of response if frequencies are incommensurate and commensurate?

(vi) How can parametric excitation be connected to ship dynamics? How can roll damping be assessed from roll decay experiments? In terms of the experimental analysis, what does the scattering effect in the equivalent linear damping against mean of successive peak amplitude plot represent? Why is there deviation at low roll amplitudes? Is this phenomenon only visible in trimaran models? How can heave and roll be coupled under a single degree of freedom equation for trimaran and monohull models? Does the simulation confirm a spread of equivalent linear damping values? If so, what does this suggest?

(vii) How can the issue of escape from the potential well for the parametrically excited pendulum model be connected to ship capsize? What is the importance of transient capsize?

With these questions in mind, we advance to the overview of the Chapters where we aspire and attempt to respond to the best of our capabilities, to the above points raised.

1.5 Structure of the thesis

In progressing through the work of this thesis, our guiding principles were firstly to examine in depth the parametrically excited pendulum system, concentrating also on the issue of symmetry breaking, and secondly to apply the model to the field of our growing interest ship dynamics as a new approach for roll damping assessment.

In this spirit, the contents of this thesis can be broadly divided into two parts. The first part is composed of Chapters 2,3,4 and 5, where in the initial Chapters we discuss a wide variety of dynamical responses of the single parametrically excited pendulum.

More specifically, in Chapter 2, we discuss stability regions of the model with the aid of the Mathieu equation and we analytically and numerically determine these zones. The Chapter gives emphasis on oscillatory behaviour of the parametrically driven pendulum and by implementing analytical techniques, we produce the escape zone for the major tongue, that leads to the unsafe operation of systems. In Chapter 3, we discuss further oscillatory behaviour and consider symmetry breaking within the response of the model with the view of predicting the onset of non-oscillatory solutions. In Chapter 4, we investigate symmetry breaking but of the actual parametrically excited pendulum model and examine the nonlinear behaviour undergone with the effect of asymmetry. Two types of methods for breaking the symmetry are studied and compared. Chapter 5 does not study the parametrically excited pendulum model as such, but we concentrate on the matter of asymmetry and its application to the world of ship stability.

The second part of the thesis is made up of Chapters 6 and 7. In Chapter 6, we return our attention to the study of the vertically driven pendulum and examine

the case when excitation consists of two frequencies. In Chapter 7, we are able to conduct and provide experimental testing on two types of vessels with the purpose of roll damping determination. A different approach compared to the usual one, for the assessment of roll damping is proposed by showing evidence of the application of the pendulum equation, under single and double forcing excitation, for simulation analysis. Transient capsize experiments are also undertaken to provide a practical link with the theory of escape examined within the first part of the thesis.

The thesis ends up with Chapter 8, which summarises our main findings and highlights the key observations. To conclude we point to future research directions.

1.6 Analytical techniques

A wide variety of analytical techniques exist for the analysis of nonlinear ordinary differential equation (Nayfeh and Mook, 1979, Hayashi, 1985, Guckenheimer and Holmes, 1983). These typically involve linearisation of the system to give an approximate solution and then additional nonlinear terms are accounted for by small perturbations from the original linear solution. There are however many problems associated with such an approach. The predicted solution might not provide a good enough approximation to the system and the only way of verifying is to undertake physical experimental testing or numerical integration. Also, inadmissible sequences of bifurcations may be predicted as noted by Thompson (Thompson, 1989).

The advantages of analytical methods as opposed to numerical techniques are evident when a general picture of the dynamics of a system is required instead of the detailed behaviour of one particular solution. Hence a broad outline of the possible parameter regions of interest may be produced and the areas where numerical study may be beneficial, highlighted.

Moreover, analytical methods may provide bounds on the system. For instance, when escape from a potential well for a system is permitted, it may be considered as useful if a region exists, where if any trajectory enters, it must escape to an attractor at infinity, or certainly distant to the one of interest.

Analytical methods are historically considerably older than numerical techniques and it may be expected that these methods could fall into disuse with the advent of computing power.

In this thesis, we utilise different types of analytical techniques, but harmonic balance (Hayashi, 1985), may be considered as possibly the oldest analytical method. It

is based on the traditional method of solving linear ordinary differential equations by substituting in, an assumed solution of sinusoidal nature with unknown amplitudes and thus calculating the unknown coefficients. In the case of nonlinear ordinary differential equations, an initial sinusoidal approximate solution is presumed and the coefficients are equated. There will be terms with frequencies other than the assumed solution and so another approximate solution containing these terms is assumed and unknown coefficients are evaluated by substituting back into the initial equation. This process may be repeated to include a large number of terms to give a closer approximation to the true solution.

The method has experienced recent advances to improve accuracy and speed of calculating solutions (Lsu *et al*, 1982, Wong *et al*, 1991). For the purpose of our study, we require a simple term as an approximate solution to the behaviour of the system and further reference and usage of this method may be seen in the first few Chapters of the thesis.

1.7 Numerical Issues

Simulation based upon rapidly expanding computational power has underpinned the rapid growth of interest in nonlinear dynamics. The numerical solution of nonlinear ordinary differential equations occupies a rather central place in applied mathematics and a vast assortment of techniques are available. In general, a fourth order Runge-Kutta algorithm is used in the thesis as this is a particular method that combines both speed and accuracy (Parker and Chua, 1989).

An important recent development involves the use of continuation methods, in which solutions paths are followed (Parker and Chua, 1989, Seydel, 1991). These methods have an advantage that unstable solutions can be obtained which are not ordinarily attainable using direct numerical integration.

Although most of the numerical results presented in this research work were based on conventional programming (C++ programming), increasing use by researchers is being made of software libraries (Matlab including Simulink (Matlab, 1989)), algebraic manipulation packages (Mathematica, (Wolfram, 1996) and Maple (Robertson, 1996)), general dynamics programs (dstool (Guckenheimer and Worfolk, 1993) and Dynamics (Nusse and Yorke, 1994)) and special dynamics programs (Auto (Doedel, 1986)). All these computational tools, except the latter, played a role in the numerical exploration of the depth of nonlinear behaviour in this thesis.

The data acquisition software used in the last section of the thesis was Origin (*www.OriginLab.com*) since that was the most attainable and readily available program by our department. It was also a familiar and user-friendly environment to work on.

One of the particular advantages of using packages is that sophisticated graphics

are routinely made use of, a feature that is crucial whilst delving into the world of nonlinear dynamics.

Chapter 2

Parametrically Excited Pendulum

2.1 Introduction

The simple pendulum suspended in the uniform gravitational field is a very useful and versatile physical model. The model is not only interesting as it is one of the most familiar examples of a nonlinear mechanical oscillator but more importantly because many problems in various engineering sectors may be reduced to the differential equation describing the motion of a pendulum (recall Chapter 1). Thus the pendulum is a rather classical nonlinear mechanical device which provides an intuitive understanding of complex phenomena.

Within this thesis, our special interest lies when the external frequency is approximately twice the natural frequency of the pendulum, so that the hanging position of the pendulum, becomes unstable and the system is left executing oscillations. The amplitude of this oscillation increases progressively, provided that the forcing amplitude also exceeds some threshold value, leading to parametric resonance. As a summary to this phenomenon, we also note that parametric resonance is possible

when forcing cycles occur during approximately one, two, three, and any other integer number of natural periods and with increasing damping, parametric resonance of higher orders become weaker and disappear (Butikov, 1999, 2001).

Our concern here within, is to study the various types of motion for a pendulum whose suspension point is driven periodically in the vertical direction. Depending on the amplitude and the frequency of the excitation of the pivot point, this seemingly simple system exhibits a rich variety of nonlinear phenomena, characterised by amazingly different types of behaviour and motion. Some of these motions of the parametrically forced pendulum may be very complicated and counterintuitive and which type of motion is activated depends on starting conditions.

The aim of this Chapter is to prepare a combined analytical and numerical approach to the problem of the parametrically excited pendulum. We attempt to determine the quantitative conditions that provide the stabilization of the hanging and inverted position of the pendulum in the presence of friction and the force of gravity.

In many applications of the parametrically excited pendulum, the main aspiration and attention is in achieving solutions that do not exceed the vertical static equilibrium, as this might correspond to failure in some sense, such as ship capsize. For this reason within this thesis, solutions that capture our intrigue are ones whose characteristics are of oscillatory nature. That is, motions that describe a pendulum swinging back and fro, instead of obviously undergoing rotations around the pivot point.

The parametrically excited pendulum system may be simplified for small oscillations to the damped Mathieu equation, and this Chapter is concerned initially with determining the corresponding zones of instability (Stoker, 1950, Jordan and Smith, 1987, Grimshaw, 1993). It is important to investigate these instability regions since this

is where oscillatory and rotational motion of the pendulum are initially instigated.

As mentioned above, since we are interested in oscillatory behaviour, it is also significant to be able to determine the boundaries where such oscillatory motions seize to exist for this system and where zones of any other types of motion, such as rotational, oscillating-rotational, or chaotic, are first established.

Such parameter regimes that lead to solutions of the latter nature or in other words regions where executed solutions that go beyond the vertical condition, after a finite number of cycles of applied parametric excitation, are termed as "Escape Zones". This Chapter adopts two different methods to provide approximate escape boundaries, which are compared with existing research literature (Clifford and Bishop, 1994, 1996) with the hope of providing a complete agreement or even better approximations to already cited material.

Much work has been undertaken on the subject of escape, particularly in understanding escape from an asymmetric potential well under direct forcing (Thompson, 1989, Szemplińska-Stupnicka, 1995). Such a problem is common in engineering and physical sciences, such as the possible capsize of ships, which is an issue we shall tackle within other parts of the thesis.

Moreover, the deep analytical and numerical work within this Chapter will also provide the necessary mathematical skills and foundations for the Chapters that follow.

2.2 Equation of motion

A pendulum consisting of any rigid body that can swing and rotate about some fixed horizontal axis, is called a *compound* (or *physical*) pendulum. We shall however, consider a *simple* pendulum as it is the simplest form of a pendulum, represented by a small bob at the end of a rigid rod of negligible mass. We employ a rigid rod rather than a flexible string, in order to examine strictly swinging to and fro motions and revolutions of the pendulum at pivot point.

The idealised model of the simple pendulum consisting of a point of mass m and length l, constrained to move in a vertical plane under the influence of gravity and whose suspension point is subjected to a vertical time-history displacement $z(\tau)$, is shown below in Figure 2.1.

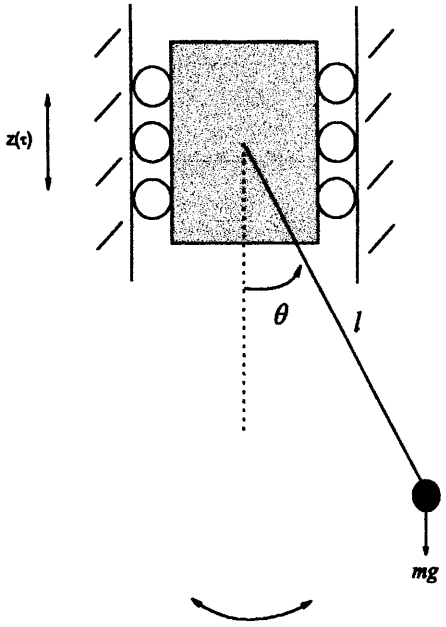

Figure 2.1: *Idealised model of the parametrically excited pendulum.*

The equation of motion of the forced pendulum in terms of the angle of oscillation θ that defines its configuration, is:

$$l^2\ddot{\theta} + \frac{\beta}{m}\dot{\theta} + l(g - \ddot{z})\sin\theta = 0 \tag{2.2.1}$$

where β corresponds to a linear viscous damping and an overdot, differentiation with respect to time, τ. Scaling time and using the following notation where ω_0 represents the natural frequency of the pendulum and Ω the frequency of the cosinusoidal time-history displacement,

$$\omega_0 = \sqrt{(\tfrac{g}{l})},\ t = \omega_0\tau,\ c = \tfrac{\beta}{\omega_0 ml^2},\ z(\tau) = Z\cos\Omega\tau$$

equation (2.2.1) may now be reduced to,

$$\theta'' + c\theta' + (1 + p\cos\omega t)\sin\theta = 0 \tag{2.2.2}$$

with $p = \frac{Z\Omega^2}{g}$ and $\omega = \frac{\Omega}{\omega_0}$. The parameters c, p, ω are the scaled forms of damping coefficient, amplitude and frequency of parametric excitation and the natural frequency, ω_0 is now scaled to one. The equation of motion may be obtained using Lagrangian or Newtonian methods (Trueba *et al*, 2003). The actual derivation of the equation using Lagrangian formulation may be seen in *Appendix A*.

This equation is referred to as the vertically driven pendulum equation. It is structurally identical to equation (2.2.1) but it is written in a generalised dimensionless form. It has the advantage that of the original six parameters $(g, l, m, \beta, Z, \Omega)$ only (c, p, ω) are left. Also, due to the non-dimensional character of all the terms, equation (2.2.2) can be used to compare directly the dynamics of nonlinear driven oscillators in any field.

Without loss of generality, when $p = 0$, so with the absence of parametric forcing, the simple damped pendulum equation is recovered (Nelson and Olsson, 1986):

$$\theta'' + c\theta' + \sin\theta = 0 \tag{2.2.3}$$

As Figure 2.1 shows, the angle θ is measured from the lower hanging position. When the motion is measured from the upper position, so around $(\theta - \pi)$, equation (2.2.2) may be written as,

$$\theta'' + c\theta' - (1 + p\cos\omega t)\sin\theta = 0 \tag{2.2.4}$$

and it is said to represent the inverted case of the parametrically driven pendulum (Kalmus, 1970, Michaelis, 1985, Acheson, 1993, Sudor and Bishop, 1999, Butikov, 2001). Although equation (2.2.2) and (2.2.4) incorporate a periodically driving term, the $\theta = \theta' = 0$ position always remains a solution and similarly for $\theta = \pi, \theta' = 0$.

The parametrically excited pendulum system exhibits a large variety of responses, including symmetric oscillations, non-symmetric oscillations, whereby in a physical sense, the latter usually describes an oscillation whose swing on one side is greater than its symmetric counterpart, rotations, inverted oscillations, so called tumbling motions, which are a combination of rotations and oscillations and also chaotic motions (Bishop and Clifford, 1994a, 1994b, Capecchi and Bishop, 1994, Clifford and Bishop, 1996, Newman *et al*, 2000, Szemplińska-Stupnicka *et al*, 2000).

2.3 Downward hanging solution

2.3.1 Reduction to the Damped Mathieu Equation

Equation (2.2.2) has an obvious solution of $\theta(t) = 0$, representing the downward hanging position as previously mentioned. This equation can not be solved analytically, but if we assume that θ remains near the equilibrium point throughout the motion, it may be linearised. Linearisation around $(0, 0)$, by Taylor expansion, leads $\sin\theta$ to be approximated as θ, since

$$\sin\theta = \theta - \tfrac{\theta^3}{3!} + \ldots$$

so that the equation of motion reduces to:

$$\theta'' + c\theta' + (1 + p\cos\omega t)\theta = 0. \tag{2.3.1}$$

After some rescaling manipulation subject to $\tau = \frac{\omega t}{2}$ and further differentiating with respect to τ,

$$\ddot{\theta} + \frac{2c}{\omega}\dot{\theta} + (\frac{4}{\omega^2} + \frac{4p}{\omega^2}\cos 2\tau)\theta = 0. \tag{2.3.2}$$

A change of variable and appropriate substitution lead to the typical form of the damped Mathieu equation (McLachlan, 1947, Stoker, 1950, Guckenheimer and Holmes, 1983, Jordan and Smith, 1987, Grimshaw, 1993, Turyn, 1993)

$$\ddot{x} + d\dot{x} + (\delta + \varepsilon\cos 2\tau)x = 0 \tag{2.3.3}$$

where $d = \frac{2c}{\omega}$, $\delta = \frac{4}{\omega^2}$ and $\varepsilon = \frac{4p}{\omega^2}$. The system is π periodic in x. The undamped version was firstly derived by Mathieu (Mathieu, 1868).

It is well known that the (δ, ε) plane consists of regions of stability and instability bounded by curves that are separated by periodic solutions. Mathieu unstable zones form resonance tongues centred at $\delta = n^2$, where $n = 0, 1, 2, 3..$ and by adding the damping term, $d > 0$, the tongues shift upwards away from the δ-axis. The largest resonant zone is centered at $\delta = 1$ and it is called the primary unstable zone.

Outside the resonance tongues, the simple up and down motion of the pendulum is stable and there is no swinging from side to side. Mullin (Mullin, 1993) refers to this as the trivial solution. If a parameter such as the frequency is changed so that a resonant region is entered, in other words entering the tongue, the pendulum swings from side to side. Hence the up and down state has become unstable and is replaced by side to side swinging motion.

It is inside these resonance regions where the pendulum is said to be parametrically excited. Inside the primary resonant tongue, which covers the widest range of parameter space of any of the resonance bands, the pendulum oscillates at half the driving frequency or similarly at twice the forcing period, as any child driving a swing soon learns.

2.3.2 Stability boundaries for the damped Mathieu Equation

To determine the stability boundaries of the zones of the above Mathieu equation (2.3.3), perturbation methods are considered (Nayfeh, 1993, Grimshaw, 1993).

We shall consider the general theory of Floquet and the Wronskian (Jordan and Smith, 1987, Grimshaw, 1993, Nayfeh, 1993) for parametric resonance without any limitations or restrictions on the linear damping term d. The analysis employed below is motivated by the work of Erdos (Erdos *et al*, 1996) who examined the stability areas of the inverted damped pendulum and which we apply here for the damped Mathieu equation.

We also remark that we employ and use some theory and definitions of the Floquet theory and variational system in order to determine the stability border, without proving the theorems as such. The proof of the theorems may be found in Arnol'd (Arnol'd, 1991).

We begin by converting the second order equation for the unknown function $x(\tau)$, (equation (2.3.3)), to an equivalent first order system. Thus let

$$x_1 = x, \quad x_2 = \dot{x}$$

and form the equivalent first order system expressed as a state space matrix,

$$\begin{bmatrix} \dot{x}_1 \\ \dot{x}_2 \end{bmatrix} = \begin{bmatrix} 0 & 1 \\ -(\delta + \varepsilon \cos 2\tau) & -d \end{bmatrix} \begin{bmatrix} x_1 \\ x_2 \end{bmatrix}.$$

This has the same form as the following first order homogeneous linear system (since there is no vector function of τ on the right hand side of equation (2.3.3)):

$$\dot{\underline{x}} = A(\tau)\underline{x},$$

where $A(\tau)$ is an $n \times n$ matrix function of τ, continuous for τ on the closed interval, say $a \leq \tau \leq b$), of the real line. $\underline{x} \in \mathbb{R}^n$ and $A(\tau + T) = A(\tau)$ for all τ. The matrix is periodic with a period $T = \frac{2\pi}{2} = \pi$.

It is noted that $trA(\tau) = -d$. By properties of homogeneous systems, if $x^1(\tau)$ and $x^2(\tau)$ are solutions of the above homogeneous linear system, then so is $x = c_1x^1(\tau) + c_2x^2(\tau)$ for any two scalar constants c_1 and c_2. If $x^1(\tau)$ and $x^2(\tau)$ are two linearly independent solutions then we may now form the fundamental matrix $X(\tau)$ of the above state space matrix such that $X(0) = I$, where I is a 2×2 identity matrix. Hence,

$$X = \begin{bmatrix} x^1 & x^2 \\ \dot{x}^1 & \dot{x}^2 \end{bmatrix},$$

such that

$$x^1(0) = 1, \quad x^2(0) = 0,$$

$$\dot{x}^1(0) = 0, \quad \dot{x}^2(0) = 1.$$

Then by Floquet theory, $X(\tau + T)$ is also a fundamental matrix and there exists a non singular constant matrix M such that

$$X(\tau + T) = X(\tau)M \qquad \forall\tau.$$

The matrix M is given by, $M = X^{-1}(0)X(T)$, where $X(0) = I$, so that

$$M = \begin{bmatrix} x^1(T) & x^2(T) \\ \dot{x}^1(T) & \dot{x}^2(T) \end{bmatrix}.$$

Following theory, the determinant of matrix M is then given by:

$$\begin{aligned} Det(M) &= e^{\int_0^T trA(s)\,ds} \\ &= e^{-dT}. \end{aligned} \tag{2.3.4}$$

Since $T = \frac{2\pi}{\omega} = \pi$, then $Det(M) = e^{-\pi d}$. Indeed, more is true:

$$Det(M) = x^1\dot{x}^2 - x^2\dot{x}^1 = e^{-\pi d} \qquad \text{(for all } \tau\text{)}.$$

The stability of the hanging solution depends on the characteristic multipliers λ_1, λ_2 which are the eigenvalues of the characteristic equation of matrix M:

$$\lambda^2 - Tr(M)\lambda + Det(M) = 0, \qquad \text{where} \qquad Tr(M) = (x^1(T) + \dot{x}^2(T)).$$

Hence from equation (2.3.4),

$$\lambda^2 - Tr(M)\lambda + e^{-\pi d} = 0.$$

The roots or otherwise the characteristic multipliers, are given by

$$\lambda_{1,2} = \frac{Tr(M) \pm \sqrt{(Tr(M)^2 - 4e^{-\pi d})}}{2} \tag{2.3.5}$$

Some useful relations are noted:

$$\lambda_1\lambda_2 = e^{-\pi d} \qquad \text{and} \qquad \lambda_1 + \lambda_2 = Tr(M). \tag{2.3.6}$$

The characteristic exponents are $\mu_{1,2}$, where $\lambda_{1,2} = e^{\mu_{1,2}T}$. Consequent to (2.3.6),

$$\mu_1 + \mu_2 = -d. \tag{2.3.7}$$

In the case of negative damping, so when $d < 0$, it can be deduced from (2.3.6) that at least one of $|\lambda_1|$ and $|\lambda_2|$ is greater than one and the corresponding solution describes unstable behaviour (Guckenheimer and Holmes, 1983, Arnol'd, 1991, Arrowsmith and Place, 1992). From (2.3.7) at least one of $Re(\mu_1)$ and $Re(\mu_2)$ is positive which under the stability condition means that unstable behaviour is present.

When $d > 0$, there are two cases that we must consider. From (2.3.5), if

$$\begin{aligned} |Tr(M)| &\geq (4e^{-\pi d})^{\frac{1}{2}} \\ &= 2e^{\frac{-\pi d}{2}} \end{aligned} \tag{2.3.8}$$

then the roots of the characteristic equation for M are real and positive.

Whereas if

$$\begin{aligned} |Tr(M)| &< (4e^{-\pi d})^{\frac{1}{2}} \\ &= 2e^{\frac{-\pi d}{2}} \end{aligned} \tag{2.3.9}$$

then $\lambda_{1,2}$ are both complex-valued roots. Looking closely at the latter case first, we determine that $Det(M) = e^{-\pi d}$ is less than one since d is of positive value. From the eigenvalue product relation found above, we can conclude that

$$\lambda_1\lambda_2 = Det(M) < 1$$

corresponding to stable behaviour (Arnol'd, 1991, Arrowsmith and Place, 1992).

In the real eigenvalue case, the conditions for stability are satisfied if

$$\frac{Tr(M) + \sqrt{(Tr(M)^2 - 4e^{-\pi d})}}{2} \leq 1 \qquad \text{and} \qquad \frac{Tr(M) - \sqrt{(Tr(M)^2 - 4e^{-\pi d})}}{2} \geq 1. \tag{2.3.10}$$

Combining the stability constraints for both real and complex cases, the stability boundaries are finally defined by

$$\begin{aligned} Tr(M) &= \pm(1 + Det(M)) \\ &= \pm(1 + e^{-\pi d}). \end{aligned} \tag{2.3.11}$$

Of course, with $\varepsilon = 0$, $\delta = \omega^2$ and no damping present, equation (2.3.3), reduces to the simple harmonic oscillator equation, whose solutions are well known and understood. We make a parenthesis here, to note that the general solution of equation (2.3.3) with $\varepsilon = 0$ and $\delta = \omega^2$ is

$$x = c_1 \cos\omega\tau + c_2 \sin\omega\tau$$

and is periodic with a period $T_0 = \frac{2\pi}{\omega}$. Following previous definition:

$$x^1 = \cos\omega\tau, \quad x^2 = \tfrac{1}{\omega}\sin\omega\tau.$$

Hence, since $Tr(M) = (x^1(T) + \dot{x}^2(T))$, then following conventional notation by Grimshaw (Grimshaw, 1993), we allow the variable ϕ to be $\phi = \frac{Tr(M)}{2}$ such that,

$$\phi = \frac{Tr(M)}{2} = \cos\omega T \qquad (\text{for } \varepsilon = 0).$$

For $\varepsilon = 0$, $-1 \leq \phi \leq 1$ for all values of ω, and there is stability unless $\phi = \pm 1$, or equivalently, ωT is an integer multiple of π. The stability boundaries for $\varepsilon = 0$ are therefore given by,

$$\phi = 1, \qquad \omega T = 2k\pi \qquad \text{or} \quad T = kT_0$$

$$\phi = -1, \qquad \omega T = (2k+1)\pi \qquad \text{or} \quad 2T = (2k+1)T_0$$

where $k = 0, 1, 2, ...$ These are the conditions for parametric resonance so that when $\phi = 1$, there is a solution x with period T, while when $\phi = -1$, there is a solution x with period $2T$.

Recalling the case with damping present but still with $\varepsilon = 0$, the general solution of equation (2.3.3) is

$$x = e^{\frac{d\tau}{2}}(c_1 \cos\omega\tau + c_2 \sin\omega\tau)$$

where $\omega^2 = \delta - \frac{d^2}{4}$ (obtained by replacing back the general solution into equation (2.3.3), with $\varepsilon = 0$, and comparing coefficients). Referring now to Grimshaw (Grimshaw, 1993), if $\delta > \frac{d^2}{4}$, then the solutions are always stable (since the real parts of the characteristic multipliers are negative) and if $\delta < \frac{d^2}{4}$, then the general solution is of hyperbolic nature, with conditions of stability of solution if $\delta > 0$ and instability if $\delta < 0$, thus for positive damping, the stability boundaries cross the axis at $\delta = 0$.

So, in order to discuss parametric resonance and obtain information about the stability boundaries in the (δ, ε) plane, we suppose that d,$\varepsilon \to 0$ simultaneously

(Grimshaw, 1993). With this joint limit, the stability boundaries are given by $\phi = \pm 1$ and it follows from general theory that the conditions for parametric resonance with damping set to zero are given by:

$$\delta = (2k)^2 \quad or \quad \delta = (2k+1)^2.$$

where $k = 0, 1, 2, ...$ We note that when $\varepsilon = 0$ and $\delta = (2k)^2$, there is a solution of the undamped version of (2.3.3) with period π, but when $\varepsilon = 0$ and $\delta = (2k+1)^2$ there is a solution of undamped (2.3.3) with period 2π. The instability boundaries in the (δ, ε) plane will cross the $\varepsilon = 0$ axis at the points defined by the above conditions of δ.

Most importantly, the boundary between stable and unstable behaviour is characterized by the existence of periodic solutions of (2.3.3) with period T or $2T$. This suggests that the mechanism of instability is the occurrence of a resonance between the imposed period T and some natural period. To analyse the stability boundaries when $\delta \approx n^2$ where $n = 0, 1, 2..$, and ε and d are both small, we seek a solution of (2.3.3) of the form

$$x = e^{\mu\tau} q(\tau), \tag{2.3.12}$$

where $q(\tau)$ is a periodic function of period π when n is an even integer ($n = 2k$) and has period 2π when n is an odd integer ($n = 2k+1$). Substituting (2.3.12) into (2.3.3) we get

$$\ddot{q} + (2\mu + d)\dot{q} + (\mu^2 + \mu d)q + (\delta + \varepsilon \cos 2\tau)q = 0. \tag{2.3.13}$$

The condition that the solutions of (2.3.13) have the required periodicity determines

μ as a function of d, δ and ε. It is noticed that by letting

$$\widehat{\mu} = \mu + \tfrac{1}{2}d \text{ and } \widehat{\delta} = \delta - \tfrac{1}{4}d^2,$$

then (2.3.13) simplifies to the form,

$$\ddot{q} + 2\widehat{\mu}\dot{q} + \widehat{\mu}^2 q + (\widehat{\delta} + \varepsilon\cos 2\tau)q = 0. \tag{2.3.14}$$

Since the analyticity of the solutions of (2.3.14) with respect to the parameter ε can be assumed, this allows us to seek solutions of (2.3.14) of the form:

$$\begin{aligned} q &= q_0(\tau) + \varepsilon q_1(\tau) + \varepsilon^2 q_2(\tau) + \ldots \\ \widehat{\mu} &= \varepsilon\widehat{\mu_1} + \varepsilon^2\widehat{\mu_2} + \ldots \\ \widehat{\delta} &= n^2 + \varepsilon\widehat{\delta_1} + \varepsilon^2\widehat{\delta_2} + \ldots \end{aligned} \tag{2.3.15}$$

noting that the leading order term for $\widehat{\mu}$ is zero ($\widehat{\mu_0} = 0$) and the leading order term for $\widehat{\delta}$ is $\widehat{\delta_0} = n^2$. These equations can be substituted into (2.3.14) so that the result will be a power series in ε. Since this power series must vanish due to the equality to zero, the coefficient of each power of ε must be zero. Applying this process up to the coefficients of the second power of ε, (in other words comparing coefficients up to ε^2), we have

$$\begin{aligned} \ddot{q_0} + n^2 q_0 &= 0 \\ \ddot{q_1} + n^2 q_1 + 2\widehat{\mu_1}\dot{q_0} + (\widehat{\delta_1} + \cos 2\tau)q_0 &= 0 \\ \ddot{q_2} + n^2 q_2 + 2\widehat{\mu_1}\dot{q_1} + (\widehat{\delta_1} + \cos 2\tau)q_1 + 2\widehat{\mu_2}\dot{q_0} + \widehat{\mu_1^2}q_0 + \widehat{\delta_2}q_0 &= 0. \end{aligned} \tag{2.3.16}$$

To obtain significant information about the stability boundaries, we now look into the cases for when $n = 1, 2$. These are the equivalent $\widehat{\delta} \approx 1 - \frac{d^2}{4}$ and $\approx 4 - \frac{d^2}{4}$ cases.

(i) $n = 1$: This case provides the largest zone of instability. Since n is an odd integer, $q(\tau)$ and each $q_0(\tau)$,$q_1(\tau)$, $q_2(\tau)$ have a period 2π. From (2.3.16) we see that,

$$\ddot{q_0} + q_0 = 0$$

so that the solution is

$$q_0 = A_0 \cos\tau + B_0 \sin\tau.$$

It then follows that by substituting the above expression for q_0 into (2.3.16), we arrive at

$$\ddot{q_1} + q_1 + (\widehat{\delta_1} A_0 + \tfrac{1}{2} A_0 + 2\widehat{\mu_1} B_0)\cos\tau - (-\widehat{\delta_1} B_0 + \tfrac{1}{2} B_0 + 2\widehat{\mu_1} A_0)\sin\tau + \tfrac{1}{2} A_0 \cos 3\tau + \tfrac{1}{2} B_0 \sin 3\tau = 0$$

where trigonometric identities

$$2\cos 2\tau \cos\tau = \cos 3\tau + \cos\tau \qquad \text{and} \qquad 2\cos 2\tau \sin\tau = \sin 3\tau - \sin\tau$$

were used.

The general solution for q_1 is

$$q_1 = A_1 \cos\tau + B_1 \sin\tau + \tfrac{1}{2}(-\widehat{\delta_1} A_0 - \tfrac{1}{2} A_0 - 2\widehat{\mu_1} B_0)\tau \sin\tau - \tfrac{1}{2}(-\widehat{\delta_1} B_0 + \tfrac{1}{2} B_0 + 2\widehat{\mu_1} A_0)\tau \cos\tau + \tfrac{1}{16} A_0 \cos 3\tau + \tfrac{1}{16} B_0 \sin 3\tau..$$

For q_1 to be periodic with period 2π, the coefficients of the terms $\frac{1}{2}\tau\sin\tau$ and $-\frac{1}{2}\tau\cos\tau$ must be zero as they are the only non-periodic terms. Setting the coefficients of the non-periodic terms to zero, we get

$$\begin{aligned} -(\widehat{\delta_1}+\frac{1}{2})A_0 + 2\widehat{\mu_1}B_0 &= 0 \\ (\widehat{\delta_1}-\frac{1}{2})B_0 + 2\widehat{\mu_1}A_0 &= 0. \end{aligned} \tag{2.3.17}$$

Making B_0 the subject in the latter expression and then substituting it in the first, for a non-trivial solution (so for $A_0 \neq 0$),

$$4\widehat{\mu_1^2} = \tfrac{1}{4} - \widehat{\delta_1^2}.$$

Revisiting the definitions in (2.3.15), this corresponds to

$$4\widehat{\mu^2} \approx \tfrac{1}{4}\varepsilon^2 - (\widehat{\delta}-1)^2.$$

For $\frac{1}{4}\varepsilon^2 > (\widehat{\delta}-1)^2$ the solutions for $\widehat{\mu}$ are both real with at least one $\widehat{\mu_{1,2}} > 0$ and by the stability conditions, this corresponds to unstable behaviour.

On the contrary, when $\frac{1}{4}\varepsilon^2 < (\widehat{\delta}-1)^2$, the solutions for $\widehat{\mu}$ are both complex corresponding to stable behaviour. Therefore the stability boundary occurs when $\widehat{\mu}=0$ and is given by

$$\widehat{\delta} - 1 \approx \pm\frac{1}{2}\varepsilon. \tag{2.3.18}$$

Since initially we let $\widehat{\mu} = \mu + \frac{1}{2}d$ and $\widehat{\delta} = \delta - \frac{1}{4}d^2$, it mathematically follows from an above expression that

$$(2\mu + d)^2 \approx \tfrac{1}{4}\varepsilon^2 - (\delta - \tfrac{1}{4}d^2 - 1)^2.$$

Thus for $(\delta - \frac{1}{4}d^2 - 1)^2 > \frac{1}{4}\varepsilon^2$, the solutions are complex-valued whereas for $(\delta - \frac{1}{4}d^2 - 1)^2 < \frac{1}{4}\varepsilon^2$ the solutions are real valued. The stability boundary, is hence given by $\mu = 0$ so that

$$d^2 + (\delta - \frac{1}{4}d^2 - 1)^2 \approx \frac{1}{4}\varepsilon^2. \tag{2.3.19}$$

This equation, (2.3.19), is the same up to order d^2 to that derived by Grimshaw (Grimshaw, 1993), allowing our analysis to provide a better analytical boundary approximation. For each $d > 0$, (2.3.19) is a hyperbola in the (δ, ε) plane which is asymptotic to the straight lines $(\delta - 1) \approx \pm\frac{1}{2}\varepsilon$. We note that these lines are the stability boundaries without the presence of damping.

(ii) $n = 2$: This case provides the instability region for the second main zone. Since n is an even integer, $q(\tau)$ has a period π. From (2.3.16) we see that,

$$\ddot{q_0} + 4q_0 = 0$$

so that

$$q_0 = A_0 \cos 2\tau + B_0 \sin 2\tau.$$

Substituting the above expression of q_0 into (2.3.16) and using trigonometric identities we reach,

$$\ddot{q_1} + 4q_1 - (\widehat{\delta_1} A_0 - 4\widehat{\mu_1} B_0) \cos 2\tau - (-\widehat{\delta_1} B_0 + 4\widehat{\mu_1} A_0) \sin 2\tau +$$

$$+\tfrac{1}{2} A_0 (1 + \cos 4\tau) + \tfrac{1}{2} B_0 \sin 4\tau = 0.$$

Removing the coefficients of the non-periodic terms by equating them to zero leaves,

$$\begin{aligned} -\widehat{\delta_1} A_0 - 4\widehat{\mu_1} B_0 &= 0 \\ \widehat{\delta_1} B_0 - 4\widehat{\mu_1} A_0 &= 0. \end{aligned} \tag{2.3.20}$$

Hence by substitution and elimination, for a non-trivial solution,

$$16\widehat{\mu_1^2} = -\widehat{\delta_1^2}$$

and from the definitions in (2.3.15), this finally leads to

$$16\widehat{\mu^2} \approx -(\widehat{\delta} - 4)^2.$$

When $\widehat{\delta} \neq 4$, the roots of $\widehat{\mu}$ are both complex and purely imaginary and correspond to stable behaviour. The stability boundary is given here at $\widehat{\mu} = 0$ so when $\widehat{\delta} = 4$.

It is necessary to continue to the next order of ε as the unstable zone has not yet been distinguished since its width is $O(\varepsilon^2)$. As a result, for this purpose, we may set $\widehat{\mu_1} = \widehat{\delta_1} = 0$ (due to $\varepsilon\widehat{\mu_1} \approx \widehat{\mu} = 0$ and $\varepsilon\widehat{\delta_1} \approx \widehat{\delta} - n^2 = 0$) so that the general solution of q_1 is now of the form,

$$q_1 = A_1 \cos 2\tau + B_1 \sin 2\tau + \tfrac{1}{24}A_0 \cos 4\tau + \tfrac{1}{24}B_0 \sin 4\tau - \tfrac{1}{8}A_0.$$

Substitution of the above forms of q_0 and q_1 and using trigonometric expansions result in (2.3.16) becoming:

$$\ddot{q_2} + 4q_2 - (\widehat{\delta_2}A_0 - 4\widehat{\mu_2}B_0 + \tfrac{5}{48}A_0)\cos 2\tau - (-\widehat{\delta_2}B_0 + 4\widehat{\mu_2}A_0 - \tfrac{1}{48}B_0)\sin 2\tau + \tfrac{1}{48}A_0 \cos 6\tau + \tfrac{1}{48}B_0 \sin 6\tau + \tfrac{1}{2}A_1(1 + \cos 4\tau) + \tfrac{1}{2}B_1 \sin 4\tau = 0.$$

Removal of the secular, non-periodic terms (in other words equating the coefficients of $\cos 2\tau$ and $\sin 2\tau$ to zero), we reach

$$\begin{aligned} -(\widehat{\delta_2} - \frac{5}{48})A_0 - 4\widehat{\mu_2}B_0 &= 0 \\ (\widehat{\delta_2} + \frac{1}{48})B_0 - 4\widehat{\mu_2}A_0 &= 0. \end{aligned} \tag{2.3.21}$$

Thus for a non-trivial solution,

$$16\widehat{\mu_2^2} = -(\widehat{\delta_2} + \tfrac{1}{48})(\widehat{\delta_2} - \tfrac{5}{48})$$

and recalling the definitions in (2.3.15),

$$16\widehat{\mu}^2 \approx -[(\widehat{\delta}-4)+\tfrac{1}{48}\varepsilon^2][(\widehat{\delta}-4)-\tfrac{5}{48}\varepsilon^2].$$

For both roots of $\widehat{\mu}$ to be complex and represent stable behaviour, it is necessary that the following inequalities are satisfied:

$$\widehat{\delta}-4<-\tfrac{1}{48}\varepsilon^2 \qquad \text{or} \qquad \widehat{\delta}-4>\tfrac{5}{48}\varepsilon^2.$$

For them to be real-valued and characterise unstable behaviour,

$$-\tfrac{1}{48}\varepsilon^2<\widehat{\delta}-4<\tfrac{5}{48}\varepsilon^2.$$

Evidently the stability boundary for this case, corresponding to when $\widehat{\mu}=0$ is given by

$$\widehat{\delta}-4\approx-\tfrac{1}{48}\varepsilon^2 \text{ or } \tfrac{5}{48}\varepsilon^2.$$

By inserting the definitions of $\widehat{\mu}=\mu+\frac{1}{2}d$ and $\widehat{\delta}=\delta-\frac{1}{4}d^2$, we are able to find the stability boundaries for $n=2$ of (2.3.14) such that:

$$(4\mu+2d)^2\approx-[(\delta-\tfrac{1}{4}d^2-4)+\tfrac{1}{48}\varepsilon^2][(\delta-\tfrac{1}{4}d^2-4)-\tfrac{5}{48}\varepsilon^2],$$

and so the stability boundary corresponding again to $\mu=0$ leads to the following:

$$4d^2+[(\delta-\frac{1}{4}d^2-4)+\frac{1}{48}\varepsilon^2][(\delta-\frac{1}{4}d^2-4)-\frac{5}{48}\varepsilon^2]\approx 0. \tag{2.3.22}$$

which is again the same as the expression given by Grimshaw (Grimshaw, 1993) up to the second order in d.

Figure 2.2 aids to visualise graphically these zones of instability for the damped Mathieu equation for both cases, so when $\delta \approx 1$ and ≈ 4 on a (δ, ε) space. The dotted regions represent the area with no damping present and the red boundary, corresponds to when the damping constant d is taken to equal 0.1. The shaded regions are the regions corresponding to the unstable zones for the damped equation.

The upward shift of the tongues is clear. For the major tongue, the unstable zone is at approximately a distance $2d(1 + \frac{d^2}{16})^{\frac{1}{2}}$, so at least $2d$ from the $\varepsilon = 0$ axis whereas for the second tongue, the unstable zone shifts upwards by approximately $\frac{\sqrt{3}\sqrt{32d}}{\sqrt{\sqrt{5}}}$. This is at least a distance $\sqrt{32d}$ which agrees with Grimshaw (Grimshaw, 1993).

It is interesting to notice that this upward shift due to the damping, is of different magnitude for each tongue. Adopting the approximate bounding curves for the third and fourth tongue, so when $\delta \approx 9, 16$, given by Turyn (Turyn, 1993) in his study of the damped Mathieu equation, we are able to calculate an approximate to the least position of these tongues as well from the δ-axis for $d = 0.1$.

As a consequence, we introduce Figure 2.3 which shows in black a curve depicting the direction of the upward movement of each tongue in the (δ, ε) plane for tongues centered at $\delta \approx 1, 4, 9, 16$ for $d = 0.1$. In other words, the least distance of ε from the δ-axis for each tongue was joined to form the black curve.

Using a least squares fitting method, where we have employed a polynomial function of order-2 to the points in the (δ, ε) plane, we are able to approximate the black curve in Figure 2.3. The fitted curve is shown by the dashed red curve. Due to the limited number of points, a parabolic function was chosen as opposed to higher order polynomials to best describe the given points and their path. The equation of the fitted curve is hence given as $\varepsilon = -0.3764 + 0.633\delta - 0.0112\delta^2$.

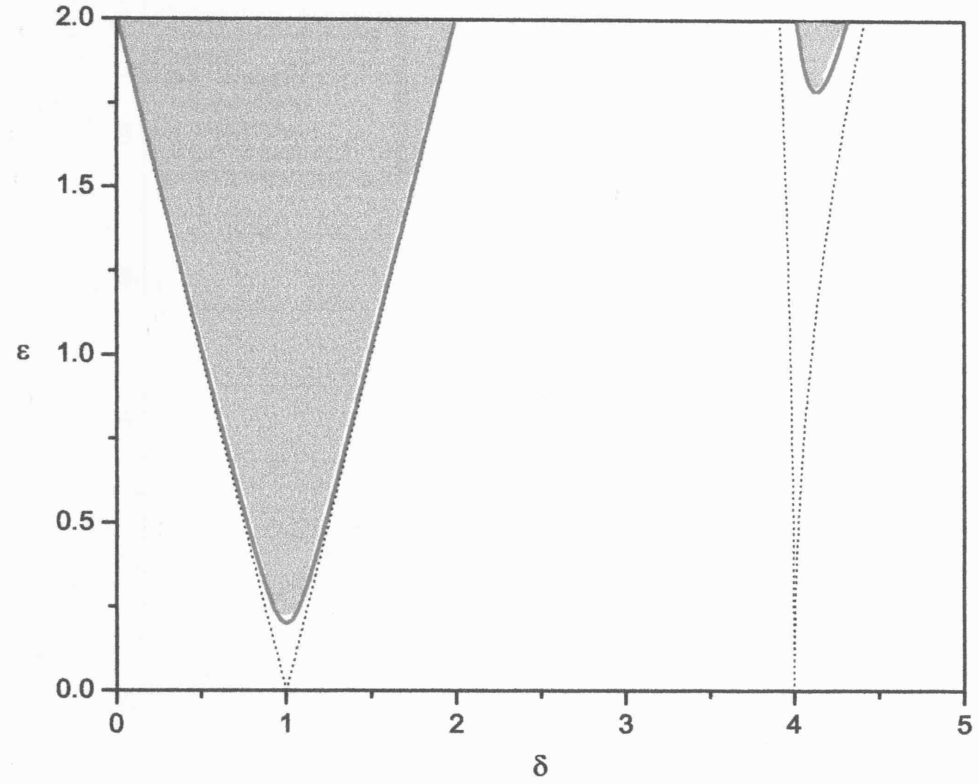

Figure 2.2: *The zones of instability for the damped Mathieu equation when* $d = 0.1$. *The dotted lines represent no damping whereas the red boundary shows the effects of the presence of damping; shifting of the tongues in an upwards manner. The shaded regions correspond to unstable regions.*

How successful the fit is in explaining the variation of the data is given by R^2, hence the square of the correlation between the response values and the predicted response values. As the value is close to one, $R^2 = 0.9994$, we may say with certainty that for these given points in the (δ, ε) plane range, the least squares parabola routine provides a very good approximation.

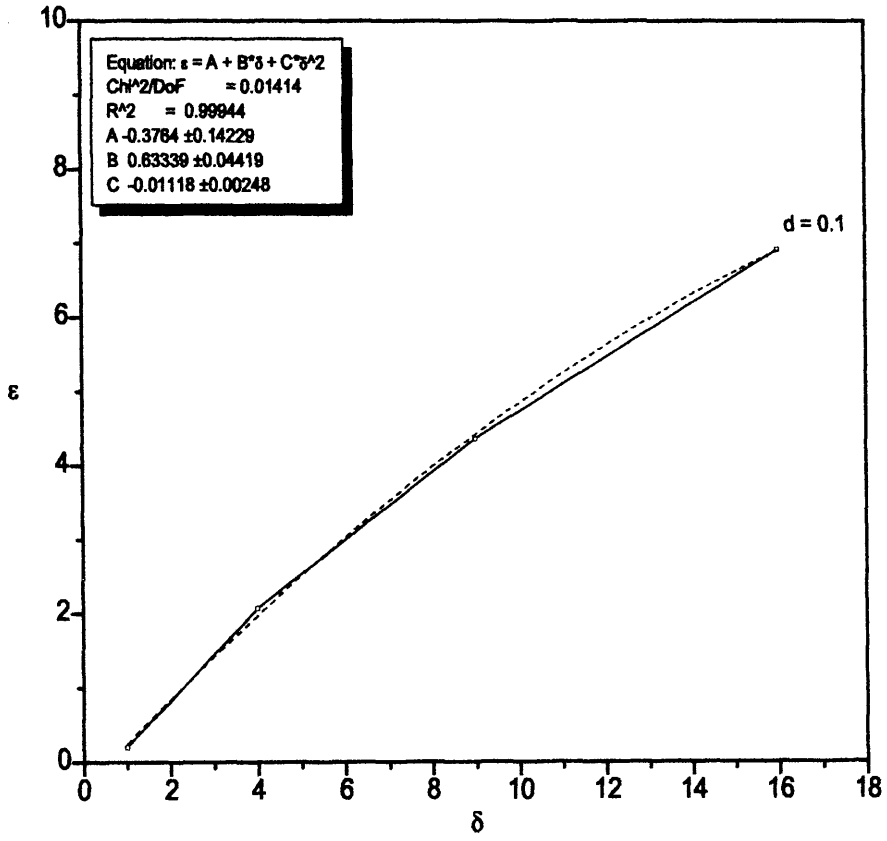

Figure 2.3: *Black squares correspond to the least distance from the δ-axis to the tongues at around $\delta \approx 1, 4, 9, 16$ at $d = 0.1$ and they are joined to form the black curve. The red dashed curve is the parabolic curve that best fits the actual response values.*

This way, for damping value set at $d = 0.1$, an approximate relation between δ and ε may be reached predicting the future effects of damping in terms of the upward movement of a tongue from the δ-axis. Of course, if more points were available from the analytical procedure for other Mathieu tongues, the predicted quadratic equation may be better examined.

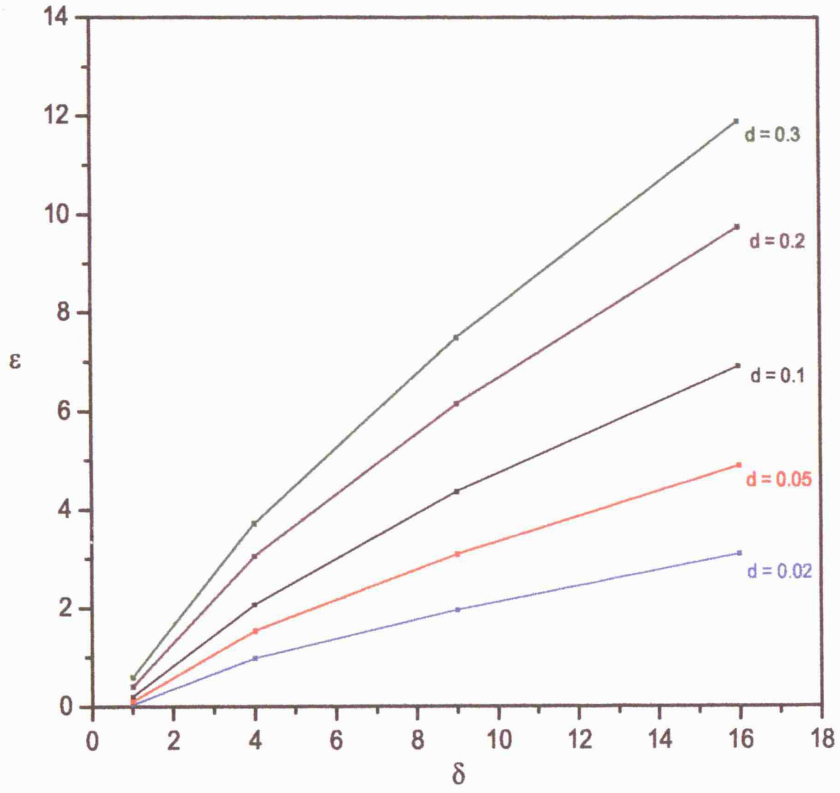

Figure 2.4: *Curves corresponding to the least distance from the δ-axis to the tongues at around $\delta \approx 1, 4, 9, 16$ at different damping values. Each point forming the coloured curves represents the upward shift of the tongues and are colour-coordinated to the respective damping values.*

Figure 2.4 shows, for different values of damping, the corresponding curve identifying the gap between the δ-axis and the least distance of each tongue at around $\delta \approx 1, 4, 9, 16$ in the (δ, ε) plane. As expected, with increasing damping the upward shift of the tongues also increases.

The above analysis of the damped Mathieu equation was necessary and important as now we may provide an approximation to the primary unstable zone of the parametrically excited pendulum equation, (2.3.2), so in terms of ω and p, by substituting the original variables $d = \frac{2c}{\omega}$, $\delta = \frac{4}{\omega^2}$ and $\varepsilon = \frac{4p}{\omega^2}$ into (2.3.19) to give:

$$(\frac{\omega^2}{4} - 1)^2 + \frac{c^2\omega^2}{4} \approx \frac{p^2}{4}. \tag{2.3.23}$$

We note that due to the change of variables, the zone is now centred around $\omega = 2$.

Figure 2.5 depicts this major tongue, where the dotted line represents the no damping case and the red coloured boundary corresponds to the damped form of the equation (2.3.23) in (ω, p) space, at $c = 0.1$. The shaded region reflects the instability region. Additional unstable zones around $\omega = 1, \frac{2}{3}...$ also exist but not shown within this figure. The reason for this is that in the following sections, we will focus on the primary tongue and so for comparison sake, we keep our concern within this zone. The following Chapter will tackle the other resonance tongues in greater detail.

So with the aid of the damped Mathieu equation, we were able to approximate the region of instability of the parametrically excited pendulum system around $\omega = 2$. It is within this region where the hanging position no longer returns to the downward state, and where oscillatory and other types of motion are undergone, once a minimum forcing amplitude and frequency are surpassed.

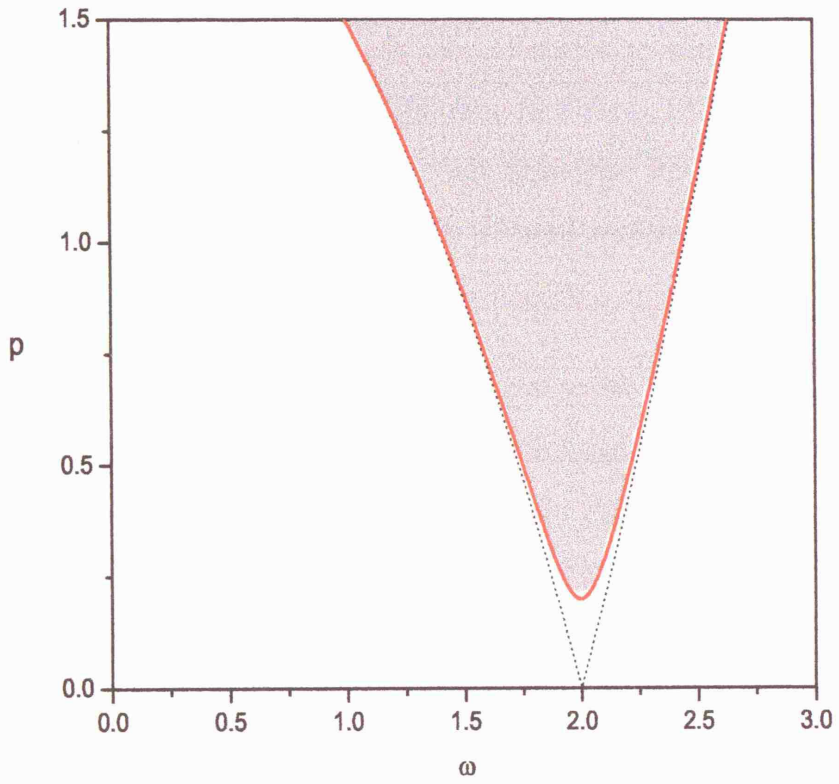

Figure 2.5: *Analytically calculated boundary of the major Mathieu unstable zone in* (ω, p) *space. The dotted lines represent no damping whereas the red boundary corresponds to when damping term* $c = 0.1$. *The shaded region illustrates the unstable region.*

2.4 Parametrically excited pendulum: Oscillating solutions

In this section we consider oscillating solutions or orbits of the parametrically excited pendulum. In many applications of this system, the main interest remains in achieving these type of solutions, which may otherwise be referred to as swinging or non-rotating orbits by other authors (Clifford and Bishop, 1996, Garira and Bishop, 2003). They represent oscillations that do not go beyond $\theta = \pm\pi$, the vertical static equilibrium, but just swing back and forth without rotating completely about the pendulums pivot point.

As mentioned earlier in this Chapter, in practical sense, exceeding this limit might indicate failure in the system such as capsize of ships, and hence we believe this reason ignites interest and moreover we are of the opinion that it is useful to be able to develop a method that may act as a precursor of the phenomenon called "escape" (Thompson, 1989). This will provide the necessary groundwork for the subsequent work in the thesis. Earlier studies on this problem of escape include Bishop and Clifford (Bishop and Clifford, 1994a, 1994b) and Stewart and Faulkner, (Stewart and Faulkner, 2000). Much work has been undertaken on this subject particularly in understanding escape from an asymmetric potential well under direct forcing (Thompson, 1989, Szemplińska-Stupnicka *et al*, 1995) and more recently on parametric escape from an asymmetric potential well (Soliman, 1996).

In the (ω, p) parameter space of the parametrically excited pendulum, values of forcing frequency and amplitude that lie within the corresponding tongue-like figured zones of the Mathieu equation calculated analytically earlier, are said to be in parametric resonance. The resonance zones in which the pendulum with equation of motion (2.2.2) is in parametric resonance occur around $\omega = \frac{2}{n}$, where $n = 1, 2, 3...$

Importantly, the exchange between the state of up and down motion and side to side swinging as a resonance curve is crossed, signifies that a bifurcation has occurred in the solutions to the equations.

Initially we include a bifurcation parameter diagram, (ω, p) parameter space, Figure 2.6, for the oscillatory orbits of the parametrically excited pendulum, taken from Clifford and Bishop (Clifford and Bishop, 1996). It shows the bifurcations around the unstable zone centered around $\omega = 2$. Their bifurcation parameter diagram was produced with numerical combinations of cell-mapping (Hsu, 1987, Alexander, 1998a, 1998b), path-following and bifurcation-following techniques (Parker and Chua, 1989, Foale and Thompson, 1991).

The figure gives an overview of the bifurcational behaviour in the (ω, p) space. The line labelled P_D^S is where small perturbations from the equilibrium $\theta = 0$ will first result in an initial growth. The equilibrium bifurcates into a stable symmetric period-2 solution at a supercritical pitchfork bifurcation whilst to the left of green point c, the equilibrium becomes unstable at a subcritical pitchfork bifurcation. Line S_N corresponds to a period-2 fold where the unstable period-2 solution from the subcritical pitchfork bifurcation stabilises at a saddle node bifurcation.

The line $S_B P_F$ represents the locus of symmetry-breaking, pitchfork bifurcation, where the symmetric period-2 solution splits into two stable anti-symmetric period-2 solutions, (more detail will be discussed in Chapter 3), and line FP_D represents the end of a pair of period doubling cascade of the two asymmetric solutions, although they only show the first sequence since the cascade is very swift.

Lines P_D^S and FP_D form the boundary of the *escape zone* where no major stable non-rotating attractors exist, shaded in grey colour. A typical trajectory for a system which has parameters in the escape zone will exceed $\theta = \pm\pi$ after a finite number

of period of applied parametric forcing.

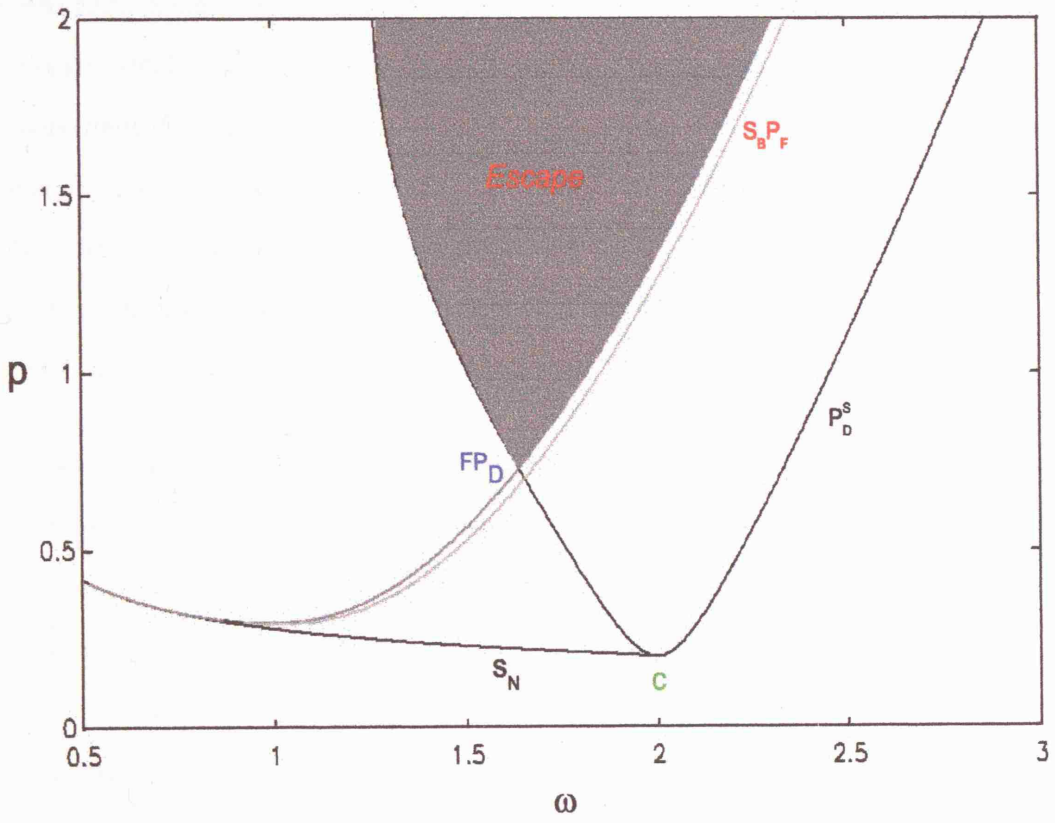

Figure 2.6: *Numerically determined bifurcation parameter diagram of the parametrically excited pendulum centred at $\omega = 2$, taken from Clifford and Bishop (Clifford and Bishop, 1996).*

The features of the bifurcation diagram agree with those produced by Mullin (Mullin, 1993). More detailed explanation of the bifurcations undergone within this major tongue will be examined in the Chapters that follow with the aim of better understanding the nonlinear characteristics of the parametrically excited pendulum system.

Figure 2.7 is our alternative version of a numerically determined bifurcation parameter diagram focusing on the major resonant tongue centred at around $\omega = 2$. This resonant zone was computed with the aid of the software *Dynamics*, (Nusse and Yorke, 1994), by considering the Lyapunov exponents while each parameter was incremented. The purpose of this diagram is to generate a set in the parameter space such that each point in this set, the trajectory through the initial condition is chaotic, that is, it has a positive Lyapunov exponent. Hence we may indicate where within the parameter space, chaos may be observed due to the positiveness of the Lyapunov exponent.

More specifically, this diagram was obtained by dividing the parameter space into a grid for which Lyapunov exponents are calculated, keeping the same initial conditions for each element of the grid, $\theta(0) = 0.1$, $\theta'(0) = 0$. Depending on the different magnitudes of the Lyapunov exponent, a different colour may be allocated. For simplicity though here, we shall consider only three types of colour for the colour code allocation: white, grey and black. The reason is because for the moment our aim is only to understand and visualise where within the control parameter space, regions of oscillatory and non-oscillatory type motions may be experienced. Also, damping is often fixed at $c = 0.1$ and we choose this value, as this is close to typical realistic measurements and allows for comparison with earlier results.

Viewing Figure 2.7, within the zone, regions of periodic oscillatory motions are realised and they are indicated via the grey colour. Outside the resonant zone the black colour represents regions where the downward hanging solution is stable. The chaotic region is coloured in white and corresponds to where no major oscillating solutions exist representing in its own way, an escape parameter region.

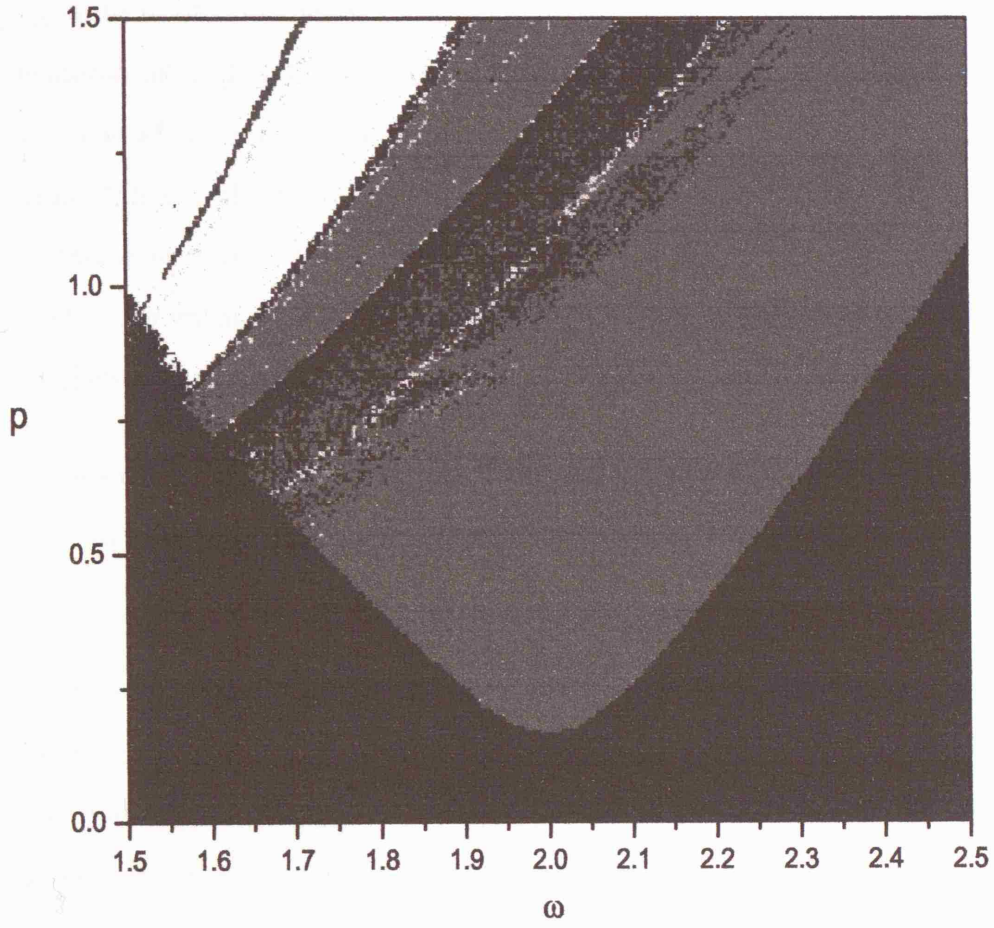

Figure 2.7: *Numerically determined parameter space plot of the parametrically excited pendulum with initial conditions* $\theta(0) = 0.1$, $\theta'(0) = 0$ *and damping* $c = 0.1$. *Grey regions represent oscillatory behaviour, while white areas represent chaotic behaviour that may also correspond to the "escape" zone where no major non-rotating solutions exist. The black area outside the resonant tongue represents regions where the downward hanging solution is stable. The darker segment separating the grey oscillatory zone within the resonant tongue is where symmetry-breaking, pitchfork and period doubling bifurcations are realised.*

Our emphasis here is on motion within the local potential well around $\theta = 0$. So that escape would be considered when almost all initial conditions starting near the hanging state would now leave the local potential well. Thus leaving the well can be considered as a shift to another state. This may also be characterised as the zone of chaos where unpredictable and aperiodic pendulum motions occur. We add the phrase "almost all" initial conditions since Bishop and Clifford, (Bishop et al, 1994a, 1994b) were able to locate initial conditions that resulted in steady state, stable solutions within the well but their basin of attraction is so small as to be most unlikely to be experienced.

We note also that the dark segment separating the grey zone within the resonant tongue is where symmetry-breaking, pitchfork and period doubling bifurcations are exhibited.

The points within the white region and the scattering effects may be accounted for because as in virtually all calculations within this software, some imprecision still remains. We cannot guarantee that the behaviour of the approximate Lyapunov exponents would not change abruptly after say, a hundred thousand iterates. If in fact we had to wait for an infinite time to make a tentative judgement of whether the Lyapunov exponents were positive, the concept of Lyapunov exponent would have little meaning in applications. Nonetheless, the software speaks loosely of Lyapunov exponents as if they can be computed with precision.

As a comparison, we also compute the parameter space plot for large initial angle $\theta(0) = 0.5\pi$, $\theta'(0) = 0$ over the same parameter range. This is seen in Figure 2.8 where the colour code corresponds to the same types of motion as described above. This parameter space plane is similar to that produced by Xu *et al* but over a smaller range of forcing frequency values (Xu *et al*, 2005) and different damping values.

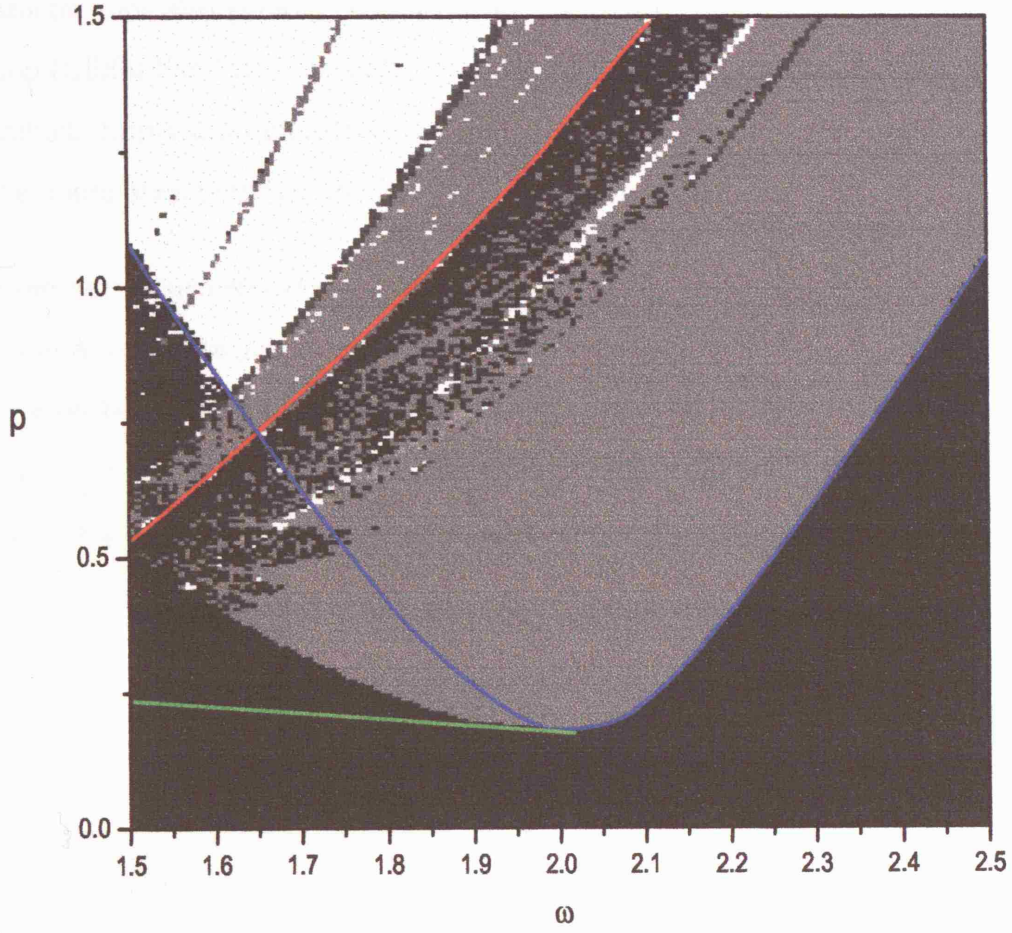

Figure 2.8: *Locus of specific bifurcations (represented by the red, blue and green curves) given by Clifford and Bishop (Clifford and Bishop, 1996) in Figure 2.6 superimposed on our numerically determined parameter space plot of the parametrically excited pendulum with initial conditions set at* $\theta(0) = 0.5\pi$, $\theta'(0) = 0$. *The damping constant is the same for both plots,* $c = 0.1$.

Moreover, this control parameter plot shows similarities to Figure 2.7, however when the motion is initiated with a large angle, the pendulum can be directed to oscillate or rotate even with the parameters outside the resonant tongue zone. This (ω, p) parameter plot also shows correspondence to Figure 2.6, obtained by Clifford and Bishop (Clifford and Bishop, 1996) where the locus of the different bifurcations were identified. Superimposing the two figures shows an adequate and good agreement of the boundaries between oscillatory motions and escape.

The red curve corresponds to their suggested escape boundary, regions within the blue curve represent the areas where oscillatory type motions are undergone and the region bounded between the green and red line is where there is coexisting of hanging and oscillatory solutions (more details shall be shared on this characteristic within Chapter 3).

2.5 Approximate escape zone

In the previous sections we focused our investigation on actually determining the boundary of where oscillatory behaviour is firstly undergone within the major resonant tongue, both analytically and numerically.

For many applications, only oscillating orbits need to be considered ($\theta_{max} < \pi$) and predicting parameter zones where no major stable non-rotating orbits exist is of particular importance for the safe operation of any system. Under such conditions, the parametrically excited pendulum is analogous to a system that permits escape from a symmetric potential well, where escape equations in general have been extensively studied by many researchers (Thompson *et al*, 1987, Thompson, 1989, Szemplińska-Stupnicka *et al*, 1995).

So it follows that we now turn our attention to analytically try and predict the parameter zone where no major oscillating solutions exist which has been termed by other researchers as the escape zone (Clifford and Bishop, 1993, 1994a, 1994b). In order to approximate the escape zone boundary, two bifurcations that bound the zone must be identified (recall Figure 2.6). We also note that since the study will be accomplished here via analytical techniques, the results may only be assumed as an approximate.

Szemplińska-Stupnicka (Szemplińska-Stupnicka *et al*, 1995) have shown that for several escape equations, these two bifurcations are a saddle node and the event at the end of a period doubling cascade of the primary response arising from the unforced equilibrium solution. Since the latter bifurcation is very hard to detect analytically, usually the first period doubling is taken as the initiator of escape. In the case of symmetric systems, the symmetry-breaking, pitchfork bifurcation, that is sufficiently

close to the final bifurcation before escape from the local potential well, may also provide a reasonable estimate. Hence, we will assume that the symmetry-breaking, pitchfork bifurcation for this symmetric system will provide the locus of a curve in the (ω, p) space that is reasonably near to the actual escape providing a good estimate for the lower boundary of the escape parameter zone.

The second bifurcation to be considered is the subcritical bifurcation and this may be determined by adopting the vertical tangency condition (Clifford and Bishop, 1993, Stewart and Faulkner, 2000). This will provide us with an approximate left hand boundary of the escape region. As a result both these approximation criteria will enable us to create sensible conservative estimates for the escape zone.

Following Bryant and Miles (1990a, 1990b, 1990c), Clifford and Bishop (1993), Capecchi and Bishop (1994), we employ the harmonic balance technique and assume a solution of equation (2.2.2) to be of the form

$$\theta(t) = \theta_0 + \alpha \cos \frac{\omega t + \phi}{v} \tag{2.5.1}$$

where $v = 2$ corresponds to the major principle unstable zone and ϕ here, the phase angle. If $\theta_0 = 0$, then $\theta(t)$ is symmetric. Direct substitution into the parametrically excited pendulum equation of motion, (2.2.2), and equating terms of cosine, sine and constant terms, allows us to obtain the following expressions respectively.

$$\begin{aligned} \frac{-\alpha\omega^2}{4} + [p(J_1(\alpha) - J_3(\alpha)) \cos\phi \cos\theta_0 + 2J_1(\alpha) \cos\theta_0] &= 0 \\ \frac{c\alpha\omega}{2} - [p(J_1(\alpha) + J_3(\alpha)) \sin\phi \cos\theta_0] &= 0 \\ \sin\theta_0 [pJ_2(\alpha) \cos\phi - J_0(\alpha)] &= 0 \end{aligned} \tag{2.5.2}$$

where $J_n(\alpha)$ is the Bessel function of order n. The above expressions were obtained with the knowledge of:

$$\begin{aligned}\cos[\alpha\cos(\frac{\omega t}{2})] &= J_0(\alpha) + 2\sum_{n=1}^{\infty} J_{2n}(\alpha)\cos[2n(\frac{\omega t}{2})] \\ \sin[\alpha\cos(\frac{\omega t}{2})] &= 2\sum_{n=1}^{\infty} J_{2n-1}(\alpha)\cos[(2n-1)(\frac{\omega t}{2})].\end{aligned} \tag{2.5.3}$$

Equation (2.5.2*c*) shows that for a symmetric solution to be obtained then

$$\sin\theta_0 = 0. \tag{2.5.4}$$

We note that $\theta_0 = 0$ is automatically satisfied. The asymmetric solution depends on the condition

$$pJ_2(\alpha)\cos\phi - J_0(\alpha) = 0. \tag{2.5.5}$$

Considering the symmetric solution, (2.5.2a,b) reduces to

$$\begin{aligned}\frac{-\alpha\omega^2}{4} + [p(J_1(\alpha) - J_3(\alpha))\cos\phi + 2J_1(\alpha)] &= 0 \\ \frac{c\alpha\omega}{2} - [p(J_1(\alpha) + J_3(\alpha))\sin\phi] &= 0\end{aligned} \tag{2.5.6}$$

and eliminating the constant ϕ by suitably squaring (2.5.6), the relevant symmetric equation becomes

$$[\alpha\omega^2 - 8J_1(\alpha)]^2 + \bar{c}^2\omega^2\alpha^2 - 16p^2[J_1(\alpha) - J_3(\alpha)]^2 = 0 \tag{2.5.7}$$

where we introduce, $\bar{c}$, defined as

$$\bar{c} = 2c\frac{J_1(\alpha) - J_3(\alpha)}{J_1(\alpha) + J_3(\alpha)}. \tag{2.5.8}$$

For the case of the asymmetric solution, for $c = 0$, $\phi = 0$ and for $\phi \approx 0$ corresponding to light damping (Capecchi and Bishop, 1994) equation (2.5.5) reduces to

$$p = \frac{J_0(\alpha)}{J_2(\alpha)}. \tag{2.5.9}$$

The symmetry-breaking, pitchfork bifurcation in the (ω, p) parameter space may be obtained by numerically solving the symmetric (2.5.7) and asymmetric (2.5.9) equations simultaneously. Firstly substituting (2.5.9) for p into (2.5.7).

To be able to proceed the following definitions of the Bessel functions are needed and applied:

$$J_n(\alpha) = \sum_{m=0}^{\infty} \frac{(-1)^m (\frac{\alpha}{2})^{2m+n}}{m!\Gamma(m+n+1)} \tag{2.5.10}$$

$$J_0(\alpha) = 1 - \tfrac{\alpha^2}{4} + O(\alpha^4) \qquad J_2 = \tfrac{\alpha^2}{8} + O(\alpha^4)$$
$$J_1(\alpha) = \tfrac{\alpha}{2} - \tfrac{\alpha^3}{16} + O(\alpha^5) \qquad J_3 = \tfrac{\alpha^3}{48} + O(\alpha^5)$$
$$\text{and} \qquad \tfrac{J_1(\alpha)-J_3(\alpha)}{J_1(\alpha)+J_3(\alpha)} = 1 - \tfrac{\alpha^2}{12} + O(\alpha^4).$$

To be consistent with earlier parts in the thesis, we choose $c = 0.1$ and for a specific starting value of ω, (near the major zone $\omega = 2$), equation (2.5.7) was solved numerically for α using a Newton-Raphson method initiated at $\alpha = 1$. The resulting value of α was then placed back into (2.5.9) so as to determine the corresponding

value of p for the original value of forcing frequency. The procedure was repeated for a range of ω values, incremented by 0.05 and finally the resulting points of ω and p were plotted to produce a locus of the symmetry-breaking, pitchfork bifurcation curve as depicted in Figure 2.9. The red coloured curve represents the locus of symmetry-breaking, pitchfork bifurcation (labelled SBPB).

Hence an approximation for the lower bound of the escape zone is constructed where symmetry-breaking, pitchfork bifurcation was employed to act as a precursor of chaotic behaviour leading to escape from the potential well.

The subcritical bifurcation is determined and applied here using the usual vertical tangency condition, (Clifford and Bishop, 1993, Stewart and Faulkner, 2000), where $\frac{d\alpha}{d\omega} = \infty$.

Allowing (2.5.7) to be defined as a function y, so in other words,

$$y(\alpha,\omega) = [\alpha\omega^2 - 8J_1(\alpha)]^2 + \overline{c}^2\omega^2\alpha^2 - 16p^2[J_1(\alpha) - J_3(\alpha)]^2 \tag{2.5.11}$$

then $\frac{d\alpha}{d\omega} = -\frac{y_\omega}{y_\alpha}$ in terms of the partial derivatives of y.

The standard series representations for Bessel functions can be used to expand $y(\alpha,\omega)$ around $\alpha = 0$. In this case, equation (2.5.11) can be expressed as

$$\begin{aligned} y(\alpha,\omega) &= [\alpha\omega^2 - 4\alpha]^2 + \overline{c}^2\omega^2\alpha^2 - 16p^2(\tfrac{\alpha}{2})^2 \\ &= \alpha^2(\omega^2 - 4)^2 + 4\omega^2c^2 - 4p^2 + O(\alpha^4). \end{aligned}$$

So for small α,

$$\frac{d\alpha}{d\omega} = -\frac{y_\omega}{y_\alpha} = -\frac{2\alpha\omega((\omega^2-4)+2c^2)}{[(\omega^2-4)^2+4c^2\omega^2-4p^2]}.$$

The vertical tangency condition holds whenever

$$(\omega^2 - 4)^2 + 4c^2\omega^2 - 4p^2 = 0$$

or

$$(\frac{\omega^2}{4} - 1)^2 + \frac{c^2\omega^2}{4} - \frac{p^2}{4} = 0 \qquad (2.5.12)$$

This equation is expected to provide a reasonable estimate to the left hand boundary of the escape region. Figure 2.9 shows this curve in blue colour and labelled SB. What is of main interest here for the construction of the escape boundary is the left straight section of the blue curve, hence its continuation for $\omega > 2$ has been shown with dotted blue points.

With a slight change in the damping term, this expression is equivalent to the equation for the left hand boundary of escape employed by Clifford and Bishop in their literature (Clifford and Bishop, 1994), so that there is agreement with our observations.

It is important to also note that this equation (2.5.12), is identical to the primary unstable zone of the linearised form of the Mathieu equation (2.3.23) proved earlier.

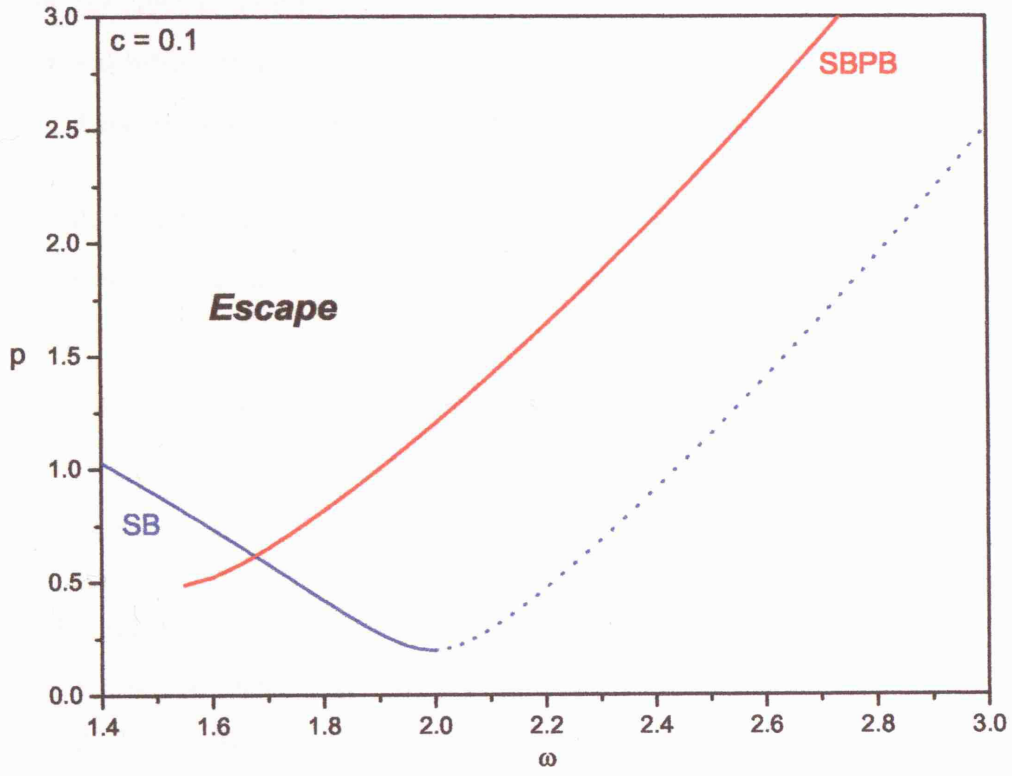

Figure 2.9: *The escape region constructed by considering the boundaries of the locus of symmetry-breaking pitchfork bifurcation, SBPB, (in red) and the subcritical bifurcation, SB, (in blue) around the principle resonant zone near* $\omega = 2$.

Figure 2.10 is a superimposition of analytical and numerically computed diagrams, in order to assess the accuracy of our analytical boundaries of the escape zone. Our previously numerically determined parameter space plot for small angle initial conditions is overlaid with the approximate analytical locus of the symmetry-breaking pitchfork bifurcation, in red, and the subcritical bifurcation, in blue, where now we allow the dotted blue points of Figure 2.9, to continue to form the locus of the supercritical bifurcation curve. To clarify, to the left of $\omega = 2$, the bifurcation is of subcritical nature and to the right, supercritical (recall also Figure 2.6).

We remark that for this tongue, there is a very good agreement both to the upper and lower boundary of the escape zone, where the symmetry-breaking, pitchfork bifurcation curve is within the region where as mentioned previously, oscillatory and rotational behaviour co-exist thus meaning that no major stable non-rotating orbits purely exist. We also note that the range of the (ω, p) plot differs from that in Figure 2.9.

These two approximate bifurcation curves together give a sensible approximation to the escape zone, and moreover, bifurcational behaviour analysis in the Chapters that follow will also verify this prediction and accuracy. Hence, the agreement may be thought of as fairly good considering the approximations employed in the analytical solution.

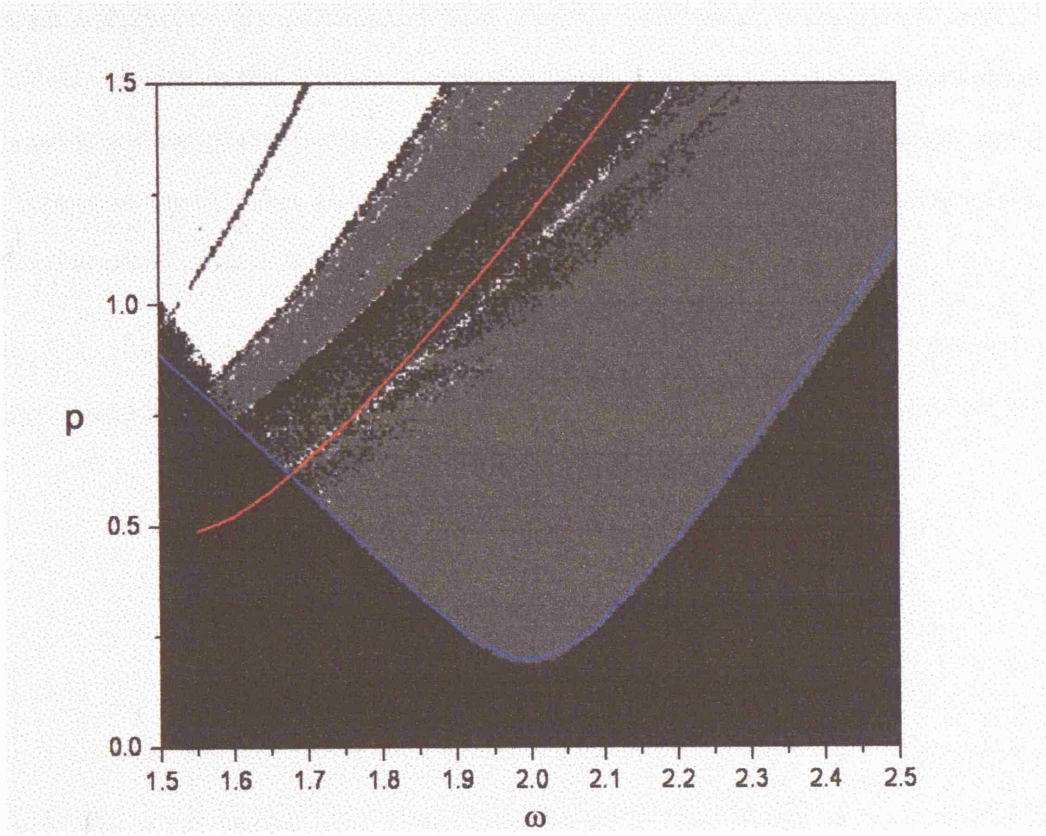

Figure 2.10: *Superimposition of our analytical boundaries found for the locus of the symmetry-breaking pitchfork bifurcation (in red) and the subcritical and supercritical bifurcation (in blue) together with our numerically constructed parameter plane over the same range around the principle resonant zone near* $\omega = 2$. *Damping is again set to* $c = 0.1$.

2.5.1 Critical Velocity Criteria

Based on numerical experiments, Moon (Moon, 1987) proposed another approximation method for the prediction of escape from the potential well for the undamped, unforced oscillator. He postulated that chaotic behaviour is imminent when the maximum velocity of the motion is near the maximum velocity on the separatrix for the corresponding phase portrait. In other words, the boundary between motions that represent oscillations about the hanging stable position and those involving a continuous rotation around the pendulums pivot point.

Figure 2.11 below shows a numerically determined phase space plot for the undamped and unforced pendulum system (undamped version of equation (2.2.3)).

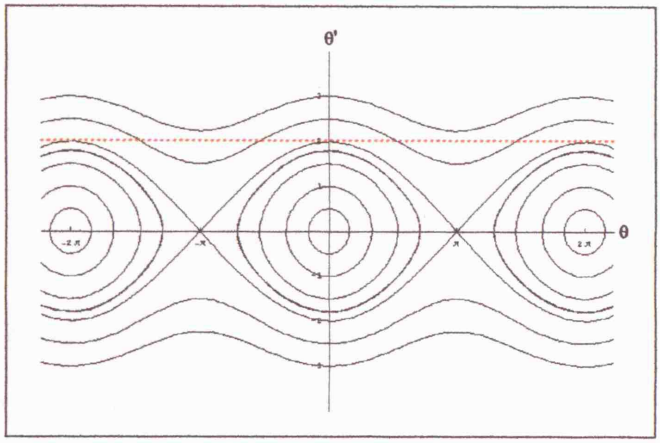

Figure 2.11: *Phase portrait for the undamped unforced pendulum system.*

Considering a small amplitude oscillation starting at say $\theta_0 = \frac{\pi}{8}$, this appears in the phase diagram as an approximate circle. As the pendulum moves in its steady oscillations about the vertical hanging position, the trajectory in phase space sweeps round this small circle and the next motion is again roughly circular and a closed

orbit.

This is typical of undamped systems of this type, that all phase trajectories around equilibria are closed and cyclic. As the starting condition θ_0 is increased, the trajectories in the phase space are observed to become less circular.

Despite the non-appearance of the time variable in Figure 2.11, it is still possible to deduce several physical features of the pendulum's possible motions. There is a stable equilibrium state when the pendulum hangs without swinging ($\theta = 0, \theta' = 0$) corresponding to the origin. The second equlibrium position is where the pendulum is balanced vertically upright ($\theta = \pi, \theta' = 0$) and this an unstable equilibrium state that appears as a saddle point in the figure.

The wavy lines at the top and bottom, correspond to the whirling motions of the pendulum or otherwise known as the rotational motions. A *separatrix* separates motions that represent oscillations about the hanging stable state from the motions involving a continuous rotation of the pendulum. The separatrix here is asymptotic to a saddle point as $t \to \infty$ and as $t \to -\infty$.

Due to the periodicity of the system, with θ a cyclic coordinate in the sense that the state of the pendulum is unchanged by the addition of 2π to θ, we may consider the phase space as three-dimensional. Geometrically, this might be represented by a cylindrical phase space (Koch and Leven, 1985, Thompson and Stewart, 1986). For example, the periodic solutions circle the stable equilibrium position on the surface of the cylinder, without encircling the cylinder, whereas the large rotational motions of the pendulum correspond to curves that enclose the cylinder. A cylindrical phase space shows that a separatrix is asymptotic to the same saddle point both at $t \to \infty$ and $t \to -\infty$.

Returning to Figure 2.11, the dotted line indicates when the maximum velocity on the separatrix occurs, and that is at

$$\theta'_{separatrix} = 2.$$

Just as in Clifford (Clifford and Bishop, 1993), we assume that the solution of this pendulum system is of the form

$$\theta(t) = \alpha \cos \tfrac{wt+\phi}{2} \qquad \text{so that} \qquad \theta'(t) = -\tfrac{\alpha\omega}{2} \sin \tfrac{wt+\phi}{2}$$

$$\text{Therefore,} \qquad \theta'_{max} = \tfrac{\alpha\omega}{2}.$$

Noting that $\theta_0 = 0$ due to the symmetry of the system. In practice, it is necessary to introduce a correction factor ϵ so that escape occurs when $\theta'_{max} = \epsilon\ \theta'_{separatrix}$. From Moon (Moon, 1987), a factor of $\epsilon \approx 0.86$ seemed to give an excellent agreement between analytical criteria for chaotic oscillations and experimental chaos boundaries and so we also adopt this value as our correction factor.

By appropriate substitution, we obtain

$$\theta'_{max} = \epsilon\theta'_{separatrix} = 2\epsilon$$

$$\Longrightarrow \tfrac{\alpha\omega}{2} = 2\epsilon$$

$$\therefore \alpha = \tfrac{4\epsilon}{\omega}.$$

Truncating the Bessel functions of equations (2.5.7) and (2.5.8) and neglecting higher orders of α, we reach

$$\frac{((\frac{\omega^2}{4} - 1) + \frac{\alpha^2}{8})^2 + c^2\omega^2 - \frac{c^2\omega^2\alpha^2}{12})}{(1 - \frac{\alpha^2}{6})^2} = p^2. \tag{2.5.13}$$

Replacing α by $\frac{4\epsilon}{\omega}$ into equation (2.5.13) ,

$$\frac{9[(\omega^4 - 4\omega^2 + 8\epsilon^2)^2 + 4c^2\omega^6 - \frac{16}{3}\epsilon^2 c^2 \omega^4]}{4(3\omega^2 - 8\epsilon^2)^2} = p^2. \tag{2.5.14}$$

For the low damping case, we may assume that (2.5.14) reduces to

$$p_c = \frac{3(\omega^4 - 4\omega^2 + 8\epsilon^2)}{2(3\omega^2 - 8\epsilon^2)}. \tag{2.5.15}$$

Using this criterion method, we were able to obtain another approximate lower bound for the escape zone, (2.5.15). Figure 2.12 identifies this escape boundary in the (ω, p) space.

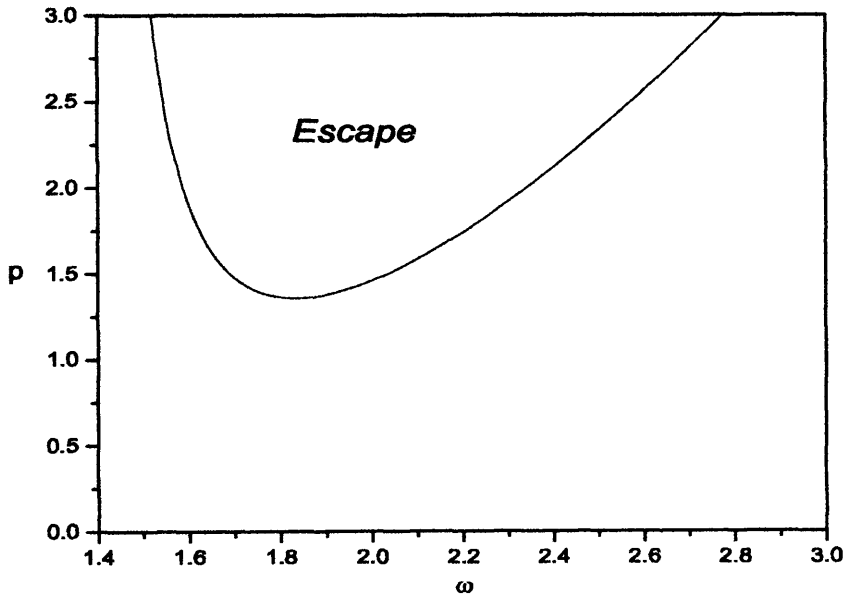

Figure 2.12: *Approximate escape boundary using the critical velocity criteria for the parametrically excited pendulum system with low damping.*

For comparison purposes and to show relevance to the approximate escape zone using this analytical technique, we include Figure 2.13. This is a combination diagram of results from both the analytical methods performed within this Chapter, harmonic balance and critical velocity criteria for the major resonant tongue of the parametrically excited pendulum system.

What is clear, is that at higher frequencies, both analytical methods compare well between themselves giving very close results.

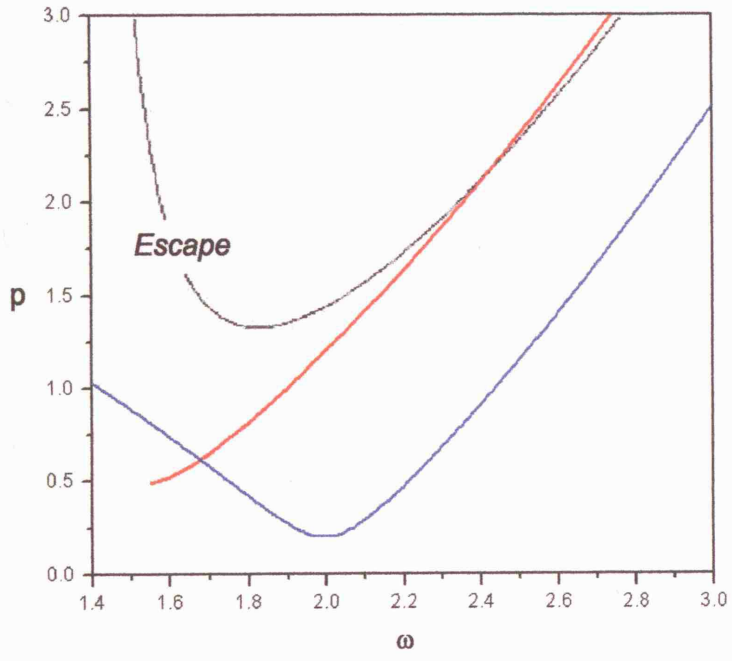

Figure 2.13: *Combination diagram of results from both analytical techniques in order to approximate the escape boundary for the parametrically excited pendulum system.*

Both analytical methods provide reasonable and good approximations to the escape zone which we compared together with our numerical alternatives of the control parameter plots. Moreover, we will also verify using actual bifurcational diagrams under specific amplitude and frequency forcing values in the Chapters that follow the quantitative accuracy of the analytical techniques.

Another method also used to produce escape boundary is that of the homoclinic orbit criterion using the Melnikov function (Moon, 1987, Bountis *et al*, 1992). Moon suggests that the critical velocity criterion for the case of low damping does however provide a better escape boundary. We shall not employ such a method but here we merely mention its existence and applicability (Thompson and Stewart, 1989).

2.6 Upright solution

2.6.1 Inverted Pendulum

It has been well known that the upside down and more specifically the inverted position of the parametrically excited pendulum may be stabilised by applying certain values of forcing amplitude and frequency. This type of dynamic stability probably was first pointed out by Stephenson almost a century ago (Stephenson, 1908). In 1951, such extraordinary behaviour of the pendulum was explained and investigated experimentally in detail by Kapitza (Kapitza, 1951).

Simple hand made devices are often used to show in lectures this fascinating phenomenon of classical mechanics. An old electric shaver's mechanism can serve perfectly well to force the pivot of a light rigid pendulum vibrating with a high enough frequency and sufficient amplitude to make the inverted position stable (Butikov, 2001). Such demonstrations evoke a response and some kind of bewilderment, leaving us and the viewer perplexed and astonished once seen for the first time.

After Kapitza, this simple yet curious system attracted the attention of many researchers and the theory of the phenomenon begun to be investigated and elaborated experimentally as well (Phelps and Hunter, 1965, Kalmus, 1970, Blackburn *et al*, 1992, Mullin, 1993, Clifford and Bishop, 1994, Kim and Hu, 1998, Bishop and Sudor, 1999, Butikov, 2001).

In order to be able to integrate results from this thesis with these other advances, we shall also consider analytically the stability region of the inverted pendulum. The forcing parameters which bound the region of stability can roughly be found using analytical methods and we apply them here to produce the stability boundary around the major zone.

The equation of motion of the inverted parametrically excited pendulum may be formed by substituting $y = \pi - \theta$ into (2.2.2) to produce

$$y'' + cy' - (1 + p\cos\omega t)\sin y = 0 \tag{2.6.1}$$

with c, p, ω representing the usual scaled damping coefficient, scaled amplitude and frequency respectively. y is the angle of oscillation measured from the upward hanging position.

Undertaking the same analytical techniques as the harmonic balance method for the downward hanging state, the following equation may be obtained:

$$[\alpha\omega^2 + 8J_1(\alpha)]^2 + \bar{c}^2\omega^2\alpha^2 - 16p^2[J_1(\alpha) - J_3(\alpha)]^2 = 0. \tag{2.6.2}$$

with $\bar{c}$ defined as before. By appropriate expansion of the Bessel functions, as achieved earlier and by applying the vertical tangency condition, we reach

$$(\frac{\omega^2}{4} + 1)^2 + \frac{c^2\omega^2}{4} - \frac{p^2}{4} = 0. \tag{2.6.3}$$

This provides us with an analytical estimate for the boundary of the stable zone for the inverted damped parametrically excited pendulum motion and Figure 2.14 depicts this equation curve. The value of the damping term c is taken again as 0.1 for consistency.

Two visible observations that appear from the diagram are that for each value of forcing amplitude only one value of ω exists and moreover solutions exist only if $p > 2$. This can also be verified by simply placing $\omega = 0$ into (2.6.3) so that for

positive forcing amplitude, $p = 2$. Compared to the stability boundaries of the downward position, the results here are less satisfactory.

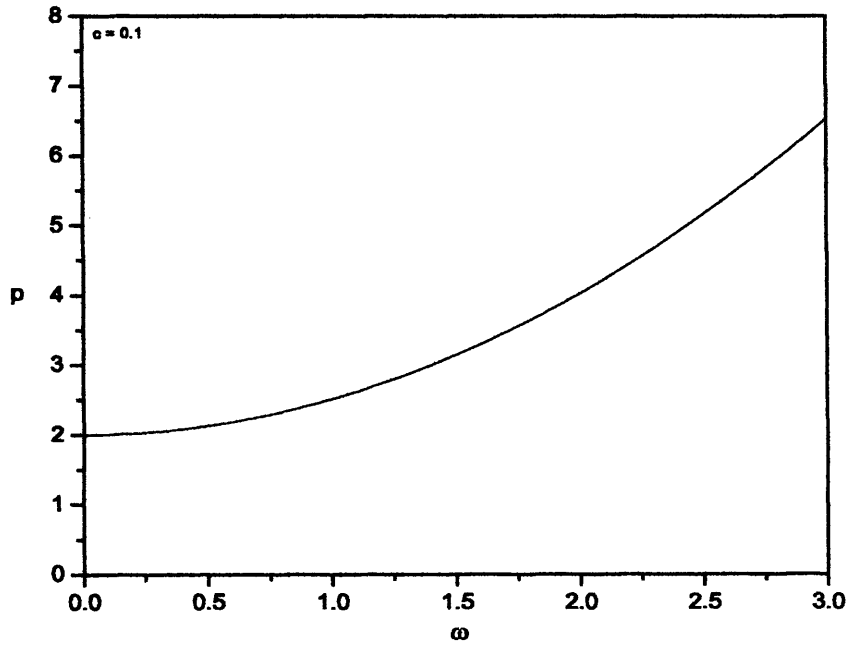

Figure 2.14: *Approximate stable boundary of the inverted parametrically excited pendulum around the first major zone and with* $c = 0.1$.

Clifford *et al* (Clifford and Bishop, 1994) show a schematic bifurcation diagram for the inverted parametrically excited pendulum around $\omega = 2$ where they suggest that the inverted solution becomes stable at approximately $p \approx 3.1$ and where the final period doubling of the sequence of cascade leading to possibly chaotic attractors occurs at $p \approx 3.4$, unlike our analytical stability boundary which shows the forcing amplitude p occurring at ≈ 4 for when $\omega = 2$. Maybe a reason for this unsatisfactory fit might be due to the fact that the inverted solution is not successfully approximated by a sinusoidal function. In Chapter 4, we shall also

examine the inverted solution of the parametrically excited pendulum model with more care, with the aim of producing reliable bifurcation diagrams as opposed to the schematics seen in Clifford and Bishop (Clifford and Bishop, 1994).

2.7 Final Remarks

The parametrically excited pendulum is a system that has undergone investigation by analytical, numerical analysis and experiments over recent years (Leven and Koch, 1981, Koch and Leven, 1985). Many phenomena associated with nonlinear systems such as bifurcations and chaos have been identified making the parametrically excited pendulum a rich area for research.

The importance of the pendulum in modelling engineering systems, such as buildings in earthquakes (Housner, 1963), offshore platforms (Bishop, 2000) and ship dynamics (Contento, Francescutto, Piciullo, 1996, Spyrou, 2000, Shin *et al*, 2004) (which is a field much attention will be paid to in forthcoming Chapters), makes its study of relevance to a wide audience of theoretical and applied scientists and engineers alike.

For many applications only oscillating orbits need to be considered, $\theta_{max} < \pi$, and predicting parameter zones where no major stable non-rotating orbits exist is of particular importance. Under such conditions, the parametrically excited pendulum is analogous to a system which permits escape from a symmetric potential well.

In this Chapter, we initially configured the equation of motion for a vertically driven pendulum and then related this to the Mathieu equation. We considered the theory of parametric resonance to be able to distinguish stability boundaries for the resonance zones over a certain parameter range.

Moreover, a short overview of oscillatory motions was incorporated in order to prepare the groundwork for the Chapters that lie ahead, where the physical system of the parametrically excited pendulum may exhibit complicated nonlinear behaviour including that of chaos.

The resonance tongues exhibited within the control parameter space of the parametrically excited pendulum system have been related to the Mathieu equation. Analytical techniques were employed to determine the stability boundaries of these zones for the Mathieu equation and then compared with the major zone of the control parameter space of the parametrically excited pendulum.

Two approximate techniques were applied to predict the parameter zone in which no major stable non-rotating orbits exist for the parametrically excited pendulum termed as the escape zone.

Our adopted analytical methods were compared with numerical findings and compared with current sightings (Clifford and Bishop, 1994), providing very good approximations to the escape zone. Contrasting both methods between themselves also give reasonable and fairly good representations to the escape zone, allowing for better accuracy at higher frequencies.

On the other hand, an analytical boundary of the stable zone for the inverted damped parametrically excited pendulum motion was also estimated but comparing it with results found in recent literature, it seems to provide us with a less satisfactory level of accuracy.

Chapter 3

Symmetry-breaking in the response of the parametrically excited pendulum model

3.1 Introduction

This Chapter considers the parametrically excited pendulum where the amplitude and frequency of excitation are used as control parameters. For moderate levels of forcing, there are zones that exist in the space of control parameters, where the downward hanging position is unstable and initial conditions that are close to the hanging position lead to steady state symmetric oscillations of twice the period of forcing. To review this situation, this Chapter describes the development of these oscillations as the amplitude of forcing is varied.

In the largest zone, a symmetry-breaking occurs for increasing amplitude of excitation, which brings about a pair of asymmetric oscillations. This break in symmetry

of the period-2 solution can lead to either an increase or decrease in the amplitude of the motion and reference to the experimental significance of this angle change is noted. Typically, further increases of the parameter produce a cascade of period doubling bifurcations, before most oscillating solutions eventually lose their stability so that the system must experience a rotation (Clifford and Bishop, 1996, Garira and Bishop, 2003).

As a result we emphasise that symmetry-breaking becomes an effective precursor of escape from the local potential well around the hanging position. In this Chapter we compare this behaviour and response with that in other resonance zones. The change of geometric structure when the symmetry-breaking, pitchfork bifurcation occurs is examined and graphically represented as a 'pinched' cylinder-like shape, compared with the Möbius strip that has been associated with the period-doubling bifurcation (Thompson and Stewart, 1986).

The Chapter also includes references to practical problems, where the introduction of nonlinearity means that potentially all frequencies below the main zone of the control space lead to dangerous effects and, in some scenarios, disastrous outcomes.

3.2 Bifurcation structure of the parametrically excited pendulum

We show as Figure 3.1 a schematic diagram that conveys the behaviour and indicates the different types of motions and the characteristic locus of the various bifurcations in each resonant tongue for the mathematical model investigated in Chapter 2 equation (2.2.2). This figure is an extension of Figure 2.6 or alternatively Figure 2.7, where the first three resonance tongues are now included as opposed to only the primary zone. In the absence of damping, the zones would extend to the $p = 0$ line.

Previously, we examined briefly the largest zone in the parameter space around $\omega = 2$ and as damping increases, the other zones only appear at much higher values of p. In Chapter 2, we also showed evidence of the effects of damping on the resonance tongues to the corresponding system of the Mathieu equation. For the parametrically excited pendulum system, if we fix the driving frequency ω to a value slightly greater than the centre of the main resonant zone, $\omega = 2.1$ say, then for motions starting close to the hanging state, as the amplitude of the driving, p, is increased, the subsequent motion becomes a symmetric oscillation of twice the forcing period at the line P_D^S (see Figure 3.1). More specifically, this bifurcation is a period doubling that gives birth to symmetric orbits of period $2T$, where $T = 2\pi/\omega$ is the period of the forcing. Prior to the bifurcation, although $\theta = \theta' = 0$ is an equilibrium, special attention must be paid to the parametric nature of the forcing that allows us to consider this position as a period-1 solution in the full phase space (Bishop, Sofroniou, Shi, 2005).

As p is increased further, but still given at $\omega = 2.1$, the symmetric oscillation loses symmetry via a symmetry-breaking, pitchfork bifurcation (denoted as $S_B P_F$

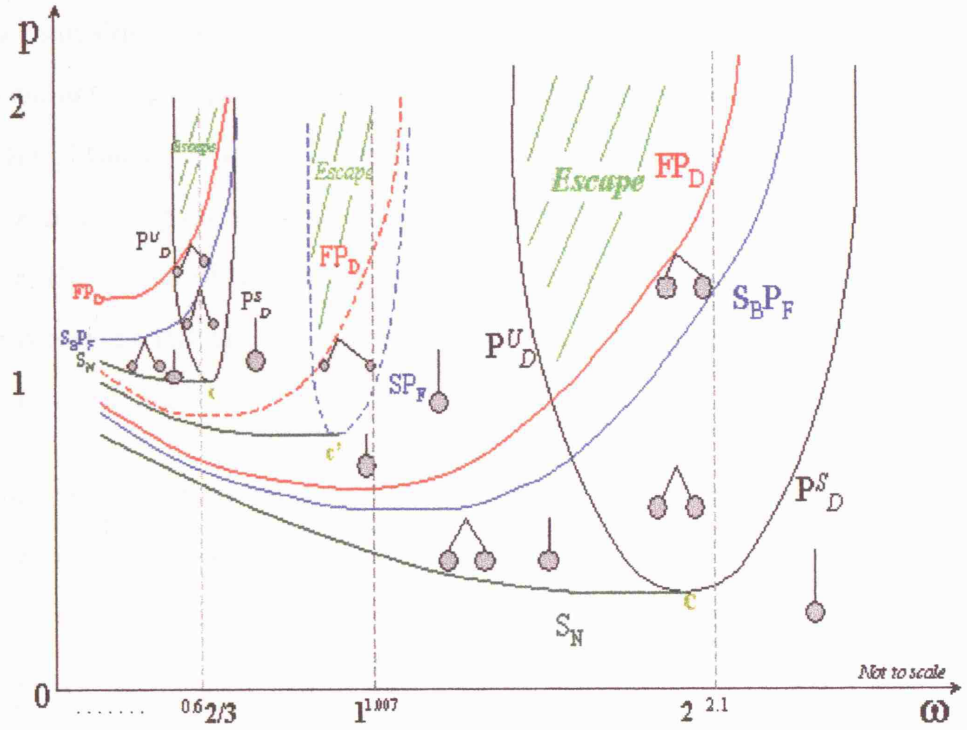

Figure 3.1: *Schematic representation of the stability regions in the* (ω, p) *parameter space.* P_D^S *is where the equilibrium loses stability at a period doubling bifurcation, which is of subcritical form to the left of* c. S_BP_F *is the locus of a symmetry-breaking, pitchfork bifurcation.* FP_D *represents the first bifurcation in a sequence of period doublings.* S_N *denotes a line of saddle node bifurcations. "Escape" is the parameter zone where no major stable non-rotating solution exists.* SP_F *represents zones where asymmetric oscillatory orbits are realised via a supercritical pitchfork bifurcation (subcritical to the left of* c'*) and* FP_D *shows the first period doubling occurrence. The behaviour of the system in the different areas is also depicted via pendulum-like figures.*

in Figure 3.1), whereby a pair of asymmetric solutions appear, still of period $2T$. Physically, one oscillation swings higher to the right while the other swings higher on the left hand side. Strictly speaking, a pitchfork bifurcation breaks symmetry so the term "symmetry-breaking" is superfluous yet it is useful to retain the term to remind us of the physical response. These asymmetric orbits then period double before undergoing a complete cascade of period doubling leading to a chaotic oscillation. However, the region of oscillating chaos is so small in terms of the parameters that we can represent the entire sequence by the line FP_D in Figure 3.1 (Szemplińska-Stupnicka *et al*, 1995).

This chaotic oscillation itself rapidly loses stability so that almost all initial conditions that started near the hanging state now leave the local well and result in motions that include rotation. Following usual conventions and in reference to Chapter 2, this zone is denoted as escape since our emphasis here is on motion within the local potential well around $\theta = 0$. The notation of the main zone shows correlation with the labelling of Figure 2.6.

The schematic control (ω, p) space of Figure 3.1, also shows the regions where hanging motions, symmetric and non-symmetric oscillations are realised via a pendulum-like figure. Many physical systems from the engineering world can be modelled as the parametrically excited pendulum as mentioned in earlier parts of the thesis but even more recently another version of the system has been employed by considering coupled pendula to model multiple legged robots (Banning, 1998, Berkemeier, 1995). It is important to note further that any type of oscillation (either of swinging, rotational or of tumbling nature) may lead to hazardous outcomes, whereby large amplitude swings can be catastrophic.

It is necessary to emphasise here, that not only areas within the major tongue can

exhibit oscillatory-type motions, but also for ω less than 2 values, in other words to the left of $\omega = 2$, hanging and oscillatory solutions co-exist, as depicted in Figure 3.1 (recall also Figure 2.9). These regions contribute to a difficult operation of a system and hence we are of the opinion that engineers should always aim to work with larger values of forcing frequency, so with $\omega \gg 2$.

In a practical sense, areas where any type of oscillation is induced must be avoided so that smoother handling of systems can be achieved without dangerous consequences. In terms of ship dynamics for example, this severe result may be analogous to the capsizing of vessels, where the waves act as the driving force of the model (Spyrou, 2000). Similarly, if one considers the behaviour of a crane mounted on a barge driven by the sinusoidal motion wave, any induced oscillation is not a comforting idea as it may lead to severe operational problems and difficulties (Bishop, 2000).

To further illustrate the dynamics of the single parametrically excited pendulum, we include as Figure 3.2(a) a numerically determined bifurcation diagram that shows the development of the symmetric oscillation of the parametrically excited pendulum for $\omega = 2.1$. This is a forcing frequency value chosen to the right of yellow point c in Figure 3.1 so that a clearer picture of the bifurcational behaviour may be obtained.

The bifurcation diagram was constructed by solving the equation of motion of the parametrically excited pendulum system for the specific value of ω and by numerical time integration using the classical fourth order Runge-Kutta method with initial conditions very near the hanging state solution for $p = 0.25$ (Parker and Chua, 1987). Alternative numerical time integration schemes also produce closely similar diagrams. Transients are then allowed to die away and the next 50 cycles are plotted. Maximum angular displacement is determined from the steady state time history.

The forcing amplitude p is then incremented slightly and time integration continues

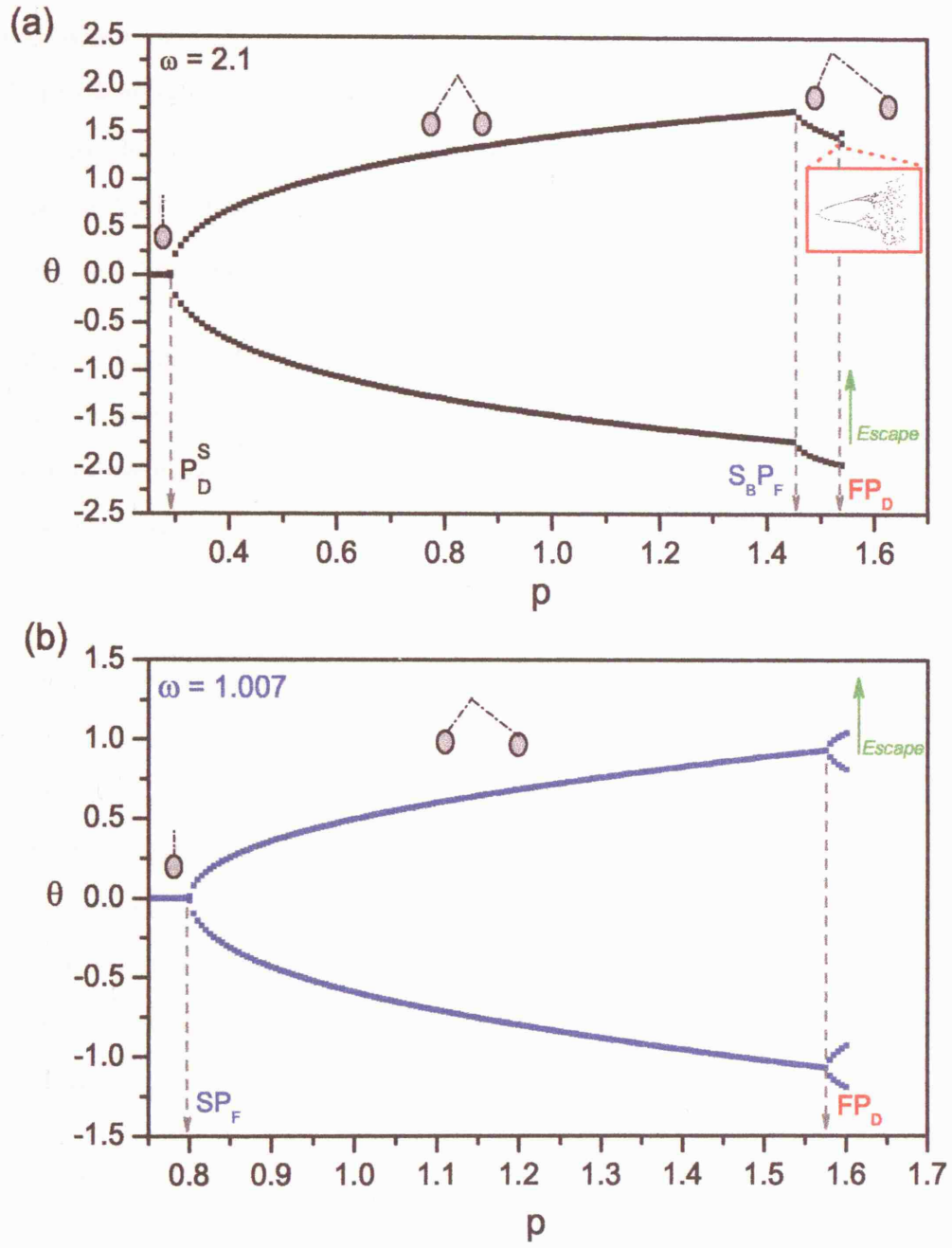

Figure 3.2: *Numerical bifurcation diagrams plotting the maximum amplitude of response over a variation of p for $\omega = 2.1$ and $\omega = 1.007$. The labelled points on these diagrams are echoed in Figure 3.1.*

from the steady state as opposed from the initial condition set near the hanging position. Transients are left to die away again and the results are plotted. This procedure is repeated until the solution increases beyond $|\theta| = \pi$, meaning that the motion now is not restricted to be within the well and escape from the potential well occurs. For clearness, we mention that due to the forcing, θ can exceed $|\theta| = \pi$ and yet be "safe", however in most cases $\theta \approx \pi$ can imply danger and so we must be strict and consider the condition $\theta = \pi$ as escape.

This figure, Figure 3.2(a), plots maximum amplitude of steady state solution versus p, and indicates the initial period doubling occurrence at P_D^S just before $p = 0.3$, symmetry-breaking at $S_B P_F$ around $p \approx 1.45$ and the first period doubling, FP_D, in a sequence of period doubles leading to escape from the potential well. The magnified inset box confirms this scenario.

Comparing this numerically determined point of the occurrence of the symmetry-breaking, pitchfork bifurcation ($p \approx 1.45$), with that of our analytical results of Chapter 2, red curve SBPB in Figure 2.9, ($p \approx 1.43$) at the same forcing frequency magnitude, it can be deduced that there is a good agreement, considering the approximations employed in the analytical solution. Hence at this instance analytical and numerical results are fairly accurate and roughly concur with each other, helping to strengthen the usefulness of the analytical approximations of the escape zone studied in the previous Chapter.

It is also important to note here that the symmetry-breaking, pitchfork bifurcation gives birth to a pair of asymmetric solutions where the asymmetric swings either show an increase or decrease in their motion. Figure 3.2(a), however, only depicts one of the asymmetric solutions showing the effects of a reduction in amplitude oscillatory motion in the positive direction (this is assumed to occur when $\theta > 0$).

Experimentally this can be considered as a vital observation. An increase in amplitude is not likely to be noticed in an experiment, since the amplitude is increasing anyway but experience tells us a decrease probably would be and hence, symmetry-breaking of the oscillatory solution would be visible and more noticeable in this case. We believe that this drop in amplitude of the oscillatory motion can act as a good predictor of the escape boundary provided we see this.

In terms of experimental observation, we had the opportunity to view from an existing set-up consisting of a simple rig model of the vertically driven pendulum, a change in the swinging angle or more specifically a drop in amplitude in one of the directions of swing, preparing us that something will soon happen that will probably lead to rotational motion.

Figure 3.3 shows a photo of this simple rig set up in the workshop of the Civil Engineering Department at UCL for graduate purposes. As a sign of visible endorsement to the above numerical finding, we performed simple experiments that enhance the drop in swinging motion before non-oscillatory behaviour is to be experienced. At that time, the department lacked the resources to record the response data and so it is left to fellow researchers to prove this numerical inspection with precise experimental methods since an experimental observation such as this may be regarded as a very significant one to the boundary of escape and to the safe operation of systems.

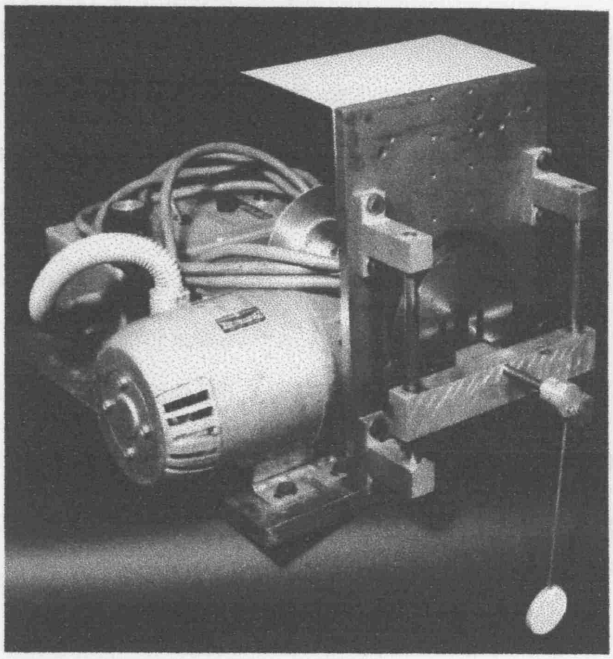

Figure 3.3: *Photo of the simple rig model of the parametrically excited pendulum set up at the Civil Engineering department of UCL.*

Returning to Figure 3.1, at a driving frequency slightly less than $\omega = 2$ a different sequence of events would be experienced; solutions with initial conditions close to the hanging state would remain stable until a subcritical bifurcation of period-2 is encountered at P_D^U, as opposed to the supercritical period doubling for higher than $\omega = 2$ values. For increasing p, the system would jump from the hanging state to a pre-existing period-2 oscillation. For decreasing p, this period-2 solution remains stable (coexisting with the hanging state) until it would reach S_N, (see Figure 3.1), which represents a locus of saddle node bifurcations. Returning to a value slightly less than $\omega = 2$ with p increasing, symmetry-breaking is again present as the driving amplitude increases further and the solution undergoes a cascade of period doubling.

If we now turn to the second resonant zone around $\omega = 1$ and follow the behaviour as we increase p for $\omega = 1.007$ say, then bifurcation lines appear which indicate that the period-2 oscillation may be viewed but only for specific initial conditions. For initial conditions close to the bottom of the well, $\theta \approx 0$, $\theta' \approx 0$ the hanging position remains the only stable solution that the system experiences until on crossing the equilibrium stability boundary at SP_F, where the system exhibits asymmetric orbits of period T due to a pitchfork bifurcation (indicated by the line SP_F in Figure 3.1 at $\omega = 1.007$). For values slightly less than $\omega = 1$, so on the left of yellow point c' in Figure 3.1, the pitchfork bifurcation is subcritical. These asymmetric oscillations then period double (line FP_D in second zone of Figure 3.1) before escaping the local well as p increases further.

Figure 3.2(b) is a numerically determined bifurcation diagram showing the transition for the non-symmetric orbit when $\omega = 1.007$ calculated as before. The hanging state is initially stable but at SP_F becomes an asymmetric period-1 solution. It can be seen that the asymmetric orbit of period T, undergoes a period doubling bifurcation (denoted as FP_D for first period doubling occurrence before escape) where a new solution appears of period $2T$ nature. A further increase of p results in escape from the local well leading to rotations, tumbling and chaotic motions. These bifurcations are indicated in Figure 3.1 by following the dotted path at $\omega = 1.007$ upward and noticing the bifurcation boundaries that are crossed.

The further tongues for smaller values of ω follow the same qualitative response, alternating period-2 near $\omega = 2, 2/3..$, period-1 near $\omega = 1, 2/4...$ and so on. In other words, either admitting symmetric solutions satisfying $\theta(t + T) = -\theta(t)$ with $2T$-periodic oscillations as the first motions to occur once stable equilibrium boundary is crossed or not admitting symmetric solutions in which case $\theta(t + T/2) = -\theta(t)$ with asymmetric T-periodic oscillations as the first motion to occur after that boundary

is crossed (Bryant and Miles, 1989a, 1989b, 1989c), similar to the Mathieu equation case in Chapter 2 (Jordan and Smith, 1987).

Not much attention and research work has been payed on the second tongue or even on the other lower frequency resonance tongues and that is why it was felt necessary to provide an overall picture of the single parametrically excited pendulum. The section that follows concentrates on the 3^{rd} resonant tongue so that we do not overlook the behaviour of the system in the lower resonance zones.

3.3 Analysis of the symmetry-breaking, pitchfork bifurcation

This section focuses on the symmetry-breaking, pitchfork bifurcation occurring in the 3^{rd} tongue near $\omega = 2/3$. In particular, the analysis treatment that follows is for $\omega = 0.6$, which shows behaviour similar to the 1^{st}, 5^{th}, 7^{th}.. tongues, where the tongues are numbered from the right (Figure 3.1).

Applying stability analysis for determining the eigenvalue of a solution (Seydel, 1991), it is noted that symmetry-breaking, pitchfork bifurcation is signified by an eigenvalue of $+1$. This type of bifurcation, for this driven oscillator system, gives birth to a pair of asymmetric oscillations, one whose swing is higher on the left side than the right, while its counterpart is higher on the right side than the left.

3.3.1 Eigenvalue Analysis

For a stability analysis and for the purpose of numerical simulation, it is convenient to transform the second order and nonautonomous equation (2.2.2) into an autonomous system of first order ordinary differential equations of the following form:

$$\frac{d\theta}{dt} = y \tag{3.3.1}$$

$$\frac{dy}{dt} = -cy - (1 + p\cos z)\sin\theta \tag{3.3.2}$$

$$\frac{dz}{dt} = \omega \tag{3.3.3}$$

where z is used as a dummy variable such that $z = \omega t$. The system is symmetric

since the transformation $S : (\theta, y, z) \longrightarrow (-\theta, -y, z + 2\pi)$ leaves (3.3.1-3) invariant. If an orbit $x(t) = [(\theta(t), y(t))]$ is invariant under S, it is called a symmetric orbit otherwise, it is called an asymmetric orbit.

The surface section for the parametrically excited pendulum is the Poincaré time-$T(=\frac{2\pi}{\omega})$ map. The Poincaré maps of an initial point $x_0 = [\theta(0), y(0)]$ can be computed by sampling the orbit points x_m at the discrete time $t = m$ (m=1,2,3..). We call the transformation $x_m \longrightarrow x_{m+1}$ the Poincaré map and write $x_{m+1} = P(x_m)$ (Ott, 1993).

The linear stability of a T-periodic orbit of P such that $P^T(x_0) = x_0$, is determined from the linearised map matrix DP^T of P^T at an orbit point x_0.

Using the Floquet theory (Seydel, 1991, Grimshaw, 1993, Guckenheimer and Holmes, 1983), the matrix DP^T may be obtained by integrating the linearised differential equations for small perturbations as follows.

Let $x^*(t) = x^*(t + T)$ be a solution lying on the closed orbit corresponding to the T-periodic orbit. In order to determine the stability of the closed orbit, we consider a small perturbation $\delta x = [(u, v, r)]$ to the closed orbit. Linearizing (3.3.1-3) about the closed orbit, we obtain

$$\begin{bmatrix} \dot{u} \\ \dot{v} \\ \dot{r} \end{bmatrix} = J(t) \begin{bmatrix} u \\ v \\ r \end{bmatrix} \tag{3.3.4}$$

where

$$J(t) = \begin{bmatrix} 0 & 1 & 0 \\ -(1+p\cos z)\cos\theta & -c & p\sin\theta\sin z \\ 0 & 0 & 0 \end{bmatrix} \tag{3.3.5}$$

and $J(t)$ is a 3×3 T-periodic matrix. Following Floquet theory, we allow $W(t) = (w_1(t), w_2(t), w_3(t))$ be a fundamental solution matrix with $W(0) = I$, where $w_1(t), w_2(t)$ and $w_3(t)$ are three independent solutions expressed in column vector forms and I is the 3×3 identity matrix. Then the general solution of the T-periodic system has the following form:

$$\begin{bmatrix} u(t) \\ v(t) \\ r(t) \end{bmatrix} = W(t) \begin{bmatrix} u(0) \\ v(0) \\ r(0) \end{bmatrix}. \tag{3.3.6}$$

Substituting equation (3.3.6) into (3.3.4) leads to an initial value problem to determine $W(t)$,

$$\dot{W}(t) = J(t)W(t), \qquad W(0) = I. \tag{3.3.7}$$

From equation (3.3.6), $W(T)$ is just the linearised map matrix $DP^T(x_0)$, with $x_0 = x(0)$ and hence the matrix DP^T may be obtained through integration of (3.3.7) over the period T. The characteristic equation of the linearised map matrix $M(=DP^T)$ is

$$\lambda^2 - Tr(M)\lambda + det(M) = 0.$$

where $Tr(M)$ and $det(M)$ denote the trace and determinant of M respectively. The eigenvalues λ_1 and λ_2 of M are called the Floquet multipliers. Floquet multipliers

are a generalisation of the eigenvalues at an equilibrium point. From Chapter 2, we recall that the $det(M)$ is calculated from a formula

$$det(M) = e^{\int_0^T trJ\,dt} = e^{-cT}.$$

(We note that $det(M)$ is a constant, independently of the orbits). The pair of Floquet multipliers of a periodic orbit with period T lies either on the circle of radius $e^{-\frac{cT}{2}}$, since the product of the multipliers is equal to the square of the radius of the circle, or on the real axis in the complex plane. The periodic orbit is stable only when both Floquet multipliers lie inside the unit circle. They never cross the unit circle except at the real axis and hence Hopf bifurcations can not occur. So, a stable periodic orbit can lose its stability when a Floquet multiplier decreases (increases) through -1 (1) on the real axis. Conversely, an unstable periodic orbit can gain its stability when a Floquet multiplier increases (decreases) through -1 (1) on the real axis (Thompson and Stewart, 1986, Guckenheimer and Holmes, 1983).

When a Floquet multiplier λ decreases through -1, the stable periodic orbit loses its stability via period doubling bifurcation. On the other hand, when a Floquet multiplier λ increases through 1, it becomes unstable via pitchfork bifurcation.

Figure 3.4(a) shows a numerically determined bifurcation diagram for $\omega = 0.6$ consisting this time of a plot of angular velocity versus the amplitude of forcing p while Figure 3.4(b) shows a plot of the corresponding largest eigenvalue in magnitude of the periodic orbit. We choose to plot for the bifurcation diagram, angular velocity instead of angular displacement against p, in order to show that the bifurcational sequence does not change with this alteration. This bifurcation diagram also includes points which denote the response in the range beyond the escape from the local well when $p \approx 1.15$. For $p < 0.842$, small disturbances from the hanging state eventually

return to the equilibrium state $\theta = \theta' = 0$. The full phase space is however periodic thus this hanging equilibrium solution can be taken as having period-1.

As p is increased beyond 0.842, the hanging solution remains stable until $p = 0.887$, where it loses stability at a period doubling bifurcation, P_D^U on Figure 3.4(a). Viewing Figure 3.4(b), we can see that this is associated with an eigenvalue -1, corresponding to period double. This bifurcation is subcritical so that initially the period doubled solution is in fact unstable (indicated also in Figure 3.1 by P_D^U, denoting unstable, subcritical period doubling). So, in other words, for the subcritical case of the period doubling, the stable periodic orbit becomes unstable by absorbing an unstable period doubled orbit and a pair of unstable orbits with the same period respectively.

If we were considering states near the hanging state of the third tongue, for increasing p, then at $p = 0.887$ we would see a jump to the oscillating period-2 solution which has been formed when the unstable period-2 solution undergoes a saddle node bifurcation at 0.842 producing a stable symmetric oscillation (indicated at this point by the solution path coloured by blue squares and by the eigenvalue of $+1$ in Figure 3.4(b)). This bifurcation is also depicted in the third zone of Figure 3.1 as S_N, showing the characteristic locus of this bifurcation (see Figure 3.1).

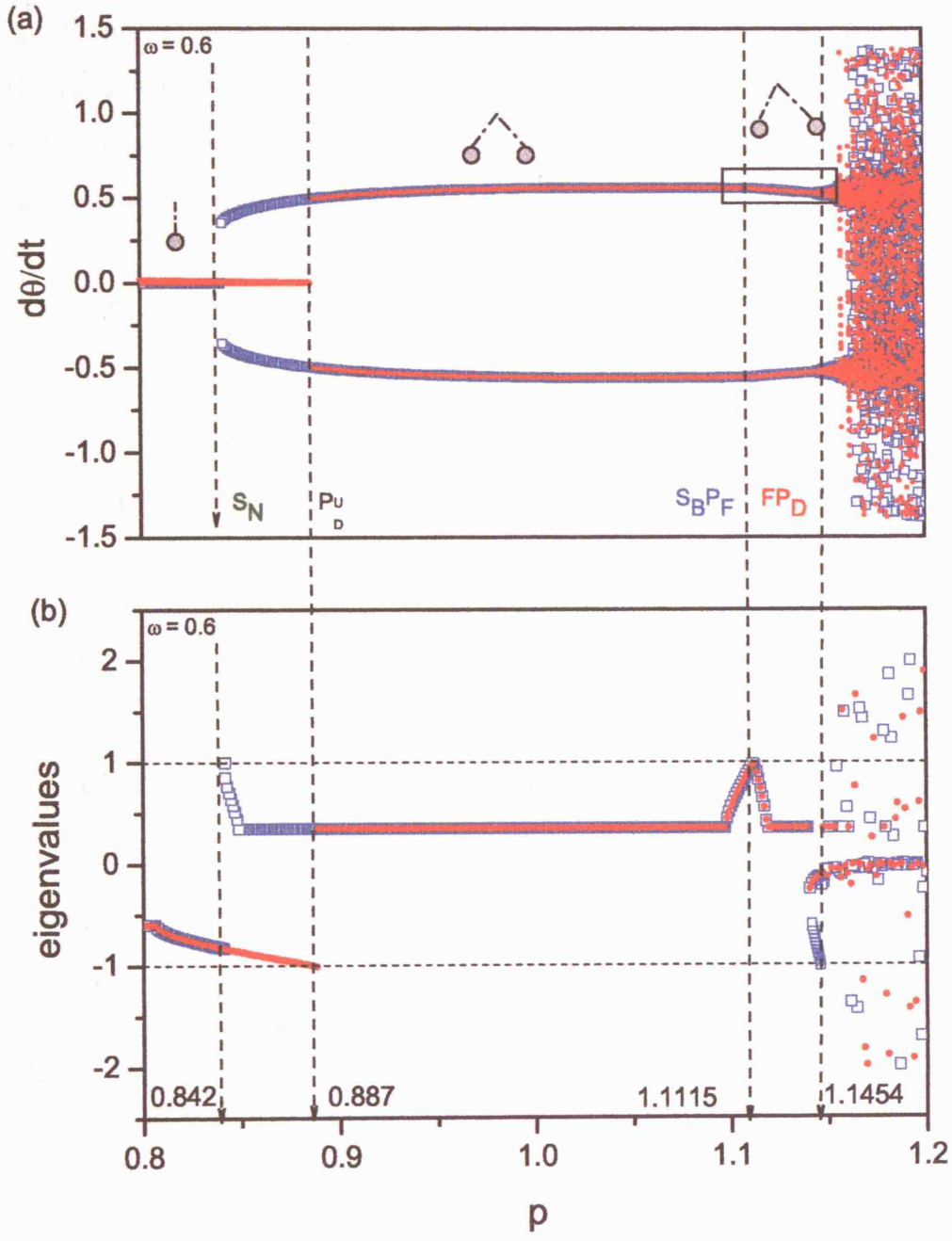

Figure 3.4: *Bifurcation diagram plotting the sampled angular velocity of the steady state solution at* $\omega = 0.6$. *(b) plots the corresponding largest eigenvalue in magnitude of the stable solution.*

In the present case, we have the additional restriction that the swinging solutions correspond to oscillations at half the drive frequency or equally at twice the forcing period. Figure 3.5 consists of a numerically determined time series plot under the conditions $p = 1.0$, $\omega = 0.6$. It identifies that the period of the response T_1, calculated by the time elapsed between dashed blue Poincaré cross-sectional surfaces where the response repeats itself, is equal to twice the period of the forcing:

$$T = \frac{2\pi}{\omega} = \frac{2\pi}{0.6} = \frac{T_1}{2}.$$

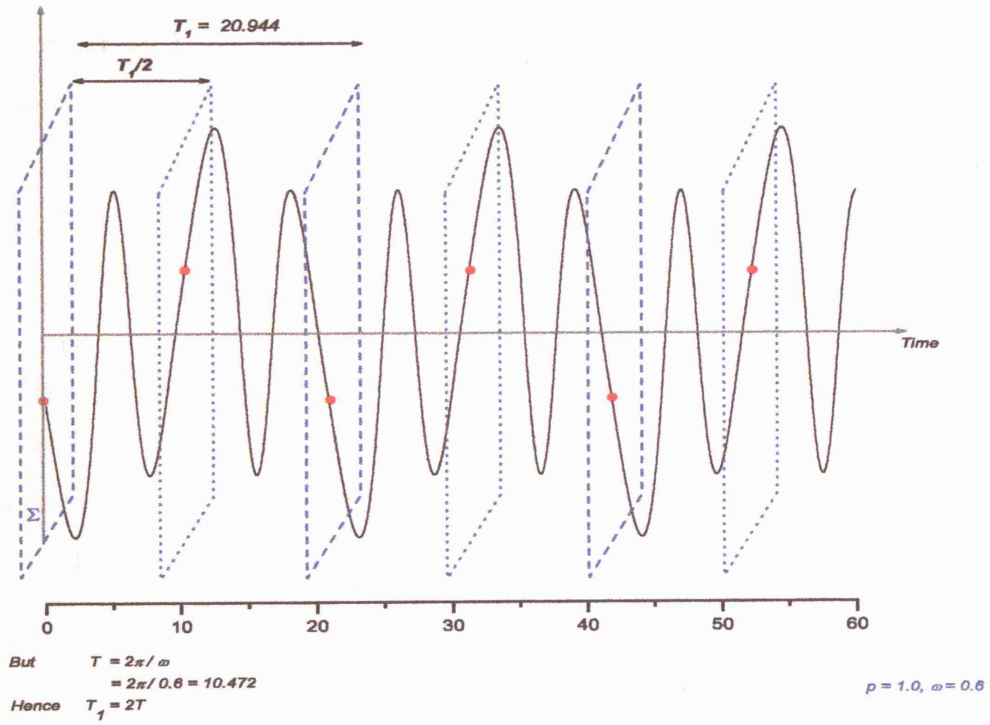

Figure 3.5: *Sample of time series indicating a period-2 solution of the parametrically excited pendulum system at* $p = 1.0$, $\omega = 0.6$. *The period of response is equal to twice the period of forcing.*

Hence at this value of forcing frequency and amplitude, the oscillatory solutions are of period-2 nature.

We also note that after $p = 0.887$, the equilibrium state solution still exists but is now unstable (hence not shown here within). For further increases in p, the symmetric oscillation continues to exist in a stable form until $p = 1.1115$ when a symmetry-breaking, pitchfork bifurcation occurs, shown as $S_B P_F$ in Figure 3.1 and in Figure 3.4(a). Two asymmetric solutions are born at this bifurcation point, one whose amplitude is slightly higher to the right.

In Figure 3.4(a), for convenience we only plot one of these solutions. The corresponding eigenvalue is $+1$ as can be seen in Figure 3.4(b), but for the reverse sequence reducing p, no unstable asymmetric solution exists, so this is not a saddle-node. Around $p = 1.15$, a sequence of period doubling bifurcations culminate in chaotic motion, firstly in an oscillatory manner and then a tumbling chaos which includes rotations as identified by Bishop and Clifford (Bishop and Clifford, 1996).

We should note here the special nature of the system. The initial bifurcation at $p = 0.887$ resembles a Hopf type as an apparent stable equilibrium state loses its stability to a periodic solution. Szemplińska-Stupnicka *et al* (Szemplińska-Stupnicka, Tyrkiel and Zubrzycki, 2000) wrongly identified this as a super-critical Hopf bifurcation for their analysis of the major resonant tongue. But, the corresponding eigenvalues do not cross the imaginary axis as in the case of the Hopf bifurcation, shown both analytically and numerically, and so care must be taken when considering the special nature of the parametric forcing.

To explore the nature of the symmetry-breaking, pitchfork bifurcation further, corresponding phase portraits of (θ, θ') are plotted Figure 3.6. In fact, Figure 3.6(a) shows a close up of the boxed region in the bifurcation diagram of Figure 3.4(a).

At this scale, for low values of p, the black curve in Figure 3.6(a) represents the symmetric period-2 oscillations while the blue and red lines, correspond to the two asymmetric period-2 solutions.

The associated phase diagrams of the steady state solutions are shown in Figure 3.6(b). For $p > 1.145$ the asymmetric solutions simultaneously period double and the corresponding yellow and green phase portraits for $p = 1.15$ are shown in Figure 3.6(b). The transition from the black symmetric to the blue attractor or equivalently to the red attractor (asymmetric) depends on the initial conditions. The blue and red phase portraits at $p = 1.14$ show how symmetry has been broken.

To envisage the nature and difference between the period doubling and symmetry-breaking bifurcations we schematically plot in Figure 3.6(d) a 'pinched' cylinder shape and, in Figure 3.6(e) a Möbius Strip. At the symmetry-breaking, the phase space locally to the periodic symmetric solution changes so that now, two separate (blue and red) asymmetric solutions exist, each with a share of the previous basin of attraction.

At the period doubling bifurcation, the space resembles a Möbius strip (Thompson and Stewart, 1986), so that now, the asymmetric blue solution becomes unstable and a stable solution occurs whose period is twice that of the original (in yellow). Similarly the asymmetric red solution becomes unstable and a green stable solution with twice the period emerges.

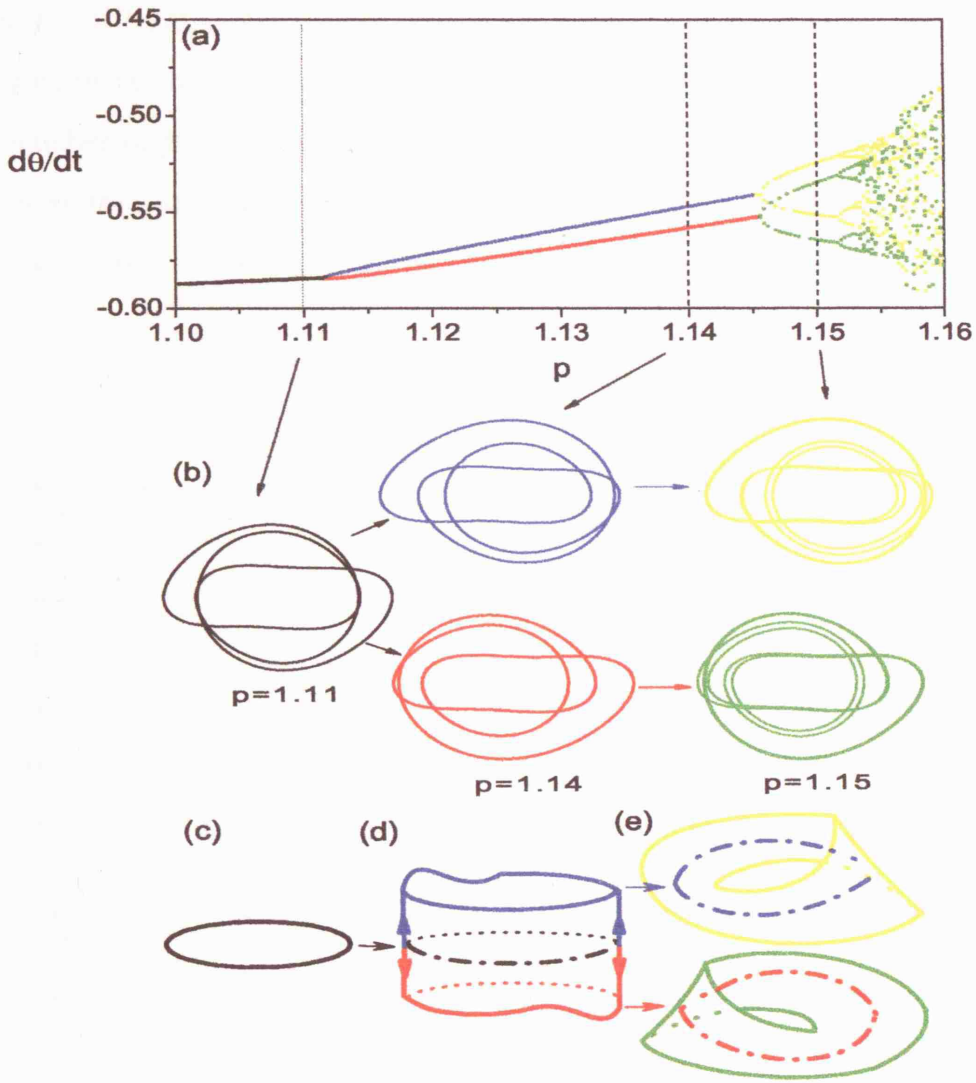

Figure 3.6: *Amplified window of box in Figure 3.4(a). (a) Black line up to* $p = 1.1115$ *corresponds to symmetric period-2 oscillation. Red and blue lines* $1.1115 < p < 1.1454$ *denote two asymmetric period-2 solutions. (b) Corresponding phase portraits of attractors for p=1.11, 1.14 and 1.15. (c) Single black stable periodic solution. (d) Black solution on the surface of the 'pinched'cylinder is unstable and two stable asymmetric solutions appear (blue and red). (e) Blue (or red) solution becomes unstable and follows a path at the edge of the top Möbius strip where period of attractor doubles.*

Figure 3.7 incorporates four phase portraits, (θ, θ'), under the specific forcing amplitudes, $p = 0.7, 1.0, 1.14, 1.15$ respectively, with their corresponding Poincaré points indicated by the red crossed points on each plot. Their transient path is also shown. The number of Poincaré points on each phase space represents the period of the system at that specific driven amplitude whilst $\omega = 0.6$ and these were attained by stroboscopically sampling the phase planes with a period equal to the forcing period.

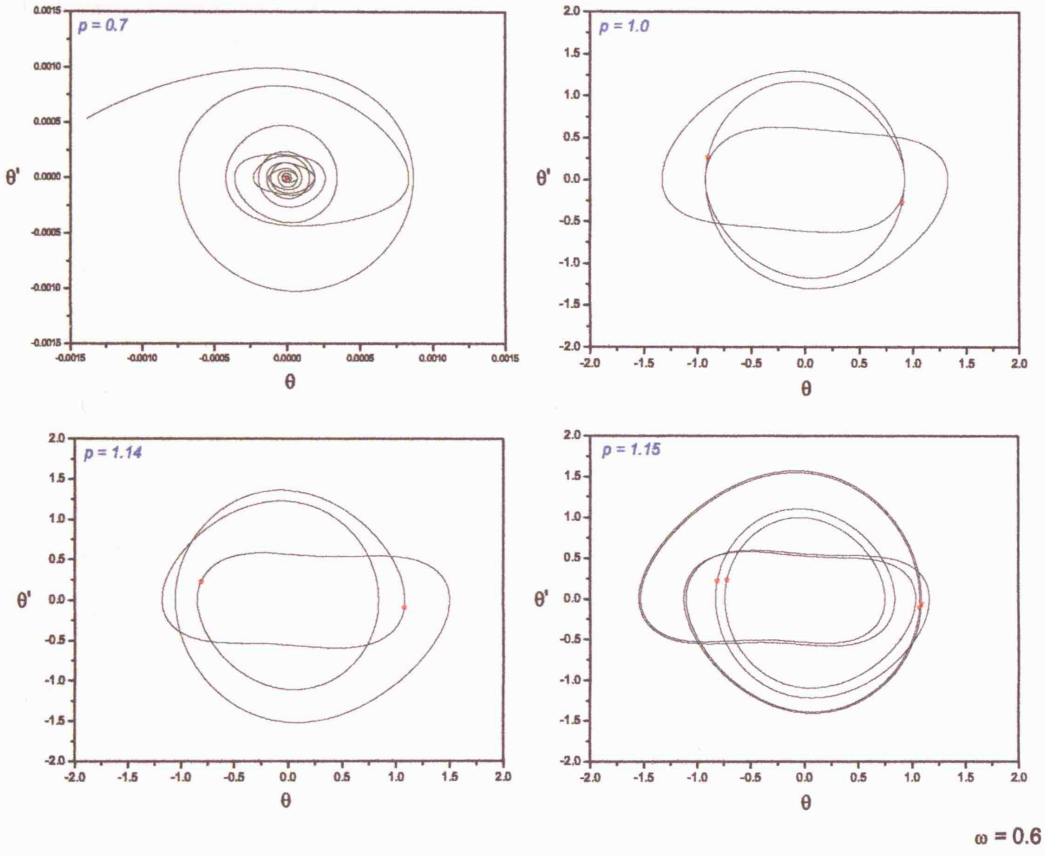

Figure 3.7: *Phase portraits computed under the specific parameter conditions with their corresponding Poincaré points indicated by the red crossed point on each plot.*

At $p = 0.7$, the period of the orbit is taken as 1 whereby only one point is shown in the Poincaré plane. This is in agreement with our earlier analysis where at this forcing amplitude, the pendulum is moving up and down with no swing thus allowing the hanging solution, $\theta = 0$, to have periodicity 1.

At $p = 1.0$ and $p = 1.14$ both symmetric and asymmetric solutions include two points, showing their period-2 nature. Following Figure 3.4 and Figure 3.6, at $p = 1.15$, the first period doubling in the sequence of cascade has been experienced, thus the periodicity of the original period-2 orbit has been doubled leaving stable period-4 oscillations, as also verified by the four number of points in the phase plane.

3.4 Cubic Map

The behaviour of the symmetry breaking, pitchfork bifurcation is not specific to the pendulum system and to confirm this, we examine the cubic map (Mullin, 1993),

$$x_{n+1} = M(x_n) = ax_n^3 + (1-a)\,x_n, \tag{3.4.1}$$

where a is a parameter value. Figure 3.8(a) and (b) identify the corresponding bifurcation diagram and eigenvalue plot over the same parameter range, $1.5 \leq a \leq 3.5$. The period-1 solution is stable for $1.5 < a < 2$ and at $a = 2$ the map bifurcates whilst the eigenvalue of one of the fixed points touches the value of -1 with increasing a at a typical super-critical period doubling bifurcation. Hence at $a = 2$ symmetric fixed points of period-2 are born. On the other hand, with decreasing a, this bifurcation becomes subcritical with its corresponding eigenvalue of 1.

At $a = 2$ with eigenvalue 1, the slope of the eigenvalue decreases to zero at $a = 2.5$ and then increases again to 1 at $a = 3$. Here, a symmetry-breaking, pitchfork bifurcation occurs where at $a = 3$, the symmetric period-2 cycle becomes unstable and asymmetric fixed points of the same period are produced. The corresponding eigenvalue of this bifurcation, is identified as 1 enhancing the studies of symmetry-breaking in the response of the parametrically excited pendulum system.

The period doubling that follows soon after before the cascade of period doubling leading to chaos, is also shown in Figure 3.8(a) with an eigenvalue at this point reaching -1.

Analytically, viewing (3.4.1), in order to determine the stability of a fixed point, one must consider the slope, or eigenvalue, of the map at the specific fixed point and

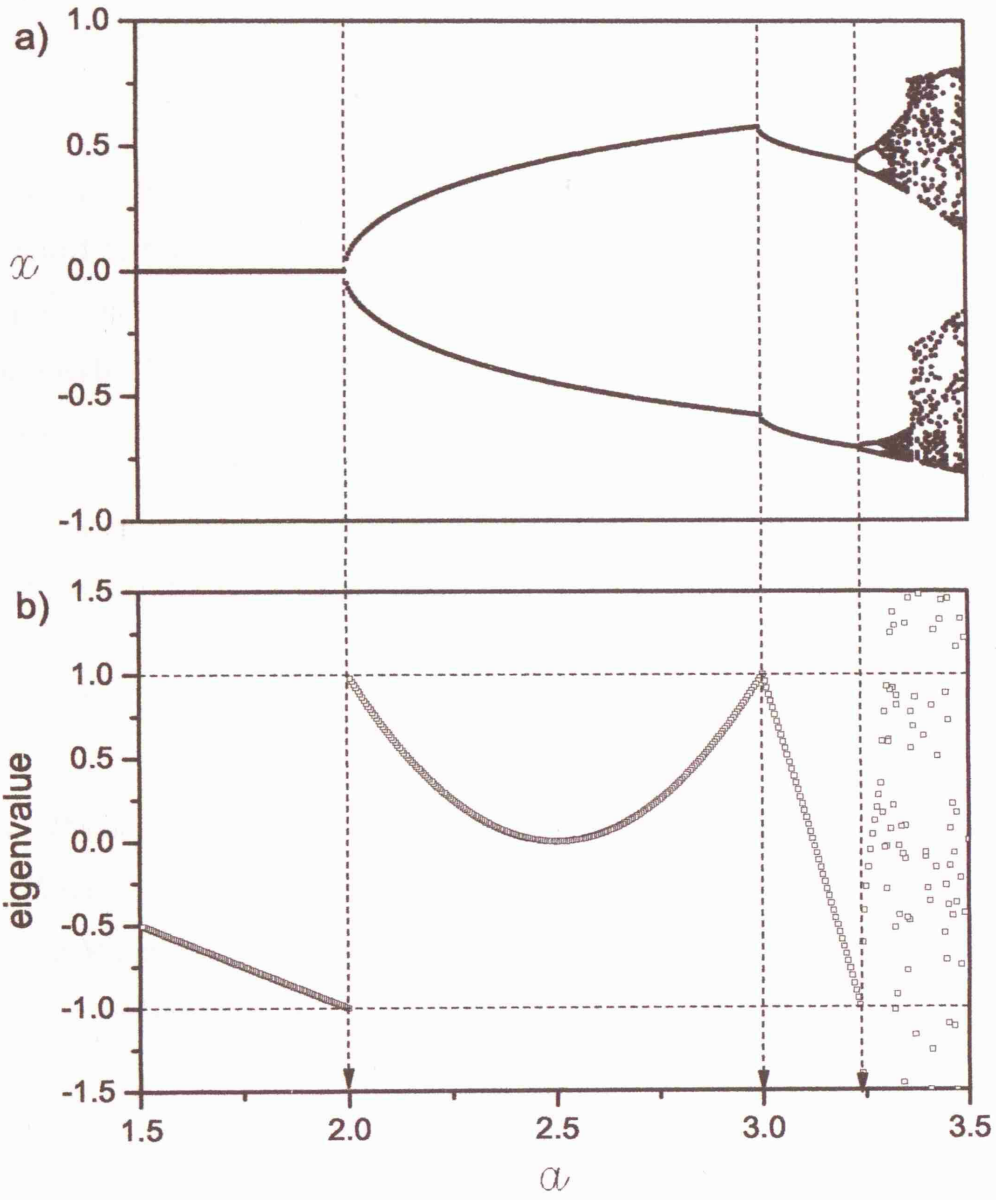

Figure 3.8: *Bifurcation diagram of x versus a for the cubic map. (b) plots the corresponding eigenvalue.*

this is of the form,

$$\frac{dM}{dx_n} = 3ax_n^2 + (1-a). \tag{3.4.2}$$

The fixed points are found by requiring that $x_n = x_{n+1}$ and we find that the map is anchored to three fixed points at $x = 1, 0, -1$. We focus on the stability of the fixed point at $x = 0$. This is determined by $\frac{dM}{dx_n}|_{x_n=0} = (1-a)$. The period-1 orbit is hence stable for $1.5 < a < 2$. When $a = 2$, $\frac{dM}{dx_n}|_{x_n=0} = -1$ representing the period doubling occurrence.

To see what happens as this fixed point of period-1, $(x = 0)$, becomes unstable, we turn to the map for the second iterate:

$$x_{n+1} = M^{(2)}(x_n)$$

where M^k denotes the k-times composed mapping of M. The second-iterate of the map bifurcates to give symmetric fixed points of period-2, for $a > 2$, at say $x = \pm\Upsilon$. Following Mullin (Mullin, 1993) and the fact that the map is antisymmetric $(M(-x) = -M(x))$, this is where, $\pm\Upsilon = M(\mp\Upsilon)$ we obtain,

$$-\Upsilon = a\Upsilon^3 + (1-a)\Upsilon.$$

This gives $\Upsilon = \pm[\frac{a-2}{a}]^{\frac{1}{2}}$ and the stability of these new fixed points of period-2 in turn may be determined by the eigenvalues (slope) of the $M^{(2)}$-map (where $M^{(2)}(x) = M[M(x)]$):

$$\frac{dM^{(2)}}{dx_n}|_{x_n=\pm\Upsilon} = \frac{dM}{dx_n}|_{x_n=-\Upsilon}\frac{dM}{dx_n}|_{x_n=\Upsilon} = [3a(\Upsilon)^2 + (1-a)]^2 = (2a-5)^2.$$

At $a = 2$, the slope is equal to $+1$. The slope decreases to zero at $a = 2.5$, as also seen from Figure 3.8(b), and then increases to 1 at $a = 3$. Hence, the slope must always be positive, ruling out a period doubling bifurcation at $a = 3$.

The analytical solving of the subsequent asymmetric fixed points of period-2 and the first period doubling occurrence in the possible sequence of cascade can be found in the literature given by Mullin (Mullin, 1993).

To complete the study of the cubic map, we also include as Figure 3.9 a computation of the maps Lyapunov exponent plotted against the parameter a to aid us in quantifying chaotic behaviour (Ott,1993). For the cubic map, the Lyapunov exponent, h, is given by

$$h = \lim_{n\to\infty}[\frac{1}{n}\sum_{t=0}^{n} \ ln\frac{dM(x_t)}{dx}] \tag{3.4.3}$$

such that h gives the average exponential rate of divergence of infinitesimally nearby initial conditions. The map is allowed to settle down by ignoring the first thousand iterates and then the average of the slope of the map is calculated, in other words the Lyapunov exponent.

From the diagram, below $a = 2$ where there is a stable fixed point, the Lyapunov exponent is consequently negative. As we enter the region of period doublings (period-2, 4, 8,..), the Lyapunov exponent remains negative.

It is observed that at approximately $a > 3.25$, the chaotic region has commenced where the Lyapunov exponent generally takes positive values, $h > 0$. This is the case where two nearby points initially separated by an infinitesimal distance, typically diverge from each other with time.

The bifurcation diagram of Figure 3.8(a) also verifies this behaviour where at approximately the same value of a, the cascade of period doubling sequence lead to chaos such that it suffices to say that a chaotic orbit is identified by a positive Lyapunov exponent.

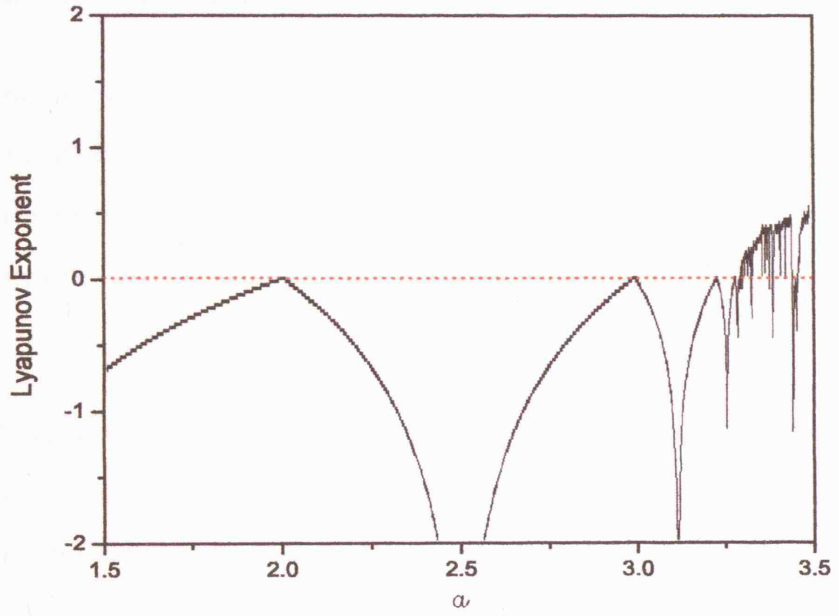

Figure 3.9: *Lyapunov exponent plotted against the parameter a for the cubic map.*

3.5 Final Remarks

In this Chapter the special nature of a parametrically forced system has been highlighted and the mechanism of the symmetry-breaking, pitchfork bifurcation has been characterised by a pinched cylinder.

An overview of the first three tongues has been given and the bifurcations exhibited described in detail. Current research material seems to focus mainly on the first tongue and so this Chapter gives a detailed bifurcational study of the second and third tongue respectively thus producing a more complete picture of the phenomena undergone and that characterise the control parameter space.

Numerical work aided to exemplify that the symmetry-breaking, pitchfork bifurcation takes place when one eigenvalue of the solution reaches 1. This result was validated analytically and numerically by considering the cubic map.

The experimental importance of the symmetry-breaking phenomenon undergone by the oscillatory symmetric solution of the model is also discussed whereby a reduction in amplitude swing can act as a precursor of the bifurcations that will soon follow and more specifically of the escape boundary. More precise and careful experiments are needed to endorse this numerical observation and hence fellow researchers are welcome to provide a much clearer experimental vindication of this result.

This Chapter also gives a major emphasis on the nonlinearity of this model and its application extended to engineering problems. The system's nonlinearity means that possibly all frequencies below the largest zone in the control space have potential dangers and our advice to engineers is that they should always aim to operate at larger than $\omega = 2$ values.

The study of oscillatory periodic solutions of the parametrically excited pendulum presented in this Chapter was carried out to ascertain the existence and location in parameter space of oscillatory periodic solutions and notify their different types using numerical methods.

Finally, the need to understand more about the different types of oscillatory solutions was motivated by the fact that in some applications of the parametrically excited pendulum, the main interest is in achieving periodic solutions that do not exceed $\theta = \pm\pi$, also mentioned in Chapter 2, as this might correspond to some failure in operation in some sense.

Moreover, knowledge of oscillatory behaviour for this system provides the necessary groundwork for subsequent work in the thesis, where in Chapter 4 for example, we study ways of breaking the symmetry of the parametrically excited pendulum model and investigate the effects when the dynamics is oscillatory.

Chapter 4

Breaking the symmetry in the model of the parametrically excited pendulum

4.1 Introduction

This Chapter begins by considering the mathematical model of the parametrically excited pendulum whose symmetry is destroyed by a bias term. The effects of symmetry breaking are investigated by comparing the control parameter space of frequency and amplitude of the forcing with its symmetric counterpart. For clarity purposes, we note that the previous Chapter was concerned with symmetry-breaking in the response of this system.

Approximate bifurcation analysis is used to predict the new altered escape boundary using a harmonic balance scheme for the asymmetric model. We examine the impact that a variation in the bias term causes in terms of the changes to the region of safe,

oscillatory motion. Applications to the field of ship dynamics give an example of a physical significance of this sections findings.

The experimental importance of this alteration is furthermore discussed with a view to predicting the onset of rotating motions. More specifically, an easily viewed drop in amplitude experienced by the asymmetric oscillatory solution may be considered as the trigger of escape and can therefore be regarded as a precursor of imminent danger or operational difficulties.

Further on, another approach to breaking the symmetry of a model is considered whereby the inverted parametrically excited pendulum system is assumed to have been inclined by an angle in the vertical direction. An investigation into the bifurcational behaviour is discussed and compared with findings to that of the parametrically excited pendulum model that incorporates an imperfection term. This way, we are able to integrate results from this thesis with other advances and also compare our analytical and numerical findings of the asymmetric (tilted) inverted case with recent experimental work conducted by other researchers.

Implementation of analytical techniques verify the disappearances of the supercritical pitchfork bifurcation in the biased parametrically excited model and the subcritical pitchfork bifurcation in the tilted inverted case, that are undergone in their symmetric counterparts, and we show their replacement by the disconnected branches.

4.1.1 Importance of asymmetric model

The parametrically excited pendulum can exhibit many nonlinear phenomena as confirmed in the earlier parts of the thesis (Capecchi and Bishop, 1994, Clifford and Bishop, 1994, Szemplińska-Stupnika, 2000, Bartuccelli *et al*, 2001) and more recently by (Bishop, Sofroniou and Shi, 2005). In any physical model however, perfect symmetry can never quite be realised, even with detailed experimental arrangements, and so it is necessary to gain a deeper understanding on how breaking the symmetry of a system can affect its bifurcational behaviour with the aim of developing a better physical realisation for any specific practical problem.

Yabuno and his fellow researchers in Japan, (Yabuno *et al*, 2003) experimentally investigated the effect on the dynamics of the inverted pendulum with tilted high frequency excitation using a simple apparatus. This tilt has an effect of breaking the symmetry of the model. They managed to obtain bifurcation diagrams that seem to be in qualitative agreement with theoretical ones for their system, providing an adequate confirmation for both experimental and theoretical methods.

Furthermore, Michaelis (Michaelis, 1985) observed that the stable inverted state of a vertically excited pendulum rig was not in fact purely vertical but slightly offset suggesting an asymmetry in the apparatus due to a perceptible tilt in the line of excitation. Hence it only seems fair now to consider cases where the symmetry of the model has been broken in order to be able to predict bifurcational behaviour with the view of creating a better mathematical approximation of a physical system.

Sudor and Bishop, (Sudor and Bishop, 1998) also examined the nature of the stable inverted solution as the symmetry is broken via numerical investigations. Their addition of tilt was shown firstly to admit further bifurcation sequences and secondly to give a degree of deflection to the stable inverted state so that this position will

never be truly inverted and may only approach this state asymptotically.

Mullin, (Mullin, 1993) suggested that "perfect symmetry is a non-robust mathematical abstraction" while discussing experimentally observed disconnections of the symmetry-breaking, pitchfork bifurcations in the Euler strut problem and the van der Pol oscillator implying that asymmetry should play a vital role when considering a mathematical model of an engineering or physical system and so we believe that its effects must be understood undoubtedly and clearly.

4.2 The equation of motion for the proposed symmetry broken model

In the present Chapter, we extend from our earlier work of the thesis, numerical and analytical treatments to the case of the parametrically vertically driven pendulum whose initial symmetry has been destroyed by a bias term. To the best of our knowledge this case has not yet been fully examined and we feel it is to the advantage of every researcher to be able to understand the effect of asymmetric models.

The symmetry may be broken in a number of ways, but here we initially consider breaking the symmetry of the model of the parametrically excited pendulum by regarding the modelling equation as:

$$\theta'' + c\theta' + (1 + p\cos\omega t)\sin\theta + \Delta\gamma = 0 \tag{4.2.1}$$

where p and ω, respectively, are the scaled amplitude and frequency of the excitation and c is the damping constant, taken as usual to be 0.1. The angle θ is measured from the downward hanging position. The symmetry has been broken by the addition of a constant bias term ($\Delta\gamma$) to the usual equation of motion (2.2.2), in which γ is a positive parameter with Δ having only $+1$ or -1 values (Sofroniou and Bishop, 2006). The so called parametrically excited pendulum can be recovered by setting γ=0. This model's dynamics is similar to the "inverted tilted parametric pendulum" (Sudor and Bishop, 1999) except that in the latter, the system consists of two components of forcing, vertical and horizontal.

In terms of physical representation this bias term may represent an offset in the hanging position of the pendulum, maybe due to a constant wind force that causes the pendulum to shift slightly from the hanging position. In the study of ship roll

dynamics, this bias term may represent a constant wind load or even an imbalance in cargo loading (Bikdash *et al*, 1994) however practical consideration in this area is left to be discussed and investigated in the Chapters that follow.

4.3 The systems governing potential well, phase space and its safe basin

Figure 4.1 shows how this imperfection term affects the governing potential well of the undamped system, consisting of the individual potential wells for specific values of the bias term, at $\gamma = 0$ and $\gamma = 0.02$ respectively. The effect of the inclusion of the bias term, causes the potential well to have a higher peak to the right for $\Delta = +1$, whilst for $\Delta = -1$ the well has a higher peak on the left.

Throughout this Chapter, $\Delta = +1$ has mainly been chosen, in order to examine the dynamical changes of the system but we mention here that strictly speaking there and no bifurcational differences for when choosing $\Delta = -1$. The choice of $\Delta = +1$ or -1 determines only the branch that the solution subsequently follows but we choose to embrace it in order to emphasise the effects of a bias term on the amplitude of the response. Its use will also become evident further on, during the examination of the symmetry broken pitchfork bifurcation.

The potential energy function, $V(\theta)$, is given by the form $V(\theta) = -\cos\theta + \gamma\theta$. Clearly when $\gamma = 0$, the underlying potential energy function is symmetric. Again referring to Figure 4.1, with no forcing applied and when $\gamma = 0$, the stable equilibrium solution, $\theta = 0$ (the hanging position), is indicated by a shaded ball whereas the unstable equilibrium solution (corresponding to the inverted position of the pendulum at $\theta = \pm\pi$) is shown by the unshaded ball on the 'hilltops' of the well. We recall that the term escape represents motions starting within the well whose subsequent motion grows large enough to leave the well, so that the ball may escape. This is most likely to happen under large forcing magnitude but resonance and nonlinearity play a vital role here and the system does not always respond as a casual observer might imagine.

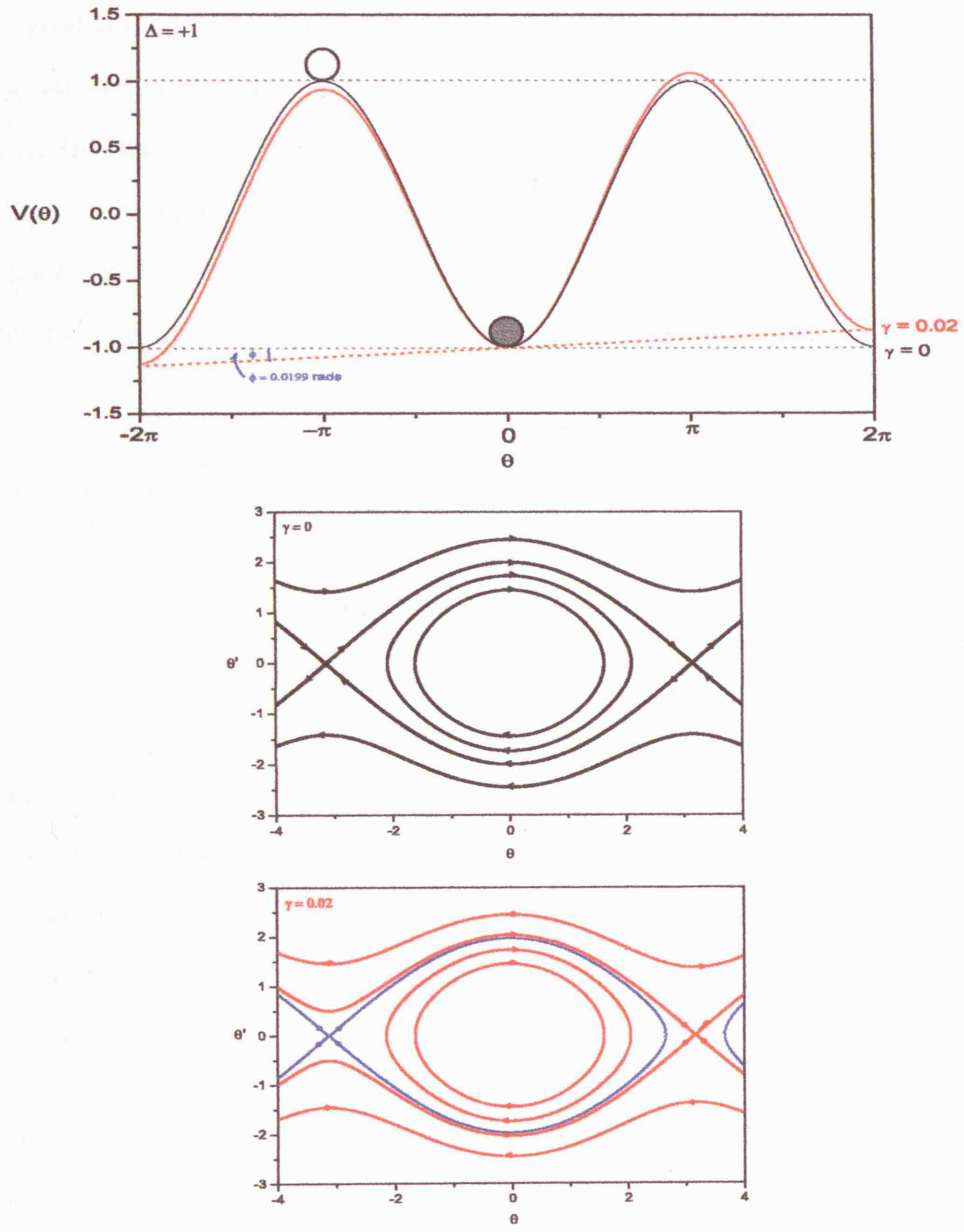

Figure 4.1: *Systems dynamics viewed in terms of the potential well, where $V(\theta)$ is the potential-energy function. Individual potential wells for the specific values of the bias term, at $\gamma = 0$, and $\gamma = 0.02$ (in red), with $\Delta = +1$ are shown. Below are two sets of phase portraits for the undamped and unforced system, drawn for $\gamma = 0$ and $\gamma = 0.02$ respectively.*

Two sets of phase portraits are also shown in Figure 4.1 for the corresponding potential energy curves for when $\gamma = 0$ and $\gamma = 0.02$ accordingly, for the undamped and unforced system. The idea of the separatrix is displayed again (since this case was touched earlier in Chapter 2 equation (2.5.1)) in the (θ, θ') plane when $\gamma = 0$, identifying the stable $\theta = 0$ solution as a centre and the unstable solution at $\theta = \pm\pi$ as saddles. It is worth including here this more detailed numerically determined phase space, as it serves a more accessible comparison with the phase portrait for the different γ value.

For the unbiased case, the two saddles points are connected by two symmetrical orbits known as heteroclinic orbits (Arrowsmith and Place, 1990, 1992, Guckenheimer and Holmes, 1983). More specifically, an orbit which converges to the saddle point as $t \to \infty$ is called the stable manifold, whereas if it converges to the saddle point as $t \to -\infty$ it is called the unstable manifold. The heteroclinic orbit is one that connects both the orbit which starts at the unstable manifold of the saddle at $-\pi$ that then finishes at the saddle at π, approaching it on the saddle manifold of π, and the orbit that starts at the unstable manifold of the saddle at π and tends to the other saddle (at $-\pi$). The oscillatory and rotating trajectories are separated by the heteroclinic orbits.

In nonlinear systems, different initial conditions will evolve towards one or other of the co-existing attractors and the closure of the set of initial conditions which approaches a given attractor is called the basin of attraction of that attractor. When there are two or more co-existing attractors, the boundary between one basin of attraction and another is called the basin boundary and here, motions initiated inside the region enclosed by the heteroclinic orbits are bounded and safe and can be characterised as the *safe basin* region of the system and the heteroclinic orbits are the *basin boundaries*. The motions outside of this region correspond to escape

from the potential well.

In the asymmetric, biased system, shown in red, the two saddles points are now not connected but the left saddle point is connected to itself by a homoclinic orbit that may form the boundary of a smaller safe basin. Hence the area of the safe basin may have decreased. The homoclinic orbit also acts as a separatrix as it still separates bounded and unbounded motions (Thompson and Stewart, 1986).

In the unbiased case, the safe motions stay bounded forever. Under very small harmonic excitation and small damping, the oscillatory motion generally remains periodic and bounded, whilst we consider the hanging position to be of period 1. As the excitation levels are increased, the motion becomes more complicated and even might possess chaotic behaviour.

In terms of ship dynamics, motions occurring inside the region enclosed by the heteroclinic orbits that are bounded and safe, correspond to the non-capsizing regions whereas motions outside the heteroclinic boundary invariably lead to capsize. Hence, in the asymmetric biased system, the safe non-capsizing region may become smaller (Thompson, 1989, Virgin, 1987, Falzarano, 1992).

Moreover, with the introduction of damping at $\gamma = 0.02$ and $\Delta = +1$, the unstable manifold from $-\pi$ leads to the stable solution at $\theta = 0$ and the unstable manifold at the saddle at π approaches the stable solution at 2π (Aston, 1996). Figure 4.2 is a phase plane diagram (θ, θ') showing this attraction of points. With note that with $\Delta = -1$, the reverse effects occur.

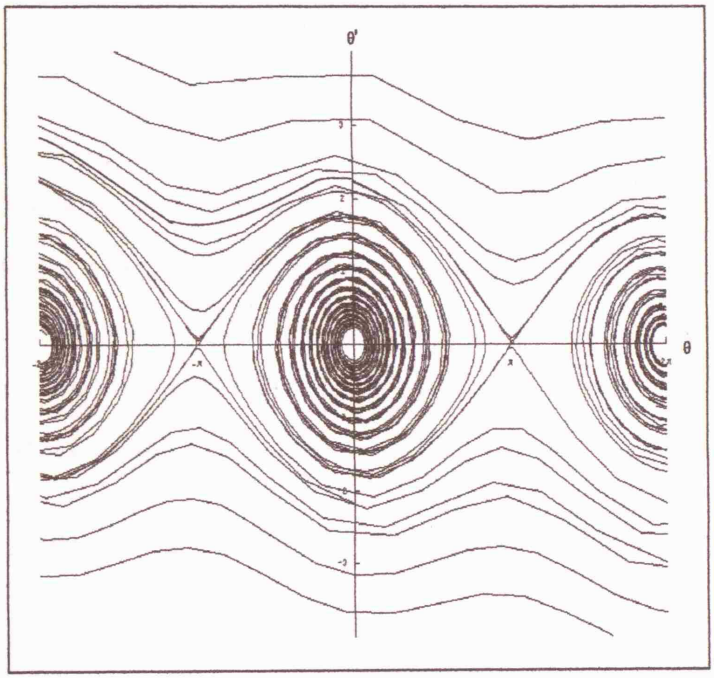

Figure 4.2: *Phase plane diagram for the nonlinear damped biased pendulum* ($c = 0.1, \gamma = 0.02$).

4.4 Approximate bifurcation analysis of the asymmetric model

Parameter regions of escape and bifurcational behaviour have been studied in earlier parts of the thesis for the symmetric parametrically excited pendulum and we now extend these ideas for the asymmetric model with $\gamma \neq 0$, specifically in the main zone, say for $\omega > 2$ regions. Due to the $\Delta\gamma$ term, the altered equation of motion now does not have $\theta = 0$, $\theta' = 0$ as one of its equilibrium solutions anymore (similarly for $\theta = \pm\pi$).

The harmonic balance method (Hayashi, 1985, Nayfeh, 1993, Bryant and Miles, 1990a, 1990b, 1990c) is applied but instead we express $\sin\theta$ in Taylor series up to the third order so that $\sin\theta \approx \theta - \frac{\theta^3}{6}$. This is similar to truncating the series that defines the Bessel functions to third order as accomplished in Chapter 2.5 (also Capecchi and Bishop, 1994).

We assume as an approximation that the solution to (4.2.1) is of the form,

$$\theta(t) = \theta_0 + a\cos(\frac{\omega t + \phi}{v}) - \xi(t) \tag{4.4.1}$$

where $v = 2$ corresponds to the primary zone around the region $\omega = 2$, θ_0 is near zero for downward oscillation, ϕ is the phase angle and $\xi(t)$ represents some small perturbation or disturbance of the original solution.

By substituting (4.4.1) into (4.2.1) we get an equation relative to the small perturbation quantity $\xi(t)$. After high powers of small quantity $\xi(t)$ are dropped and after some manipulation of trigonometric identities, the terms of constants, cosine and sine terms are equated respectively, to obtain the following three equations:

$$\theta_0\left[1-\frac{a^2}{4}-p\frac{a^2}{8}\cos\phi\right]-\frac{\theta_0^3}{6}=\Delta\gamma \tag{4.4.2}$$

$$\left[1-\frac{\omega^2}{4}-\frac{\theta_0^2}{3}-\frac{a^2}{8}\right]^2+\left[\frac{c\omega}{2}\right]^2=p^2\left[\frac{a^2}{12}-\frac{1}{2}-\frac{\theta_0^2}{6}\right]^2 \tag{4.4.3}$$

$$\ddot{\xi}+c\dot{\xi}+\left[1-\frac{\theta_0^2}{2}-\frac{a^2}{4}-p\frac{a^2}{8}\cos\phi\right]\xi+O(\xi^2,\xi^3)+g\left(\cos\omega t,\xi\right)+h\left(\cos\omega t,a,\theta_0\right)=0 \tag{4.4.4}$$

where g and h represent collected-like terms that depend on the parameters inside their brackets. If $\xi<0$, then (4.4.3) would read:

$$\left[1-\tfrac{\omega^2}{4}-\tfrac{\theta_0^2}{2}-\tfrac{a^2}{8}\right]^2+\left[\tfrac{c\omega}{2}\right]^2=p^2\left[\tfrac{a^2}{12}-\tfrac{1}{2}+\tfrac{\theta_0^2}{4}\right]^2.$$

Equation (4.4.4) is now an ordinary linear differential equation in $\xi(t)$ of the second order with a varying coefficient. This latter equation leaves us with the so called variational equation (Hayashi, 1985, Nayfeh, 1993).

Following Kan and Taguchi (Kan *et al*, 1991) and their study of their proposed asymmetric roll capsize equation, in order to avoid the divergence of the solution due to the negative stiffness, the coefficient of $\xi(t)$ in equation (4.4.4) must be positive leading to the following condition

$$\left[1-\frac{\theta_0^2}{2}-\frac{a^2}{4}-p\frac{a^2}{8}\cos\phi\right]>0. \tag{4.4.5}$$

Since symmetry no longer holds due to the existence of the bias term, we may assume an approximate right hand boundary of escape defined by the critical period

doubling bifurcation that is supposed to initiate the sequence of cascade bifurcations that lead to escape from the potential well.

We recall that in the symmetric case, we assumed that the symmetry-breaking, pitchfork bifurcation acts as an indicator of escape. But since the first period doubling of cascade occurs soon after the symmetry-breaking, pitchfork bifurcation, we may consider that for the asymmetric case, it is this period doubling bifurcation that may serve as a good predictor of escape. Hence, the asymmetric oscillations will soon experience their first period doubling bifurcation at the critical condition given by

$$\left[1 - \frac{\theta_0^2}{2} - \frac{a^2}{4} - p\frac{a^2}{8}\cos\phi\right] = 0. \tag{4.4.6}$$

From (4.4.2) and (4.4.6), we obtain the following relation,

$$\theta_0 = (3\Delta\gamma)^{\frac{1}{3}} \tag{4.4.7}$$

and similarly by substituting (4.4.7) into (4.4.6), we get

$$a^2 = \frac{8 - 4(9(\Delta\gamma)^2)^{\frac{1}{3}}}{2 + p\cos\phi}. \tag{4.4.8}$$

It is important to note here that a is independent of the sign of $\Delta\gamma$, due to the squared operation.

With the aid of equations (4.4.3) and (4.4.8), the approximate forcing amplitude value of the period doubling bifurcation that leads to escape, p_f may be given by:

$$\left[1-\frac{\omega^2}{4}-\frac{\theta_0^2}{3}-\frac{a^2}{8}\right]^2+\left[\frac{c\omega}{2}\right]^2=p_f^2\left[\frac{a^2}{12}-\frac{1}{2}-\frac{\theta_0^2}{6}\right]^2 \tag{4.4.9}$$

where $a^2=\frac{8-4(9\gamma^2)^{\frac{1}{3}}}{2+p_f}$ for small ϕ ($\cos\phi\approx(1-\frac{\phi^2}{2})\approx 1$).

Therefore, this last equation, (4.4.9), gives an analytical approximation of where the asymmetric solution will experience the critical period doubling bifurcation that leads the sequence of cascade, so that if escape is to occur via a period doubling cascade then this must follow p_f.

Figure 4.3 shows the control parameter space for different values of γ where the lower boundary of the escape region for each bias term is identified.

Just as in Chapter 2, equation (4.4.9) was solved numerically for a using the Newton Raphson method initiated at $a=1$. The resulting value of a was placed back into (4.4.8), for small phase angle ϕ, in order to determine the corresponding p value for a set of forcing frequency. This procedure is repeated for a range of ω and γ values.

For the case of $\gamma=0$, so in other words for the parametrically excited pendulum with no asymmetry, the black curve represents the locus of symmetry-breaking, pitchfork bifurcation as seen in Chapter 2. This curve is equivalent to the red labelled $SBPB$ curve in Figure 2.9 where the first is drawn using Taylor Series approximations whereas the latter computed with the aid of Bessel functions.

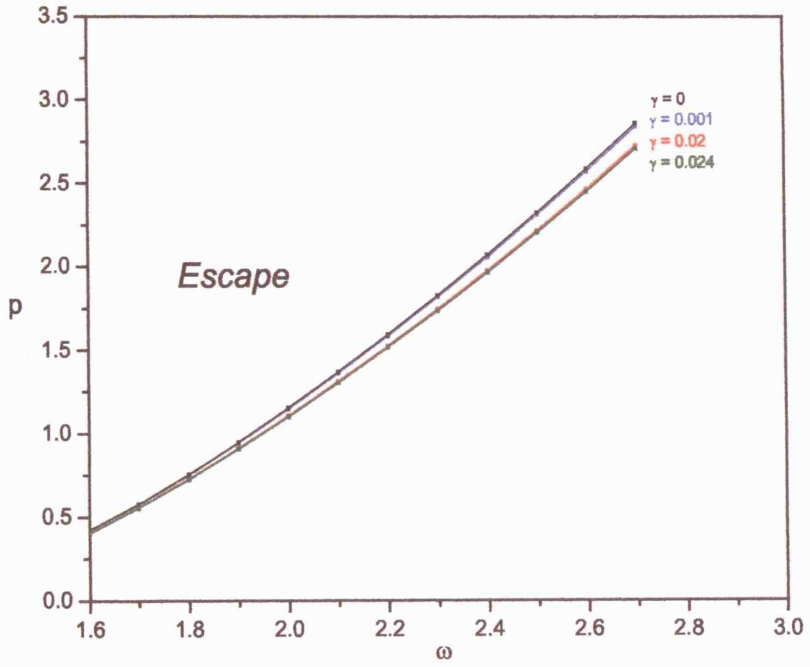

Figure 4.3: *Analytical lower boundary of escape for various imperfection terms in the (ω, p) parameter space. For the asymmetric model, if escape is to occur via a period doubling cascade it will do so by following p_f, equation (4.4.9), which produces the locus points of each curve.*

To visualise their differences we include Figure 4.4, which shows the boundary of escape for $\gamma = 0$, hence the symmetric case, using both approximation methods. Both methods provide us with close results, especially the higher the forcing frequency. We expect however slight differences due to the approximations made for each method.

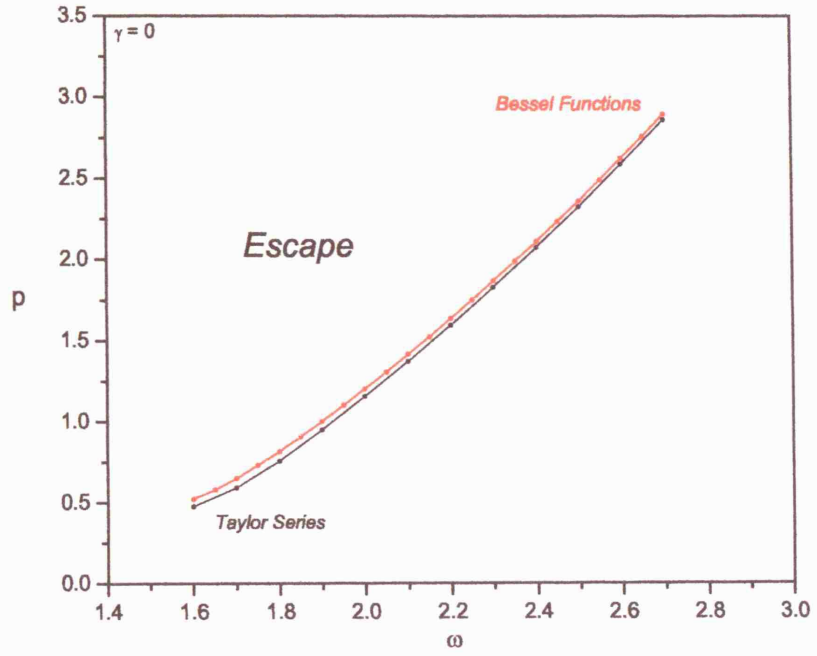

Figure 4.4: *Analytical lower boundaries of escape. Red curve corresponds to the SBPB curve of Figure 2.9, calculated using Bessel functions whereas the black curve was computed using Taylor Series approximations.*

The validity of the red curve calculated with the aid of Bessel functions (equivalent to SBPB in Figure 2.9) was given in Chapter 2, by comparing it with numerical findings and so since the boundaries in Figure 4.4 are close in proximity to each other, we may suggest that both methods provide adequate readings to the boundary of escape.

Returning now to Figure 4.3, incorporating the bias term, we notice that with increasing γ, the right hand boundary of escape lowers implying that the greater the asymmetry, the quicker the route to escape. This is an expected outcome. Since symmetry no longer holds, $\gamma \neq 0$, the asymmetric (period-2) solution loses stability

through a period doubling bifurcation which is followed through a second period doubling bifurcation and so on through a period doubling cascade to chaos (more detail on this will be given later). To verify the fall in these curves and the reason for these chosen imperfection values numerical examination is necessary and the following section of this Chapter sets out to do so.

The previous analysis of Chapter 2 leads to a plot of the locus of the subcritical bifurcation corresponding to the left hand boundary of the escape zone. By similarly applying the vertical tangency condition, $\frac{da}{d\omega}=\infty$ to

$$y(a,\omega) = a^2\left[\left[1-\frac{\omega^2}{4}-\frac{\theta_0^2}{3}-\frac{a^2}{8}\right]^2+\left[\frac{c\omega}{2}\right]^2-p^2\left[\frac{a^2}{12}-\frac{\theta_0^2}{6}-\frac{1}{2}\right]^2\right]$$

then

$$\frac{da}{d\omega}=\frac{\frac{dy}{d\omega}}{\frac{dy}{da}}=-\frac{2\omega a^2[\frac{1}{2}(1-\frac{\omega^2}{4}-\frac{\theta_0^2}{3}-\frac{a^2}{8})-\frac{c^2}{4}]}{2a\left[[[1-\frac{\omega^2}{4}-\frac{\theta_0^2}{3}-\frac{a^2}{8}]^2+[\frac{c\omega}{2}]^2-p^2[\frac{a^2}{12}-\frac{\theta_0^2}{6}-\frac{1}{2}]^2]-\frac{a^2}{4}(1-\frac{\omega^2}{4}-\frac{\theta_0^2}{3}-\frac{a^2}{8})-\frac{a^2p^2}{6}(\frac{a^2}{12}-\frac{1}{2}-\frac{\theta_0^2}{6})\right]}.$$

Hence $\frac{da}{d\omega}=\infty$ when the denominator is zero and for small a,

$$\left[1-\frac{\omega^2}{4}-\frac{\theta_0^2}{3}\right]^2+\left[\frac{c\omega}{2}\right]^2=p^2\left[-\frac{\theta_0^2}{6}-\frac{1}{2}\right]^2.$$

This equation is plotted in Figure 4.5 together with (4.4.9) to produce left and right hand boundaries for the region of escape in terms of γ when $\gamma = 0$, 0.001 and $\gamma = 0.02$ respectively. We notice that the imperfection term also has an effect on the left hand boundary of escape as the imperfection term increases. For $\omega > 2$, the boundary does not shift to the same magnitude as for the case for $\omega < 2$. As in Figure 4.4, each coloured curve represents the allocated imperfection term.

Moreover, when $\gamma = 0$, the above expression becomes,

$$\left[1 - \tfrac{\omega^2}{4}\right]^2 + \left[\tfrac{\alpha\omega}{2}\right]^2 = p^2 \left[\tfrac{1}{2}\right]^2$$

which agrees with the analytical findings using the Taylor series expansion of $\sin\theta$ for the simple parametrically driven pendulum $\gamma = 0$ case studied by other fellow researchers (Capecchi and Bishop, 1994) and the analytical findings of Chapter 2 equation (2.5.12) using Bessel functions. This equation furnishes a good approximation of the boundaries for the Mathieu first zone (Clifford, 1994).

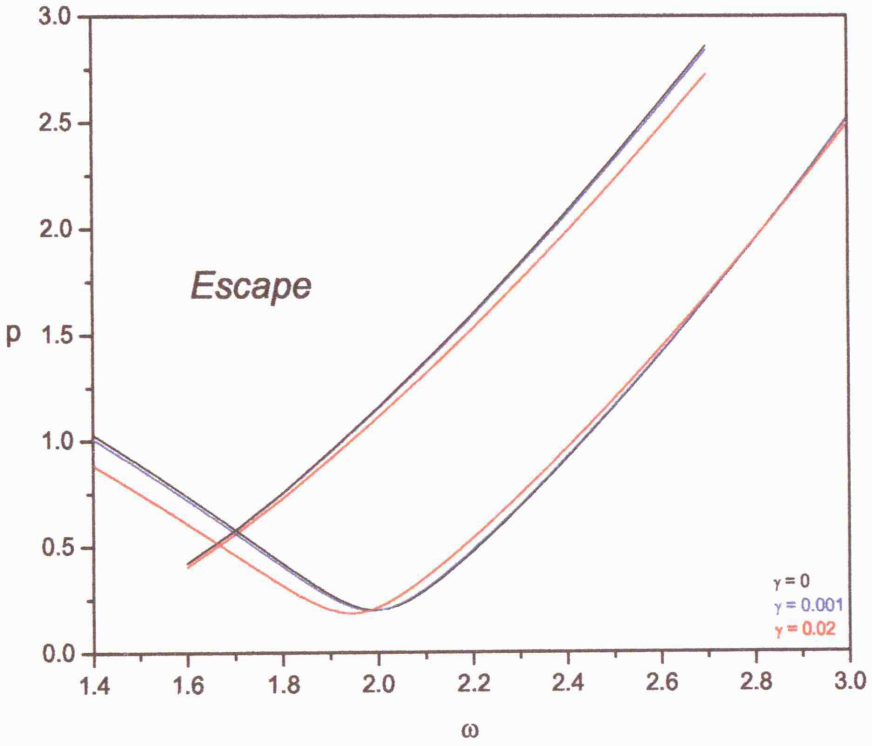

Figure 4.5: *Analytical left and right hand boundary for escape for the various imperfection terms stated in the* (ω, p) *parameter space.*

It is also noted that since the proposed model incorporates the bias term γ, it can be easily deduced from (4.4.7) that $\theta_0 = 0$ is not a solution of this system due to its dependency on γ. Thus, indicating that indeed the symmetric equilibrium solution, $\theta_0 = 0$, is no longer possible and an asymmetric solution is now expected.

Most importantly, equation (4.4.2) resembles the algebraic form $F(x, \lambda) = x^3 - \lambda x - I$, which model a physical situation undergoing symmetry breaking, with I representing a constant imperfection term (Mullin, 1993). Figure 4.6 shows for clarification purposes the plot of the bifurcation diagram for the analytical expression (4.4.2) showing the effects of including a symmetry breaking imperfection $\gamma = 0.2$, for $\Delta = +1$ (red) and $\Delta = -1$ (blue). We choose this higher value of bias to show clearly the effects.

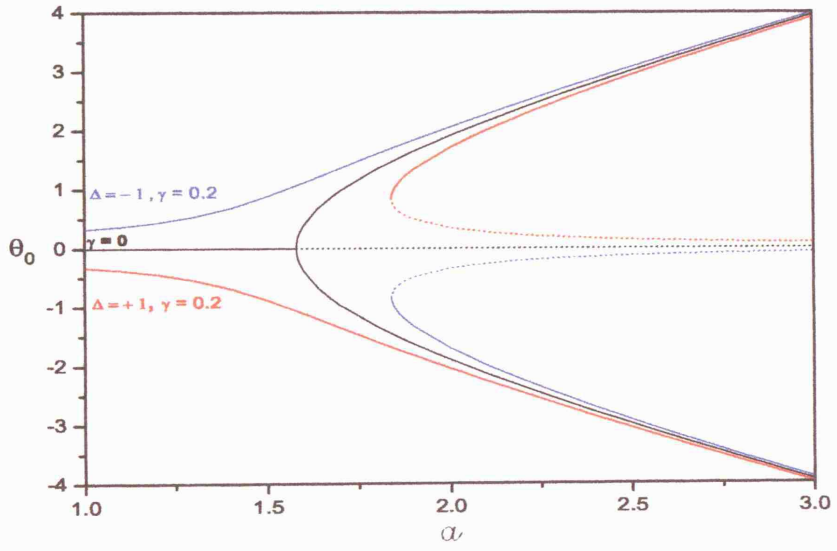

Figure 4.6: *Bifurcation diagram based upon analytical expression (4.4.2), showing the effects of including symmetry breaking imperfection.*

Using results of Chapter 2 and more specifically the numerically determined bifurcation parameter diagram of Figure 2.6, we are able to extract the critical value of forcing amplitude where the symmetry-breaking, pitchfork bifurcation occurs around $\omega = 2$, $p \approx 1.25$, which we employ and place back into equation (4.4.2) for p, so that we are able to compute Figure 4.6.

We see that γ has the effect of disconnecting the supercritical pitchfork bifurcation ($\gamma = 0$ black curve at about $a \approx 1.58$) so that there will now be a smooth evolution of one its solution, with increasing forcing amplitude, characterised as the lower branch, and a disconnected solution, upper branch (shown in red for $\gamma = 0.2$). Depending on Δ, so if it is $+1$ or -1, the upper and lower branch alter in position. We emphasise also that such an imperfection term may be present in any physical realisation of a practical problem.

Consequently we have shown here from our analytical expressions that by including a bias term in the initial symmetric system will cause the symmetry-breaking, pitchfork bifurcation to disappear and to be replaced by a preferred smooth branch evolution and a disconnected branch which itself bifurcates at a saddle node bifurcation. Numerical work that follows re-enforces this scenario with increasing forcing amplitude.

4.5 Numerical simulations and discussions of the asymmetric model

To fully appreciate the effects of symmetry breaking, we include as Figure 4.7, numerically determined bifurcation diagrams computed for equation (4.2.1) for a range of imperfection values. The bifurcation diagrams were obtained in a similar manner with those described in Chapter 3.

Figure 4.7(a) consists of a bifurcation diagram for when $\gamma = 0.001$ with $\Delta = +1$ and $\omega = 2.1$ for steady state solutions within the well. It must be noted that for $p < 0.29$, the system undergoes a periodic variation but the amplitudes are so small that on this scale they cannot be distinguished from the $\theta = 0$ line. At $p = 0.29$, a period doubling is encountered leaving an asymmetric period-2 orbit formation. Analytical findings gathered in Figure 4.5 agree precisely to two decimal places with this value of forcing amplitude. This is where the blue curve in Figure 4.5, at $\omega = 2.1$ is first crossed with increasing p, producing a pair of new asymmetric solutions that correspond to the swinging motion at twice the driving period.

As p increases, this $2T$-periodic asymmetric solution increases in amplitude but at about $p = 1.45$ it smoothly tends to decrease in swing before another period doubling is experienced around $p = 1.53$ and very soon thereafter escape occurs.

In the symmetric case, with $\gamma = 0$, (recalling Figure 3.2(a)), the system experiences a symmetry-breaking, pitchfork bifurcation (Bishop, Sofroniou and Shi, 2005), but in this broken symmetry type model, this pitchfork-type bifurcation is split into two branches. Moreover, this phenomenon also appears when dealing with the simple perturbed pitchfork bifurcation, where the structure is broken into disconnected branches (Mullin, 1993).

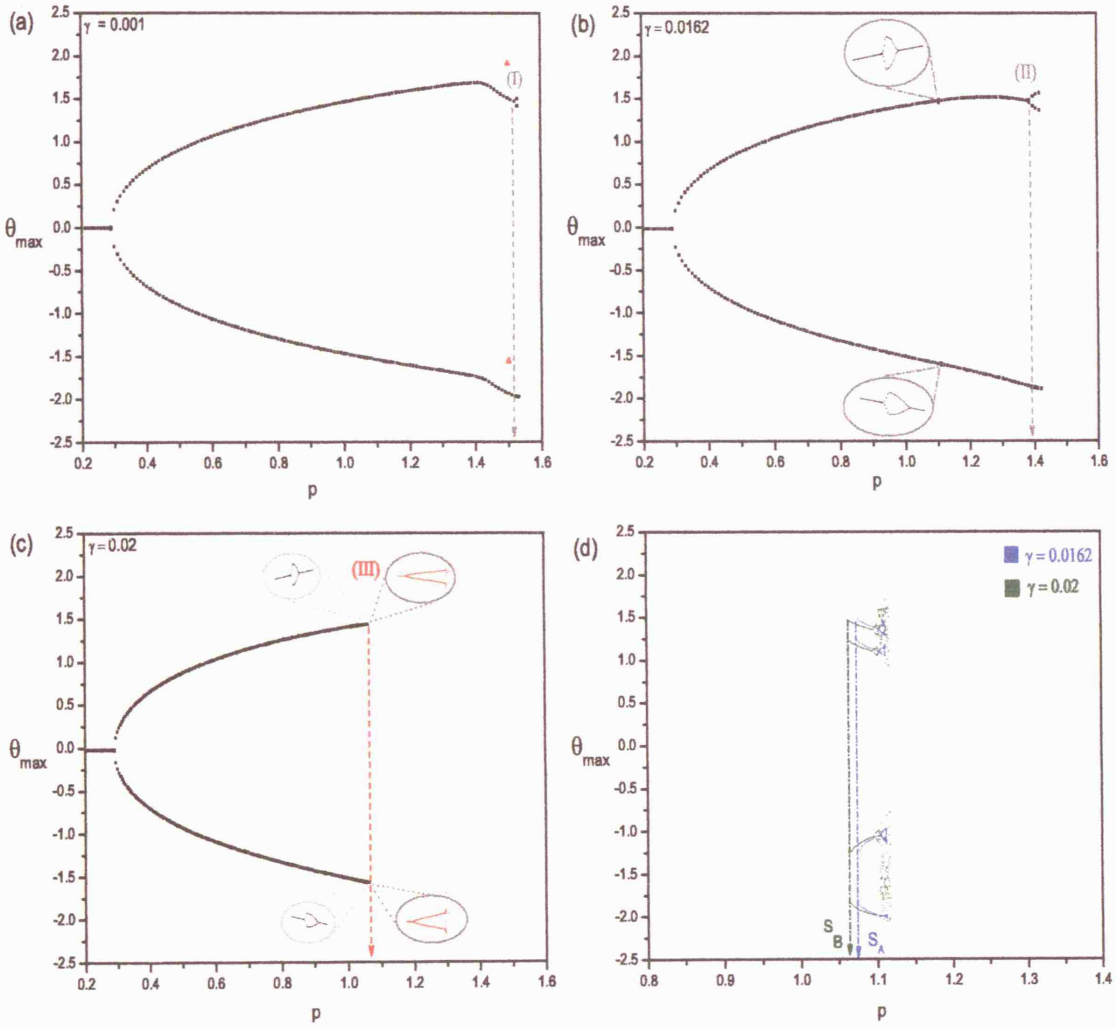

Figure 4.7: *Numerically determined bifurcation diagrams at* $\omega = 2.1$, $\Delta = +1$. *(a)* $\gamma = 0.001$. *The first period doubling of the sequence leading to cascade is labelled (I). Triangular red points indicate existence of saddle node. (b),(c)* $\gamma = 0.0162$ *and* $\gamma = 0.02$. *In (b),* (II) *denotes period doubling occurrence that leads to escape. Elliptical insets are enlargements of two opposing supercritical period doubling bifurcations generating a closed loop. In (c),* (III) *denotes the period doubling just before escape, with elliptical windows indicating "bubble-like" behaviour as in (b). (d) Co-existence of the stable-unstable pair of subharmonic orbits for* $\gamma = 0.0162$ *and* $\gamma = 0.02$.

The lower branch, for example, consists entirely of stable fixed points, whereas the upper disconnected piece has both stable and unstable fixed points (see also Figure 4.6).

If Δ is taken as $+1$ so that the bias term is positive, for increasing p the branch is continuous, but decreasing in positive response amplitude. Whereas for negative bias, the opposite effect occurs; the positive amplitude increases smoothly thus having a lower disconnected piece as its partner. In this proposed model, there is no longer a sharp transition due to the pitchfork nature but on the contrary, a smooth evolution of the lower branch leading to the cascade of period doublings. These numerical observations confirm the analytical diagram of Figure 4.6 so that we may expect that due to the nature of the system, equation (4.2.1), this bifurcational behaviour will be anticipated.

The disconnected upper piece however, created at the saddle node bifurcation is much more difficult to locate, and so the existence of such a solution is indicated only by the triangular shaped points shown at about $p = 1.5$ in Figure 4.7.

Looking ahead at Figure 4.8, time histories and corresponding phase planes for when $p = 1.5$ are shown corresponding to Figure 4.7(a). They depict the case when the system is on the lower branch as well as when the solution is on the upper disconnected piece where in the latter case, this verifies the occurrence of the saddle node bifurcation. Since this solution is very hard to detect, merely a triangular shaped point portrays that at that certain value of forcing amplitude a solution characterising a saddle node bifurcation does exist. The difficulty in detecting this second solution is probably due to this stable solution having a relatively small, but non-zero basin of attraction in terms of angular position and velocity.

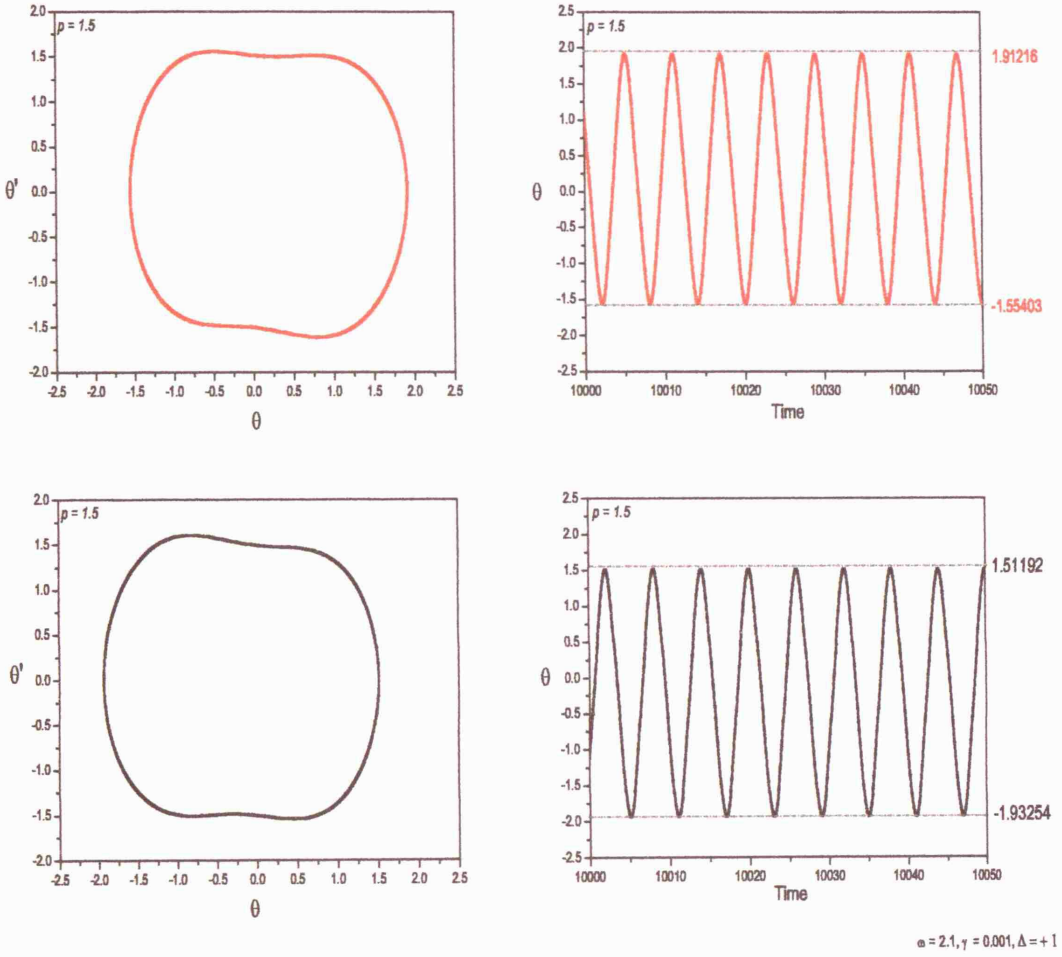

Figure 4.8: *Phase planes and corresponding time histories when* $p = 1.5$, $\gamma = 0.001$ *and* $\omega = 2.1$ *depicting the existence of both the stable solutions of the asymmetrical system. The red set of phase portrait and time series correspond to the red triangular points of Figure 4.6(a) verifying the existence of an upper branch for the disconnected pitchfork bifurcation.*

In Figure 4.7(a), the drop in amplitude experienced for when $\Delta = +1$, as explained above, has a very significant experimental implication. This is because the decrease in amplitude of the asymmetric oscillation may be visualised and may act as a precursor that something will soon happen that will lead to rotational motion. The drop in amplitude of the oscillation is more visible to the eye and hence acts as a good predictor of the escape boundary.

Our numerical work and experimental observation is that after the near hanging solution loses its stability and undergoes a period-2 asymmetric oscillatory motion the amplitude initially increases. At a certain value of forcing amplitude, around $p \approx 1.45$, the pendulum naturally decreases its angle of swing and thereafter rotational behaviour is anticipated. Hence, this experimental significance may be regarded as a warning sign of the imminent chaotic behaviour.

While this has been viewed experimentally for the symmetrically parametrically excited pendulum model, using our crude rig (see photo in Figure 3.3), along with asymmetrical transients prior to rotations, no further experimental evidence is available for the asymmetric problem.

In Figure 4.7(a) with $\gamma = 0.001$, the position along the p-axis of the first period doubling in the sequence of cascade leading to chaos is denoted by (I). Only the first period doubling in the sequence is shown in the diagram as the transition to chaos via the cascade is very swift. Our analytical work shows that at this imperfection term, the assumed approximate boundary of escape occurs at $p \approx 1.45$ which is the instance where in this bifurcation diagram the oscillatory amplitude begins to decrease in angle and period doubling occurs soon-after followed by escape. Hence the analytical boundary of escape seems to be more conservative under this bias term, implying a better predictor of escape.

In Figure 4.7(b) with $\gamma = 0.0162$, (II) denotes a period doubling bifurcation, whereby final escape from the well follows soon thereafter. The increase in imperfection term sees the escape event occurring earlier along the p-axis remaining in agreement with the analytical findings where escape was found to occur sooner as the bias term increases.

However (II) is not the first period doubling encountered. The elliptical insets are enlargements of a phenomenon occurring in a very narrow window of the p parameter, resembling a "bubble-like" picture. Within the windows, the stable asymmetric period-2 solution undergoes a period doubling bifurcation at about $p \approx 1.10$, giving birth to a pair of period-4 asymmetric orbits, which they in turn experience an inverse period doubling bifurcation, so that the resulting solution is of period-2 nature again.

This behaviour has also been numerically observed by Thompson (Thompson, 1989) for his study of the escape equation. For a specific external forcing magnitude, two opposing supercritical period doubling bifurcations generate a closed loop of subharmonic attractors just like in our Figure 4.7(b). We do not produce any analytical evidence of this phenomenon. Thompson also discusses that increasing slightly the external forcing amplitude this feature may be developed into two opposing cascades to chaos (Thompson and Stewart, 1986) however we have not come across this characteristic here within our study and within our chosen parameter ranges.

(II) and (I) both represent the first period doubling of the cascade leading to chaos, but (II) differs in the sense that it has occurred after this closed loop phenomenon, which in itself incorporates other period doubling bifurcations.

Similarly, in Figure 4.7(c) with $\gamma = 0.02$, a computed bifurcation diagram is shown consisting of enlargement areas shown by elliptical windows. It must be noted

that very close to the supercritical period doubling bifurcation, leading to escape, (denoted by (III)), the closed loop of subharmonic attractors is again present but of much smaller amplitude range, so that almost undetectable.

The red boundary of escape in Figure 4.4 and 4.5 for $\gamma = 0.02$ anticipates that escape is to occur at $p \approx 1.29$, later than what the numerical analysis indicates, $p \approx 1.06$. So analytical predictions of escape seem to be closer to numerical ones when the imperfection terms are smaller.

Figure 4.7(d) shows the co-existence of saddle node bifurcations, at S_A, while moving forwards in p, for when $\gamma = 0.0162$. To be precise, our numerical techniques allow only detection of stable solutions thus S_A is actually a fold, but our knowledge of similar systems, lets us assume that unstable solutions also exist and this resembles a saddle node bifurcation. So stable-unstable pair of subharmonic orbits are formed by a saddle node creation. Whilst on a blue branch, the solution then in itself exhibits a period doubling sequence leading to chaotic behaviour. This means that a jump from the stable asymmetric period-2 solution to the saddle node bifurcation could imply another route to escape for the system. If conversely, the forcing amplitude is slowly decreased from an initially high value, we arrive at the saddle node (with a relatively lower response amplitude), from which the system would jump back on to the stable asymmetric state.

The co-existence of the stable-unstable pair of subharmonic orbits for the specific value of $\gamma = 0.02$ are also shown in Figure 4.7(d), at S_B. The stable orbit period doubles to a chaotic attractor, which loses its stability at a crisis, when it probably hits the unstable orbit (Thompson and Stewart, 1986). These type of events are not easily found numerically because the stable orbits often have very small basins and only exist in a very small parameter regime.

To verify the phenomena experienced by the bifurcation diagrams of Figure 4.7(a) and (c), we present Figure 4.9 for the cases of $\gamma = 0$ and $\gamma = 0.02$ respectively around the major resonant zone. These parameter space plots graphically depict the distribution of different types of steady state motions when two parameters are varied, p and ω. These plots were obtained computationally by the use of the computer program *Dynamics* (Nusse and Yorke, 1994). Similarly to Figure 2.7, the parameter space is divided into a grid whereby Lyapunov exponents are calculated keeping the same initial conditions for each element of the grid.

Alternatively, for this figure, we add a chosen colour code where different colours are allocated to the different Lyapunov exponents and we obtain a parameter space plot. Their meaning depends on the colour settings as summarised in *Dynamics* (Nusse and Yorke, 1994). The initial conditions are taken here to be $\theta(0) = 0.1$, $\theta'(0) = 0$ and $c = 0.1$ for both unbias and bias term cases, keeping $p \ \epsilon(0, 1.5)$ and $\omega \ \epsilon(1.5, 2.5)$. For both parameter space plots, dark blue colour corresponds to period-one oscillatory motion and fixed points (region labelled O_1 and F for clarity), green represents period-two oscillatory motions (corresponding to O_2 regions), yellow coloured parts correspond to chaotic motion (shown as C), and red regions the area around period doubling bifurcations.

In regions where there is evidence of scatter within the tongues, rotational behaviour is exhibited and depending on the nature of the periodicity, are denoted by R_1 (period-one rotation) and R_2 (period-two rotation). Oscillatory-rotational motions are also experienced within this area of the tongue and these are defined as rotations that change the direction of rotation. More detail is needed to determine the parameter space regions but rotations and subharmonics co-exist (Clifford and Bishop, 1993, Szemplińska-Stupnika *et al*, 2000, Garira and Bishop, 2003), so any scatter implies uncertainty which from a practical engineering perspective entails danger.

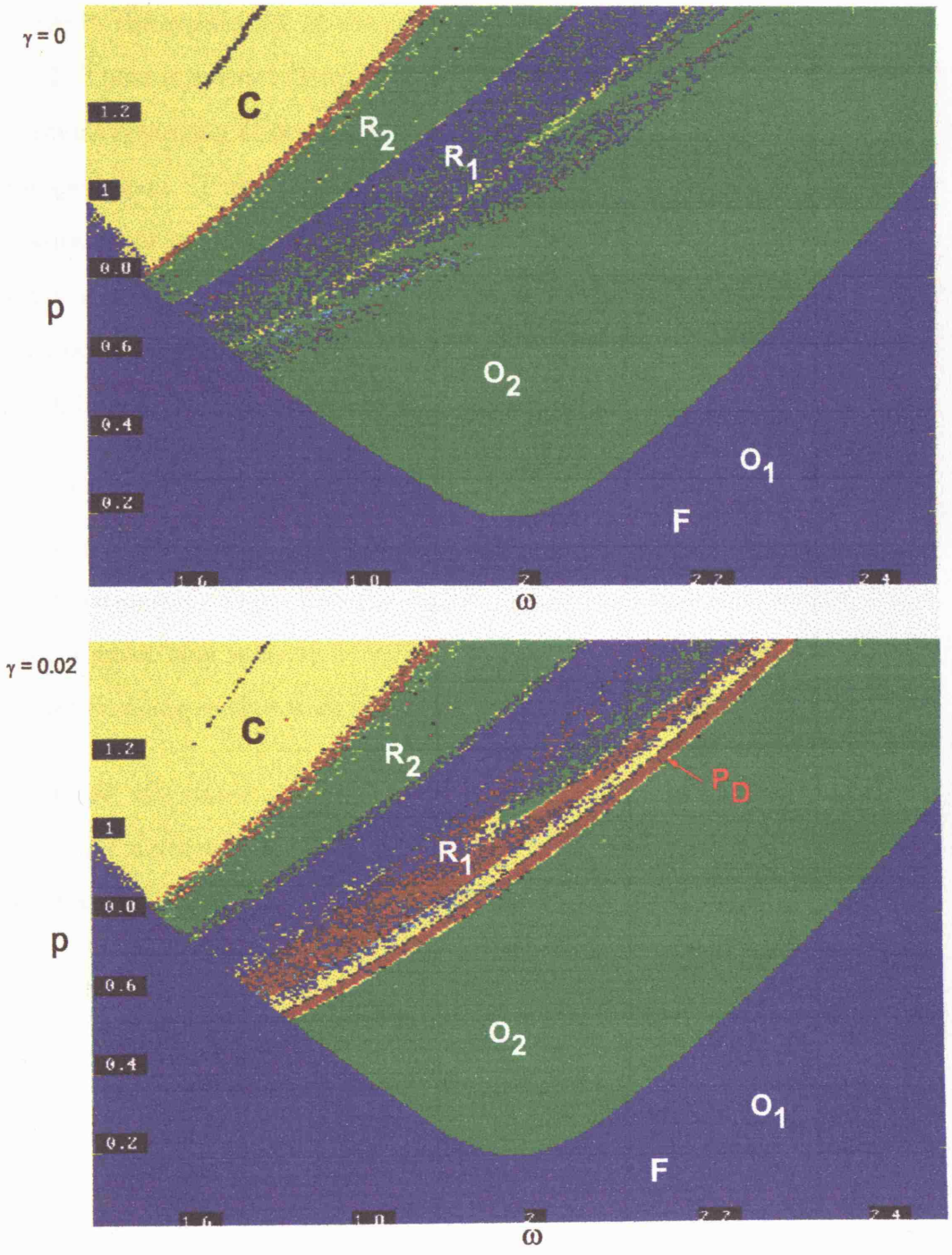

Figure 4.9: *Numerically determined parameter space plots near the first major resonant zone for* $\gamma = 0$ *and* $\gamma = 0.02$ *respectively.*

Comparing the two parameter space plots, one is able to distinguish a distinct difference in the separation of the regions O_2 and R_1 within the resonant zone for $\gamma = 0.02$. There is a strict boundary (in red), that divides these two areas, so that any motions occurring above the locus of red points are considered to have entered the escape region. This locus of red points represent the locus of period doubling bifurcations that initiate the cascade of period doubling sequence leading to escape. With the view of Figure 4.7(c), this instance is denoted as (III) and occurs roughly at $p \approx 1.06$, which is echoed and verified accurately in the parameter space diagram for $\gamma = 0.02$.

For $\gamma = 0$, the primary period doubling bifurcation leading to the route to chaos occurs at $p \approx 1.53$ (see Figure 3.2(a)), which is not shown in Figure 4.9 due to the chosen p parameter range. But the significance here of this justification is to show that for a small bias term, $\gamma = 0.02$, the region of purely oscillatory motions has decreased enabling escape from the potential well to occur much sooner.

Furthermore, the phase portraits accompanying Figure 4.1 for the perturbed undamped and unforced simple pendulum is also in agreement since we mentioned earlier that the basin of safe oscillatory motions may become smaller.

4.6 Basin of attraction

The *Dynamics* software also allowed us to perform numerical studies on the basin of attraction for both the symmetric and asymmetric model of the parametrically excited pendulum system.

Given that a nonlinear system may posses more than one attractor, we need to have some kind of measure of the relative importance of each attractor in terms of how likely we are to achieve each solution. Basins of attraction hence describes the set of all initial conditions that lead to an attractor or in other words to the settled solution of the equation after the transient behaviour has died down (Hsu, 1987, Bishop, Virgin and Leung, 1988, Soliman and Thompson, 1992, Capecchi and Bishop, 1994, Alexander, 1998).

In this work, the basin of attraction is numerically calculated by dividing the phase plane into a 300×300 grid of initial conditions with the aim of integrating each point until an attracting solution is achieved. The basin resolution is chosen to be high so that the grid may be fine enough to provide an accurate and clear definition of the basin of attraction but also low enough as to be computationally efficient.

Different shades of grey are used to colour the grid boxes indicating that they contain points of attractors. Initially all grid boxes are unshaded but as the routine for basin of attraction proceeds, all grid boxes eventually become coloured with different levels of shading. The process begins by selecting an uncoloured box and testing it by examining the trajectory that begins at the centre of the grid box. The trajectory may or may not pass through grid boxes that have been previously shaded, but what it encounters will determine the colour of the initial grid box (Nusse and Yorke, 1994). A more detailed explanation on the basin of attraction routine may

be found in Nusse and Yorke (Nusse and Yorke, 1994).

The basins of attraction of stable attracting steady states in a phase space can be determined by a variety of computational techniques. A more conservative and highly successful algorithm for computing basins of attraction is given by Alexander (Alexander, 1989) but not adopted here within as *Dynamics* software was more attainable.

Figure 4.10 shows a basin of attraction for the unbiased parametrically excited pendulum at $p = 0.8$ and $\omega = 2.1$. The attracting basin looks quite regular.

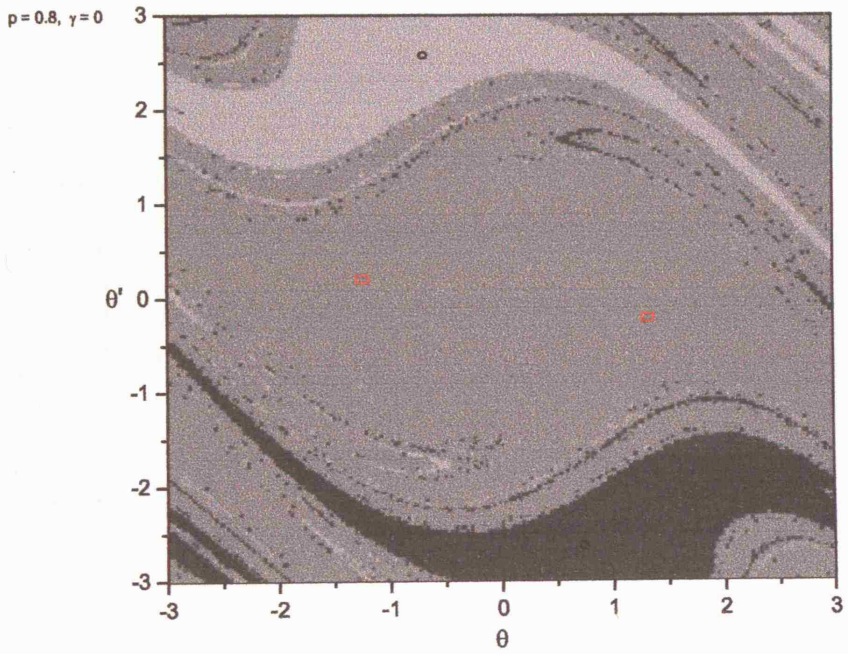

Figure 4.10: *Basin of attraction for $\gamma = 0$, $p = 0.8$ at $\omega = 2.1$. Red rectangular points correspond to period-two oscillatory attractors and black circular marks represent period-one rotational attractors.*

Most of the phase plane considered corresponds to the basin of the symmetric oscillating motion of period $2T$ (coloured as grey) and indicated also by the red rectangular points within the basin for clarity. The basin of the oscillating motion is evident and seems to be more predominant. The remaining part consists of the two quite large zones, indicated with the help of the black circular marks, representing the basins of attraction of period-one rotating motion.

We are able to say with confidence that the oscillating motions within the grey region are of period $2T$ because if we consider the time series in Figure 4.11, computed for $p = 0.8, \omega = 2.1$ and for initial conditions within the grey region (transients are let to die away then plotted), we see that the period of the response is approximately $12.55 - 6.57 = 5.98$ which is $2 \times \frac{2\pi}{2.1}$, hence twice the period of forcing.

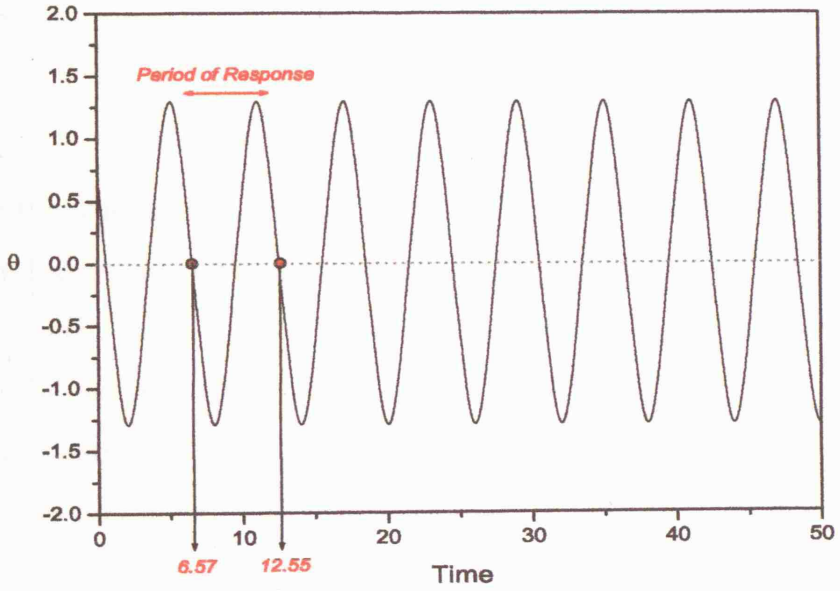

Figure 4.11: *Time series for* $\gamma = 0$, $p = 0.8$, $\omega = 2.1$ *at initial conditions* $\theta(0) = 0.69$, $\theta'(0) = 0$.

We note that the boundary of the basin of attraction in Figure 4.10 of the three coexisting attractors is of slight fractal structure. This provides us with numerical evidence that the system is sensitive to initial conditions. So called *fingers* of initial conditions are situated on the edges of the middle portions of the basin (Thompson and Stewart, 1986). This structure of the basins of attraction imply that if the system is set into motion with initial conditions that belong to the fractal areas, the resulting transient trajectories are chaotic and may involve both clockwise and anti-clockwise rotating motions. After the transient, the system starting with very close initial conditions may settle onto one of the three coexisting attractors. However the region over which we can see the fractal character may be small.

Capecchi *et al* (Capecchi and Bishop, 1994), Szemplińska-Stupnicka *et al* (Szemplińska-Stupnicka, Tyrkiel and Zubrzycki, 2000) and Xu Xu *et al* (Xu Xu, Wiercigroch and Cartmell, 2005), computed similar basins of attraction for the parametrically excited pendulum system but under different control parameter conditions.

Increasing the amplitude of forcing to a level so that symmetry breaking, pitchfork bifurcation has been exhibited, we show as Figure 4.12 another basin of attraction phase plane. The basin for the asymmetric $2T$ oscillating motion is depicted with the aid of the red rectangular marks and it is further mentioned that the area of the basin of these attractors has decreased immensely. The basin indicated via blue circular marks may identify $2T$ oscillating motions for the second pair of asymmetic solutions or maybe might correspond to $2T$ oscillatory-rotational attractors. The green triangular points symbolize the basin of $1T$ rotating attractors. Everywhere else there is a mixing of attracting basins suggesting an evident fractal nature of the basin boundary so that for many initial conditions, the fate of a trajectory is unpredictable.

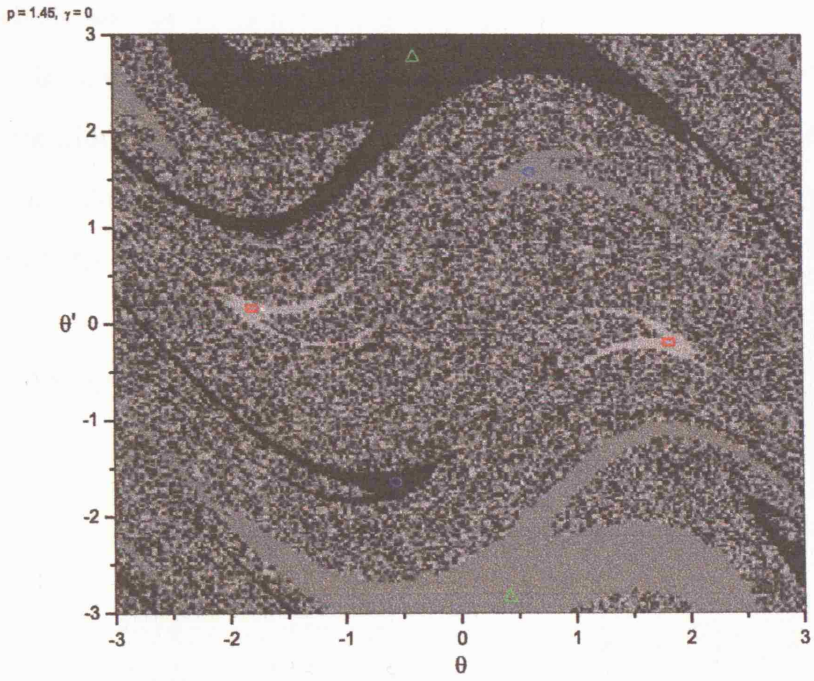

Figure 4.12: *Basin of attraction for* $\gamma = 0$, $p = 1.45$ *at* $\omega = 2.1$. *Red rectangular points correspond to the basins of period-two asymmetric oscillatory attractors. Blue circular marks may represent the basins of the second pair of asymmetric attractors or the basin of period* $2T$ *oscillatory-rotational motions. Green triangles correspond to the basin of period-one rotational solutions.*

For the purpose of comparison, we finally show as Figure 4.13, the attractor basin for the asymmetric model of the parametrically excited pendulum with $\gamma = 0.02$. From our earlier numerical investigation of the bifurcation diagram for this case (Figure 4.7(c)), we remind ourselves that at $p \approx 1.06$, the system escapes from the potential well so that oscillatory motions are no longer realised.

Figure 4.13 shows the disappearance of the basin for the asymmetric $2T$ oscillatory attractor which was previously evident for the same forcing amplitude but when $\gamma = 0$. The circular blue marks seem here to represent the basin of $2T$ asymmetric oscillatory-rotational attractors and green triangular points the basin for $1T$ rotational motion. The fractal structure is again visible and dominant signifying the interlinking of the attractor basins.

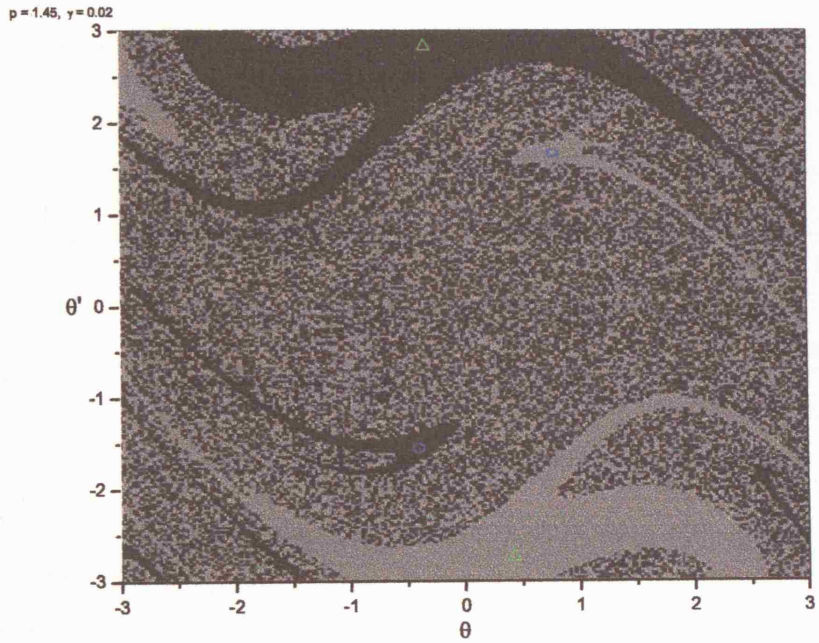

Figure 4.13: *Basin of attraction for* $\gamma = 0.02$, $p = 1.45$ *at* $\omega = 2.1$. *Blue circular points seem to correspond to the basins of period-two oscillatory-rotational attractors and green triangular marks represent the basins of period-one rotational attractors.*

The above study of the basins of attraction manages to exemplify the diminishing region of safe oscillatory motion as the bias term is increased and manifest the importance of understanding how breaking the symmetry of a model may affect the nonlinear and bifurcational nature of a system.

Another new feature of this Chapter can be seen in Figure 4.14. For motions started within the potential well close to $\theta{=}\theta'{=}0$, the figure is a plot of the boundary between those parameters for which subsequent motions remain in the well, considered as safe, and those which typically leave the well. Thus if we require the dynamics to be bounded within the well, we then need parameters chosen within the Safe Zone. The figure was constructed over a range of γ terms incremented by 0.001 with the forcing frequency still remaining at $\omega = 2.1$.

Results from numerical work in Figure 4.7(a,b,c) allow us to assume that the period doubling bifurcations incurred, labelled as points (I), (II), (III) accordingly, may act as precursors to the escape phenomenon that occurs soon after. The value in each bifurcation diagram of the forcing amplitude that invokes the initial period doubling leading to the cascade route to chaos aids to configure this safe area or zone. Points denoted as (I), (II), (III), S_A and S_B in Figure 4.14 correspond to the meaning of the notation and the bifurcation phenomena undergone in the earlier bifurcation diagrams in Figure 4.7.

Regions between $\gamma \approx 0.016$ and $\gamma \approx 0.019$ that are also shaded in between black dotted and blue dotted curves correspond to asymmetric oscillatory solutions that exist after the bubble-like behaviour occurs as described earlier whilst increasing p.

Moreover, if a jump was to occur from an asymmetric solution in Figure 4.7(b) ($\gamma = 0.0162$) to one of the corresponding blue folds in Figure 4.7(d) at the specific forcing amplitude and bias, then it would escape via the blue route of period doublings that instigate escape instead via the period doubling denoted (II). Hence the shaded extra area includes such scenarios.

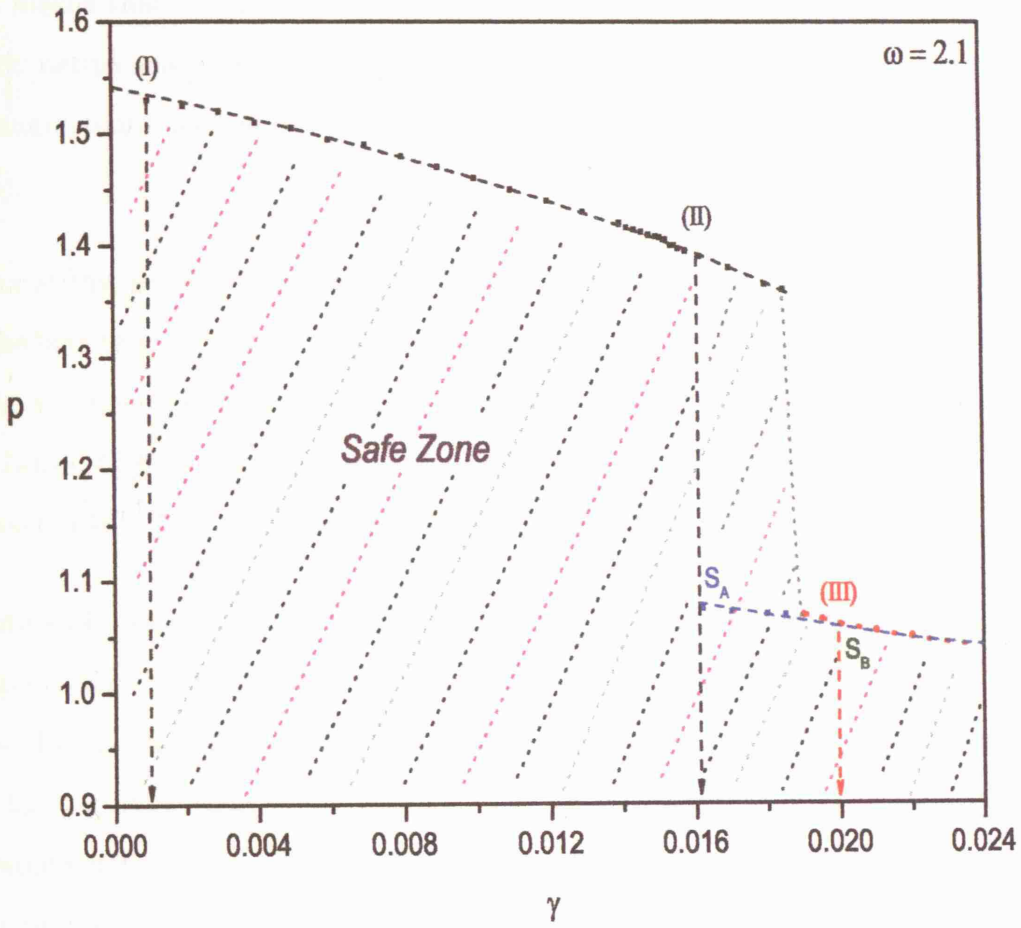

Figure 4.14: *Shows a locus of the amplitude forcing values determined by the first period doubling in the sequence of cascade, that can act as precursors of escape, over a range of γ terms, incremented by 0.001. Points labelled as (I), (II), (III), S_A and S_B correspond to the notation and phenomena undergone in Figure 4.7. The shaded area represents a region where safe oscillatory motions can be experienced, which is denoted as 'Safe Zone', and everything above this boundary level are analogous to the escape zone present within the resonance tongues.*

This key figure indicates a smooth initial decrease in amplitude of forcing at which escape must occur and soon after a drop in the boundary of safe oscillatory motions. This means that within the shaded area, the system exhibits oscillations of asymmetric nature and everything slightly above portrays the escape region within the resonance zones, as described and seen in Clifford and Bishop (Clifford and Bishop, 1994).

In our study, small changes in the symmetry of the proposed model, accomplished by the bias term γ, initially lead to little reduction in the safe zone, but as the value of the imperfection term increases, there is a rapid erosion process, which echoes the *Dover Cliff* fall in basin area described by different scientists (Thompson and Stewart, 1986, Thompson and Bishop, 1994).

Figure 4.14 may act as a safety assessment or a benchmark to future work, where the escape scenario is initiated by the first period doubling in the sequence of cascade, shown by the black dashed line for about $\gamma < 0.019$ and shown by the circular dotted line for γ greater than 0.019 values. Most importantly, a major deduction is that we would not want to operate any system at values of forcing magnitude greater than that of the safe oscillatory boundary, even though there may still exist stable periodic motions within the well.

In view of ship dynamics (Virgin, 1987, Spyrou and Thompson, 2000, Spyrou, 2002), the idea of this safe area can be identified as a non-capsizing region. More specifically, the appearance of the period doubling phenomenon in the roll motion of ships, should be regarded as a sign of the impending danger of capsizing and so, generally for any system, the aim would be to remain within the safe zone so that prevention of operational difficulties can be accomplished. But, being strict and precise, areas where any type of oscillation is induced must be avoided when operating an

engineering system so that smoother operational handling can be achieved without disastrous consequences.

Another important observation of this figure is that for an asymmetric system, where imperfection is present, escape occurs earlier than in its symmetric counterpart and moreover, as the value of the bias term increases, the asymmetric case becomes more dangerous which can be seen from the dramatic drop in the boundary of the safe zone of oscillatory motions.

4.7 Breaking the symmetry of the inverted parametrically excited pendulum by inclining the model by an angle

In this section we consider breaking the symmetry of the model of the parametrically excited pendulum in a different manner, in order to analyse the effect this alteration has on the dynamics of the system and compare techniques and outcomes with the method of bias term inclusion adopted earlier.

We assume that the physical model is inclined at a certain angle. For clarity, it is noted here that in terms of visualising an experimental apparatus, it is not the actual pivot point that has undergone a tilt but the whole rig has been tilted onto one side by an angle, say ϕ. Mathematically though, the effects are the same in terms of the equation. To understand the setting it is best to envisage that the rig in Figure 3.3 has been placed, on one of its sides, on top of a board whose thickness is such that it raises the apparatus by an angle ϕ.

In Chapter 2, we analytically found an estimate to the boundary of the stable zone for the inverted damped vertically parametrically excited pendulum and we provide here an extension to that work by considering the inverted solutions of the tilted vertically driven pendulum.

Sudor and Bishop (Sudor and Bishop, 1999, Bishop and Sudor, 1999, Koplow and Mann, 2005) also examined this case but their study lies mostly on numerical investigations. We shall include numerical computations as well as analytical studies, to produce a wider and more complete picture for this system. Our aim is to show how breaking the symmetry of the inverted model via this different method affects the

bifurcational behaviour and moreover confirm the disappearance of the symmetry breaking, pitchfork bifurcation due to this initial asymmetry.

Similar analysis may be made to a horizontally tilted parametrically excited pendulum but for consistency and completeness we remain examining vertically driven systems.

We consider angular oscillations about the pivot point given by θ and governed by the following non-dimensional equation of motion:

$$l^2\ddot{\theta} + \frac{\zeta}{m}\dot{\theta} - lg\sin\theta - lZ\Omega^2\cos\Omega\tau\sin(\theta-\phi) = 0 \qquad (4.7.1)$$

where $\theta(\tau)$ is the angular displacement of the pendulum measured from the upward vertical position, ζ is the damping constant and l is the effective pendulum length. The pivot point is subjected to a harmonic displacement of amplitude Z and frequency Ω and may be approximated as $z(\tau) = -Z\cos\Omega\tau$ when the pivot point is at the top of a cycle. The angle ϕ is the tilt angle measured in the gravity direction.

Rescaling time according to $t = \omega_0\tau$ and under the following notation,

$$\omega_0 = \sqrt{(\tfrac{g}{l})},\ c = \tfrac{\zeta}{\omega_0 ml^2},\ \omega = \tfrac{\Omega}{\omega_0},\ p = \tfrac{Z\Omega^2}{g}$$

reduces (4.7.1) to

$$\theta'' + c\theta' - \sin\theta - p\cos\omega t\sin(\theta-\phi) = 0 \qquad (4.7.2)$$

(see *Appendix B* for derivation). Evidently with no inclination angle, $\phi = 0$, equation (4.7.2) reduces to the usual form of the inverted parametrically excited pendulum equation (2.2.4).

We present firstly as Figure 4.15 a bifurcation diagram for the inverted solution, ($\theta = \pi$), of the parametrically excited pendulum, $\phi = 0$, where the solid lines have been numerically computed and indicate stable solutions for $\omega = 2$ and the dotted lines are schematic positions of the unstable solutions. Also the damping coefficient is taken to be $c = 0.1$ as in previous numerical computations. We are especially interested in solutions near $\theta = \pi$ *rad*, which for the unforced pendulum is unstable but when forcing is applied this solution may stabilise (Stephenson, 1908). This stable solution will possibly coexist with various other solutions, the hanging state, oscillations or rotations, and it is characterised by having a relatively small non-zero basin of attraction in terms angular displacement and velocity (Butikov, 2001).

The dynamics of the inverted position shown here are similar and of the same bifurcation sequence as the schematic contribution of Clifford and Bishop (Clifford and Bishop, 1998) who looked briefly into the inverted parametrically excited pendulum. In this figure, as we increase the forcing amplitude, the inverted solution stabilises at a subcritical pitchfork bifurcation (with an eigenvalue going through the unit circle at $+1$ by theory and results of Chapter 3) at approximately $p = 3.12$ where the unstable inverted solution collides with two unstable mirror-image period-1 solutions.

With increasing p, this inverted solution becomes unstable at $p \approx 3.42$ where a period doubling is exhibited accompanied theoretically by an eigenvalue going through the unit circle at -1. At this point, two stable symmetric period-2 oscillatory solutions are born. We note that this bifurcation was wrongly identified as a Hopf bifurcation by Blackburn *et al* (Blackburn and Smith, 1992).

Following typical bifurcation sequence, the symmetric period-2 solution undergoes a symmetry-breaking, pitchfork bifurcation at $p \approx 3.55$ leaving two stable mirror-image asymmetric period-2 oscillating solutions, only which one is shown for con-

venience. At $p \approx 3.575$, the period-2 asymmetric oscillating solutions undergo a period doubling that initiates the cascade of period doubling bifurcations that possibly later lead to chaotic attractors, where only the first period doubling is shown as the sequence is very rapid. This sees the end of stable inverted solutions that stem from the $\theta = \pi$ solution.

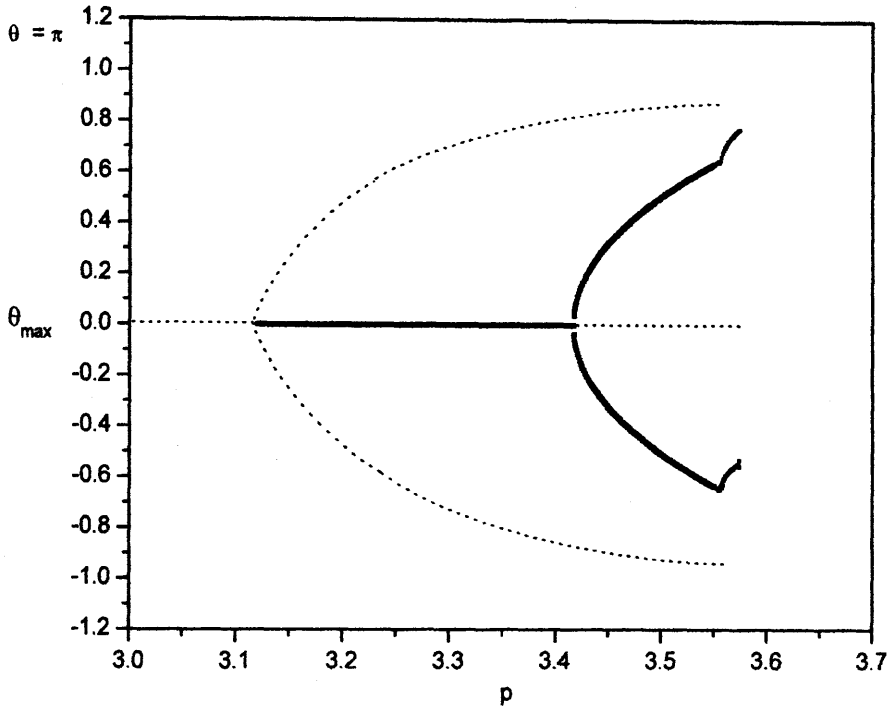

Figure 4.15: *Bifurcation Diagram for the inverted solution of the vertically parametrically excited pendulum for $\omega = 2$ over a variation in p. Solid lines indicate stable solutions whereas dotted lines are schematically drawn to represent unstable solutions.*

For the pendulum with tilt, $\phi \neq 0$, the system is no longer symmetrical so that a typical bifurcation sequence, while similar to the symmetric counterpart posses some differences. Figure 4.16 consists of a bifurcation diagram showing the evolution of the inverted solution for a variation in p with $\omega = 2$ and the small tilt angle of say $\phi = 0.001$. As above, the solid lines correspond to true numerical readings of the stable states whereas the dotted lines are schematics and included for the purpose of analysis.

In Figure 4.16, as we increase p, the inverted solution firstly stabilizes at a saddle node bifurcation at $p \approx 3.14$. The saddle node bifurcation is formed from the disconnection of the subcritical pitchfork bifurcation which was present in the symmetric counterpart system. Sudor and Bishop (Sudor and Bishop, 1999) apply bifurcation following algorithms (Foale and Thompson, 1991) to the equation of their tilted parametrically driven pendulum to produce the loci of bifurcations in a parameter space diagram. Their study verifies the occurrence of the initial bifurcation undergone as a saddle node one and so we may assume that the fold bifurcation here does imply a saddle node bifurcation even if unstable solutions were not detected.

As a consequence of the asymmetry of the system, $\theta = \pi$ (or $\theta = 0$ measured from the upward vertical) is no longer a solution to equation (4.7.2) and stable inverted dynamics proceed with small amplitude asymmetric period-1 oscillations which are offset from the upward vertical. At $p \approx 3.417$ the period-1 asymmetic inverted oscillation loses stability at a period doubling bifurcation where asymmetric period-2 oscillations follow, $p \approx 3.56$. This period doubling occurs after a slight increase in the oscillatory amplitude is experienced, as opposed to the reduction in swinging amplitude magnitude we came across during the earlier analysis of the proposed biased parametrically excited pendulum.

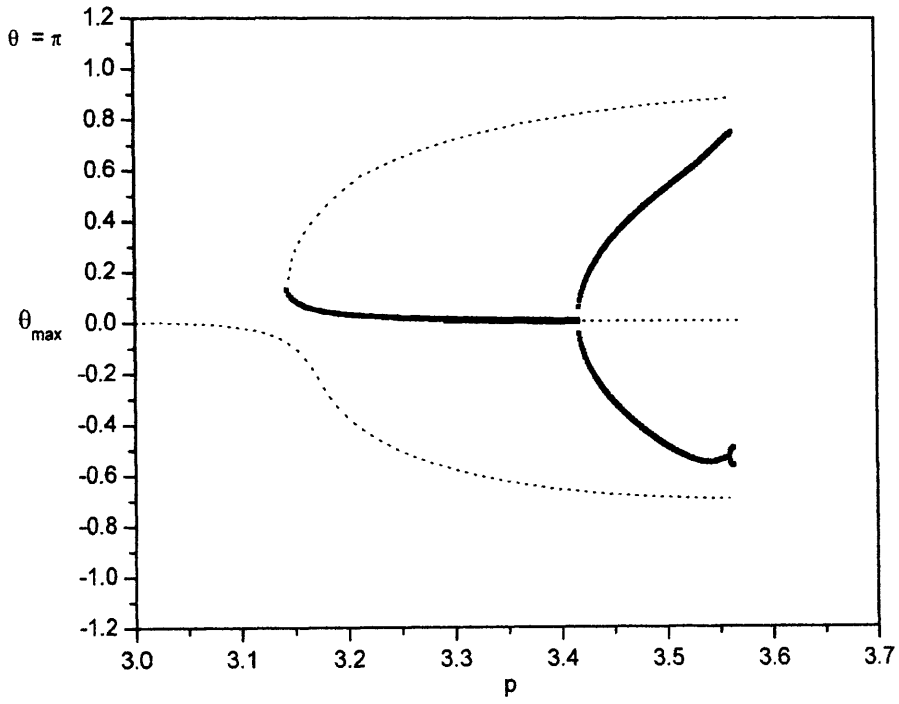

Figure 4.16: *Bifurcation Diagram for the tilted inverted solution of the parametrically excited pendulum at* $\omega = 2$ *over a variation in* p *when* $\phi = 0.001$ *rad. Solid lines indicate stable solutions whereas dotted lines are schematically drawn to represent unstable solutions.*

In the case of adding ϕ to (4.7.2) the effect just after the symmetry-breaking, pitchfork bifurcation is that the oscillatory amplitude will experience a drop instead of a rise, just like we have seen and examined in the near hanging solution of the parametrically excited pendulum.

Due to the asymmetry, a symmetry-breaking, pitchfork bifurcation does not occur and the mirror image asymmetric solutions of the symmetric counterpart are no longer present. This is expected following the analysis of the near hanging solution of the parametrically excited pendulum with bias. Moreover, for the asymmetric case, escape occurs earlier than the symmetric counterpart problem, agreeing with earlier findings within the Chapter.

The numerical analysis hence shows that there is no striking difference in the dynamics of this tilted inverted system with that of the bias hanging model. The order of the bifurcations undergone seem to be in agreement after the first stability boundary is crossed, and the phenomenon of drop/increase in amplitude of oscillation, which may be used as a precursor of the forthcoming danger of chaos, is present in both cases.

Hence, we are allowed to suggest that small inclination angles and small imperfection terms on the model of the parametrically excited system possess the same symmetry breaking effects in terms of dynamics.

Moreover, we may add that including just a small bias term in the mathematical analysis of a physical system will provide similar nonlinear and bifurcational behaviour to that of a more complex symmetry broken model hence offering adequate results and outcomes.

We note further that our numerical simulations for the inverted pendulum at $\omega = 2$,

so at forcing frequency magnitude equal to that used in the various analyses for the corresponding hanging system within this thesis, are novel and fresh and form better comparison with the hanging parametrically excited pendulum model.

4.8 Theoretical analysis

For the first case of breaking the symmetry of the model via an inclusion of a bias term emphasis was placed on numerical investigation as well as analytical for an approximate escape boundary within the parameter space to show the reduction in safe oscillatory motions.

For the second approach of breaking the symmetry, for the inverted tilted model, we attempt to show analytically how the subcritical pitchfork bifurcation has been replaced by two disconnected branches leaving an asymmetric solution of periodicity one so that symmetry-breaking, pitchfork bifurcation may no longer be present and period doubling expected to ensue. An analogous system is beam buckling found in structural dynamics where the buckling of a beam with a large imperfection under a static load will result to nonlinear characteristics of the pitchfork bifurcations (Mullin, 1993).

Recalling equation (4.7.1) it is convenient to rescale time according to $t = \Omega\tau$ so that the governing equation may now be written in the form,

$$\theta'' + \mu\theta' - \omega^2 \sin\theta - \kappa \cos t \sin(\theta - \phi) = 0 \tag{4.8.1}$$

where now, μ is set to be equal $\frac{\zeta}{\Omega m l^2}$, $\omega^2 = \frac{g}{l\Omega^2}$ and $\kappa = \frac{A}{l}$. The analytical method implemented here to be able to derive an approximate bifurcation equation from (4.8.1) is the method of multiple scales (Nayfeh, 1993). This is a different approach as opposed to the method of strained parameters applied in Chapter 2 in order to show analytical variety in our study and wider understanding of mathematical tools.

Before applying the analytical method, we perform the scaling of some parameters

according to

$$\omega^2 = \varepsilon^2\hat{\omega}^2, \quad \kappa = \varepsilon\hat{\kappa}, \quad \text{and} \quad \mu = \varepsilon\hat{\mu}$$

where ε is a bookkeeping device (Grimshaw, 1993, Nayfeh, 1993) and $\hat{}$ denotes *of the order* $O(1)$. The equation now becomes

$$\theta'' + \varepsilon\hat{\mu}\theta' - \varepsilon^2\hat{\omega}^2 \sin\theta - \varepsilon\hat{\kappa}\cos t \sin(\theta - \phi) = 0 \tag{4.8.2}$$

and we analyse (4.8.2) using the method of multiple scales introducing three independent time scales defined as

$$t_0 = t, \qquad t_1 = \varepsilon t \qquad t_2 = \varepsilon^2 t.$$

We seek an approximate solution in the form

$$\theta(t;\varepsilon) = \theta_0(t_0,t_1,t_2) + \varepsilon\theta_1(t_0,t_1,t_2) + \varepsilon^2\theta_2(t_0,t_1,t_2) + ...$$

With the aid of the chain rule,

$$\frac{d}{dt} = \frac{\partial}{\partial t_0} + \frac{\varepsilon\partial}{\partial t_1} + \frac{\varepsilon^2\partial}{\partial t_2} + ..$$

$$\frac{d^2}{dt^2} = \frac{\partial^2}{\partial t_0^2} + 2\varepsilon\frac{\partial^2}{\partial t_0 \partial t_1} + \varepsilon^2[2\frac{\partial^2}{\partial t_0 \partial t_2} + \frac{\partial^2}{\partial t_1^2}] + ..$$

and appropriate substitution (also neglecting higher orders of ε), (4.8.2) becomes

$$[\frac{\partial^2\theta_0}{\partial t_0^2} + \varepsilon\frac{\partial^2\theta_1}{\partial t_0^2} + \varepsilon^2\frac{\partial^2\theta_2}{\partial t_0^2}] + 2\varepsilon[\frac{\partial^2\theta_0}{\partial t_0 \partial t_1} + \varepsilon\frac{\partial^2\theta_1}{\partial t_0 \partial t_1} + ..] \quad +$$

$$+\varepsilon^2[2\frac{\partial^2\theta_0}{\partial t_0\partial t_2}+2\varepsilon\frac{\partial^2\theta_1}{\partial t_0\partial t_2}+\ldots+\frac{\partial^2\theta_0}{\partial t_1^2}+\varepsilon\frac{\partial^2\theta_1}{\partial t_1^2}]+\varepsilon\hat{\mu}[\frac{\partial\theta_0}{\partial t_0}+\varepsilon\frac{\partial\theta_1}{\partial t_0}+..\varepsilon\frac{\partial\theta_0}{\partial t_1}+\varepsilon^2\frac{\partial\theta_1}{\partial t_1}+..]$$

$$-\varepsilon^2\hat{\omega^2}\sin(\theta_0+\varepsilon\theta_1+\varepsilon^2\theta_2)-\varepsilon\hat{\kappa}\cos t_0\sin(\theta_0+\varepsilon\theta_1+\varepsilon^2\theta_2-\phi)=0.$$

We note that we have replaced the original ordinary differential equation by a partial differential equation and consequently it appears that the problem has become more complicated. But as Nayfeh (Nayfeh,1993) mentions, experience with this method has shown that the disadvantages of introducing this complication are far outweighed by the advantages.

Equating coefficients of like powers of ε yield the following equations of the orders $O(\varepsilon^0)$, $O(\varepsilon^1)$ and $O(\varepsilon^2)$ respectively.

$$O(\varepsilon^0): \qquad \frac{\partial^2\theta_0}{\partial t_0}=0 \tag{4.8.3}$$

$$O(\varepsilon^1): \qquad \frac{\partial^2\theta_1}{\partial t_0^2}+2\frac{\partial^2\theta_0}{\partial t_0\partial t_1}+\hat{\mu}\frac{\partial\theta_0}{\partial t_0}-\hat{\kappa}\cos t_0\sin(\theta_0-\phi)=0 \tag{4.8.4}$$

$$O(\varepsilon^2): \qquad \frac{\partial^2\theta_2}{\partial t_0^2}+2\frac{\partial^2\theta_1}{\partial t_0\partial t_1}+2\frac{\partial^2\theta_0}{\partial t_0\partial t_2}+\frac{\partial^2\theta_0}{\partial t_1^2}+\hat{\mu}\frac{\partial\theta_1}{\partial t_0}+\hat{\mu}\frac{\partial\theta_0}{\partial t_1}-\hat{\omega^2}\sin\theta_0+..$$
$$-\hat{\kappa}\cos t_0\cos(\theta_0-\phi)\theta_1=0 \tag{4.8.5}$$

The latter term in the last two equations, (4.8.4, 4.8.5) came about by applying and manipulating trigonometric identities:

$$\varepsilon\hat{\kappa}\cos t_0\sin((\theta_0+\varepsilon\theta_1)-\phi)=\varepsilon\hat{\kappa}\cos t_0[\sin(\theta_0+\varepsilon\theta_1)\cos\phi-\cos(\theta_0+\varepsilon\theta_1)\sin\phi]$$

$$=\varepsilon\hat{\kappa}\cos t_0[(\sin\theta_0\cos(\varepsilon\theta_1)\cos\phi+\cos\theta_0\sin(\varepsilon\theta_1)\cos\phi)]$$
$$-\varepsilon\hat{\kappa}\cos t_0[(\cos\theta_0\cos(\varepsilon\theta_1)\sin\phi-\sin\theta_0\sin(\varepsilon\theta_1)\sin\phi)]$$

$$= \varepsilon\hat{\kappa}\cos t_0[\sin(\theta_0 - \phi) + \varepsilon\theta_1\cos(\theta_0 - \phi)]$$

The general solution of (4.8.3) can be written as,

$$\theta_0 = c_0(t_1, t_2) + c_1(t_1, t_2)t_0. \tag{4.8.6}$$

However, the second component is a secular term and for a uniform expansion, this term must be eliminated by setting c_1 equal to zero. In other words, for the solution to be bounded, c_1 must approach zero rapidly. The general solution now becomes,

$$\theta_0 = c_0(t_1, t_2). \tag{4.8.7}$$

Substituting equation (4.8.7) into (4.8.4), we obtain

$$\frac{\partial^2\theta_1}{\partial t_0^2} = \hat{\kappa}\cos t_0\sin(\theta_0 - \phi). \tag{4.8.8}$$

The right hand side does not contain terms that may produce secular terms in θ_1, so the particular solution of (4.8.4) is

$$\theta_1 = -\hat{\kappa}\cos t_0\sin(\theta_0 - \phi). \tag{4.8.9}$$

Furthermore, substituting θ_1 into (4.8.5) we reach,

$$\frac{\partial^2\theta_2}{\partial t_0^2} = -2\frac{\partial^2\theta_1}{\partial t_0\partial t_1} - 2\frac{\partial^2\theta_0}{\partial t_0\partial t_2} - \frac{\partial^2\theta_0}{\partial t_1^2} - \hat{\mu}\frac{\partial\theta_1}{\partial t_0} - \hat{\mu}\frac{\partial\theta_0}{\partial t_1} + \tag{4.8.10}$$

$$+\hat{\omega^2}\sin\theta_0 + \hat{\kappa}\cos t_0\cos(\theta_0 - \phi)(-\hat{\kappa}\cos t_0\sin(\theta_0 - \phi))$$

which finally becomes

$$\frac{\partial^2\theta_2}{\partial t_0^2} = -\frac{\partial^2\theta_0}{\partial t_1^2} - \hat{\mu}\frac{\partial\theta_0}{\partial t_1} + \hat{\omega^2}\sin\theta_0 - \hat{\kappa}\hat{\mu}\sin t_0\sin(\theta_0-\phi) - 2[\hat{\kappa}\sin t_0\cos(\theta_0-\phi)\frac{\partial\theta_0}{\partial t_1}]$$

$$-2[\hat{\kappa}\sin t_0\cos(\theta_0-\phi)\frac{\partial\theta_0}{\partial t_2}] - \tfrac{1}{4}\hat{\kappa^2}\sin 2(\theta_0-\phi) - \tfrac{1}{4}\hat{\kappa^2}\sin 2(\theta_0-\phi)\cos 2t_0.$$

The right hand side contains terms that produce secular terms in θ_2. So, for a uniform expansion, these terms must be eliminated. This is accomplished by setting the sum of the terms that do not include $\sin t_0$ and $\cos 2t_0$ equal to zero.

$$-\frac{\partial^2\theta_0}{\partial t_1^2} - \hat{\mu}\frac{\partial\theta_0}{\partial t_1} + \hat{\omega^2}\sin\theta_0 - \frac{1}{4}\hat{\kappa^2}\sin 2(\theta_0-\phi) = 0. \tag{4.8.11}$$

Then multiplying both sides by ε^2 and recalling the definition of t_1 we have,

$$\theta_0'' + \mu\theta_0' - \omega^2\sin\theta_0 + \frac{1}{4}\kappa^2\sin 2(\theta_0-\phi) = 0. \tag{4.8.12}$$

Moreover, neglecting higher order terms in θ, θ may be approximated by θ_0 so that the equation of motion of the pendulum may be described as:

$$\theta'' + \mu\theta' - \omega^2\sin\theta + \frac{1}{4}\kappa^2\sin 2(\theta-\phi) = 0. \tag{4.8.13}$$

This equation is in agreement to the autonomous differential equation of motion found in recent studies and experiments performed on the inverted pendulum with tilted high-frequency excitation by Yabuno *et al* (Yabuno, Miura and Aoshima, 2004).

With, $\frac{d^2}{dt^2} = \frac{d}{dt} = 0$ then equation (4.8.13) leads to the transcendental equation

$$\omega^2 \sin\theta = \frac{1}{4}\kappa^2 \sin 2(\theta - \phi). \tag{4.8.14}$$

where equilibrium states are satisfied. Their stabilities may be estimated by using the potential energy of the system, whereby the equivalent dimensionless potential energy is expressed by the negative integral of equation (4.8.14) with respect to θ. Equally, differentiating equation (4.8.14) with respect to θ and noting the sign of the differential, allows us to estimate the stability of the equilibria solutions according to the argument in Golubitsky *et al* (Golubitsky and Schaeffer, 1985). More specifically, when the differential is positive (negative), then that corresponds to unstable (stable) solutions.

We employ the above equation, (4.8.14), to present Figures 4.17 and 4.18. They include bifurcation diagrams of κ against θ for the cases $\phi = 0$ (no tilt) and $\phi = 0.1$ (with tilt) over a variation of ω values. We chose this value of ϕ so the effects on the bifurcation diagrams may easily be distinguished. The figures show the relationship between the excitation amplitude and the stable inverted states in the cases of vertical excitation along the gravity direction and tilted excitation respectively. The solid lines and dashed lines denote stable and unstable equilibrium solutions. These figures and the explanation below provide an extension to the work by Yabuno *et al* (Yabuno *et al*, 2004).

We note from Figure 4.17, that as the frequency ω (ratio of the excitation frequency to the natural frequency of the pendulum) increases, the point of forcing amplitude where a subcritical pitchfork bifurcation is predicted also increases. For each bifurcation diagram, beyond the point of forcing amplitude where the subcritical pitchfork bifurcation occurs, the inverted state becomes stable so that the solution now bifurcates into two unstable symmetric oscillating solutions.

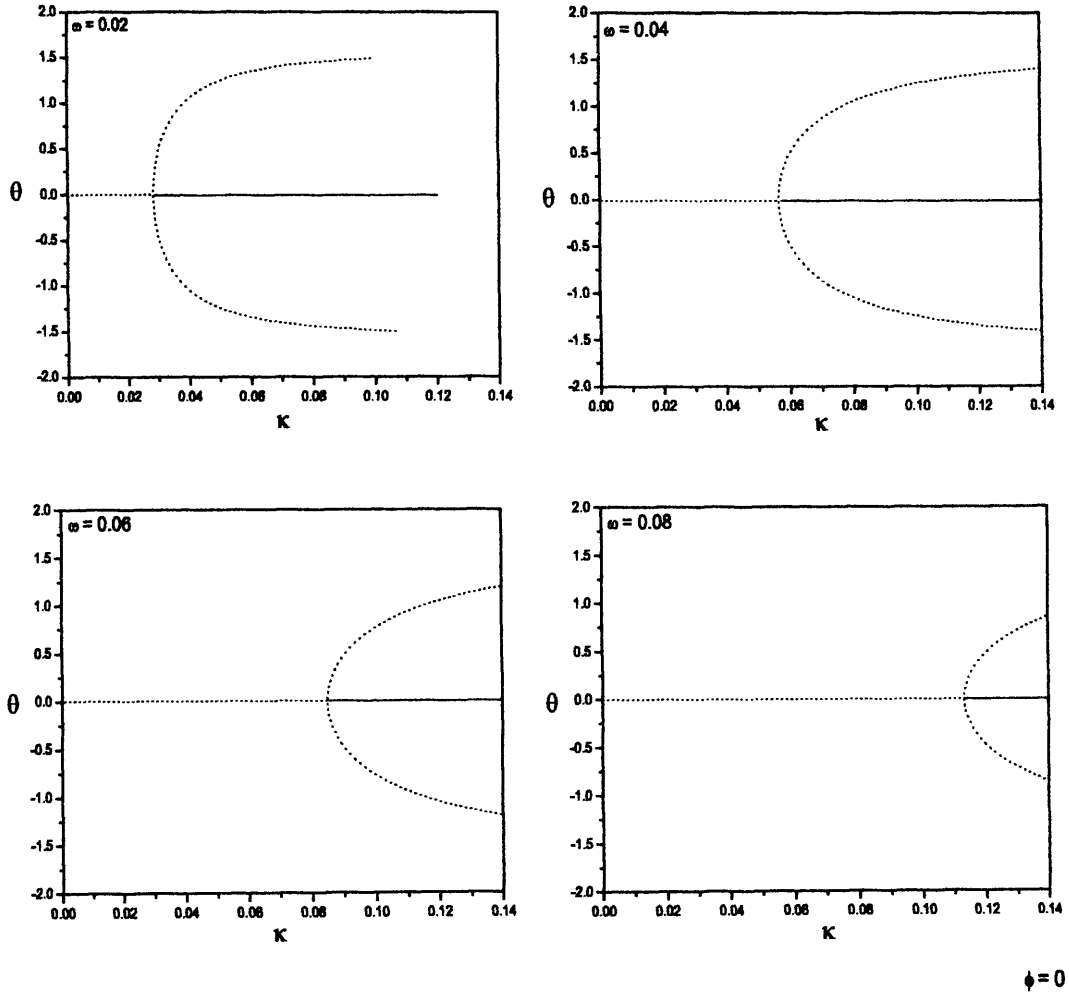

Figure 4.17: *Bifurcation diagrams of κ against θ when $\phi = 0$ (no tilt), over a range of ω values.*

For the tilted excitation case, with $\phi = 0.1$, Figure 4.18 is accompanied by four bifurcation diagrams for a range of ω values showing forcing amplitude κ, against θ. The subcritical pitchfork bifurcations exhibited in Figure 4.17, have now been shown to be replaced by disconnected branches. Thus, there is a smooth unstable downward evolution of one state with increasing forcing amplitude and a disconnected stable upper branch. On the upper branches, the system undergoes a saddle node bifurcation which tends to increase in its forcing amplitude position as the value of frequency ω goes up.

Also, focusing on the first bifurcation diagram of Figure 4.17 for $\omega = 0.02$, while on the upper disconnected branch, moving backwards in forcing amplitude direction, so in other words starting at a high value of κ, and decreasing downwards, the system will inevitably jump down to the lower branch path.

Finally, we have shown analytically how the subcritical pitchfork bifurcation, experienced once the initial stability boundary is crossed for the inverted solution of the tilted problem, disappears to become disconnected upper and lower branches due to the asymmetry of the model. Hence the analytical work seems to be in coherence and agreement with the earlier numerical simulation outcomes.

We further suggest as an extension to our work that Center manifold theory may be applied to show that for the inverted case, the pendulum system undergoes a classical subcritical pitchfork bifurcation if the system is perfect, or a saddle node bifurcation if an imperfection exists.

The basic idea of center manifold theory is that the fixed point undergoing a bifurcation has a center manifold associated with it, with a dimension less than the full dimension of the system. In a center manifold analysis, one effectively reduces the dynamics of the full system to the dynamics on the center manifold (Nayfeh and

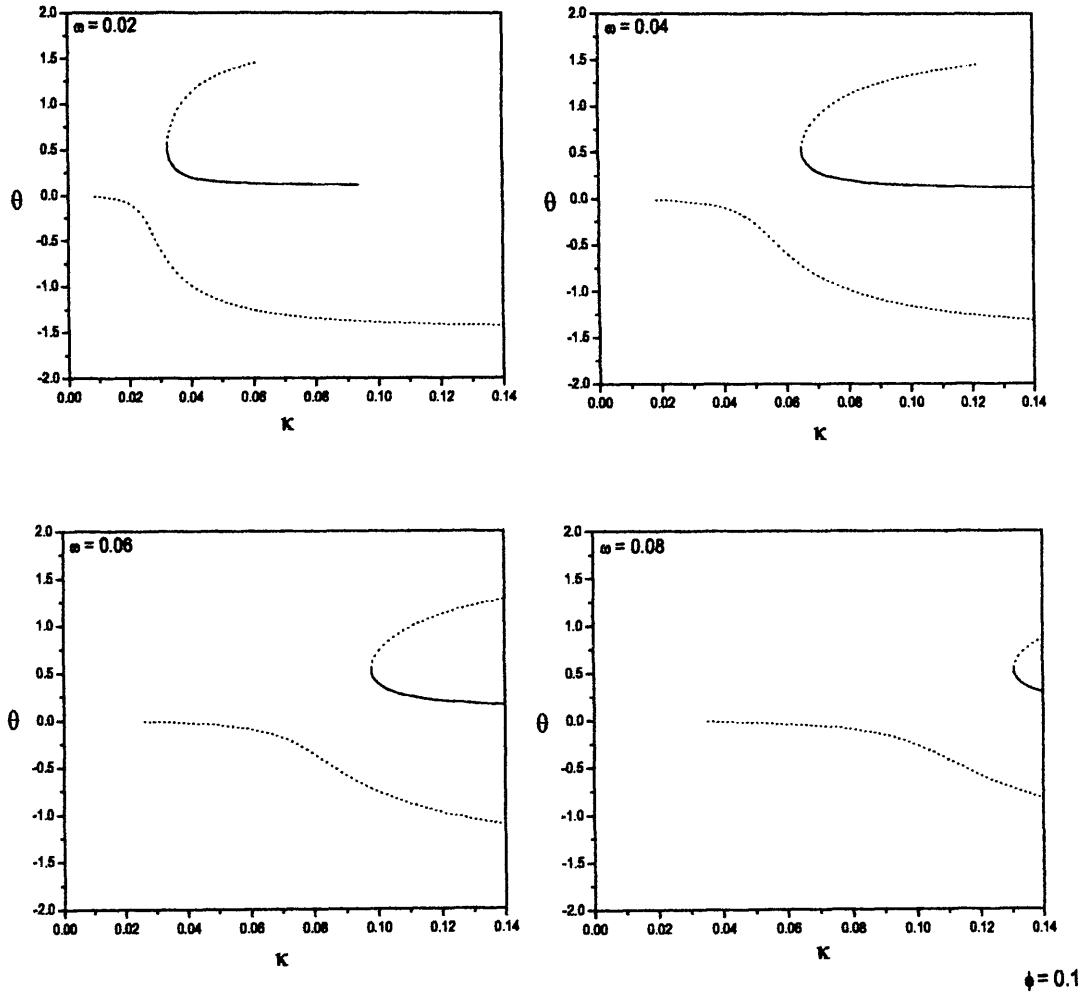

Figure 4.18: *Bifurcation diagrams of κ against θ when $\phi = 0.1$ (with tilt), over a range of ω values.*

Balachandran, 1995, Guckenheimer and Holmes, 1983).

Schmitt and Bayly (Schmitt and Bayly, 1998) examined both analytically and experimentally the bifurcations in the mean angle of a horizontally shaken pendulum. They employed Center manifold reduction and stability analysis to confirm that the bifurcation in their model is of supercritical pitchfork nature. So we may add that for the sake of comprehensiveness and completeness, similar Center manifold reduction analysis may be attempted for the inverted and tilted vertically driven system.

4.9 Final Remarks

This Chapter has examined a parametrically excited pendulum system whose usual symmetry was destroyed by firstly adding an imperfection term and later by inclining the corresponding inverted model by an angle.

For comparison, a brief overview was included of the behaviour of the symmetric parametrically excited pendulum equation focussing on the bifurcational behaviour experienced under variation of the forcing amplitude.

Particular attention is paid again here to escape where most trajectories must now include a rotation. For the non-symmetric problem, a harmonic balance approach was employed to evaluate an approximation of the boundary of the escape region as the symmetry breaking term is varied.

As would be expected, the simple asymmetric equation of motion proposed in this Chapter leads to various nonlinear phenomena, such as cascades of period doubling bifurcations, which were examined and compared with other similar models.

Emphasis is given to the disappearance of the symmetry-breaking, pitchfork bifurcation, that is present in the symmetric equation, due to the bias term added in the altered equation of motion studied in this Chapter. Analytical work showed how the bias term contributes to the disconnected branches of the pitchfork bifurcation. Also, the drop in response amplitude experienced by the oscillatory solution when considering the positive θ_{max} values, has a significant experimental result, whereby a visible decline in the swing angle can predict that something will 'soon' happen as parameters are varied which will be of rotational nature. The asymmetric perturbation produced a qualitative change in the behaviour of the system, which is also apparent for the inverted tilted driven pendulum case.

It is also confirmed that an appearance of the first period doubling in its sequence triggers escape from the potential well and should be regarded as a precursor of the imminent danger and difficult operation of a practical system. Moreover, a safe zone in terms of the (γ, p) control space was constructed with the aid of numerically determined bifurcation diagrams for different values of γ. The significance of the region within the boundary points was noted.

Basins of attraction were studied and compared for the symmetric and asymmetric counterpart, to show the reduction in basin of the oscillatory solutions as the bias term increases.

In ship dynamics, similar mathematical models have been proposed to study heave excited roll as will be discussed in later Chapters. If such a model were appropriate, for the large amplitudes required in this study, then capsize would result and moreover, the safe area described above, can be linked with a non-capsizing region that serves an important comparison to the field of ship dynamics.

Moreover, in this Chapter, we considered breaking the symmetry of the inverted parametrically excited pendulum by tilting the model by an angle. Numerical investigations were undertaken for the tilted inverted system and compared with its symmetric counterpart. We sought out to examine the origin of how the subcritical pitchfork bifurcation experienced in a symmetric system is replaced in the asymmetric case by disconnected branches, one of which undergoes a saddle node bifurcation. Analytical techniques using the method of multiple scales allowed us to verify the above behaviour of the inverted solution of the vertically tilted parametrically excited pendulum model.

We are of the opinion that perfect symmetry assumed in any physical representation of a mathematical model can never quite be accomplished, even with thorough and

detailed experimental arrangements and this Chapter successfully gave an insight into the effects of asymmetry in systems.

Imperfections and unforeseen uncertainties in experimental testing may make it difficult to yield accurate results and may also cause significant discrepancies between experimental data and analytical expectations. This Chapter sought to examine the origin of such deviations by considering two mathematically modelled cases, the addition of a simple bias term within the model and a small tilt in angle for the inverted vertically parametrically excited pendulum.

Overall, we believe it is necessary to gain a deeper understanding on how breaking the symmetry of a system can affect its bifurcational behaviour so that to present a better physical realisation of the problem and create more feasible and strict boundaries for the safe operation of systems.

Chapter 5

Symmetry breaking with applications to ship dynamics

5.1 Introduction

In this Chapter we continue our interest on breaking the initial symmetry of models, aiming to improve our understanding of practical problems. In particular, we focus on examples taken from the field of ship dynamics.

The previous Chapter was firstly concerned with the parametrically excited pendulum system whose usual symmetry was destroyed via a slight imperfection. The significant effects that the bias term has on the domain of safe oscillatory motion were discussed and briefly referred to as the non-capsizing region in terms of ship dynamics.

The nonlinear modelling of roll and capsize as escape from a potential well was mapped out by Thompson, Rainey and Soliman (Thompson *et al*, 1990). In recent years there have been considerable advances in the nonlinear modelling of ship cap-

size but there remains though still, a lack of experimental work (Contento *et al*, 1996). Whilst the modelling of the large amplitude motions, such as those leading to capsize, has often taken a multi degree of freedom approach (Kan, Saruta and Taguchi, 1991, Chen, Shaw and Troesch, 1999), the ultimate precursor of capsize must be large angle roll motion. For this reason, we focus here on the problem of beam sea roll and in following the approach of Thompson, Rainey and Soliman (Thompson *et al*, 1990) we formulate a single degree of freedom model for roll motion but with the influence of a static bias. We investigate the safety of a ship using the theory of safe basin when the ship experiences a wave forcing.

The purpose of this Chapter is to examine how asymmetry can lead to diminishing regions of safe roll motion and to relate the outcomes to the analogous region of escape in the oscillatory swinging motion of the parametrically excited pendulum model.

Francescutto *et al*, (Francescutto, Nabergoj and Hsiu, 1991) mention that one of the key steps in the design of a safe ship lies in the understanding of the physical mechanisms behind capsize. Hence it is vital to be able to comprehend how asymmetry may affect the prediction of the phenomenon of capsize. As seen earlier by our investigation of the asymmetric parametrically excited pendulum it seems that, in relation to ship motion, the asymmetry must aggravate the tendency for capsize and ought to be addressed when the operational capabilities of a ship are determined. Within this Chapter we aim to accomplish this as it is an important aspect for naval architects and their design purposes.

For instance, under real circumstances, such as for example a loaded cargo ship cruising in a seaway, one can never expect and assume modelling mathematically the equation of roll motion under perfect symmetry. In a typical ship, we may

expect wind conditions or a shift of cargo that might break the initial assumption of symmetry. Hence it seems that the use of symmetric ship roll motions may be characterised as unrealistic and impractical.

Since we are concerned here with the subject of ship capsize, it is probably useful to start by explaining the general meaning of this phrase. We shall be referring to ships, boats and vessels as synonymous throughout this thesis, without any particular sense of size necessarily attached to any of these terms.

From a naval architecture point of view, ship capsize may be defined by the inability of a vessel to recover its normal floating position without an external aid after it has capsized. In other words, the loss of stability of the upright position due to excessive roll motion.

5.1.1 Useful preliminary definitions

The *centre of gravity* of a body, denoted as G in Figure 5.1, is the point through which the force of gravity is considered to act vertically downwards with a force equal to the weight of the object.

The *centre of buoyancy*, B, is the point which the force of buoyancy is considered to act vertically upwards, with a force equal to the weight of water displaced. Or in other words the centre of gravity of the underwater volume (Rawson and Tupper, 1968).

To be able to float upright at rest in still water, a ship must displace her own weight of water and the centre of gravity must be in the same vertical line as the centre of buoyancy (as may be seen from the left diagram of Figure 5.1 for a body).

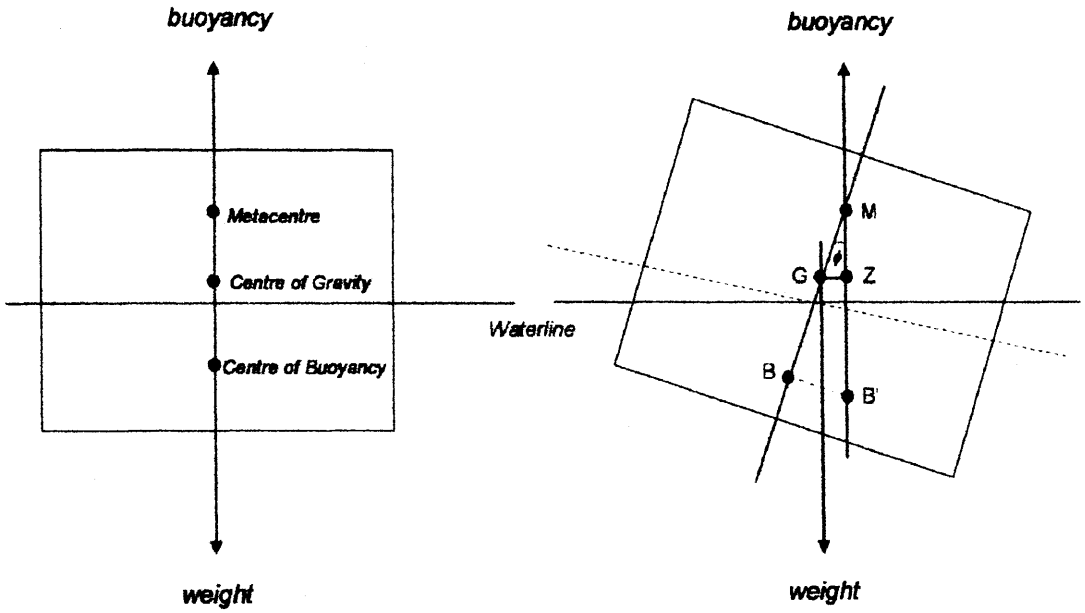

Figure 5.1: *Forces acting on a body which is immersed in water, at stable equilibrium for the upright position and for when the object is heeled by an angle* φ.

Permitting a ship to correspond to the object in Figure 5.1, and allowing her to be inclined as the result of an external force, to an angle φ, (called heel angle), see figure, we notice that the centre of gravity remains at G, since there has been no change in the distribution of the mass and the weight of the ship is still considered to act vertically downwards through point G. Due to the heel, the centre of buoyancy now shifts from B to B' to take up the new centre of gravity of the underwater volume. The verticals through the centres of buoyancy at the angle of heel intersect at a point called the Metacentre, denoted by M (Rawson and Tupper, 1968a, 1968b). The vertical distance between G and M is referred to as the *Metacentric Height.*

We say that a ship is to be in stable equilibrium if, when inclined, she tends to

return to the initial upright position. For this to occur, the ship must have positive metacentric height, in other words, the centre of gravity must be below the metacentre. The left diagram of Figure 5.1 shows a ship in the upright position having a positive GM. If moments are taken about G, there is a moment to return the ship to the upright position and this moment is referred to as the *restoring* or *righting moment*. It is equal to the product of *weight* and the length of the lever GZ. Putting this into mathematical context, we have the following:

$$Restoring \quad moment = weight \times GZ.$$

GZ in turn, is called the *restoring lever* or *arm* and is the perpendicular distance between the centre of gravity and the vertical through the new centre of buoyancy. At small angles of heel (less than 15^o),

$$GZ = GM \times \sin\varphi.$$

For negative metacentric height, so that now G is above M, the ship is unstable so, when inclined the restoring moment is a capsizing moment which will tend to heel the ship still further (Derrett and Barrass, 1964).

At large angles of heel, so for greater than 15^o, the force of buoyancy can no longer be considered to act vertically upwards through the initial Metacentre (M) so that the righting lever GZ is no longer equal to $GM \sin\varphi$ but

$$GZ = (GM + \tfrac{1}{2}BMtan^2\varphi)\sin\varphi.$$

For a clearer understanding, the derivation of this formula may be found in *Appendix C*.

The motion of a ship consists of three horizontal or vertical motions, heave, sway and surge, and three rotational motions, roll, pitch and yaw so that the motion may be modelled as six degree of freedom. Figure 5.2 schematically identifies these motions by taking an axis system located at the centre of gravity of a ship at rest (with zero velocity and acceleration) and in still water (Froude, 1863, Rawson and Tupper, 1968).

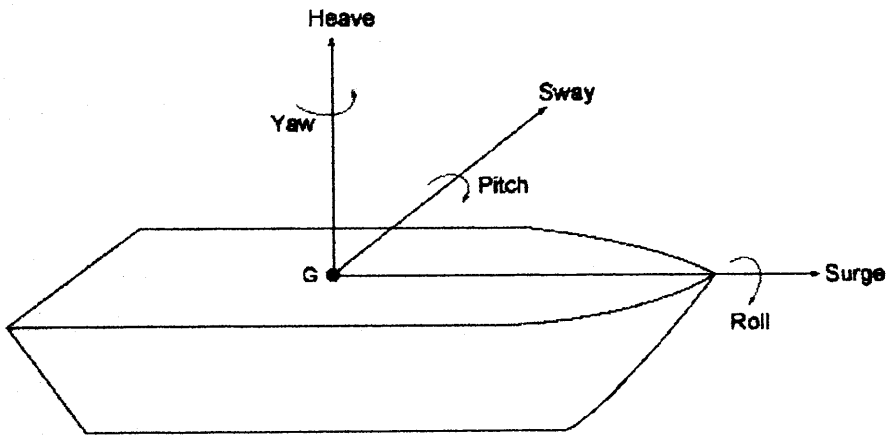

Figure 5.2: *Ship coordinate system*

5.2 Ship-roll motion in regular beam seas

The modelling of capsize as escape from a potential well was mapped out by Thompson, Rainey and Soliman (Thompson *et al*, 1990). Due to the difficulty of accurately determining large amplitude rolling response patterns that lead to the complete capsize problem (due for example to the hard task of determining the hydrodynamic forces), a roll model which decouples the six degree of freedom is generally assumed and under some conditions it is believed that this assumption is a valid one. We follow this approach here, formulating a single degree of freedom model for roll motion for a ship in beam waves (Jiang, Troesh, Shaw, 1996). These are types of waves that hit the vessel from the side and they are considered to be the most dangerous types of seas that provoke large amplitudes.

Following Wright and Marshfield (Wright and Marshfield, 1979, Spyrou, Cotton and Gurd, 2002) and balancing the moments acting on the ship, we write a typical roll equation in terms of the relative roll angle φ as,

$$(I + A(t))\varphi'' + B(\varphi)\varphi' + mgGM\varphi(1 - (\frac{\varphi}{\varphi_v})^2) = H + F_{wave}(t) \qquad (5.2.1)$$

where H is a constant bias moment which may arise due to wind, cargo shifting or ship damage. This is done in order to accomplish our investigation of an asymmetric model and to study the safety of a ship using the concept of safe basin with the aim of showing some coherence with the safe oscillatory zone of the perturbed parametrically excited pendulum we examined in the earlier chapter.

φ' and φ'' are the first and second derivatives with respect to time t of the roll angle respectively. φ_v is the angle of vanishing stability. This is the angle of heel beyond which capsize is inevitable and there is loss of roll stability of a ship. I is the

moment of roll inertia and A is the added hydrodynamic moment of inertia due to the surrounding water, where the most convenient units for inertia are taken here as kgm^2. $B(\varphi)$ is the angle dependent roll damping coefficient with units $Nmsecond$ and mg is the ships weight. GM is the metacentric height (m). The wave external forcing moment, F_{wave}, is time dependent with units Nm.

In regular beam seas, the wave exciting roll moment may be approximated by a harmonic single frequency wave. Again, we use a harmonic term because from our knowledge of resonance, we know that this is the worst case scenario. Hence we take,

$$F_{wave}(t) = F_1 \cos(\omega_e t + \epsilon)$$

where F_1 is composed by the moment amplitude per unit wave amplitude at frequency ω_e and by the wave amplitude. ϵ is the phase angle of the exciting wave moment, which we choose for convenience to set to zero.

Various expressions of damping and restoring moments may be used to simulate the characteristics of roll motion. In terms of roll damping, it may include a linear and nonlinear form, of quadratic or cubic nature. At this stage, for damping we shall confine ourselves for simplicity's sake to the equivalent linear one, B_1, however we retain nonlinearity in the restoring moment.

By appropriate substitution of the above expressions into (5.2.1) and moreover under the variable transformation $\psi = \frac{\varphi}{\varphi_v}$ with a change of variable $\tau = \omega_0 t$, (where ω_0 is the natural roll frequency) we may write equation (5.2.1) in terms of the scaled roll angle ψ as:

$$\psi'' + b_1\psi' + \psi - \psi^3 + \gamma = F\cos\omega\tau \tag{5.2.2}$$

where, $b_1 = \frac{B_1}{\omega_0(I+A)}$, $F = \frac{F_1}{\omega_0^2(I+A)\varphi_v}$, $\gamma = -\frac{H}{(I+A)\varphi_v\omega_0^2}$, $\omega_0^2 = \frac{mgGM}{(I+A)}$ and $\omega = \frac{\omega_e}{\omega_0}$.

Note that this scaling ensures that the nondimensional angle of vanishing stability is always equal to one when $\gamma = 0$. We call equation (5.2.2) an asymmetric single degree of freedom roll equation of motion in beam seas, in nondimensional form, and the case when $\gamma = 0$ a symmetrical one. We also mention that while many areas are open for future improvements, equation (5.2.1) is reasonable in that it captures the qualitative nature of roll motion.

A quadratic form of restoring arm has been commonly used by Thompson *et al* (Thompson, Bishop and Leung, 1987, Thompson, 1989, Cotton and Spyrou, 2001) and cubic restoring forces have been previously used in studies of ship roll by Kan *et al* (Kan, Sanuto and Taguchi, 1991), Cusumano and Kimble (Cusumano and Kimble, 1994) and Contento *et al* (Contento, Francescutto and Piciullo, 1996).

Figure 5.3 depicts the above nondimensional GZ curve, otherwise known as the Stability Curve and the potential function $V(\psi)$, given by the integration of the scaled restoring moment function for the case of $\gamma = 0$. A vessel's GZ curve is simply a plot of her static righting arm for a range of angles of inclination.

Typically the normal upright floating condition is stable ($\psi = 0$) and corresponds to a local minimum of $V(\psi)$. Likewise, the so called angle of vanishing stability corresponds to a local maximum of $V(\psi)$. In this sense, we can therefore see that the capsize of a ship corresponds to the escape of a particle from the potential well.

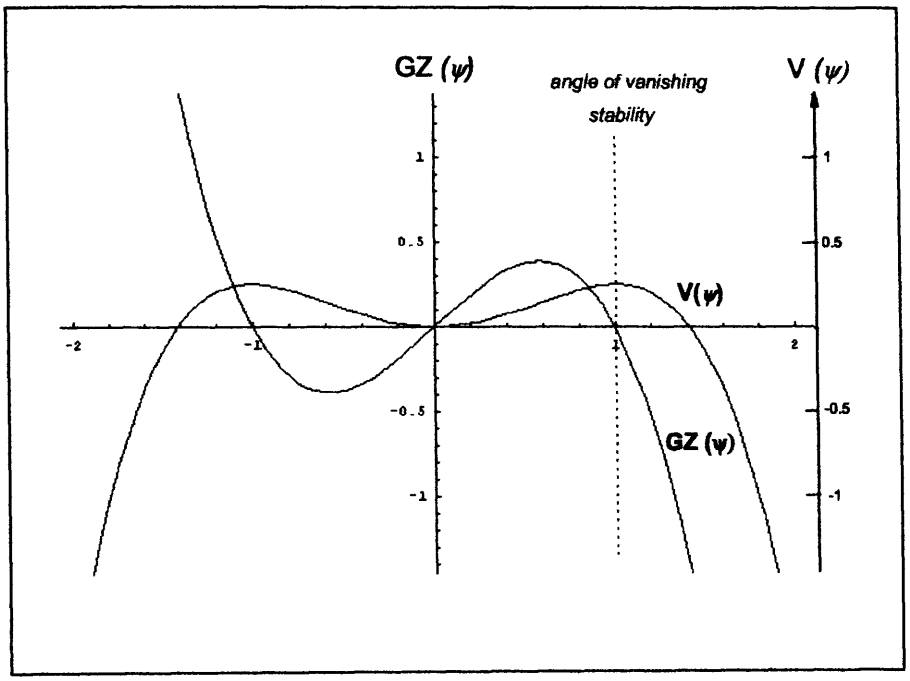

Figure 5.3: *Scaled Stability Curve and Potential Function Curve for* $\gamma = 0$.

Figure 5.4 shows the nondimensional restoring and potential function curve for the biased case, $\gamma \neq 0$, which we choose for instance as $\gamma = 0.05$. We incorporate this imperfection value in order to remain consistent with the forthcoming investigations. The angle of vanishing stability is smaller, so that with the inclusion of bias, escape from the potential well occurs earlier than its symmetric counterpart.

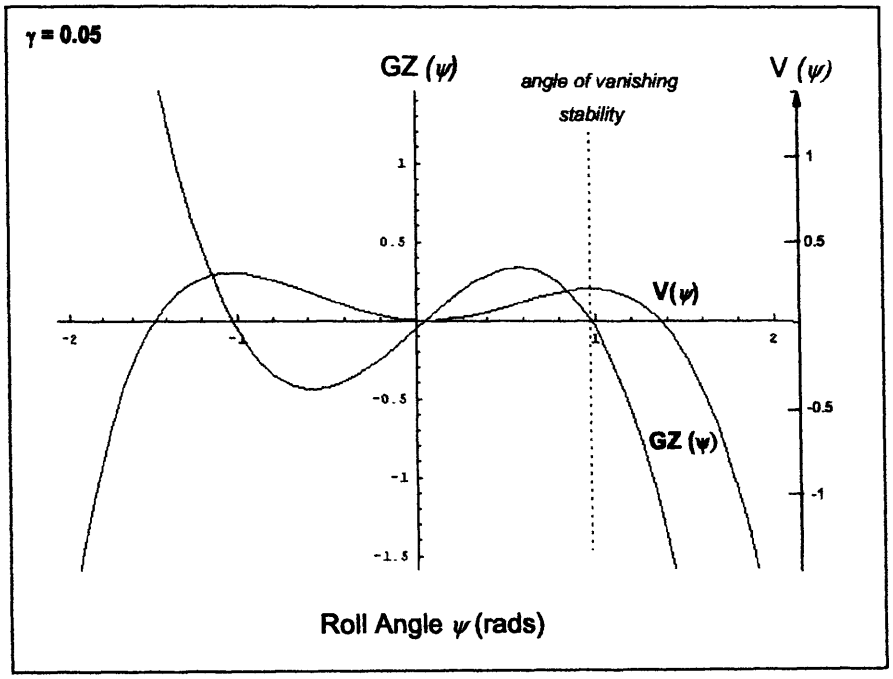

Figure 5.4: *Scaled Stability Curve and Potential Function Curve for* $\gamma = 0.05$.

In general, as a measure of the safety of a ship, a typical GZ curve gives a good description of the stability of a ship in still water, for example it depicts the largest steady heeling force that the vessel can withstand without capsizing (maximum GZ), the range of stability, the angle of heel at which the deck edge first immerses and the angle of vanishing stability.

The slope of the stability curves at small angles is known as the initial stability. It is the resistance of the ship to heel just a little bit. The slope shows how much an additional force will affect the boat if it is already heeled. A shallower, flatter slope means that an additional force will have more effect. The angle at which the curve reaches the maximum is also important as it indicates how far the ship can heel

before she starts losing stability. The heel angle at which restoring is equal to zero, corresponds to the angle of vanishing stability.

A way of combining roll angle and maximum restoring moment is to look at the size of the area between the curve and the horizontal zero line. This represents the work required in heeling the ship to that point. The larger the area under the curve, the more effort is needed to heel the ship.

5.3 Stability Curves for a specific Ship

This section is concerned with understanding how physical changes within a specific ship result in altering the stability curve. This study is performed with the purpose of acknowledging what realistic conditions a ship might incur so that a change in the stability curve, therefore in the restoring moment, might be exhibited. This way, we may say with assurance what a bias in the restoring term, thus in the ship roll equation, may correspond to in physical terms. Hence verifying further that these realistic factors may contribute to the breaking of the symmetry of the roll equation.

We employ actual dimensions of a passenger ferry which cruises today in the Mediterranean Sea (see Table 5.1). Until now we have, both in the asymmetric parametrically excited pendulum model and in our proposed asymmetrical ship roll equation, given a physical assumption of what a bias term may represent and how it may change the bifurcational and nonlinear behaviour of a system.

With the aid of a research trip to the National Technical University of Athens, NTUA (where also experimental testing was performed to contribute to the research material entailed within Chapter 7), we are now able, using *Tribon Software*, to show the actual effects on the GZ curve for the cases when considering an added external mass on the ship and also a shift in cargo mass within the vessel. We show that both cases provide physical examples of what a bias term might represent in our study of breaking the symmetry of the ship roll equation via an imperfection term inclusion. For confidentiality, the name of the passenger ferry remains unrevealed.

We note that the *Tribon Software* is a $3D$ product model used by Naval Architects and Marine Engineers for design, construction and planning of commercial and naval vessels.

Tonnage	**10,193 gross tons**
Passengers	**1,500**
Length Overall	**123.80 m**
Length between perpendiculars	**111.80 m**
Breadth/Beam	**18.90 m**
Depth up to Freeboard Deck	**7.25 m**
Depth up to Upper Deck	**12.25 m**
Meandraft at Midship	**5.10 m**
GM	**2.019 m**

Table 5.1: *Dimensions of the passenger ferry.*

Figure 5.5 is a schematic diagram of the cross section of the ferry's midship (not to scale) identifying the centre of gravity of the ship in still water as G. The coloured rectangular boxes are positions where a 200 tonne mass is added on the ship, at various distances away from G, denoted in metres on the diagram. The initial centre of gravity, G, of the ferry (without the addition of mass) is at $8.56m$ from the keel (bottom of the ship) and at $9.45m$ from the sides and it is indicated by the black oval point. Careful clarification is needed here to note that these boxes do not represent the new positions of the centre of gravity due to the addition of the mass but merely indicate where the added mass is placed with respect to G. The shaded coloured boxes are merely shaded to help distinguish that the added mass has been placed at new positions below G at the noted distances.

With Figure 5.5 in mind, we now present as Figure 5.6, the static stability curves for each coloured box position of the added mass. One first notices the grouping of the curves at three different points on the vertical axis. We may deduce from this

that it is the horizontal distance of the added mass position away from G that has an effect on the starting position of the stability curve. Therefore, the further away from G the added mass is placed, in terms of the horizontal coordinate, the further the shift below $(0, 0)$ on the stability curve.

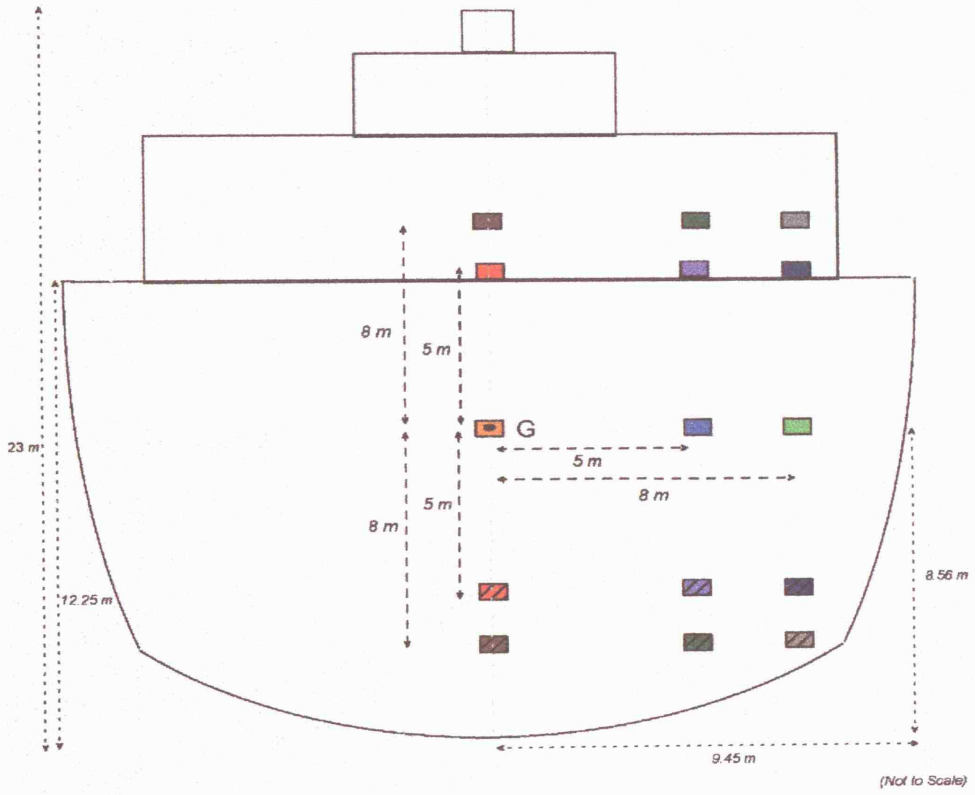

Figure 5.5: *Sketch of the cross section of the passenger ferry's midship. It identifies the original centre of gravity position, G, without any addition of mass. The coloured boxes represent the new positions of a 200 tonne added mass placed at the corresponding distances away from G. The shaded coloured boxes represent positions below the initial line of G.*

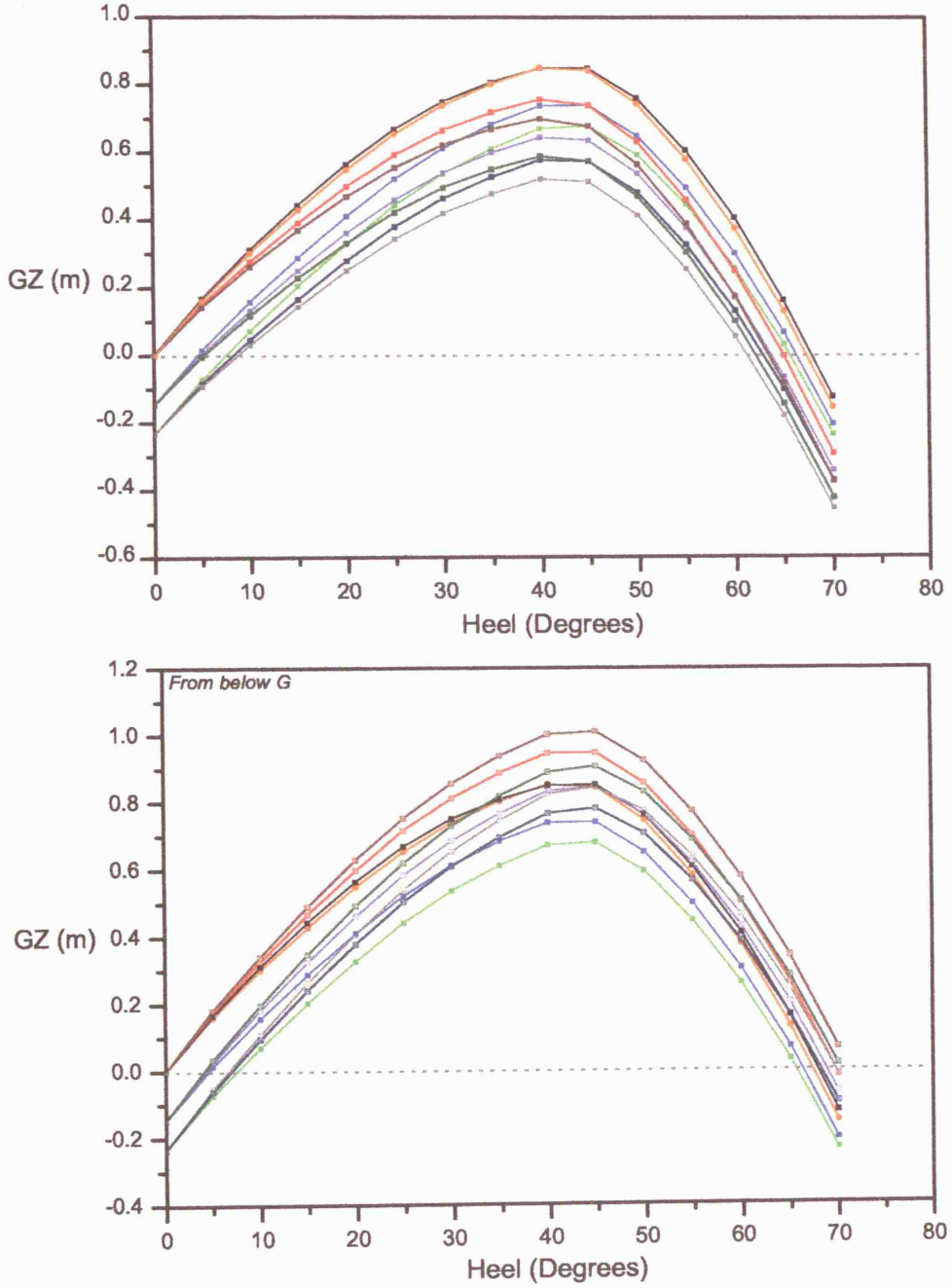

Figure 5.6: *Stability curves for the corresponding coloured boxes of Figure 5.5 for the added mass scenario, above and below G.*

This may be verified by looking ahead to Figure 5.7. The new centre of gravity position after the inclusion of the 200 mass, at say $5m$ horizontally from the old G (navy rectangular box), is at G_1 with φ being the angle of inclination once the added mass has been placed on the ship. The stability curve $GZ_{navy} = GM \sin\varphi$ for small angles and by geometry, $\tan\varphi = \frac{GG_1}{GM}$. Hence calculating the stability curve at equilibrium is $-GG_1 \cos\varphi$. $GG_1 = 0.15m$ and $\varphi = 4.52^o$ and so in turn, this means that the stability curve for a 200 added mass placed horizontally $5m$ away from G, begins at $-0.15\cos(4.52^o) \approx -0.15$. This echoes the initial stability position of navy coloured GZ curve on Figure 5.6.

Figure 5.7 also identifies some useful definitions of sections of a vessel, that will be used later within the thesis as well as showing the new position of centre of buoyancy, B_1 due to the extra immersion in still water of the 200 added mass placed horizontally $5m$ away from G.

Returning to the previous figure of the stability curves (Figure 5.6), another observation is the angle of vanishing stability which occurs at an earlier heeling angle, the further the added mass position lies both horizontally and vertically away from G. This means that as expected, the farther the added mass is placed from the original centre of gravity G in both directions, the smaller heeling angle is needed in order for the ship to capsize. Hence, the capsizing angle is smaller the greater the horizontal or vertical distance away from G the added mass is placed and as a result the range of stability decreases. The greatest effect however on the range of stability is when the added mass is placed nearest to the edge of the ferry and closest to the top deck. In Figure 5.5 this corresponds to the light grey box position and in Figure 5.6 the corresponding light grey curve which has the smallest angle of vanishing stability.

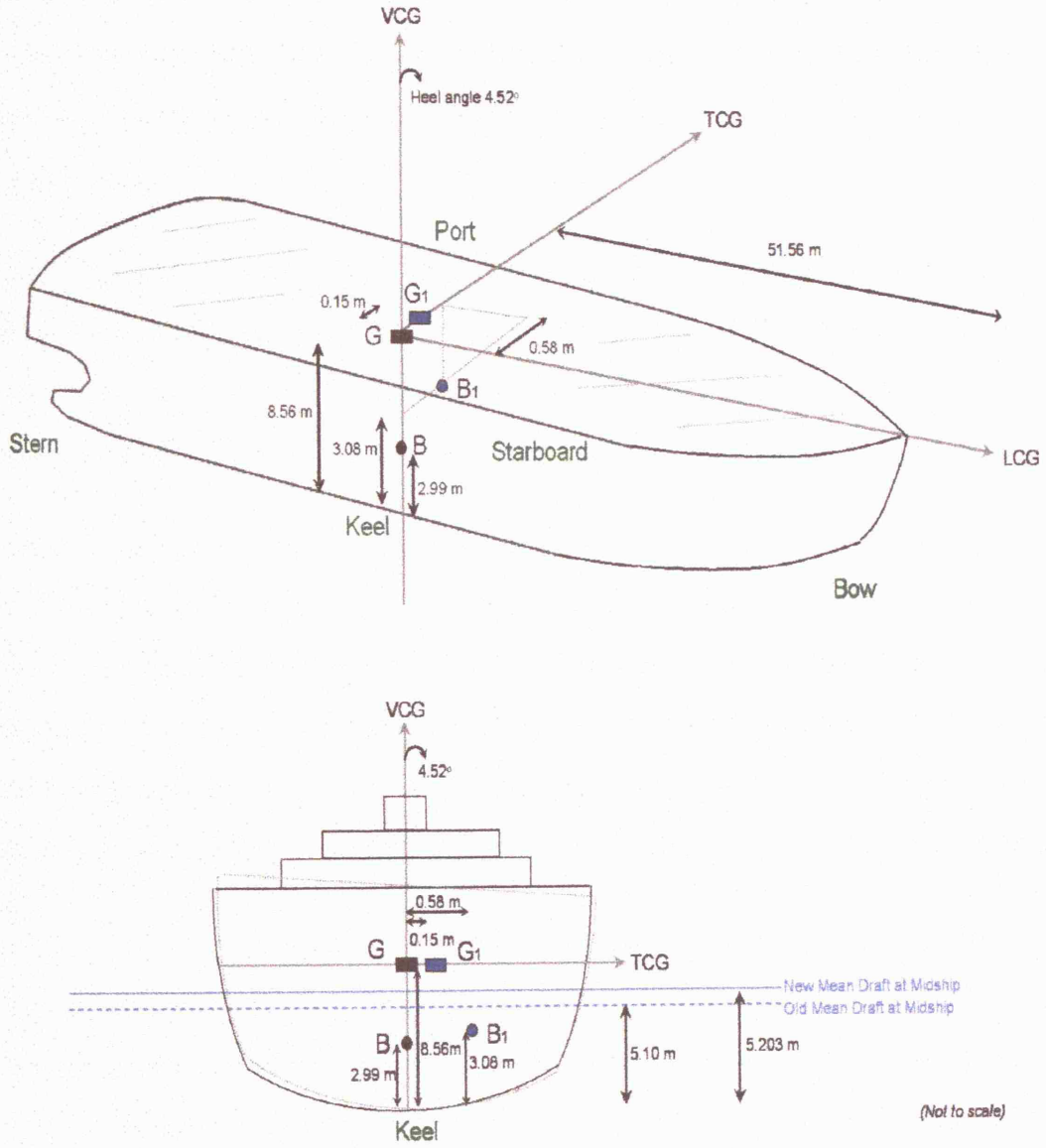

Figure 5.7: *Effects on Centre of Gravity and Buoyancy of a 200 tonne added mass set at 5 metres horizontally from the initial centre of gravity.*

It is also important to note that the maximum height of GZ also decreases as the distance from G increases both in the vertical and horizontal position. Obviously, a smaller maximum restoring moment will be less stable because you would need to apply less force to reach that angle. This implies again that in view of the light grey position of the added mass, the corresponding stability curve has the least maximum GZ, identifying this scenario as the least stable one.

The area between the curve and the horizontal line also plays a role in the static stability criteria of a ship. We notice that again the positions coloured as dark blue, light green and grey in Figure 5.6 contribute to a smaller area under their corresponding GZ curves, so that less energy and effort is required to heel the ship.

The second set of stability curves in Figure 5.6 correspond to the shaded coloured boxes of Figure 5.5, where the added masses are placed in positions below the original centre of gravity, G. Here, the ferry is more stable the closer to the keel (bottom of the ship) the mass is added and remaining in the same line as G. The larger the horizontal distance of the added mass from G moving towards the edge of the sides of the ship, the smallest the angle of vanishing stability and leaving the ship less stable.

We also note that the orange box represents placing the added mass at the same position as to where the old centre of gravity was without the addition of the 200 mass. There seems to be no major effect on the stability curve under this scenario, since the new centre of gravity has not altered in position.

Removal of mass within the ship should produce the opposite effects to the ones mentioned above for the determination of stability of a ship, with the initial GZ values at zero heel angle occurring at positive values above the horizontal zero line.

Figure 5.8 consists of the same sketched cross section of the midship of the passenger ferry, where a shift (movement) of a 200 tonne mass within the ship has occurred to the different positions indicated by the coloured circular points. Noting this time that the total mass of the ferry remains the same, so that this scenario may be considered as a shift of cargo within the vessel instead of externally adding (removing) mass on (from) the ferry.

The GZ curves that follow in Figure 5.9 show that shifting a mass of 200 tonnes within the ship has similar effects in terms of stability as an addition of an external 200 mass tonne. Hence, the closer to the sides of a vessel a cargo shifts within, the less stable that ship will be in still water, yet alone when waves are induced on the system.

These static stability curves are in agreement with the study of our asymmetric ship roll equation in beam seas, since with addition of a bias term, the capsize phenomenon occurs much earlier than its symmetric counterpart. Just as these physical changes within a ship, addition and shift of mass within the ferry, show an earlier loss in stability and a quicker route to capsize.

This section allows us to conclude with confidence that a bias term inclusion in the symmetric roll equation of motion, does pose an effect on the static stability curve of the ship (static since considering the ship at calm water) and this bias term may physically represent an addition of mass or shift in cargo from a practical point of view.

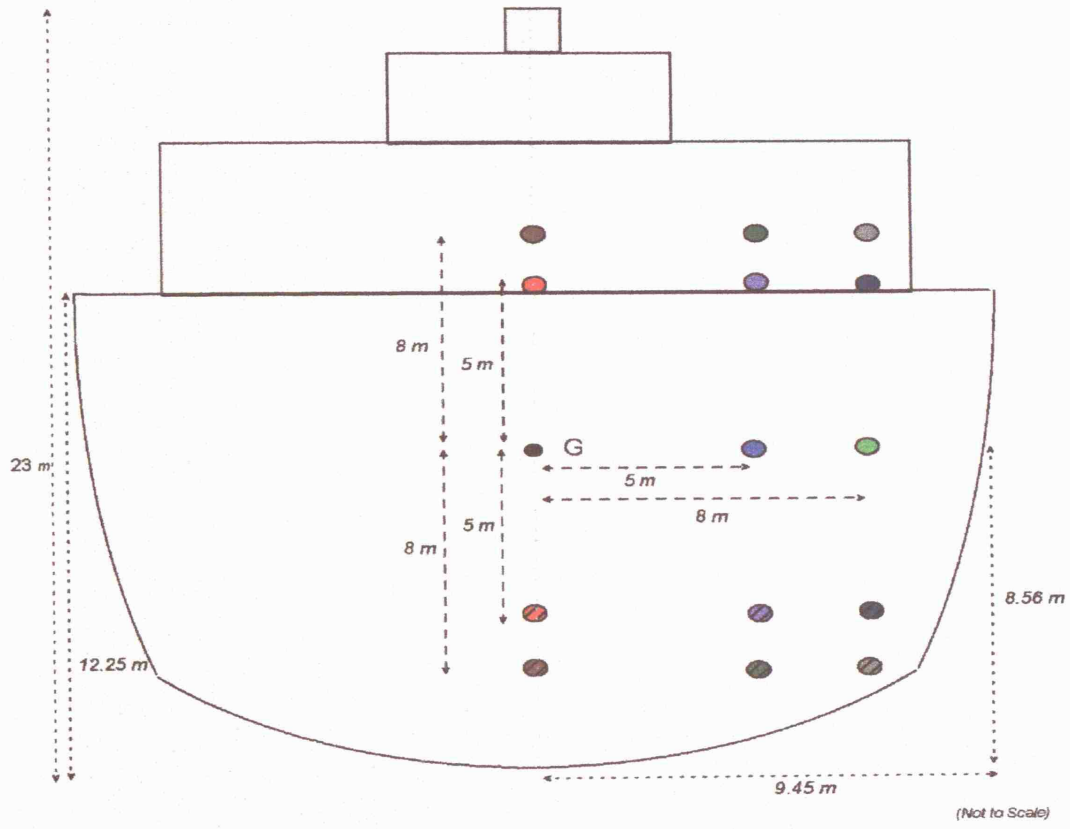

Figure 5.8: *Sketch of the cross section of the passenger ferry's midship. It identifies the original centre of gravity position, G, without any addition of mass. The coloured circular points represent the new positions of a 200 tonne shift in mass within the ship to the corresponding distances away from G. The shaded coloured circles represent positions below the initial line of G.*

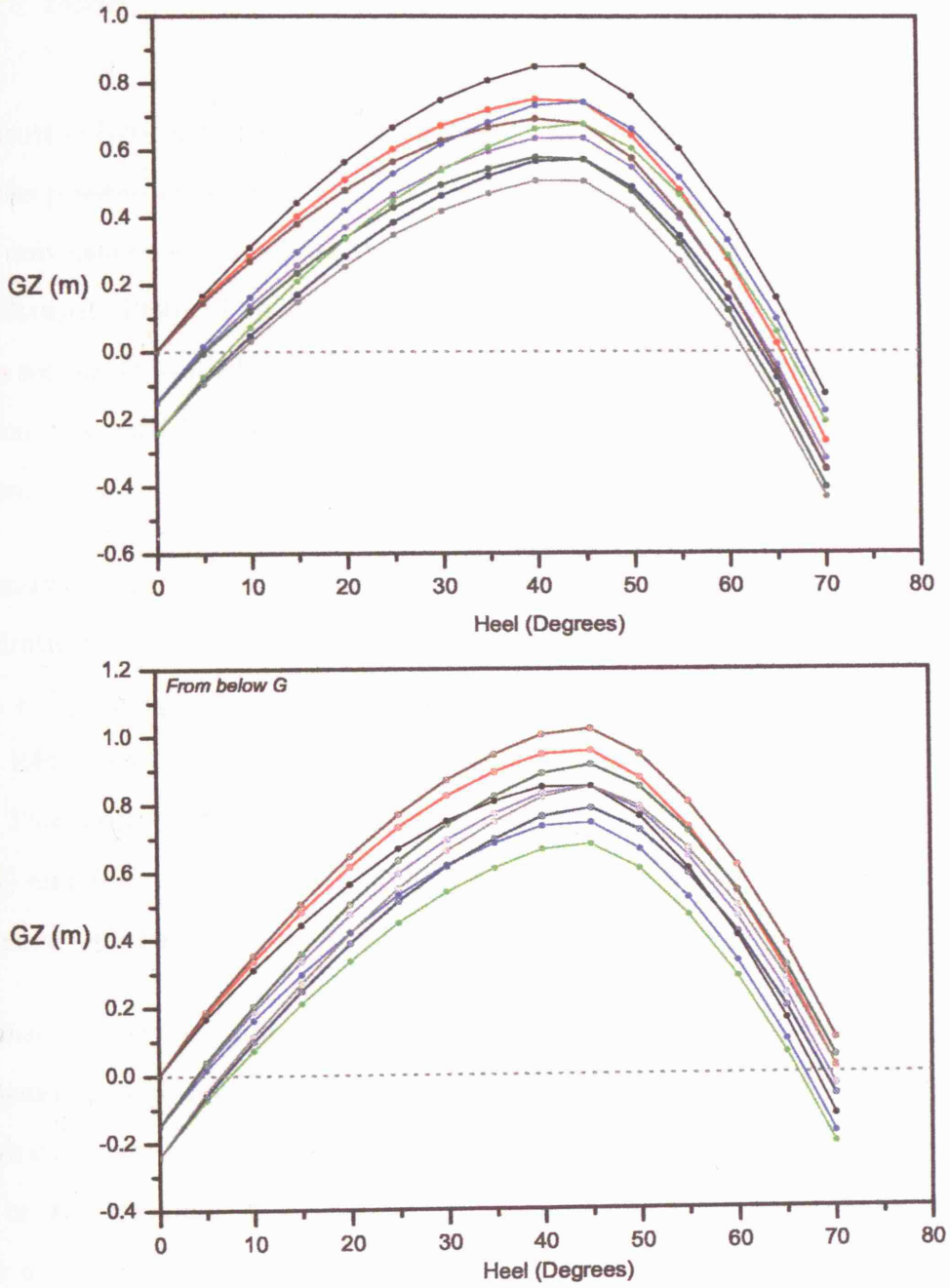

Figure 5.9: *Stability curves for the corresponding coloured circular points of Figure 5.8 for the shift in mass scenario, above and below G.*

5.4 Analysis of asymmetric roll equation in beam seas

Numerous physical phenomena of oscillatory nature have appeared in different disciplines presenting the ability to escape from the potential well and are described by a universal escape oscillator model (Guckenheimer and Holmes, 1983, Thompson and Stewart, 1986). This symmetric cubic restoring equation described in the previous section ($\gamma = 0$), has a simple mechanical interpretation, since it describes the motion of a particle unit mass in the single potential $V(\psi) = \frac{\psi^2}{2} - \frac{\psi^4}{4}$ sinusoidally driven.

Extensive numerical and analytical studies on different aspects related to the quadratic restoring roll equation in beam seas, have been carried out by researchers such as Thompson *et al* (Thompson, Rainey, Soliman, 1990), Thompson (Thompson, 1989, 1990), Thompson and Soliman (Thompson and Soliman, 1990), Soliman and Thompson (Soliman and Thompson, 1989, 1992), Stewart *et al* (Stewart *et al*, 1991) and Soliman (Soliman, 1996). Analytical work related to the escape from the potential well was also examined by Chacón *et al* (Chacón *et al*, 1997).

Soliman and Thompson (Soliman and Thompson, 1992) investigated the effect of damping on basins of attraction and steady state bifurcation patterns of the quadratic restoring roll equation. In particular they investigated the effect of damping on the resonance response curves and how the main bifurcation boundaries, such as period doubling bifurcation, are affected. They have also showed how the damping level affects the erosion of the non-escaping basin.

We provide in this section an extension to their work but where our special interest here is the comprehensive study on the effect of bias on basin and steady state

bifurcation parameters for the asymmetric roll equation in beam seas.

Even though some authors (Spyrou, Cotton and Gurd, 2002) mention the interesting role played by bias in the roll equation for a ship in beam seas, they examine a different method of breaking the symmetry, as opposed to our adoption of an imperfection term. They investigate a restoring moment which with a varying bias term allows you to arrive to a cubic or quadratic restoring term.

Moreover, we carry out here a detailed study on how the bias affects the dynamics of the roll equation, the main bifurcations and the basin of attraction patterns when different periodic attractors may coexist prior to escape from the potential well.

Employing numerical integration techniques similar to the ones used in earlier Chapters, we are able to compute bifurcation diagrams for the unbiased ($\gamma = 0$) and biased case, choosing as an example the case of ($\gamma = 0.05$) respectively of the ship roll equation in beam seas in equation (5.2.2). We choose further a typical value of linear damping coefficient of $b_1 = 0.05$ and $\omega = 0.9$ in order to analyse the main features of the steady state solution of the system for different values of forcing amplitude, F and present Figure 5.10. Jiang, Troesch and Shaw (Jiang, Troesch and Shaw, 1996, 2000) mention in their studies of a highly nonlinear rolling motion of a ship in random seas, that realistic incident wave frequencies lie between $0.5 < \omega < 1.0$ and so adopting $\omega = 0.9\ rad/sec$ is a frequency likely to occur in typical seas.

In both the symmetric and asymmetric case, there is a jump phenomenon occurring while F increases at about $F \approx 0.038$ and $F \approx 0.036$ respectively (marked with arrows). It is clear that for the biased case, $\psi = \psi' = 0$ is no longer a solution of the equation. In the return process for decreasing F, the same bifurcation is obtained except for the jump region with the hysterisis phenomenon.

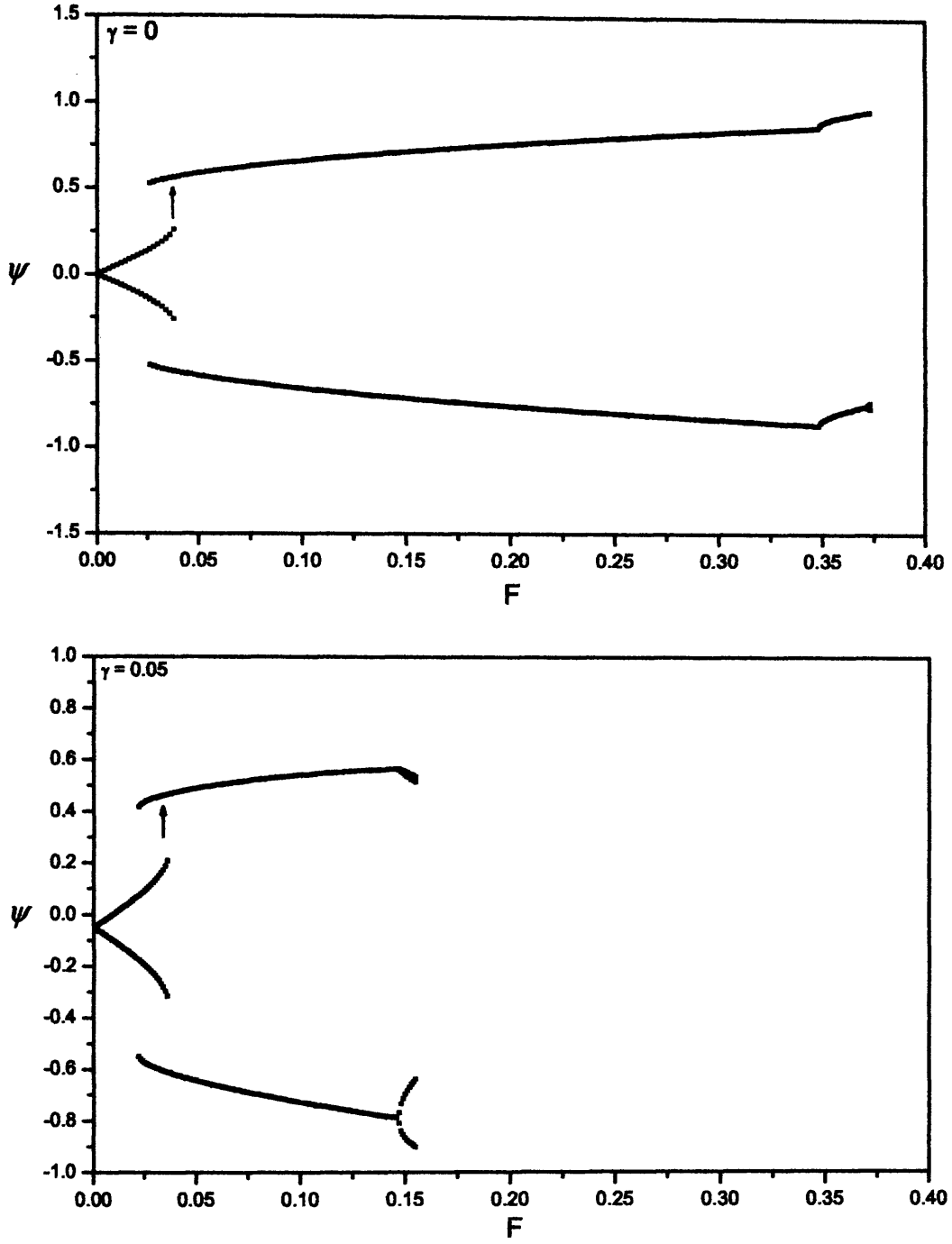

Figure 5.10: *Bifurcation diagrams for* $\gamma = 0$ *and* $\gamma = 0.05$ *respectively. The scaled damping coefficient is equal to* $b_1 = 0.05$ *and* $\omega = 0.9$ *rad/sec.*

Considering the case when $\gamma = 0.05$, as expected from the results in our earlier Chapters of the asymmetric parametrically excited system, the symmetry breaking, pitchfork bifurcation is not exhibited when $\gamma \neq 0$, since initial symmetry of the roll equation no longer holds.

At about $F \approx 0.145$, there is a period doubling bifurcation, that then leads to escape from the potential well, at about $F \approx 0.155$. This escape corresponds to the ships capsize. The appearance of this period doubling bifurcation should be regarded as a sign of the imminent danger of capsize.

Numerical work has hence showed evidence that the capsize phenomenon has been triggered to occur much earlier in the asymmetric case than the symmetric counterpart and this is also evident since both bifurcation diagrams are purposely drawn on the same scale to show the reduction in roll response.

Hence with the inclusion of bias, the period doubling-escape scenario, which is typically observed, takes place at lower forcing amplitudes.

5.5 Erosion of Safe Basin

In Chapter 4, we defined a basin of attraction as the set of points taken as initial conditions, that are attracted to a particular fixed point or an invariant set (Hsu, 1980, Nusse and Yorke, 1994). As it was mentioned earlier within the Chapter, this asymmetric system may be seen as a mechanical oscillator where a particle moves inside its potential well with the possibility of escape. This means that besides the possible attractors that may coexist in the interior of the well, the infinity may be taken as an attractor also. The basin of attraction allows us to identify the points at a particular phase space that are attracted to a safe oscillation within the potential well corresponding to non-capsizing regions and the set of points that escape the potential well leading to capsize.

A study of these basins of attraction for the quadratic scaled restoring arm have been extensively conducted by Thompson and collaborators in a series of papers (Thompson *et al*, 1987, Thompson and Soliman, 1990, Thompson and Soliman, 1991, 1992, Alexander, 1998). As seen in Chapter 4, the area that contains the initial conditions that do not lead to capsizing is called the safe basin. Numerical studies of the safe basin were carried out for the quadratic restoring term by Rainey *et al* (Rainey *et al*, 1991), Nayfeh and Sanchez (Nayfeh and Sanchez, 1990), Kan *et al* (Kan *et al*, 1993) and others.

In this Chapter however, we pay attention to the effect on the basins of attraction as the imperfection term is increased for the cubic restoring polynomial in the roll equation.

Our first strategy is to fix the wave forcing amplitude at a particular, but not specific, value and compute the basins of attraction for a range of γ terms. Then our second

strategy is to vary the forcing amplitude for each bias term. Figure 5.11 shows basins of attraction computed using the software *Dynamics* (Nusse and Yorke, 1994) for different sets of wave forcing amplitude for a variation of bias term values, $\gamma = 0$, $\gamma = 0.02$ and $\gamma = 0.05$ respectively.

Still referring to Figure 5.11, depending on the attractor an initial point converges to, it is assigned a different colour. Those initial points that tend to any attractor located in the interior of the well are assigned to the light blue colour and represent non-capsizing regions. The dark blue colour is assigned to any initial point that escapes from the potential well corresponding to capsize regions. Each phase plane consists of 720×720 grid points, (518400 grid points), with axis ranging from $-2 \leq \psi' \leq 2$ and $-2 \leq \psi \leq 2$. The first column shows the basin of attraction for $\gamma = 0$, the second column corresponds to $\gamma = 0.02$ and the third column to $\gamma = 0.05$. On the other hand, the first row corresponds to $F = 0$ (no wave excitation), the second row to a slightly higher wave forcing value, $F = 0.05$, and the rest of the rows show incremented F values until $F = 0.16$.

Observing these basins of attraction in Figure 5.11, it can be inferred that for a fixed forcing amplitude, an increase in γ, has a clear effect on the destruction of the safe areas of non-capsize or inside the well and the erosion of the basins increases notably. We notice the safe basin has eroded in a very complicated way, as the forcing amplitude F increases. By this we mean that at about $F = 0.08$ for the unbiased case, a thin whisker begins to invade into the safe basin. Thompson referred to these whiskers as fingers (Thompson and Stewart, 1986).

The whisker increases its number and grows thicker as F increases. For $\gamma = 0.02$ and $\gamma = 0.05$ these characteristics occur sooner and eventually at about $F = 0.16$ for the latter case of bias, the safe basin disappears completely.

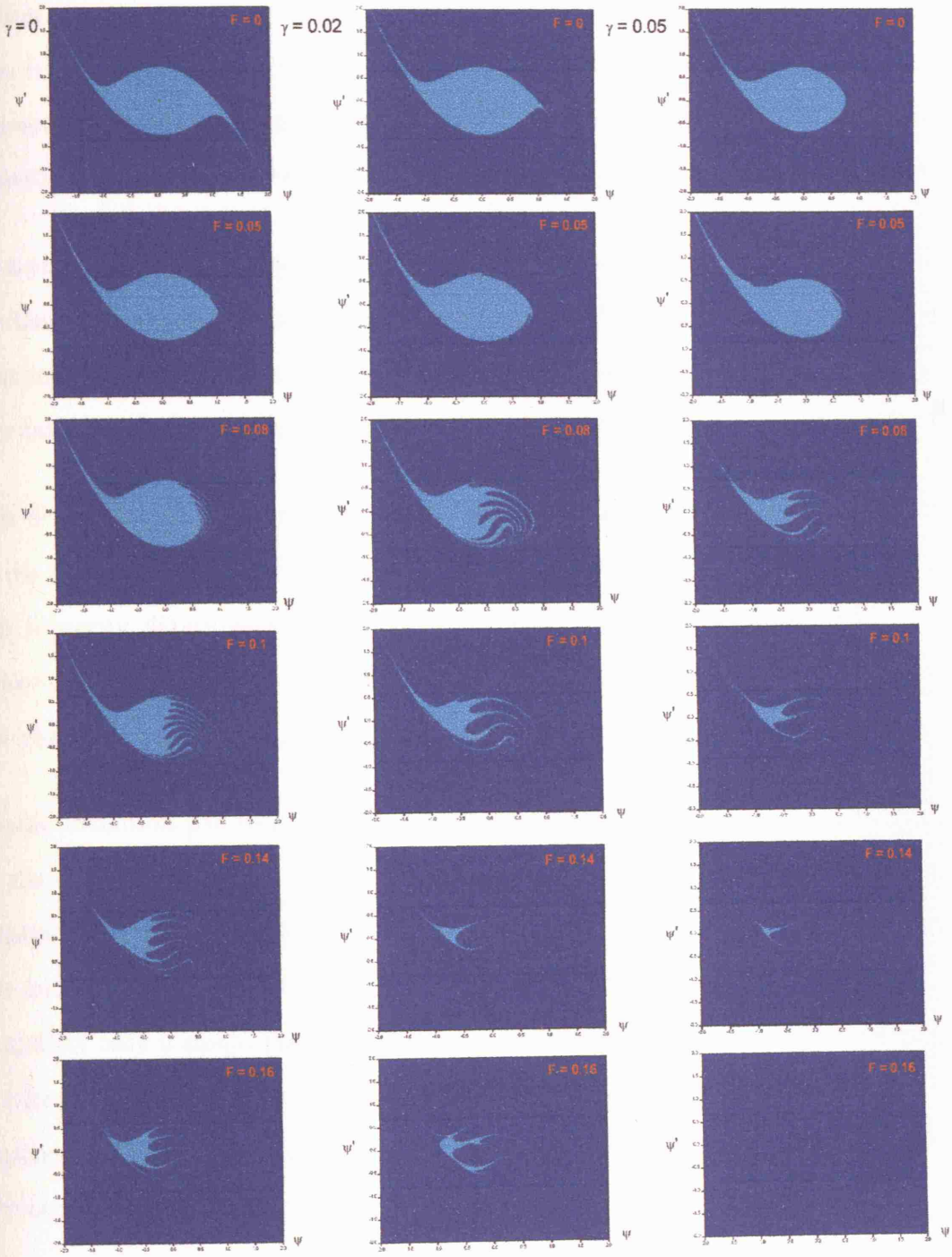

Figure 5.11: *Erosion of safe basin for the single degree of freedom roll equation at* $\gamma = 0$, $\gamma = 0.02$ *and* $\gamma = 0.05$. $b_1 = 0.05$ *and* $\omega = 0.9$. *The phase plane axes range from* $-2 \leq \psi' \leq 2$ *and* $-2 \leq \psi \leq 2$.

Moreover, Kan and Taguchi (Kan *et al*, 1991), also focus on an enlargement of a section of the basin of attraction for the unbiased case of the roll equation in beam seas, for a specific forcing amplitude discussing that the boundary between capsize and non-capsize has a fractal feature which from the viewpoint of the computational algorithm, the safe basin resembles a Julia set that is known as a typical fractal set.

As a consequence, we suggest that the use of bias suppresses large scale erosion of the basin. Thompson *et al* (Thompson *et al*, 1987) have incorporated a quadratic term in the usual odd-type polynomial of roll restoring thus rendering it asymmetric. The two approaches do show that mathematically they are equivalent.

It is also worth noting that the basins of attraction pictures depend on the phase of the section. As the phase alters, the shape and size of the basin will change. The integrity diagrams that follow in the next section are representatives of the behaviour so that whatever phase is used, the behaviour is the same, meaning that the phase you chose does not matter.

Similar attention has been paid to the study of the effect of the damping exponent in the damping function, on the erosion process of the non-escaping basin of the quadratic escape oscillator (Sanjuán, 1999). By damping exponent we mean that the author considers a nonlinear damping term of the form $b_1\psi'|\psi'|^{r-1}$ where for simplicity only a single damping term proportional to the rth power of the velocity is taken. By fixing all the parameters of the system and varying only the damping exponent r, the author's observation is that the increase of the damping exponent provokes a rapid erosion of the basin of attraction.

Similarly to our examination of the biased scaled cubic roll equation, when the forcing is increased, the erosion of the basin is greater and becomes more pronounced if at the same time the bias term, or damping exponent in the above case (Sanjuán,

1999), is increased. This is a surprising result because from our knowledge of the quadratic escape oscillator, increasing damping delays the erosion and increases the safe region instead (Thompson, Rainey and Soliman, 1990).

For the practising engineer, the information provided will be of particular value if it can be utilised effectively towards designing a safer ship. So, in this Chapter we suggest that rather than trying to discriminate between good and less effective designs in terms of resistance to capsize in beam seas, naval architects and engineers should set their focus mainly on developing an understanding of the nature of the nonlinear responses in their various manifestations.

5.6 Integrity diagrams

Several articles have been published in the recent past about the concept of loss of engineering integrity of dynamical systems (Rainey and Thompson, 1991, Thompson, 1989, Spyrou, Cotton and Gurd, 2002). The idea is that the safety robustness of an engineering system can be represented by the integrity of its safe basin, comprised by the set of initial conditions (roll angle and velocity) which lead to a bounded motion pattern.

As we showed in the previous section, the basin undergoes a serious reduction of area once the level of excitation is exceeded, given the initial damping and restoring characteristics of the ship, and an even faster reduction with the inclusion and increase in bias.

The reason for this decrease in safe basin is the complex intersection of manifolds, in other words, those special surfaces which originate from, or end on, the unstable periodic orbits corresponding to the angles of vanishing stability (Guckenheimer and Holmes, 1997). Similar to the separatrix discussed in Chapters 2 and 3, the stable manifolds form the boundary between the two areas of attraction.

The initiation of basin erosion can be used as a rational criterion of system integrity which for a naval architectural context would be translated as sufficient dynamic stability in a global sense.

The area of safe basin or non-capsizing region, may be used as a safety index as pointed out by Thompson and his colleagues (Thompson and Stewart, 1986, Thompson, 1989). In order to quantify the effect of the bias on the basin, we include as Figure 5.12 integrity diagrams based on the area of safe basin for different γ values.

Firstly, we quantify the basin occupied by the ensemble of initial conditions ending up in the non-capsizing region when $\gamma = 0$, no bias, within a suitable chosen window $-2 \leq \psi' \leq 2$ and $-2 \leq \psi \leq 2$ by counting the pixels lying within that area. Incrementing forcing amplitude and determining the same area, we scale it by dividing it with the corresponding area when $F = 0$. This process is continued until $F = 0.25$. The same technique is used to produce novel integrity diagrams with $\gamma = 0.02$ and $\gamma = 0.05$.

These diagrams show the reduction in the area of safe basin associated with the incursion of the fractal fingers (whiskers) especially as the bias term increases. The drop in non-capsizing area is much aggravated when $\gamma = 0.05$ so that it intercepts $F - axis$ at 0.16, where the safe basin has fully eroded as depicted in Figure 5.11 aswell.

In these diagrams, we also come across another fractal feature, like a devil's staircase, and this is more evident visibly when $\gamma = 0.02$ between $0.14 < F < 0.2$. This up and down behaviour in this specific integrity diagram may be explained in view of Figure 5.11. The non-capsizing region in the case of $F = 0.14$ and $\gamma = 0.02$ has decreased compared to $F = 0.1$, but with further increase in forcing amplitude, at say $F = 0.16$, the area of no capsize increases again, before it diminishes completely at $F = 0.2$ (the latter value is implied from the specific integrity diagram of Figure 5.12). Kan *et al*, (Kan, Saruta and Taguchi, 1990) also come across this behaviour for their capsizing equation of roll motion under certain conditions.

The decline in the integrity diagram due to the rapid erosion process has been called the Dover Cliff fall in basin area (Thompson, 1989). Recall also Chapter 4. Generally this cliff corresponds to a well defined loss of integrity and may be used as a design criterion.

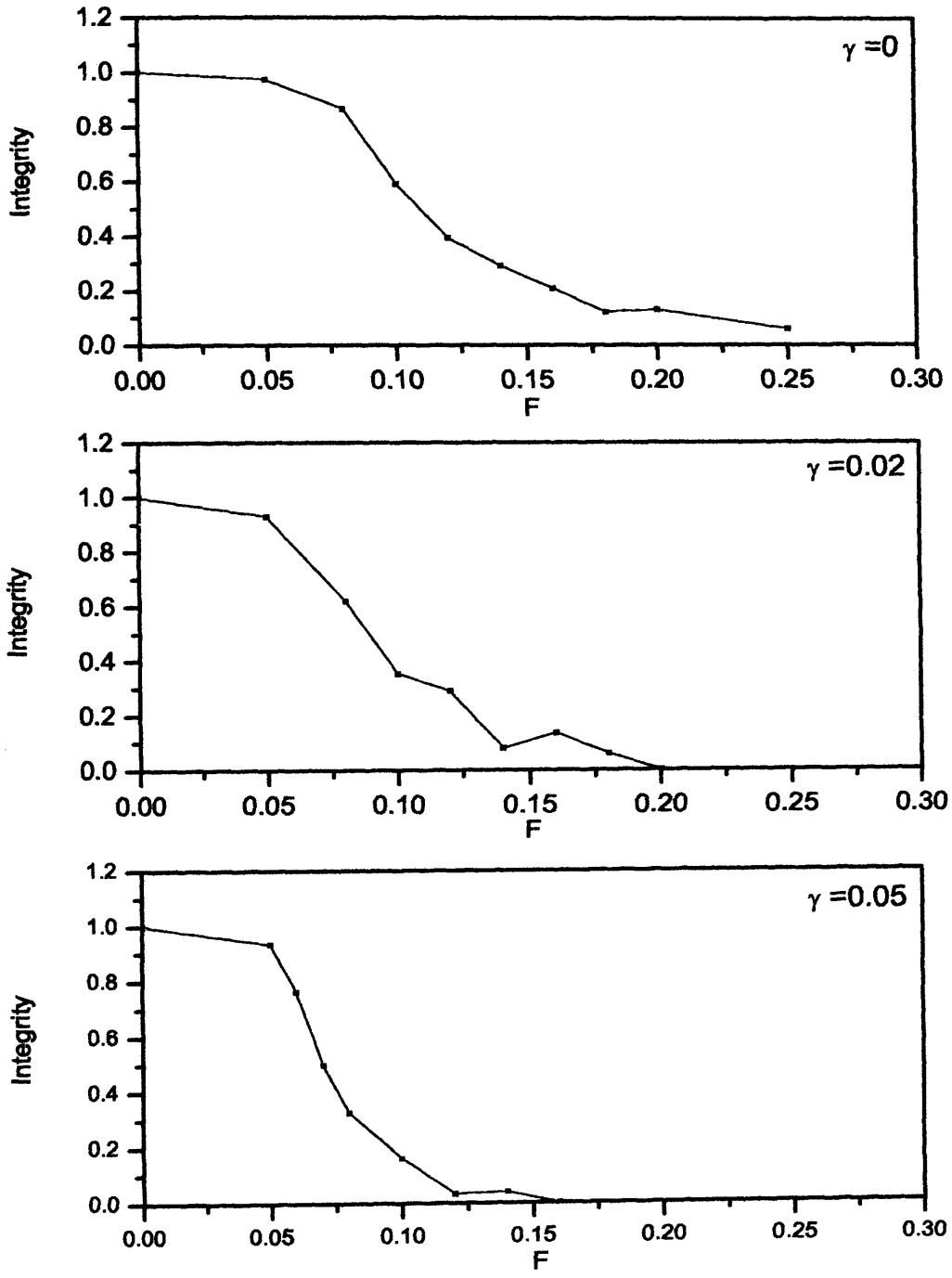

Figure 5.12: *Integrity curves of safe basin area versus forcing amplitude magnitude at different bias term values.*

For a sound and safe operation of engineering systems, we must aim to remain below the integrity curve as we do not wish to operate at values of F greater than that of the cliff face.

In Figure 5.13 we show as a new feature the effects of breaking the symmetry of the cubic ship roll equation, (5.2.2), in terms of the measure of safe basin area for certain forcing amplitude values. The collection of these integrity curves were computed in the same above manner, but this time the bias term was incremented for specific forcing amplitude.

With no forcing amplitude, but with increasing imperfection term, the area below this curve decreases smoothly unlike the cases for example where $F = 0.08$ and $F = 0.14$, where a dramatic drop rapidly diminishes the region of non-capsizing.

Hence, it is verified that the system integrity is considerably impaired as asymmetry is intensified. For instance, when $F = 0$, a 5% increase in γ leads to about a 16% reduction of the basin of non-capsizing roll. For the same increase percentage in bias but at $F = 0.08$, we have about a 68% reduction in safe basin and an 89% decline when the forcing amplitude magnitude is $F = 0.14$.

These diagrams show similar characteristics as our construction of Safe Zone in Chapter 4 for the asymmetric parametrically excited pendulum system. The drop in safe area of oscillatory and rolling motion respectively is present in both cases so that anything above these boundaries represent unsafe and difficult operations of engineering systems.

In the broken symmetry model of the parametrically excited pendulum with the bias inclusion, we managed to provide a safety benchmark of the escape scenario, based upon the final bifurcation before escape, as the bias of imperfection increases

and also in this ship roll case, we quantified the basin erosion of the non-capsizing region providing a safety index as the value of bias rises.

As a result, we have confirmed the main purpose of this Chapter, which is that there is indeed an aggravated sudden reduction of non-capsize region with the bias term inclusion.

Another method that could be used to verify the above result is that of applying Melnikov's approach (Melnikov, 1963, Thompson and Stewart, 1986, Arrowsmith and Place, 1990, Moon, 1992, Nayfeh and Balachandran, 1995). The method is based on the analytical approximation solution for the distance between stable and unstable manifolds but we have preferred to carry out basin plots using the software *Dynamics* in order to have direct view of the process of basin erosion since the objective is the testing of the concept of engineering integrity itself.

Another advantage of the direct basin plot is that it allows us to determine fractional integrities as function of bias and excitation. For instance, 80% integrity means that the remaining basin area is 80% of the initial basin area calculation.

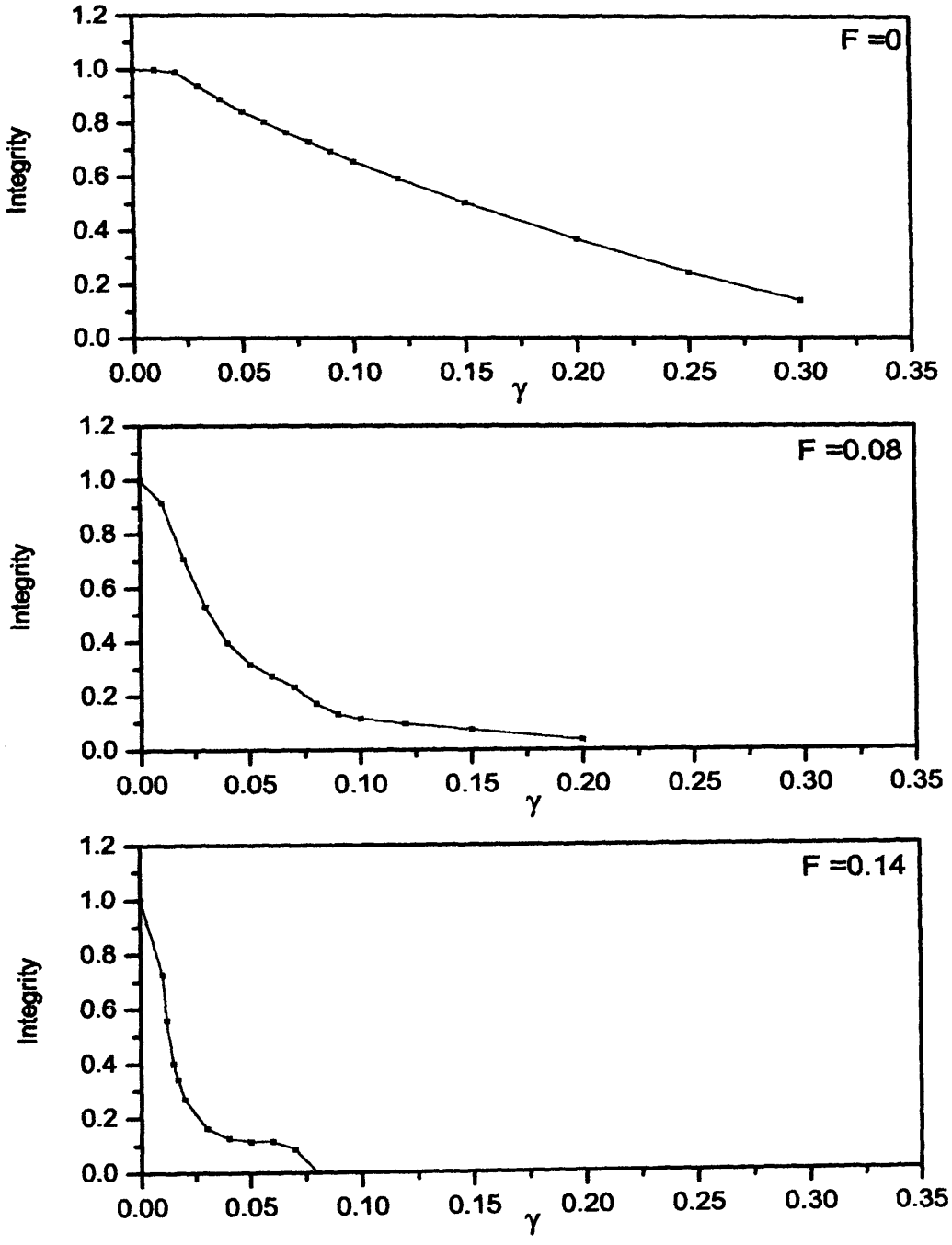

Figure 5.13: *Integrity curves of safe basin area versus increasing bias term at specific forcing amplitude values.*

5.7 Fractals in the Control Space

Thompson *et al* (Thompson, Rainey and Soliman, 1990) mention that at a fixed damping level, the safe basin of the escape equation can be thought of as a master basin in the 4D phase control space spanned by $x(0), y(0), F$ and ω. We extend this view to our case of the scaled cubic restoring arm of the ship roll equation in beam seas.

The phase space basins of Figure 5.11 are cross sections of this master basin corresponding to fixed values of F and ω. The control space basins are also just cross sections of the master basin but at the fixed values of $\psi(0) = \psi'(0) = 0$.

Figure 5.14 shows this control space cross section of the safe basin for $\gamma = 0$ and $\gamma = 0.05$ respectively for the ship roll equation. The safe non-capsizing region is represented by black whereas the unsafe capsizing region is denoted in white colour.

We note in both diagrams, the complicated nature of the boundary separating capsize and non-capsize in parameter space and the intricacies of frequency and amplitude combinations that produce narrow regions of bounded motion around the lower bound of capsize. Moreover, we observe the boundaries between these two regions that show signs of fractal nature. Kan *et al* (Kan, Saruta and Taguchi, 1990) showed evidence of fractal features for their proposed simple capsize equation, similar to our unbiased system but with damping fixed at $b_1 = 0.04455$.

Comparing both diagrams we note that with $\gamma = 0.05$, the regions of white colour, so in other words the capsizing region, has increased and moreover at around $\omega = 0.85$, the capsize boundary happens to occur at a smaller magnitude forcing amplitude value. The red dotted lines aid to highlight this difference in minimum forcing amplitude around this forcing frequency.

Following Kan *et al*, (Kan, Saruta and Taguchi, 1990) it seems that the most dangerous position for the unbiased and biased case, occurs at around $\omega \approx 0.85$ which corresponds to the bend of the amplitude response curve towards the lower frequency due to the softening spring effect.

So in other words, to guarantee safety for all ω, we need the forcing amplitude to be less than 0.05 ($F < 0.05$). For lower values of damping, the capsize area shifts vertically down, a not altogether surprising outcome given the relation between damping and (resonant) amplitude response (similar to the nonhomogenous, linear, ordinary differential equation with single harmonic excitation (Virgin, 2000)). Hence, by adjusting the damping to a higher value, this increases the minimum value of forcing amplitude for safer rolling oscillations.

We comment also that since we cannot actually alter the wave frequency or amplitude encountered by a ship in a seaway, to able to produce a greater range of F, which we recall from the scaling of our roll equation is equal to $F = \frac{F_1}{\omega_0^2(I+A)\varphi_v}$, then the natural frequency, ω_0, must be decreased. This may be accomplished by decreasing in turn m, the mass of the ship, due to the relation $\omega_0^2 = \frac{mgGM}{(I+A)}$. So in plain terms, getting rid of heavy masses of cargo intentionally off the vessel under extreme uncontrollable conditions, does not seem now as a horrific idea for the sake of non-capsize.

In physics and engineering, the steady state response of a system is often displayed by plotting the maximum displacement as a function of the forcing frequency for given fixed values of the forcing magnitude. This is done now for the present system with and without the inclusion of bias in Figure 5.15. Hence, the resonance response curves for the ship roll equation in beam seas at forcing amplitude $F = 0.07$ for when $\gamma = 0$ and $\gamma = 0.05$ are shown in Figure 5.15 respectively.

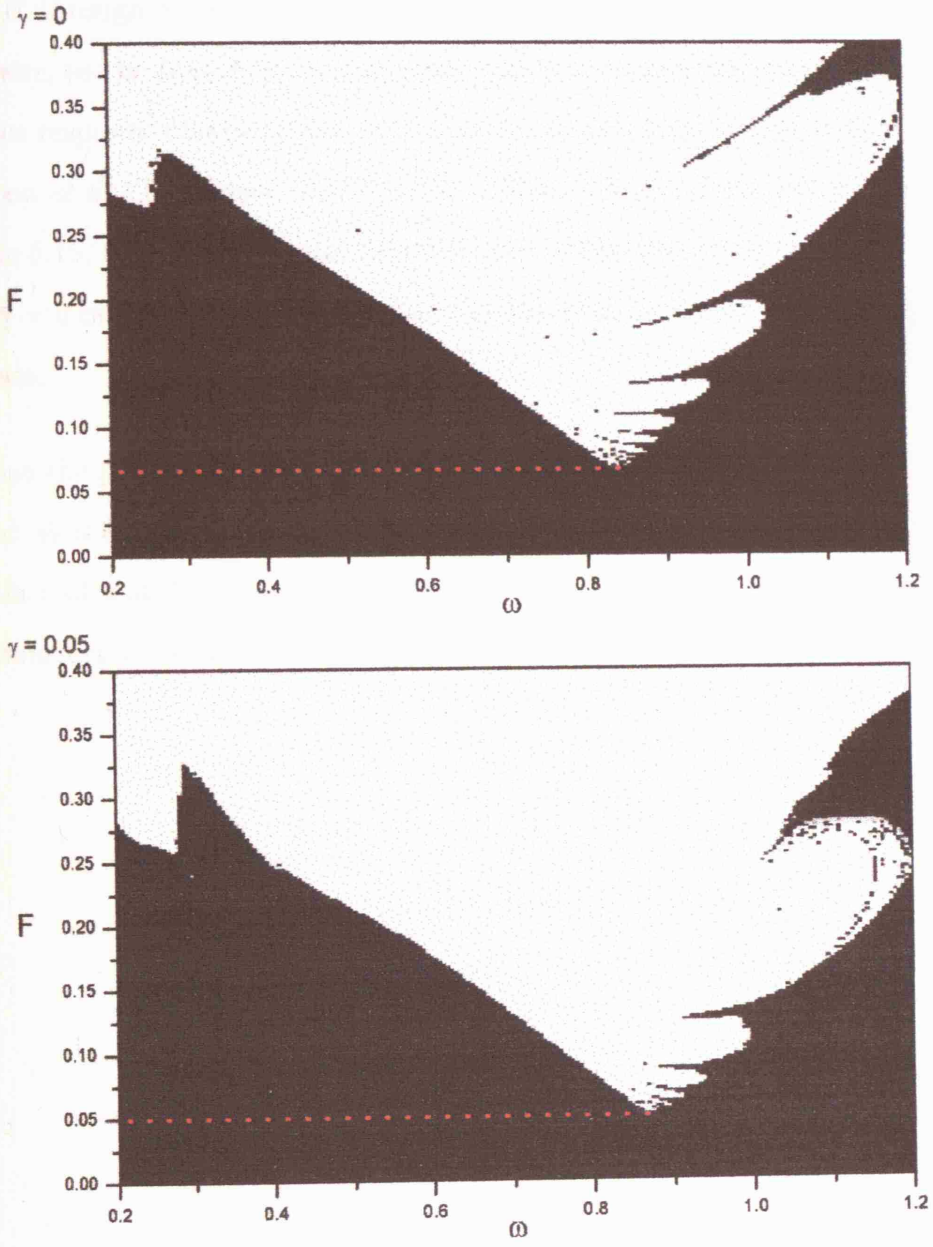

Figure 5.14: *Fractal boundaries in control space for our scaled cubic restoring arm when* $\gamma = 0$ *and* $\gamma = 0.05$ *respectively.*

In both diagrams of Figure 5.15 there is a jump to resonance at saddle node fold A as the forcing frequency is increased and a route to escape from the potential well at B through a cascade of period doubling, where only the first sequence is shown here, as the frequency is decreased. This is similar behaviour as seen in the resonance response curves of the second order polynomial scaled restoring term in Thompson *et al* (Thompson and Stewart, 1986). Clearly from our second diagram in Figure 5.15, the maximum roll displacement is less when the bias term exists and for the $\gamma = 0$ case, the maximum roll displacement is probably dangerously high roll amplitude.

Note that the present idea of a jump in the bifurcational context fold A is always classified as a dangerous bifurcation. We also notice in the asymmetric case, an appearance of a slight bump in the vicinity of $\omega = 0.5$ where this is the beginning of a subharmonic resonance (Thompson and Stewart, 1986).

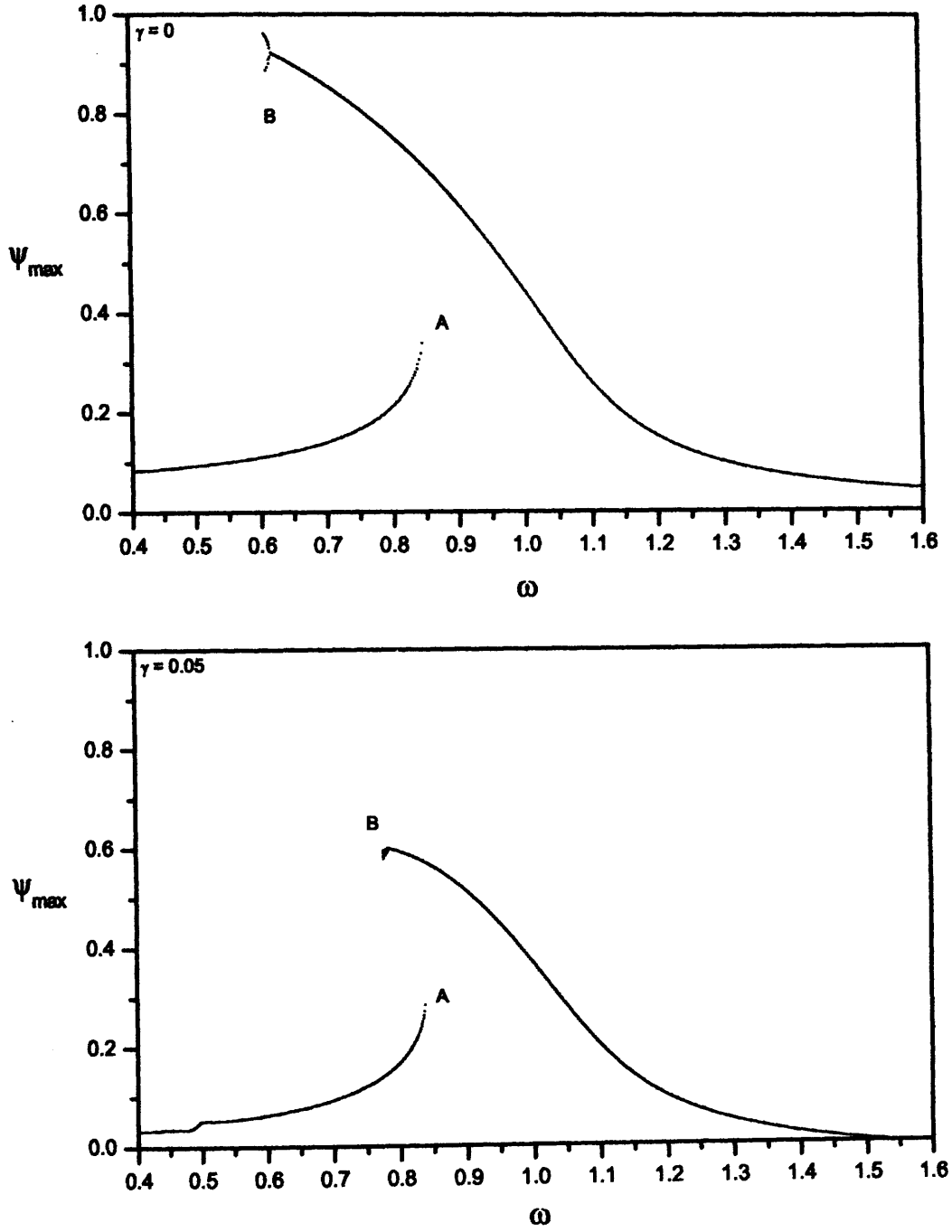

Figure 5.15: *Pair of resonance response curves for the ship roll equation in beam seas at wave forcing amplitude* $F = 0.07$ *for* $\gamma = 0$ *and* $\gamma = 0.05$ *respectively.*

5.8 Final Remarks

In this Chapter we moved our attention away form the actual parametrically driven model with the aim of concentrating on the issue of symmetry breaking but in the field of our growing interest, ship dynamics.

The purpose of this deviation is to examine how asymmetry can lead to diminishing regions of safe roll motion and relate these outcomes to the findings of Chapter 4, for the analogous region of escape in oscillatory swinging motion.

In order to accomplish our examination of an asymmetric model and to study the safety of a ship using the concept of safe basins, thus providing some coherence with the safe oscillatory zone of the biased parametrically excited pendulum researched earlier, it was necessary to investigate how the stability curves may alter due to asymmetry.

Initially some useful preliminary definitions were implemented that help to understand ship stability and aid to configure the equation of roll motion for a ship in beam seas. In this Chapter, asymmetry is characterised by a constant moment term representing maybe wind, cargo shifting or even ship damage.

To envisage the physical effects of symmetry breaking within the restoring moment of the roll equation, we employed Tribon Software, where we examined the case of shifting cargo and added mass within a specific type of ship, a passenger ferry. The software allowed us to understand and examine how these two circumstances alter the centre of gravity for example, of the vessel in calm water, thus posing an effect on the stability curves. Changes in the GZ curves in turn affect the restoring moment and thus the overall symmetry of the roll equation.

Results showed that the farther the added mass was placed from the initial centre of gravity (point of centre of gravity before the addition of the extra mass), the smaller the heeling angle that is needed to capsize the ferry, since the range of stability decreased.

We noticed that the maximum height of the stability curves also falls the greater the distance of the added mass position, both in the vertical and horizontal direction, from the initial centre of gravity. As a result, the smaller the maximum restoring moment, the less stable the vessel, as you need to apply less force to reach that angle.

In terms of shifting of mass within the ferry, similar effects on the GZ curves were seen. In general, the closer to the edges of a vessel a cargo shifts within, the less stable she will be in still water, yet alone when waves are generated on the system.

Further on, this Chapter looks into the effect on initial conditions in terms of basins of attraction, for the stated asymmetric scaled ship roll equation. We managed to show the erosion of safe basins as the bias increases and construct integrity diagrams in order to quantify the effect of the imperfection.

We considered two scenarios and produced different sets of intergity diagrams for each, Increasing wave amplitude against the measure of safe basin area at specific bias values and increasing the bias term at certain wave forcing amplitudes. Both cases showed evidence of drop in non-capsizing area which is much aggrevated the higher the bias. Thus showing similar characteristics as our earlier constructed safe zone for the asymmetric parametrically excited pendulum model. In this Chapter, we managed to quantify the basin erosion of non-capsizing regions and provide a safety index as the value of bias increases.

Chapter 6

Two frequency parametric excitation

6.1 Introduction

In earlier chapters we considered the excitation of a simple pendulum system to consist of a single vertical forcing. It is however, a matter of considerable interest from the practical, and perhaps even more from the mathematical, point of view to investigate what occurs when the excitation is a sum of two levels of parametric forcing.

Moreover, the usefulness and significance of studying a double parametric forcing system will become evident within the next Chapter, where we will adopt such forcing-type form in the field of ship dynamics with the aim of providing a more realistic mathematical model for a single degree of freedom equation of roll motion.

6.2 Adoption of two parametric forcing terms

With the above in mind, it hence seems natural to progress to oscillations which are acted on by a combination of two parametric forces. We consider therefore, what happens to the parametrically excited pendulum system when subject to a two frequency combined parametric excitation of the form,

$$\theta'' + \beta_1\theta' + \beta_2\theta'|\theta'| + \omega_0^2(1 + p\cos\omega_1 t + q\cos\omega_2 t)\sin\theta = 0 \qquad (6.2.1)$$

where in this Chapter, we have also included nonlinear damping term. β_1 is the damping coefficient of the linear damping component and β_2 corresponds to the damping coefficient of the quadratic damping term. Following usual notation, ω_0 represents the natural frequency of the pendulum. ω_1 and ω_2 are the forcing frequencies and the excitation amplitudes are p and q respectively.

This type of forcing, which leads to combination oscillation solutions or sometimes called almost-periodic behaviour has been the subject of a number of classic analytic studies especially for the Duffing Oscillator including work by Stoker (Stoker, 1950) and Helmholtz (Helmholtz, 1863) who put forward the first theory of the mammalian hearing organ, the cochlea (Kern and Stoop, 2003). Helmholtz considered a quadratic oscillator exhibiting difference tones, (for instance of frequency ω_2 - ω_1) and its relation with human hearing (Helmholtz, 1863). An excellent summary and critical discussion of such acoustical phenomena may be found in Rayleigh (Rayleigh, 1945).

Structural mechanics provides a useful context with combination resonances, a focus of attention by Plaut *et al* (Plaut, HaQuary and Mook, 1986, Plaut, Gentry and Mook, 1990). Szabelski and Warmiński (Szabelski and Warmiński, 1995) investi-

gated the influence of a self excitation on a nonlinear oscillator driven by parametric and external forcing whilst the ratio of forcing frequencies is a rational number. On the other hand, Yagazaki and co-workers (Yagasaki, Sakata and Kimura, 1990) analysed the dynamics of an oscillator subject to parametric and external excitations whilst the ratio of forcing frequencies is an irrational number but including also a weakly cubic nonlinear component.

The approximate analytical methods of harmonic balance and perturbation theory utilised within earlier chapters of this thesis (Nayfeh, 1993, Jordan and Smith, 1987) can also be applied with care for this type of problem, and so we shall only employ within this Chapter, numerical techniques to study the nonlinear behaviour of a two frequency parametric forcing system, commenting however on analytical techniques adopted by other researchers for similar systems.

Arrowsmith and Mondragón (Arrowsmith and Mondragón, 1999) considered a parametric perturbation of the Mathieu equation by introducing higher order forcing terms. Specifically they considered an augmented Mathieu equation. Their analytical and numerical work focuses on smooth curves forming the two boundaries of the stability zone, around the region where the start of the tongue touches the horizontal axis at 1, which they themselves cross-over. The authors describe precisely the degree to which this behaviour occurs and control it by using appropriate parameters. The paper also includes analytical work on the effects of this proposed augmented Mathieu equation in the tongue centered at 9/4, in the parameter control space.

Furthermore, the authors, considered the global effects of changing the tongue tip structure by parametric perturbation. For clarity purposes but also most importantly to serve our understanding of double parametric forcing, we investigate numerically the behaviour of the following system:

$$\frac{d^2x}{dt^2} + [\alpha + \beta(\cos t + \varepsilon \cos 2t)]x = 0 \tag{6.2.2}$$

where $\varepsilon \in \mathbb{R}$. The ε coefficient is included to study the shapes of the tongues within the parameter space and how the curves evolve under a variation of ε in the (α, β) plane. For the tongue centered at 9/4, in the (α, β) plane, the tongue tip remains intact but its width increases by the effect of increasing ε from zero. So, in general the condition of $\varepsilon \neq 0$ allows for the opening up of the tongues.

With this in mind, we introduce as Figure 6.1 our numerically computed version of the stability diagrams for the extended version of the Mathieu equation.

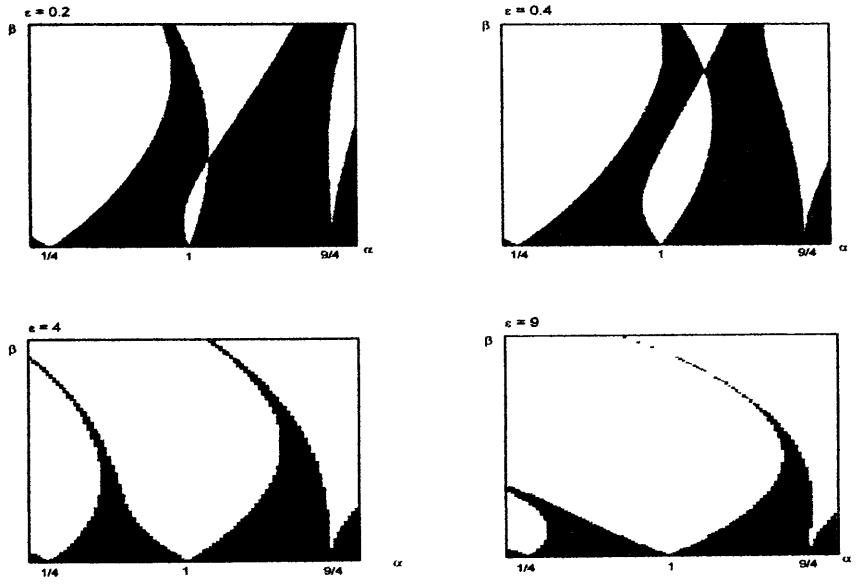

Figure 6.1: *Stability diagrams for the extended version of the Mathieu equation as* ε *is increased.*

These diagrams were computed using *Mathematica* and with the collaboration and guidance of Prof. Helmut from the Univeristy of Texas El Paso. The diagrams show the evolution of the shapes of the instability and stability regions in (α, β) space as ε is increased in equation (6.2.2). The region of the (α, β) parameter space for which $0 \leq \alpha \leq 2.4$ and $0 \leq \beta \leq 2$ is scanned for the boundaries of the stability regions as ε is varied. The shaded areas represent stable regions and the white regions correspond to unstable zones.

Specifically, one may observe the size of stable regions as the parameter ε is adjusted. The diagram confirms the results of Arrowsmith and Mondragón (Arrowsmith and Mondragón, 1999) where there is a substantial change in the shape of the stability regions as ε is increased.

It is also important to notice that the crossing over of the boundaries of the stability zones occur only for the $\alpha = 1$ tongue, within this range and for small ε, and analytical techniques employed by the above authors verify this. The essential analytical reason given by the authors for the cross-over is that the linear term and the nonzero quadratic terms for each boundary curve compete against each other.

We notice further that the relative size of the stable area changes with variations of ε. We note that when $\varepsilon = 0$, we return to the typical Mathieu equation studied extensively by many researchers (Jordan and Smith, 1987, Grimshaw, 1993) and discussed in detail within Chapter 2. The unstable region of the zone around $\alpha = 1$ is greater than when $\varepsilon = 0.25$ (see Figure 6.2 for comparison, where we consider the period-2π behaviour of this version of the Mathieu equation as opposed to period-π in Chapter 2) hence implying an increase in stable area as ε is initially increased.

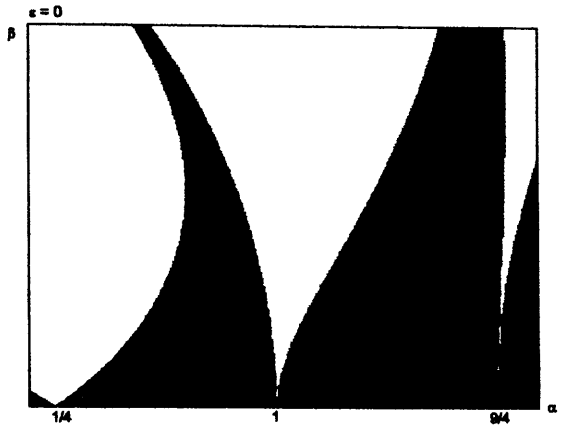

Figure 6.2: *Stability diagram for the extended version of the Mathieu equation with* $\varepsilon = 0$.

However after a certain ε parameter change, further increase of the coefficient leads to a decrease in the shaded stable region as discussed by Arrowsmith and Mondragón (Arrowsmith and Mondragón, 1999). Hence an optimal stability in the parameter space may be achieved as ε is increased.

6.3 Subharmonic and superharmonic forcing

The key to determining the anticipated form of response of our proposed double parametric forcing with nonlinear damping, is whether the frequencies are commensurate or not. So in other words, in this section we will consider the case of the two forcing terms where there is a rational multiple between ω_1 and ω_2 of equation (6.2.1) (this ratio is known as the rotation number).

The system now evolves in a four dimensional phase space with position, velocity and the two forcing phases effectively providing the unique location at a given instant of time, that is

$$(\theta, y, z_1, z_2) \quad \epsilon \quad \mathbb{R}^2 \times S^1 \times S^1$$

where $y = \theta'$, $z_1' = \omega_1$ and $z_2' = \omega_2$. The case where the two driving frequencies are incommensurate so that the ratio of the frequencies is expressed by an irrational number, will be considered briefly in the next section, in which case the output will then be nonperiodic (typically quasiperiodic).

Given the large number of parameters now available, we shall just consider two frequency ratios, one rational and one not. Initially, we impart a symmetric equation of motion where the frequencies $(\omega_1 : \omega_2)$ are of the ratio $2 : 1$ and are normalised with respect to the natural frequency of the pendulum, $\omega_0 = 1\ rad/s$. The linear damping coefficient component is taken as $\beta_1 = 0.1$ and the quadratic coefficient is $\beta_2 = 0.2$. For the second forcing amplitude component we choose the value of $q = 0.4$, this way there exists an adequate starting forcing amplitude value that kicks start the nonlinear behaviour as opposed to initiating both forcing amplitudes from zero.

Figure 6.3 consists of a three dimensional plot portraying a combination of bifur-

cation diagrams computed over the variation of forcing amplitude p for certain frequency ratios. The bifurcation diagrams for when $\omega_1 \approx 1$ and 2 with $\omega_2 = 0$, so with single parametric forcing, (equivalent to our earlier studies within the thesis but this case for nonlinear damping) are also included for comparison.

When $\omega_1 = 4$ and $\omega_2 = 2$, so that the ratio of frequencies is $\frac{\omega_1}{\omega_2} = 2$ and with secondary forcing amplitude set to $q = 0.4$, the corresponding bifurcation diagram shows no evidence of bifurcations. There is merely a gradual increase in amplitude response and then a sudden drop where the hanging position is reached, actually at approximately $p = 2.4$.

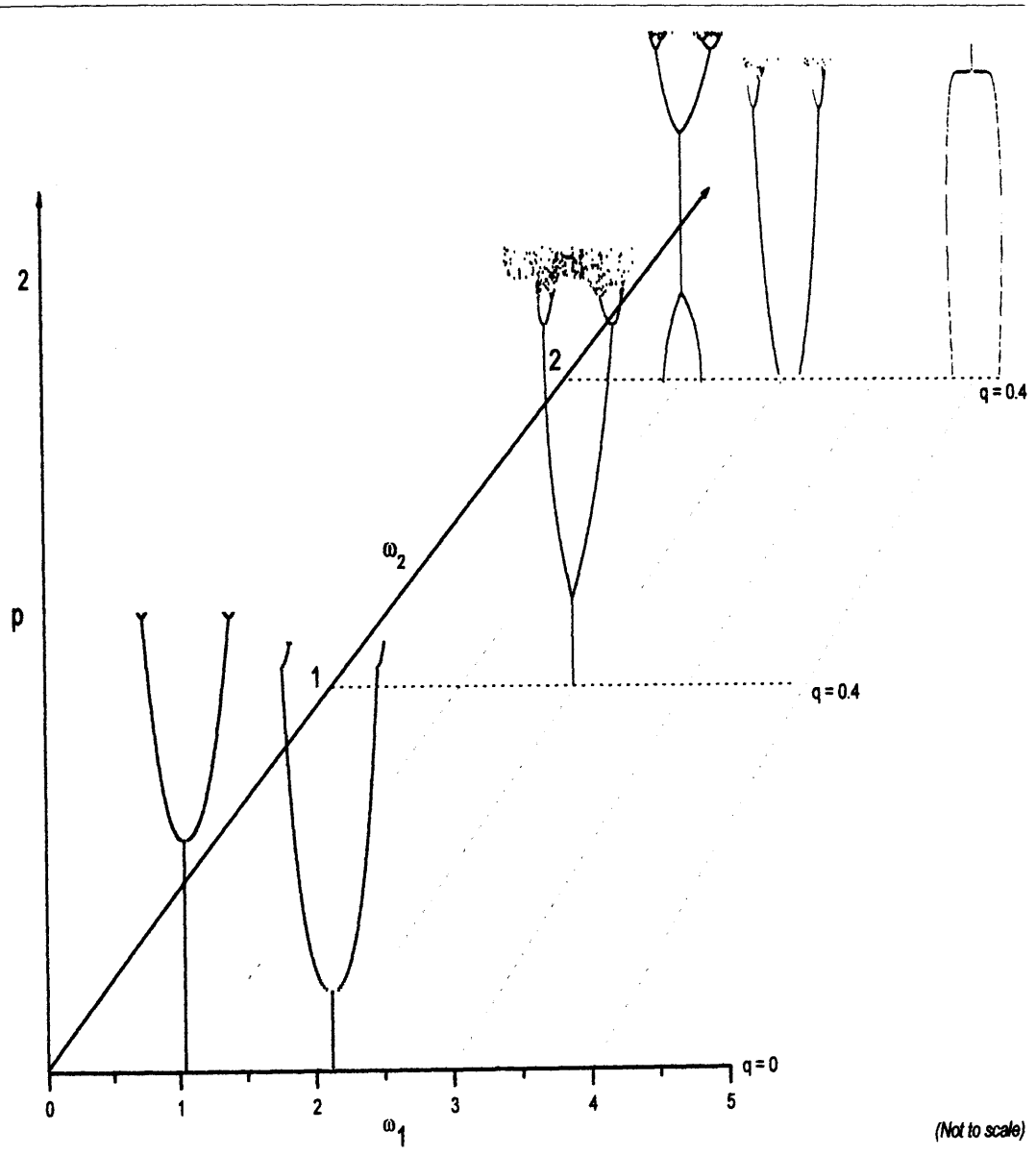

Figure 6.3: *Three dimensional plot portraying a combination of bifurcation diagrams for certain frequency ratios under the parameter conditions* $\beta_1 = 0.1$, $\beta = 0.2$, $\omega_0 = 1$. *The excitation amplitudes are as stated on the diagram.*

The phase portraits and time series that follow in Figure 6.4 and Figure 6.5 are included in order to verify the steady state solutions experienced at the specific p and q values which are echoed by the maximum amplitude response within this bifurcation diagram, at $\omega_1 = 4$ and $\omega_2 = 2$, of Figure 6.3. The time series and phase portrait of Figure 6.4 verify a decay in amplitude towards the $\theta = 0$ solution at $p = 2.45$, $q = 0.4$.

Still examining the same bifurcation diagram but at an earlier instance, at $p = 0.4$ and $q = 0.4$, Figure 6.5 shows the corresponding time history and phase portrait computed after the transient motion is allowed to die away. The three dimensional diagram also agrees with the construction of the phase and time plot diagrams.

However, Figure 6.6 shows an interesting feature which may be viewed for example under the parametric conditions $p = 0.16$ and $q = 0.4$. The phase plane and time series, as well as the three dimensional version of the response, show by numerical integration of equation (6.2.1) the behaviour of double nodding.

Multiple nodding oscillations exist as high order subharmonic resonances and they have been examined by Acheson (Acheson, 1995) and Clifford and Bishop (Clifford and Bishop, 1998), for the single parametrically excited pendulum system, existing for both the inverted and hanging down pendulum.

Returning to Figure 6.6, the solution may be generated immediately with initial conditions $\theta(0) = 0.1$ and $\theta'(0) = 0$. From the point of view of an observer, the pendulum "nods" twice on one side of the vertical and then twice on the other during each such oscillation cycle. If we take θ to measure the angle that the pendulum makes with the downward hanging position, then following Acheson, the multiple nodding oscillations have their velocity changing sign at least three times on one side of the hanging position.

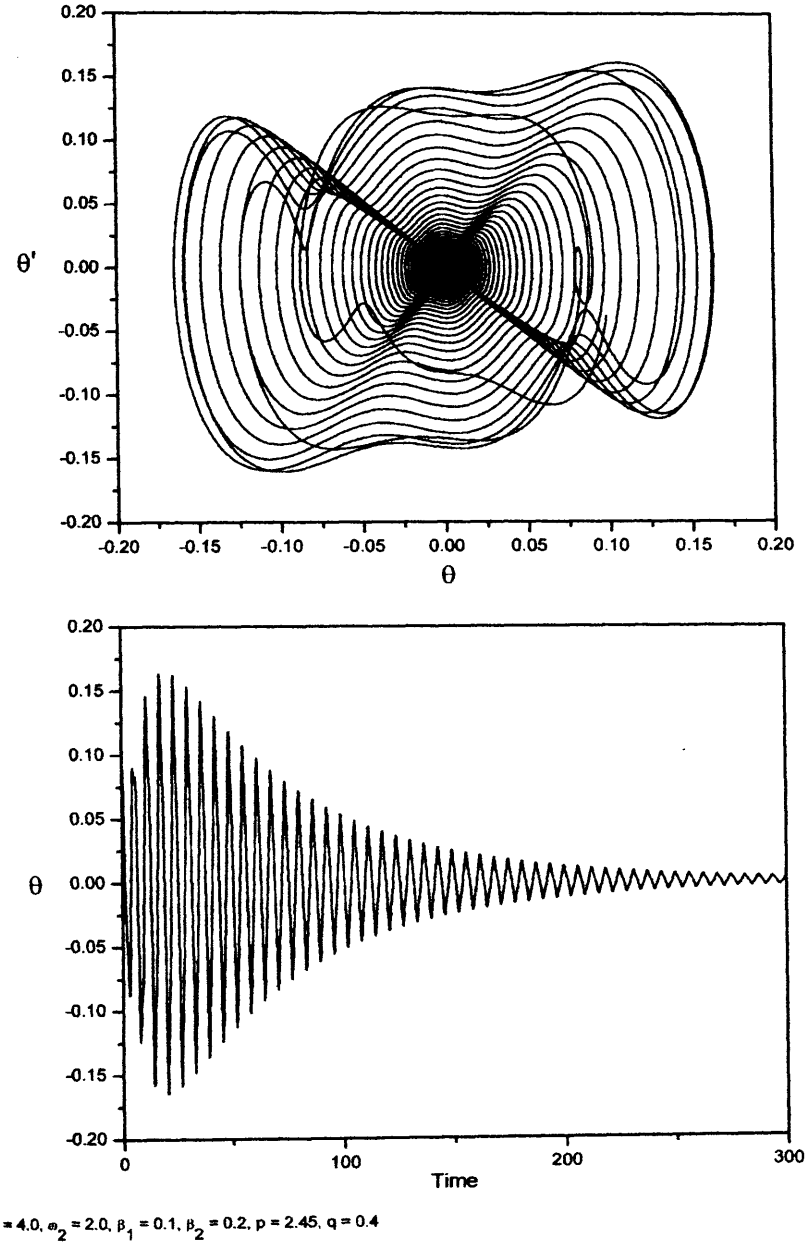

Figure 6.4: *Corresponding phase plane and time series for* $\omega_1 = 4$ *and* $\omega_2 = 2$ *for the corresponding bifurcation diagram of Figure 6.3.*

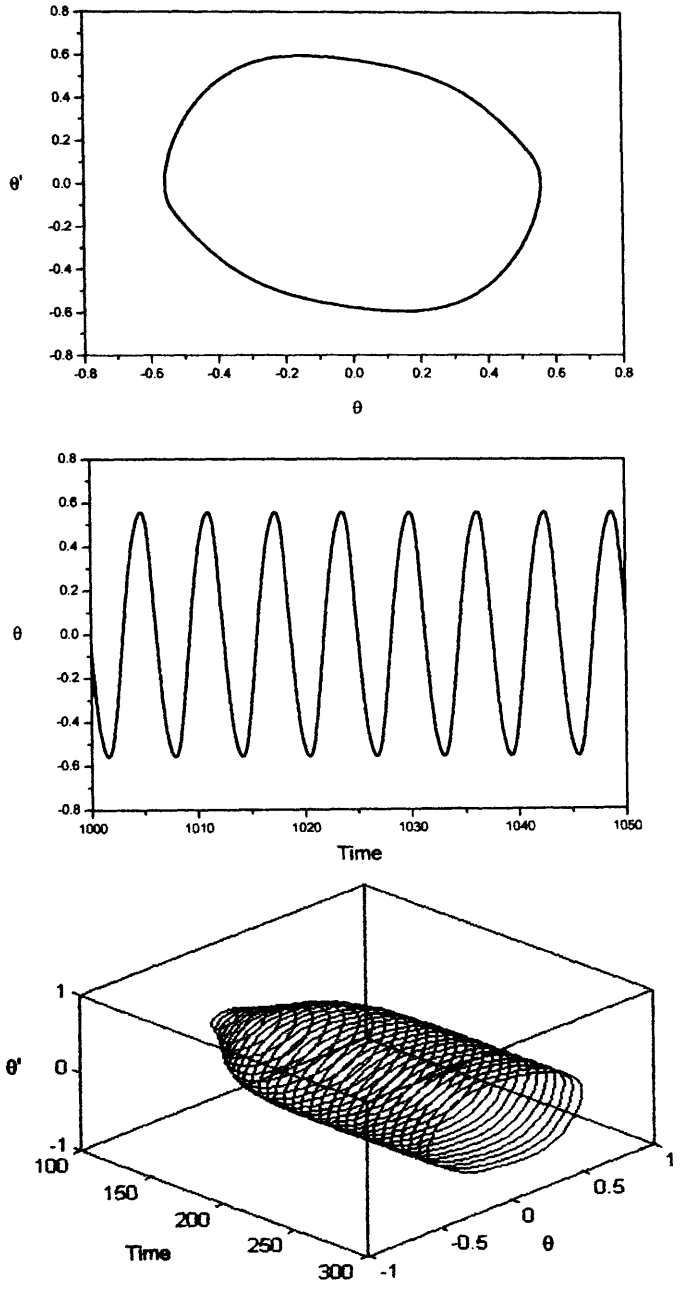

Figure 6.5: *Phase portrait and time series computed at the parameter settings noted at the bottom of the diagram. The three dimensional diagram manages to link both the phase plane and time history together.*

The phase plane diagrams show this limit cycle in (θ, θ') plane but may also be clearly observed by the time history diagram. We note further here that by choosing somewhat great damping coefficients leads to a greater separation of successive nodding paths, making them more easily distinguishable. This is also cited by Acheson within his study of the inverted single parametrically excited pendulum (Acheson, 1995).

Focusing back on Figure 6.3, we turn our attention to the case when ω_1 and ω_2 are both set to 2, so that the ratio of forcing frequencies is equal to 1 and under the same damping coefficients, natural frequency of the pendulum and second forcing excitation value, $q = 0.4$. The nature of bifurcations occurring are similar to the earlier chapters of the single parametrically excited pendulum model. We note that the red branches represent the second pair of asymmetric solutions being born after the symmetry breaking, pitchfork bifurcation at approximately $p \approx 1.2$. It is noted that the bifurcation diagram does not commence with a near $\theta = 0$ solution, (as in Chapter 3, Figure 3.2(a), for example), due to the initial forcing amplitude. This means that at $q = 0.4$, symmetric period-2 oscillations have already been exhibited so that their maximum amplitude response provide the initial starting condition amplitude displacement at $p = 0$. The period doubling leading to escape is also evident.

When the ratio of frequency excitation is 2 but with $\omega_1 = 2$ and $\omega_2 = 1$, the phase portraits and time series of Figure 6.7 verify the state of solutions at the specific forcing amplitude p and at $q = 0.4$. When $p = 0.2$, the pendulum experiences an initial oscillation which further decays as time evolves.

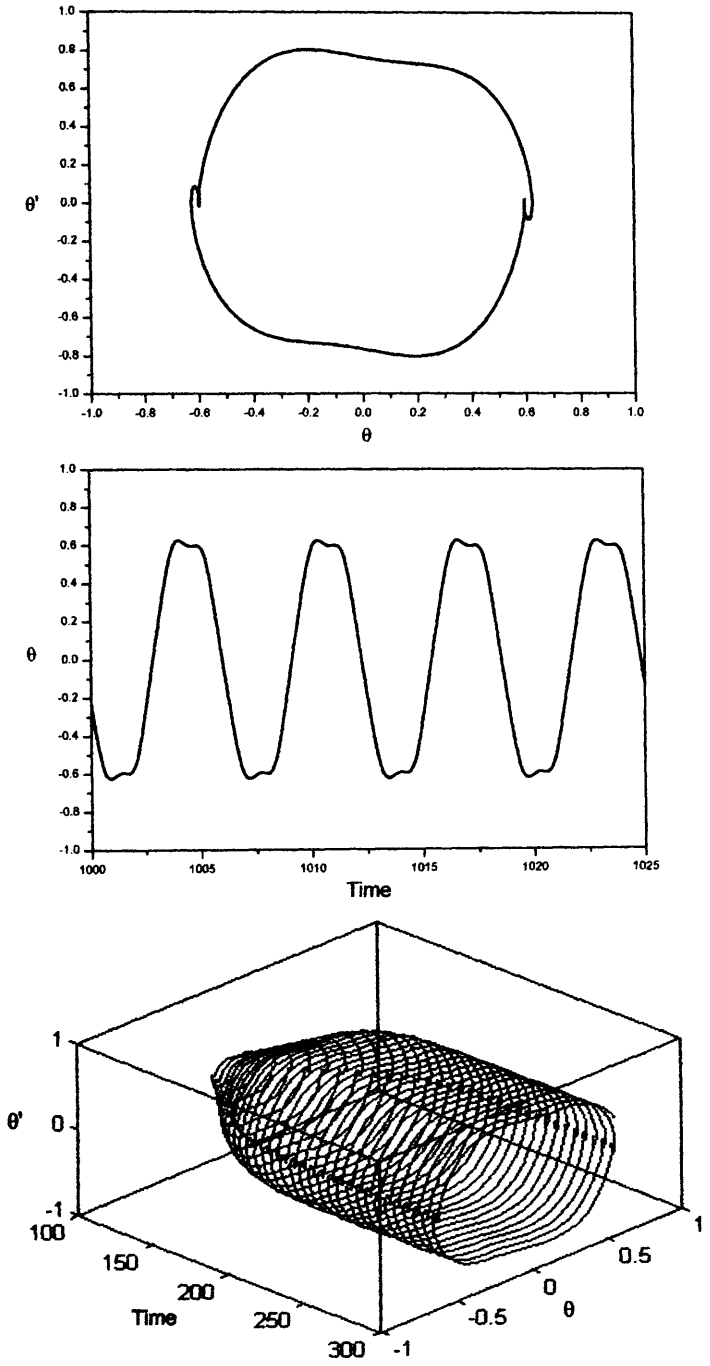

$\omega_0 = 1, \omega_1 = 4.0, \omega_2 = 2.0, \beta_1 = 0.1, \beta_2 = 0.2, p = 1.6, q = 0.4$

Figure 6.6: *Evidence of double nodding when the ratio of forcing frequencies is equal to 2. The other parameter settings are as noted on the figure.*

It is noted that at about $p \approx 0.3$, a period doubling is exhibited whereby asymmetric period-2 attractors are born. The middle set of phase portrait and time series portray asymmetic solutions of the system when $p = 0.8$. Since the system under these parameters is already asymmetric and following results from our previous Chapters, we mention with confidence that symmetry breaking, pitchfork bifurcation does not occur. The asymmetric orbits themselves then period double and contribute to the cascade of period doublings. The phase portraits and time histories chosen at $p = 1.25$ indicate this period doubling occurrence.

The shape of the bifurcation diagram at $\omega_1 = 1$ and $\omega_2 = 2$ in Figure 6.3 may seem unexpected at first instance, as it is dissimilar from the rest of the bifurcation diagrams. However, the nature of the bifurcation diagram at these forcing frequency values, may correspond to a bifurcation diagram computed over a variation of β around the second tongue region of the parametric perturbation of the augmented undamped Mathieu equation discussed within the previous section (equation (6.2.2)).

With the aid of appropriate transformation and substitution, for the case of no damping in equation (6.2.1), the forcing frequency $\omega_1 = 1$ corresponds to the tongue-tip centered around $\alpha = 1$ in the (α, β) parameter space. The fact that the bifurcation diagram begins with an amplitude oscillation that decreases in response with increasing p, becoming then stable at the equilibrium solution, $\theta = 0$, and then undergoing oscillatory type motions again which they themselves soon after undergo period doubling and chaos, corresponds in behaviour to the cross-over effect observed in the stability diagrams of the parametrically perturbed Mathieu equation.

It is important to mention that the study of the double parametrically excited

pendulum system with commensurate frequencies but more specifically under these frequency ratios, does possess nonlinear behaviour different in order and nature to that of the single forcing counterpart.

We remark that there still remains more rich material to be discovered within the proposed double forcing model, and we hereby invite researchers to investigate in greater detail this type of parametric forcing for this problem.

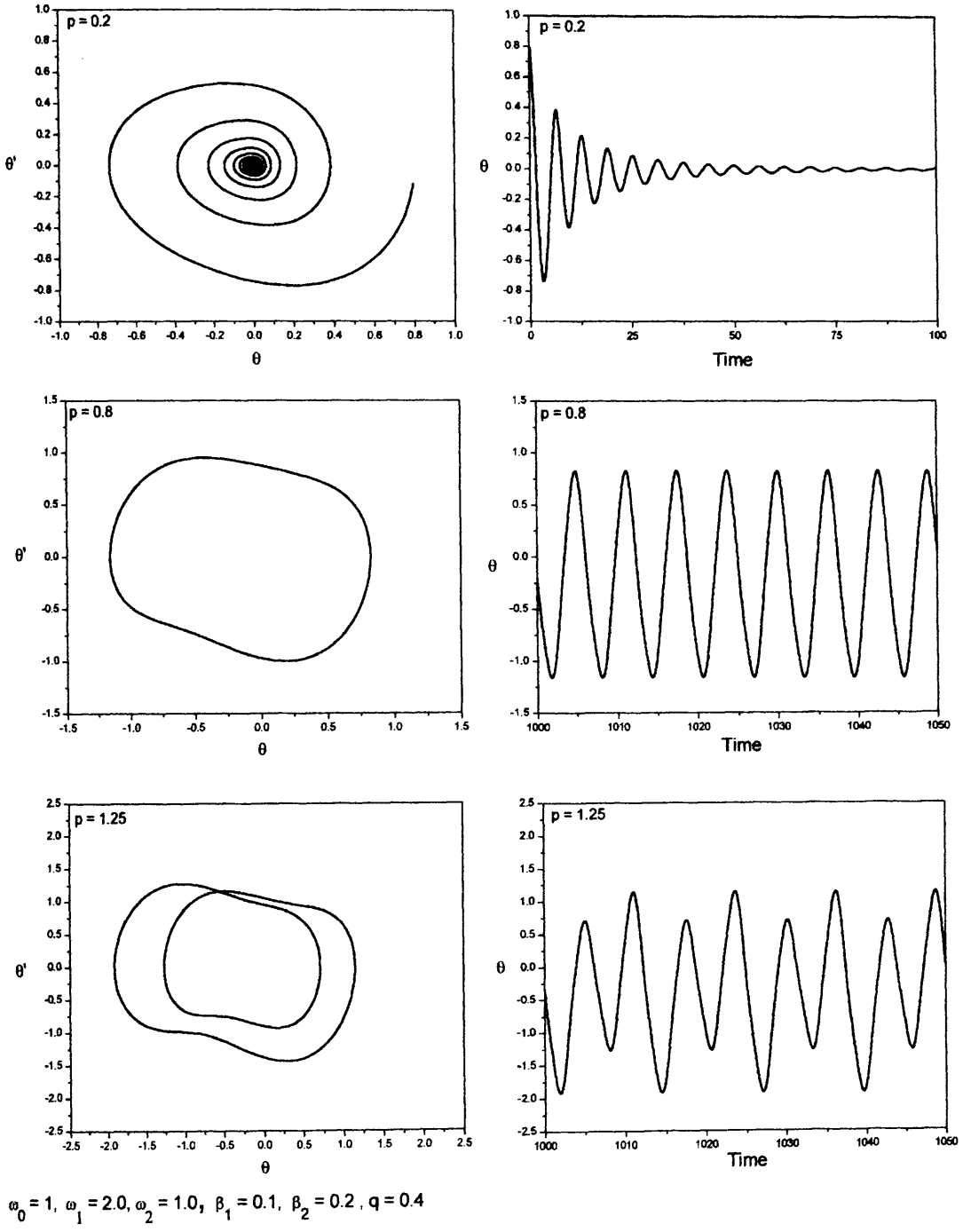

Figure 6.7: *Sets of phase portraits and time histories at different forcing amplitude p values whilst second forcing component* $q = 0.4$.

6.4 Quasiperiodic forcing

In the last two decades there has been increasing interest in studying the dynamic behaviour of quasiperiodically driven nonlinear oscillators from both the numerical and analytical points of view (Yagasaki, Sakata, Kimura, 1990, Zounes and Rand, 1996, Belhaq and Houssni, 1999, Guennon, Houssni, Belhaq, 2002). Attention has been focused on developing an analytical technique to construct approximations of quasiperiodic solutions and to analyse resonance phenomena and stability.

Chastell, Glendinning, Stark (Chastell *et al*, 1995) mention that one reason for studying quasiperiodically forced systems is that numerical observations suggest the existence of nonchaotic strange attractors in the parameter space. By a nonchaotic strange attractor we mean an attractor which is geometrically strange (fractal dimensional), but for which typical orbits on the attractor have non positive Lyapunov exponents as opposed to a chaotic attractor whose typical orbits on the attractor have a positive Lyapunov exponent (Grebogi, Ott, Pelikan and Yorke, 1984).

Belhaq, Guennoun and Houssni provided analytical quasiperiodic solutions to a weakly damped nonlinear quasiperiodic Mathieu oscillator near a double primary parametric resonance, namely the generating resonance $1:2$ and the so called "satellite" resonance (Belhaq *et al*, 2002). Their studies also showed very good agreement between analytical approximate quasiperiodic solutions and direct numerical integration from both the qualitative and quantitative aspects. The concordance of the results was obtained for both the amplitude versus time planes and the phase portraits of the quasiperiodic oscillations.

From a stand point of applications, it is important to study quasiperiodically forced systems such as equation (6.2.1) since often two or more external forces may act on

systems or even an external force has more than one frequency component.

Hence, one form of nonperiodic behaviour found quite naturally in nonlinear systems is quasiperiodicity (Davis and Rosenblat, 1980, Bergé, Pomedu and Vidal, 1984, Nayfeh and Balachandran, 1995, Rand and Hastings, 1995). This happens when more than one characteristic frequency is present in a system where the frequencies are incommensurate. Meaning that the frequency ratio is now irrational so that it cannot be expressed as a fraction. Equation (6.2.1) may serve as a one-mode model to mechanical systems subjected to two simultaneous additional parametric modulations having incommensurate frequencies (Belhaq *et al*, 2002).

In this section, we will again restrict our attention to numerical approximations of quasiperiodic solutions of the nonlinear damped quasiperiodic parametrically forced pendulum system.

We will briefly consider the response of the system to a quasiperiodic excitation input. The irrational frequency ratio we choose is on the basis of the *Golden mean* (Shenker, 1982, Ott, 1993), that is

$$R = \frac{(\sqrt{5}-1)}{2}.$$

A good reason as to why we choose the golden ratio for our numerical work is that when we approximate it by rational numbers, we find a useful pattern. The golden ratio R has a conveniently simple continued fraction. This is a number, λ, of the form,

$$\lambda = \cfrac{1}{a+\cfrac{1}{b+\cfrac{1}{c+\cfrac{1}{d+..}}}}$$

with $a, b, c, d \in \mathbb{N}$. In standard shorthand this is equal to $[a, b, c, d..]$ and it follows

that R can be expressed in the form [1, 1, 1, 1..] hence providing a straight forward approximation.

We choose to keep $\omega_1 = 2.0$ so that now $\omega_2 = \sqrt{5} - 1 \approx 1.23607$. For consistency, we let $q = 0.4$, $\beta_1 = 0.1$, $\beta_2 = 0.2$ and $\omega_0 = 1$. We firstly consider the ensuing motion when the forcing magnitude $p = 0$ and this case may be seen in Figure 6.8 and by the first set of phase planes and time histories. Numerically, this shows the existence of decay, which is however not monotonic due to the presence of forcing.

When $p = 0.4$ and $p = 0.9$, the response is typical for these quasiperiodic forcing values. The time series show a clear beat of two frequencies and the phase planes give an indication of some apparent randomness of the variability in these frequencies.

The time history plot at $p = 1.2$ does not show any repeating pattern in behaviour and what is more, is that the phase portrait indicates a strange attractor. It remains for us to determine if this is a strange nonchaotic attractor or a choatic attractor. More specifically, we suggest further that under these parameter conditions, the motion is a strange nonchaotic attractor and not a chaotic attractor. In order to enhance this suggesstion, we introduce Figure 6.9, which was numerically computed to examine the Lyapunov exponents of the system.

We mention firstly however, that in nonlinear dynamical systems, strange nonchaotic attractors are considered as complicated structures in phase space (see also bottom diagram of phase portrait in Figure 6.8), which is a property usually associated with chaotic attractors. The pioneering work of Grebogi *et al* (Grebogi, Ott, Pelikan and Yorke, 1984) revealed that there are some possibilities of strange attractors in certain types of dynamical systems that are not chaotic. These strange attractors are strange in the sense that geometrically they are strange (fractal dimensional) objects in phase space.

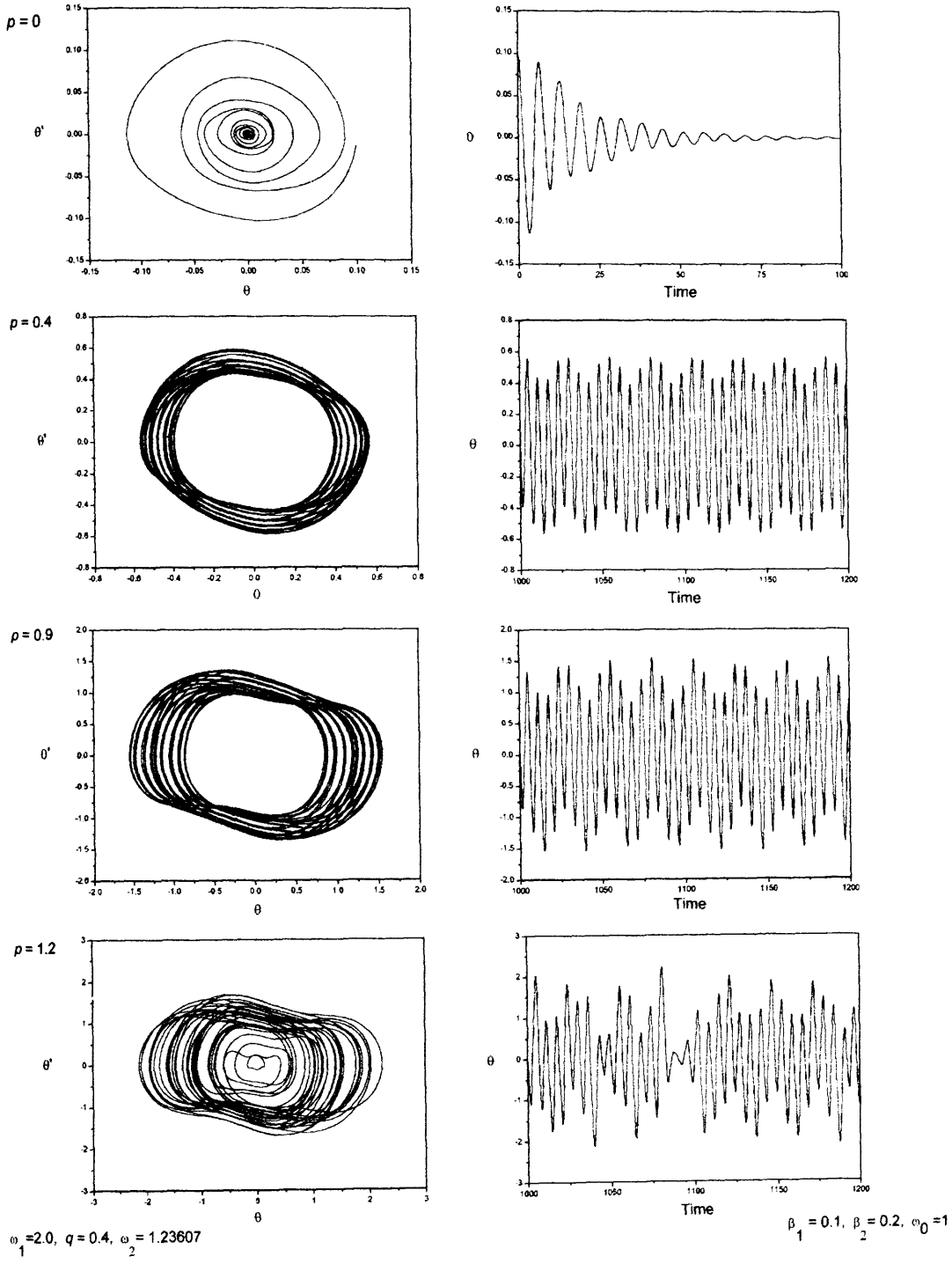

Figure 6.8: *Phase portraits and time series at the stated forcing amplitude for the quasiperiodic forcing system.*

Strictly speaking, strange nonchaotic attractors do not exhibit sensitivity to initial conditions so that if the Lyapunov exponents are negative then this implies that the attractors are not chaotic (Grebogi, Ott, Pelikan and Yorke, 1984). For the system (6.2.1), there are two Lyapunov exponents that are trivial in the sense that they are identically zero by virtue of the two excitation frequencies. The other Lyapunov exponents will either be negative, corresponding to two frequency quasiperiodic attractors or strange nonchaotic attractors, or positive to signify chaotic attractors.

Returning to Figure 6.9, each Lyapunov exponent has been allocated a colour and one may see that at $p = 1.2$, the Lyapunov exponents are negative (represented by green colour) and equal to zero (shown in black and blue colour), indicating that a strange nonchaotic attractor is present under these forcing amplitudes. Evidently after $p \approx 1.395$, chaotic attractors exist as one of the Lyapunov exponents becomes positive (shown in red).

We also remark that in Figure 6.9, the green elliptical inset shows in greater detail a focus of the Lyapunov exponent values between $1.0 \leq p \leq 1.39$ in order to show the fluctuation properties. These are small in magnitude such that under the original scaling of the figure, there is no easily visible variation from the horizontal green constant line.

In addition, Figure 6.10 and Figure 6.11 respectively, help to confirm that with these control parameters, quasiperiodic and chaotic behaviour is exhibited. This is shown not only with the time history plot but also with the aid of the frequency spectrum, where the frequency scale is in Hertz. For the construction of the Fast Fourier Transforms, a Hanning window was used and all the Fast Fourier Transforms were based on the position and range of the corresponding time series at each different p, ω_1, ω_2 value respectively.

Looking closely at Figure 6.10, considering firstly the top diagram with $\omega_1 = 2$ and one forcing amplitude $p = 0.8$, (in other words $q = 0$, $\omega_2 = 0$), we see that the time history and its corresponding frequency spectrum plot, shows that the system is undergoing a periodic motion with a single forcing frequency. Moreover, one can observe only one distinct peak in the frequency spectrum at 0.164 Hertz which corresponds approximately to a frequency 2 $rads/s$. We also note that the damping coefficients remain fixed at their usual values.

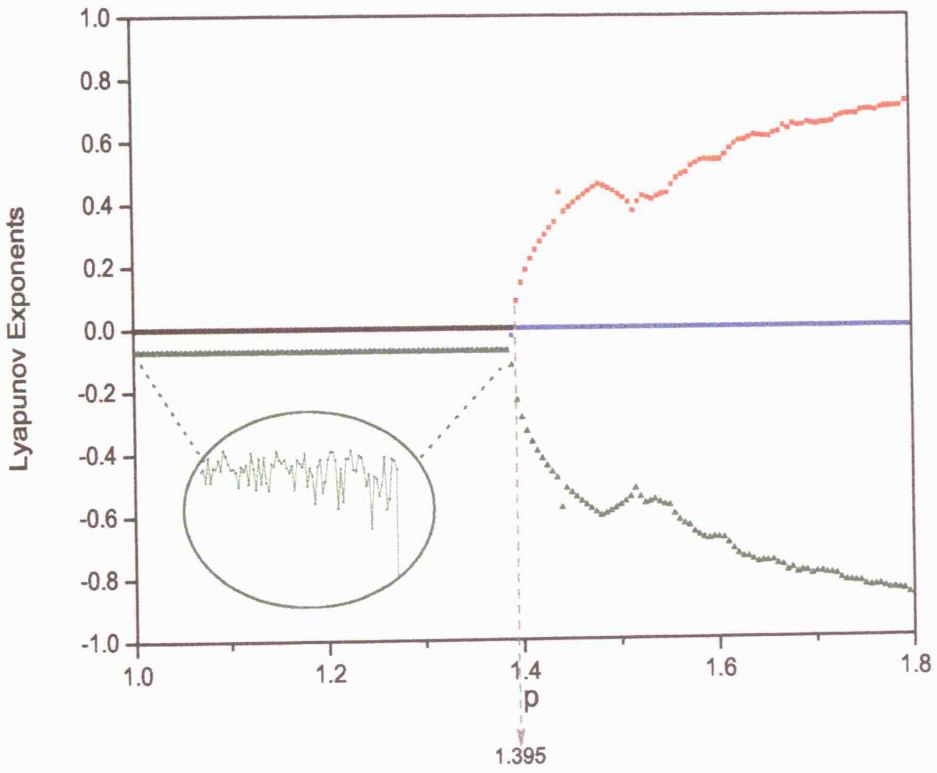

Figure 6.9: *Lyapunov exponents against forcing amplitude p at fixed parameter conditions,* $\omega_0 = 1$, $\omega_1 = 2.0$, $\omega_2 = (\sqrt{5} - 1)$, $\beta_1 = 0.1$, $\beta_2 = 0.2$ *and* $q = 0.4$.

In the bottom set of diagrams in Figure 6.10, the parameters are set at $p = 0.8, q = 0.4, \omega_1 = 2, \omega_2 = (\sqrt{5} - 1)$ where we reveal that the two forcing frequency terms are incommensurate. At these parameters, the time series is more complex than the top diagram in Figure 6.10, showing a quasiperiodic motion, where the corresponding frequency spectrum gives two distinct peaks and spikes.

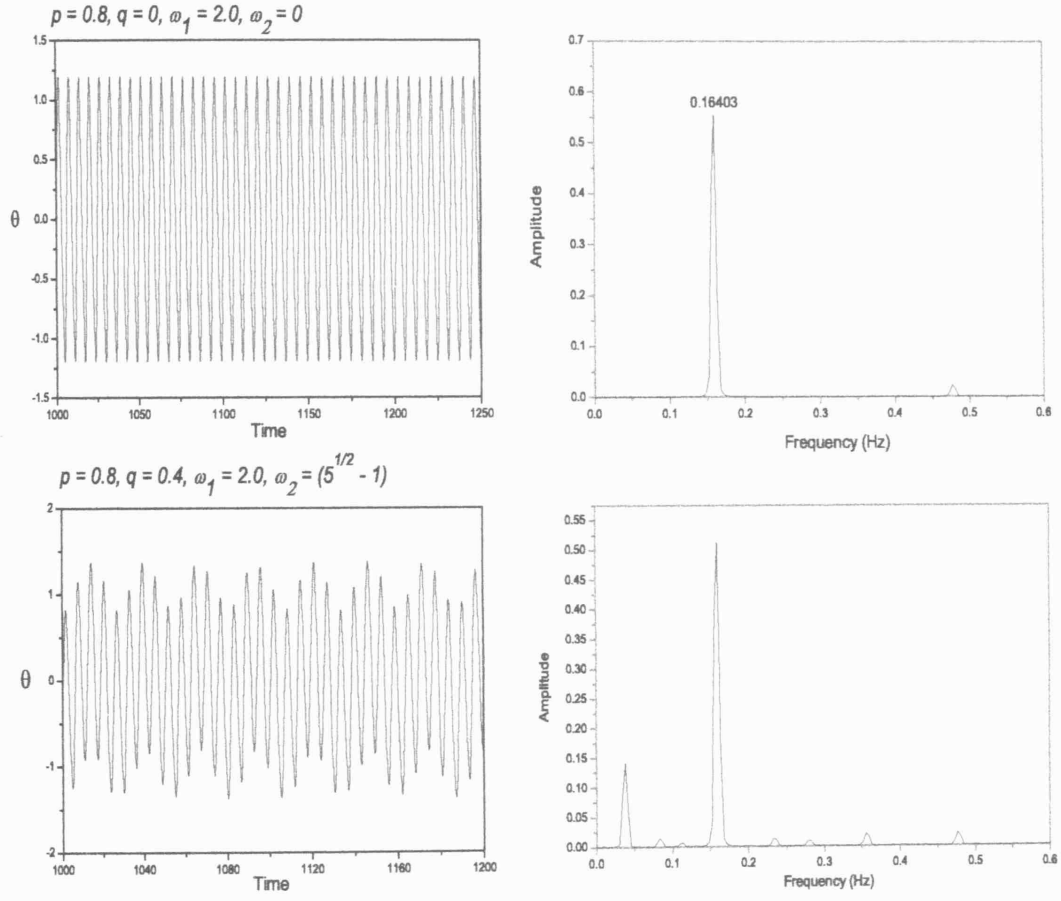

Figure 6.10: *Time histories and corresponding frequency spectra for the stated parameter conditions.*

At the same forcing frequencies but with a higher frequency amplitude, $p = 1.4$, Figure 6.11 depicts the time history plot as well as its corresponding power spectrum (as opposed to frequency spectrum). This time series seems to show an apparent chaotic motion whose corresponding power spectrum has a broad range of frequency distribution. We recall from Figure 6.9 that at $p = 1.4$, one of the Lyapunov exponents of the system is positive, strengthening our deduction that at this value of forcing amplitude the motion is unpredictable and chaotic.

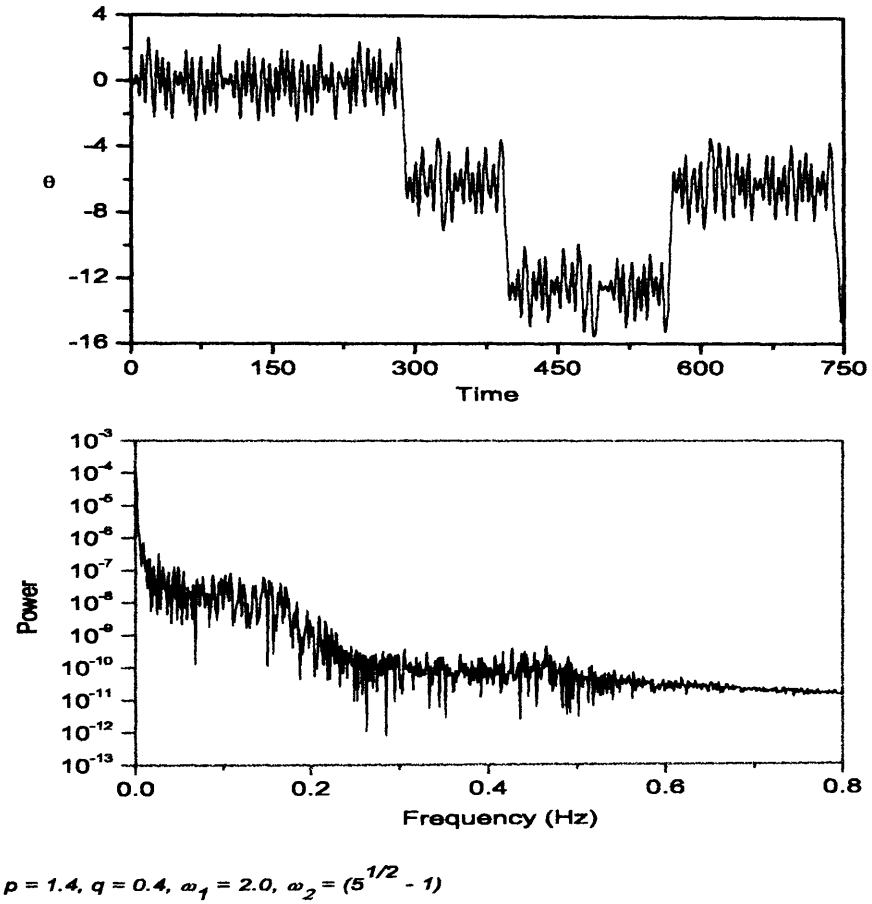

Figure 6.11: *Time history and corresponding power spectrum of the chaotic motion based on numerical model (6.2.1).*

Additionally, in Figure 6.12 we plot two phase plots and their associated Poincaré maps below them so that to portray an interesting feature. When the ratio is an irrational number, sampling at a period corresponding to ω_2, the map in the phase plane becomes a continuous closed orbit, as indicated by the red coloured Poincaré section in the right hand bottom diagram of the above respective phase portrait for when $p = 0.3$, $q = 0.4$, $\beta_1 = 0.1$, $\beta_2 = 0.2$, $\omega_1 = 2.0$ and $\omega_2 = \sqrt{5} - 1$.

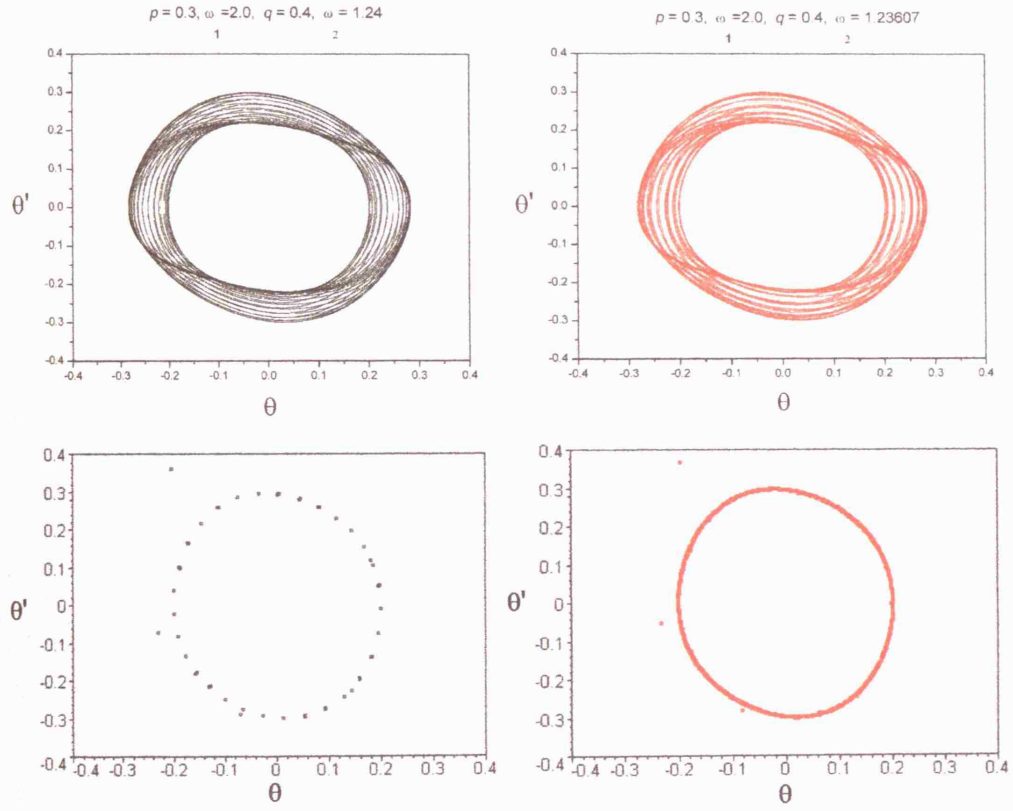

Figure 6.12: *Phase portrait and Poincaré section stroboscopically sampled at a period equal to* $\frac{2\pi}{\omega_2}$. *The black colour indicates commensurate forcing frequencies, and the red incommensurate.*

This motion is sometimes called almost periodic motion or "motion on a torus" and is not considered to be chaotic.

Quasiperiodic motions are imagined to take place on the surface of a torus or a doughnut-shaped figure in a three dimensional phase space, see Figure 6.13, where the Poincaré map represents a plane which cuts the torus (Moon, 1987). If ω_1 and ω_2 are incommensurate, the trajectories fill the surface of the torus.

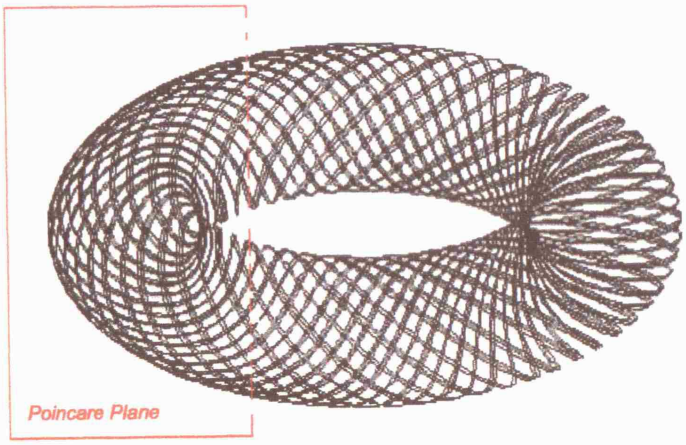

Figure 6.13: *Schematic of the two frequency forcing motion winding around the surface of a torus.*

As a comparison, we introduce also in black colour in Figure 6.12, the phase plane and Poincaré section for when the ratio of frequencies is rational. In other words,

$$\frac{\omega_1}{\omega_2} = \frac{2}{1.24} = \frac{50}{31}.$$

In this instance the trajectory on the torus will eventually close although it might perform many orbits in both angular directions of the torus before closing. The

Poincaré map will become a set of points arranged in a circle, as depicted by the black coloured Poincaré section of Figure 6.12.

We now turn our attention to the field of ship dynamics where in a fairly recent publication by Spyrou (Spyrou, 2000a, 2000b), he addressed briefly the behaviour of a ship under the effect of a wave group containing at least two independent frequencies. Otherwise known as bi-chromatic waves.

We mention that the encounter of such waves, could bring about a quasiperiodically changing restoring. We believe that the pattern of variation of time dependence under such conditions would be similar to our responses of time series for quasiperiodic parametric forcing, whereby a common characteristic may be expected.

6.5 Route to chaos

Previous Chapters showed with the aid of bifurcation diagrams that the period doubling phenomenon may act as a precursor for the route to chaos. In a symmetric system, the symmetry-breaking, pitchfork bifurcation which initiates the period doubling sequence of cascade leading to chaos may also be considered as a predictor for the route of chaos. The bifurcation diagrams hence examine the pre-chaotic or post-chaotic changes in a dynamical system under parameter variations. So while period doubling is the most recognised scenario for chaotic behaviour, there are also other schemes that have also been studied and observed.

We mentioned earlier that if ω_1 and ω_2 are incommensurate, the trajectories fill the surface of the torus. Chaotic motions are often characterised in such systems by the breakup of the quasiperiodic torus structure as the system parameter is varied (Moon, 1987).

Figure 6.14 visibly shows this type of route to chaos with the aid of Poincaré sections sampled stroboscopically at a period equal to $\frac{2\pi}{\omega_2}$ for a range of forcing amplitude p values and with the other control parameters fixed at $\omega_1 = 2.0$, $\omega_2 = (\sqrt{5}-1)$, $q = 0.4$, $\beta_1 = 0.1$, $\beta_2 = 0.2$ and $\omega_0 = 1$. With ω_1 and ω_2 incommensurate, the motion is not periodic but quasiperiodic and it is evident that as the forcing amplitude p is gradually increased, the closed curves of the Poincaré map that characterise a quasiperiodic motion, period double, become distorted, wrinkle, turn fractal and finally break the quasiperiodic torus structure resulting in chaos. Clearly, in the case of the Poincaré plot at $p = 1.4$ within this range of (θ, θ'), the Poincaré points form a scattered collection rather than a closed orbit. This fact reinforces our earlier argument that for this value of forcing amplitude, the motion is indeed chaotic.

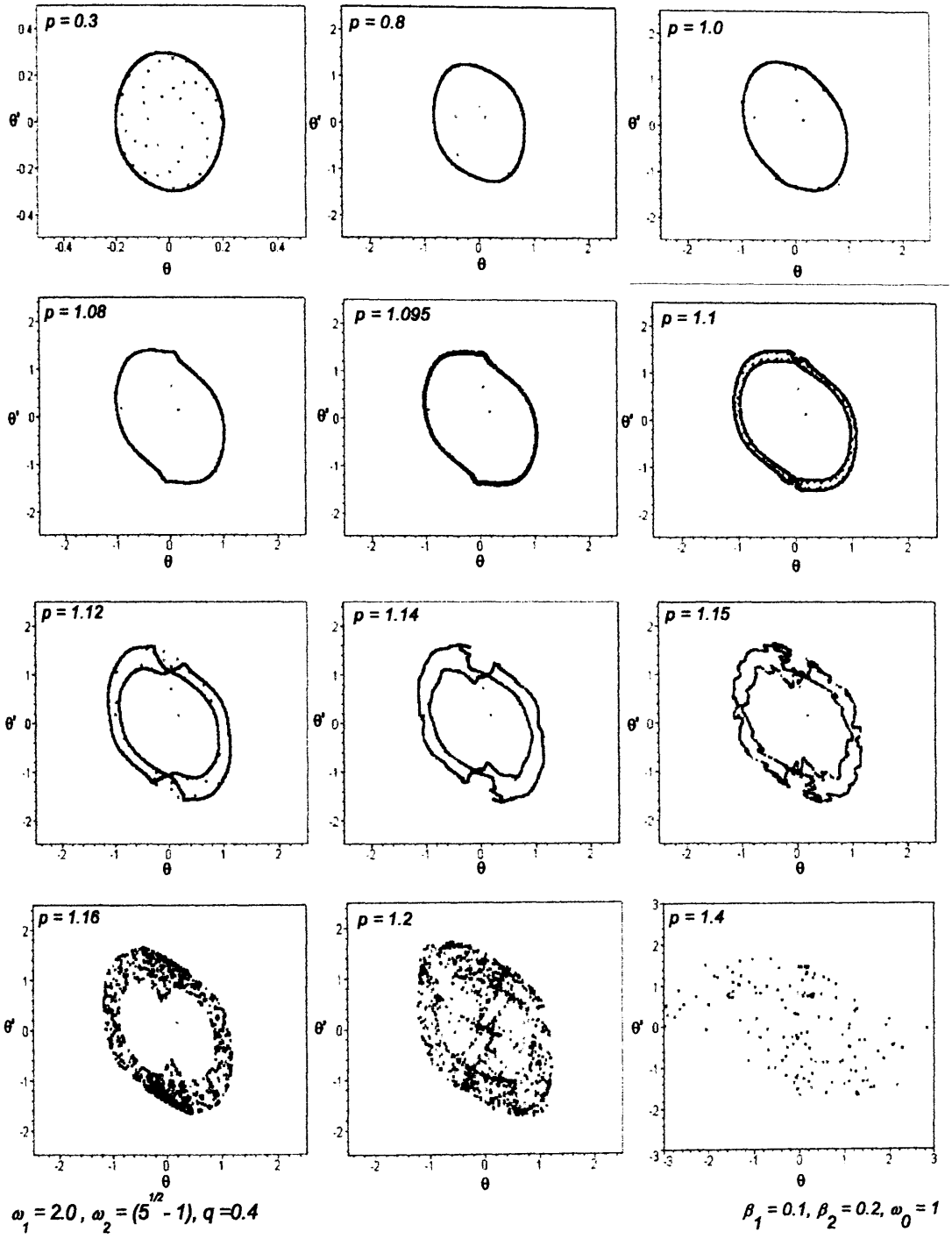

Figure 6.14: *Poincaré sections stroboscopically sampled at a period equal to* $\frac{2\pi}{\omega_2}$ *for a range of forcing amplitude p values at the stated control parameter conditions.*

Hence, in agreement to Moon (Moon, 1987), the Poincaré maps of chaotic motions often appear as a cloud of unorganised points in the phase plane.

Another route to chaos includes the scenario called *intermittency* (Kapitaniak, 1992, Yalcinkaya and Lai, 1996, Venkatesan and Lakshmanan, 1998). Here one observes long periods of periodic motion with bursts of chaos. This behaviour may also be seen in (6.2.1) but with different parameter choices. Hence, evidence of this within our quasiperiodically proposed system may be seen in Figure 6.15, which incorporates a time history and a three dimensional $(\theta, \theta', Time)$ plot for intermittent-type chaos. The conditions under which this phenomenon is undergone are $\omega_1 \approx 1.199$, $\omega_2 = 2.1$, $p = 2.0$, $q = 0.4$ and the usual values of $\beta_1 = 0.1$, $\beta_2 = 0.2$, $\omega_0 = 1$ apply. After the transient motion, the system experiences long periods of periodic motion with sudden chaotic bursts. We mention also that as a parameter is varied, chaotic bursts become more frequent and longer (Moon, 1987, Mullin, 1993).

Figure 6.16 is simply a more detailed three dimensional diagram of Figure 6.15, at a smaller time range, showing the first burst of chaos.

It should be noted that for some physical systems, one may observe all three patterns of pre-chaotic oscillations and many more depending on the parameters of the problem.

The benefit in identifying a particular pre-chaos pattern of motion with one of these now classic models, is that a body of mathematical work on each exists which may offer better understanding of the chaotic physical phenomenon under study.

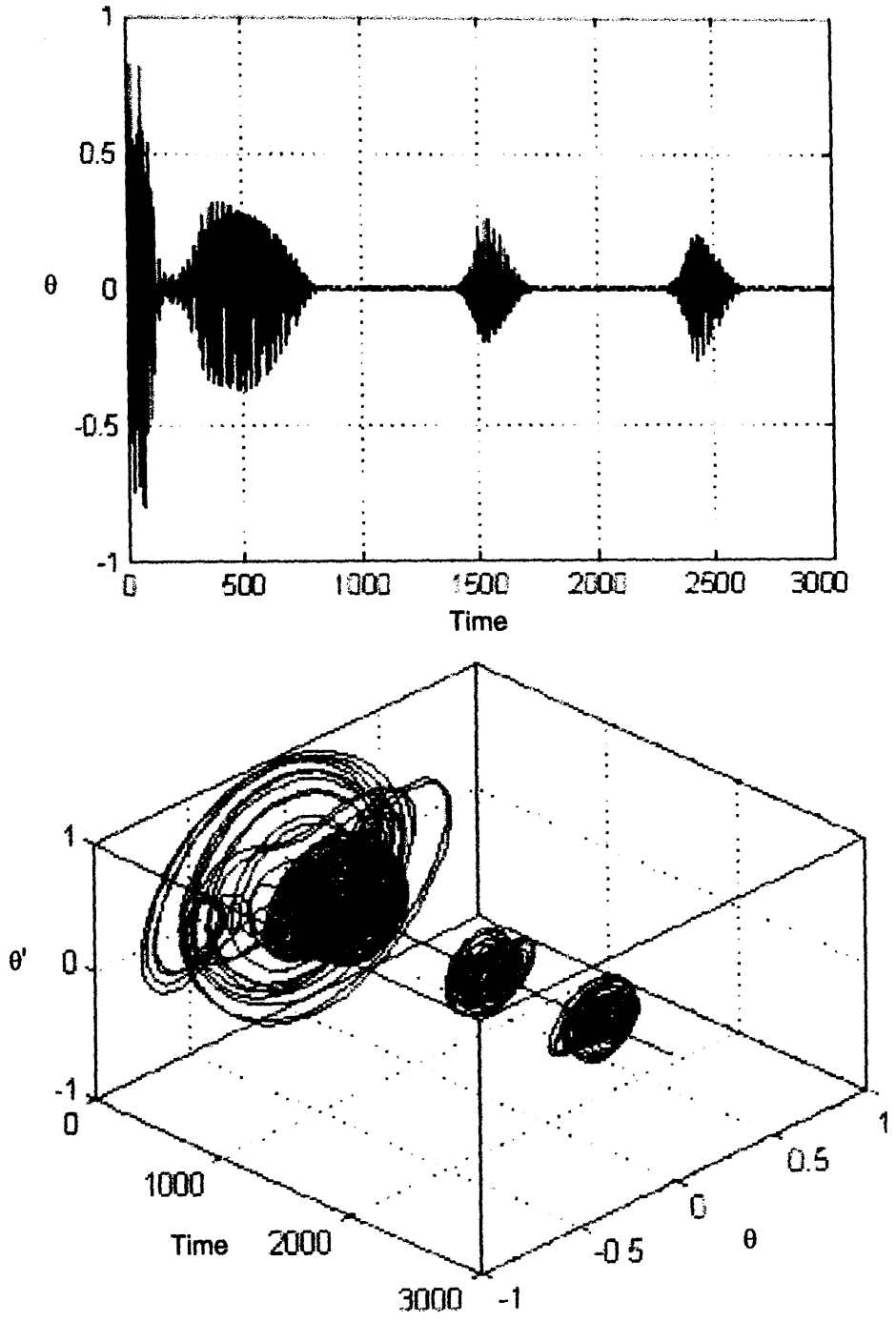

Figure 6.15: *Time history and three dimensional* $(\theta, \theta', Time)$ *plot for intermittent-type chaos.* $\omega_1 \approx 1.199$, $\omega_2 = 2.1$, $p = 2.0$, $q = 0.4$, $\beta_1 = 0.1$, $\beta_2 = 0.2$ *and* $\omega_0 = 1$.

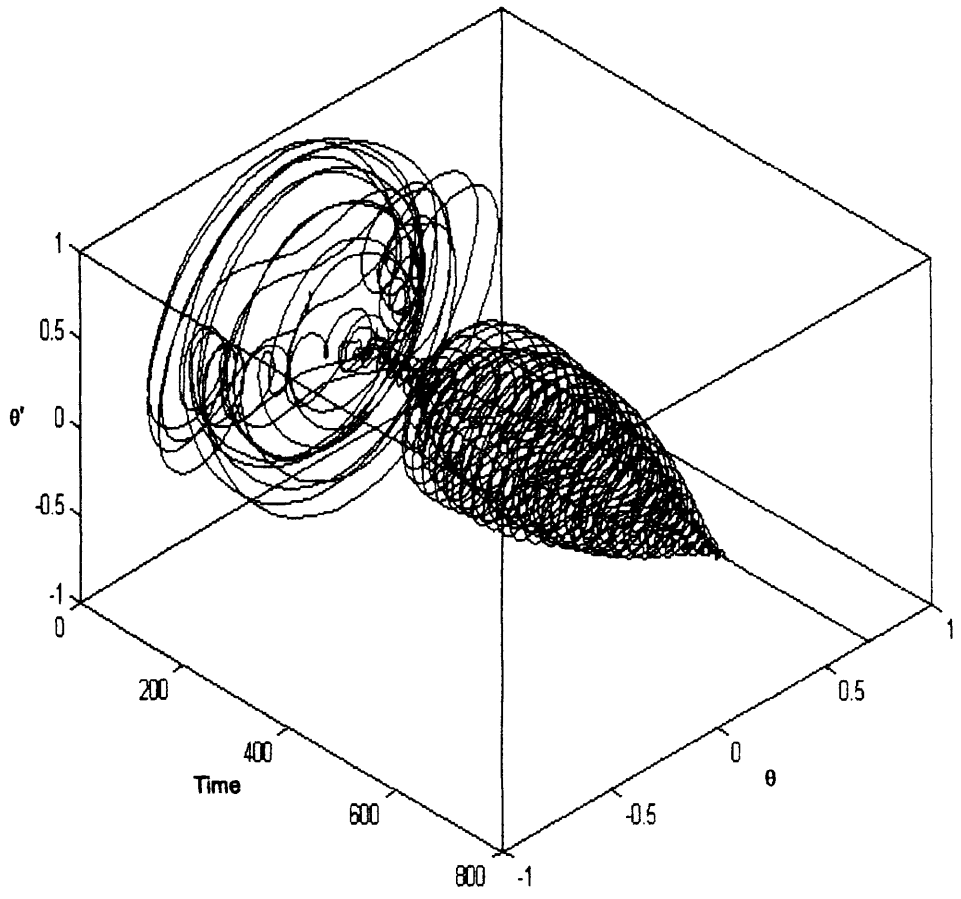

Figure 6.16: *Detailed focus diagram of Figure 6.15 but at a smaller time range, showing three dimensional* $(\theta, \theta', Time)$ *plot under the same parameter conditions.*

6.6 Final Remarks

In this Chapter we returned our attention to the parametrically excited pendulum system but we now progressed to oscillations which are acted upon by a combination of two parametric forces. We considered therefore what happens to the parametric pendulum model when subject to a two frequency combined excitation.

To provide an outline of the stability regions of our two forcing system, we considered briefly the undamped linear extended version of the Mathieu equation producing our own versions of stability diagrams as the control parameters vary. The effect was a modification on the shape of the parametric stability regions.

From the diagram we may visualise an increase and then a decrease in the area of stable region as one of the control parameters increases, giving an agreement with current research studies of the parametric perturbation of the Mathieu equation (Arrowsmith and Mondragón, 1999).

The key to determining the anticipated form of response of our proposed double forcing with nonlinear damping is whether the frequencies are commensurate or not. As a result, we initially considered a rational multiple between the forcing frequencies and produced a three dimensional plot portraying a combination of bifurcation diagrams computed over the variation of one of the forcing amplitudes at specific frequency ratios. The nature of the bifurcation diagrams and the route to escape was not always as expected. Phase portraits and time series are included to verify the response at certain parameter values.

The phenomenon of double nodding was also numerically exhibited for specific parameter conditions using time and phase portraits. Moreover, at a certain frequency ratio and forcing amplitude values, a bifurcation diagram was constructed

that showed correspondence to the cross-over of the stability tongue in the earlier illustration of the extended Mathieu equation.

The case of quasiperiodic forcing was also assessed but not in great depth due to time limitations. We found it necessary though, to still touch on this matter, since often two or more external forced may act on systems or even an external force may consist of more than one frequency itself.

Poincaré mapping, Fast Fourier Transforms and Lyapunov exponents were utilised to demonstrate quasiperiodicity and to determine the route to chaos under the given parameter conditions. Evidence of strange nonchaotic attractors were exhibited prior to the onset of chaos. The scenario of intermittency was incorporated and demonstrated under specific conditions via time history and phase space plots.

The results within this Chapter even though are worthy of further and deeper investigation, provide unique findings and alternative routes to chaos compared with the single vertically forced case. The parametrically double excitation pendulum has not yet, to the best of our knowledge, been examined and the purpose of familiarising ourselves with a double forcing excitation will become evident in the studies of Chapter 7.

Chapter 7

Parametric excitation and ship rolling: an experimental study

7.1 Introduction

Our interest in applying the parametrically excited pendulum model to the world of ship dynamics lead to our quest in collaborating with the Naval Architecture and Marine Engineering Research Group from the Mechanical Engineering Department of UCL, where research on a certain type of three-hulled vessel, called Trimaran, raised questions during their study of roll damping assessment. Their experimental data showed considerable scatter in an equivalent linear damping plot, especially at low angle roll, (detailed explanation follows within the next sections) making extraction of damping coefficients arduous and challenging.

The researchers proposed coupling between heave and roll during roll decay, and our skills were hence called upon to aid in discussing and verifying this behaviour via numerical simulations under a single degree of freedom equation. Our study of the parametrically excited pendulum system and the two frequency excitation, both

researched earlier within the thesis, showed relevance with their current work and the opportunity for us to show practical implementation and application to the field of ship dynamics was grabbed immediately.

For this to be achieved, our own analysis on one of the sets of their experimental data was necessary and permission of access to the data was granted. Therefore, this Chapter consists firstly of our own investigation into the trimaran roll decay experimental data where we also compare our findings with the recent outcomes of the Naval Architecture and Marine Engineering Research Group.

Moreover, the roll damping assessment for a trimaran vessel intrigued us and made us wonder if similar behaviour may be observed for the analysis of monohull roll decay tests. With this in mind, it was at this stage of our research that we felt it essential and crucial to undertake our own experimental investigation for a monohull model in order to produce an evaluation on the tests and resolve the skepticism on the matter of roll damping.

Previous attendance to a Conference held at UCL on Ship Dynamics, allowed us to come in contact with many researchers in this field and communication was resumed with the National Technical University of Athens, (NTUA), Greece. A research trip, funded by the UCL Graduate School (Research Project Fund) in conjunction with the UCL Mathematics Department, was organised with the aim and purpose of conducting our own roll decay tests on an existing newly designed monohull held at the NTUA laboratories. The second section of this Chapter consists of this investigation with the aspiration and intention of satisfying our curiosity.

Furthermore, in order to produce a useful application of the escape phenomenon and show the significance of Chapter 5, we conducted transient capsize tests on the monohull provided. Evidently, due to the danger of equipment becoming damaged,

actual capsize of the model was not permitted and so further on, the third section of this Chapter lies in analysing the transient roll motion (instead of the steady state roll) with the view of predicting capsize. We note also that we consider roll motion out of the six motions of a ship, (recall Figure 5.2), since it is the most critical motion leading to capsize and it has been attracting considerable attention over the years due to this reason.

Finally, since escape from the potential well of the parametrically excited pendulum system has been our major analytical and numerical concern of danger within a mechanical system, as seen in earlier parts of the thesis, it seems only logical to accomplish a link of this phenomenon with that to the analogous case of capsize in the field of ship dynamics.

7.2 Physics of Parametric Roll

Since the early fifties parametric resonance has been discussed and studied by several researchers and safety authorities in relation to ship dynamics (Kerwin, 1955, Paulling and Rosenberg, 1959). During the early nineties, adequate experimental data as well as numerical simulations appeared to confirm the possibility of ship capsize in following seas (waves arriving from the stern, back, of the vessel as opposed to heading seas which attack from the bow, front) or quartering seas (waves hitting the sides of the vessel at about forty-five degrees from behind) as a result of excessive roll amplitudes in the regime of wave induced parametric resonance.

Many disastrous outcomes occurring in the past to ships such as fishing vessels and small coastal cargo carriers have been experienced following unexpected extreme and violent ship motion relating them to the phenomenon of parametric roll resonance (France *et al*, 2003, Ribeiro e Silva *et al*, 2005). For instance, in October 1998, a post-Panamax C11 class (C11-corresponds to the type of ship design) containership traveling eastbound in the north Pacific from Kaohsiung (Taiwan) to Seattle, encountered extreme weather conditions and sustained extensive loss and damage to deck stowed containers. She carried a deck stow of some 1300 containers. The storm encounter lasted for about 11 hours, mostly at night. During the period of severest motions, port and starboard rolling of as much as 35 to 40 degrees was reported. About 400 containers were lost overboard and another 400 collapsed and crushed during these motions. The extreme waves were estimated to have reached 31 metres (France, Treakle, Moore, 2003).

The motions of the vessel during this storm event were investigated through a series of model tests and numerical analyses. These studies provide insights into the conditions in which containerships are likely to experience during head sea parametric

rolling and on the magnitude of motions and accelerations that may occur. Such analyses help to discuss how such extreme motions impact the design of a vessel and adjust the container securing systems (France *et al*, 2003).

In view of ship dynamics, parametric roll resonance is observed as a significant amplification of the roll motion in longitudinal (following and head) seas and it is related to the periodic change of stability, time varying restoring arm (variation in GZ curve, see Chapter 5 for further definitions), as the ship moves in waves at a speed when a ship's wave encounter frequency is approximately twice the rolling natural frequency and the damping of the ship to dissipate the parametric roll energy is insufficient to avoid the onset of a resonance condition. The simplest mathematical model of parametric excitation is the Mathieu equation and further the parametrically excited pendulum system we have studied within earlier chapters of the thesis.

In general, these stability variations are most pronounced in waves of length nearly equal to that of a ships length and consist of an increase in stability (GM or righting arm) when a wave trough is near the central part of the vessel, amidships, and a reduction in stability when a crest is in this position.

For clarification, we add below as Figure 7.1, a diagram taken from (France *et al*, 2003), showing the stability curves for the post-Panamax C11 containership referenced above. The figure illustrates the variation of the righting arm curve for this type of vessel in waves of length equal to that of the ship's length. The dashed curve corresponds to the righting arm curve in still water and denoted as such in cyan colour. The dotted curve corresponds to when the wave trough is amidship (labelled in light green colour) and the straight line curve when the wave crest is amidship (labelled using red colouring).

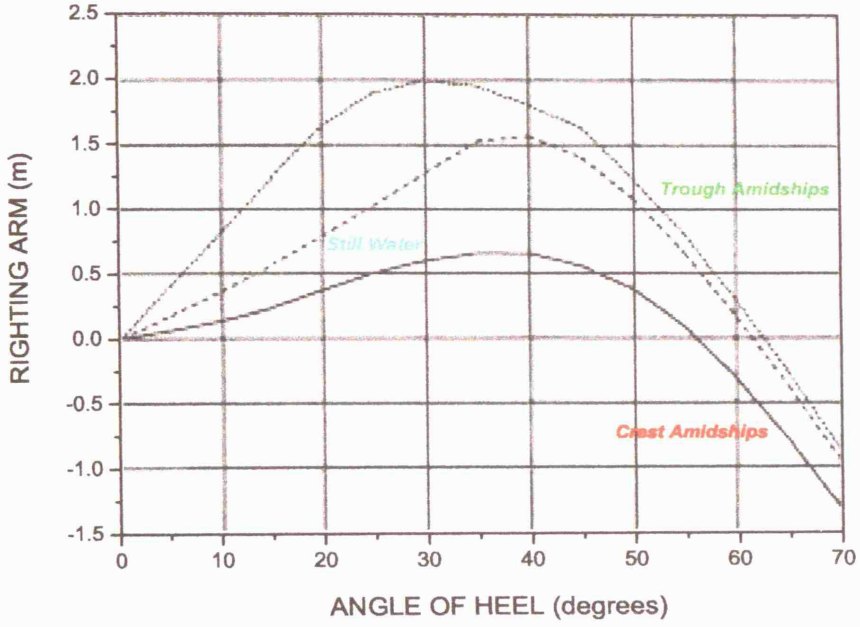

Figure 7.1: *Stability curves for post-Panamax containership (taken from France et al, 2003).*

The reason for this variation of stability with position of ship relative to wave profile may be explained by referring to Figure 7.2, which is our sketched version of the same monohull containership in waves and below an isometric view of the same ship (where the latter shaded hull form is also taken from (France *et al*, 2003)). If a typical containership is located on a wave trough amidships (so on the light green coloured wave), the average waterplane area width is significantly greater than in calm water. The full-formed parts of the bow and stern are more deeply immersed than in still water (in cyan). This makes the waterplane wider with the result that the GM is increased over the calm water value (see Figure 7.1). This has a direct relation to GZ since, the metacentric height GM is determined by the initial gradient of the stability curve GZ.

In contrast, when the ship is located with the wave crest amidships (on the red coloured wave), the immersed portion of the bow and stern sections are narrower than in still water. Consequently, the mean waterplane is narrower and the GM is correspondingly decreased in comparison to still water. Hence, the roll restoring moment of the ship will change as a function of the vessel's longitudinal position relative to the waves.

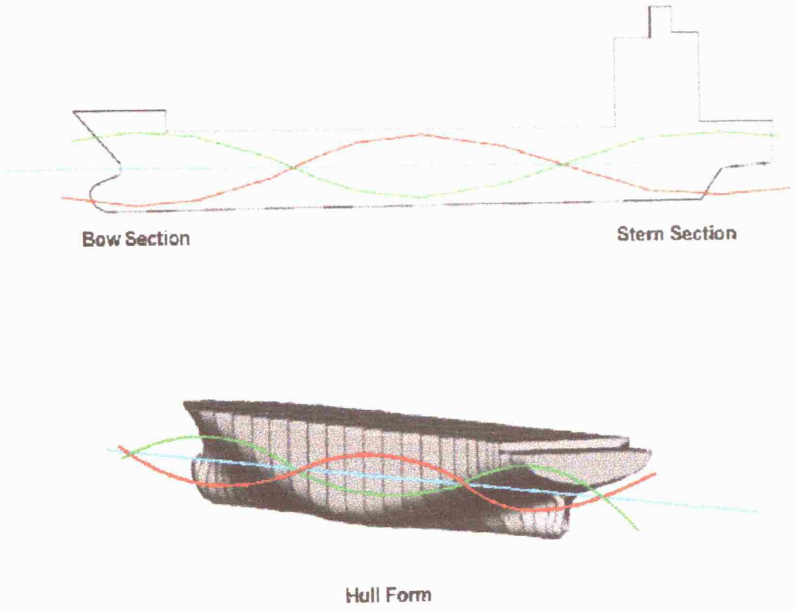

Figure 7.2: *On the top is a sketch of variation of waterplane area with ship length for a monohull on a wave. Below is an isometric view of the container ship with the corresponding wave forms taken from France et al (France et al, 2003).*

So factors such as the bow flare (the outward curvature of the bow's hull surface above the waterline) and the pronounced overhang stern, make the vessel more susceptible to parametric resonance. One may ask then, why do ship designers

not acknowledge these contributing characteristics and provide long term solutions, such as modifying the hull form so that the vessel has a better volume distribution along its length. However, to transport goods efficiently, modern containerships are designed for high service speeds necessitating a fine underwater body and in order to maximise carrying capacity on such a fine body, the deck is extended as far forward and back as possible. This results in a somewhat exaggerated bow flare and stern overhang.

From a mathematical point of view, briefly the three values which must be calculated for the study of ship stability are the longitudinal mass moment of inertia, the longitudinal second moment of area and GM (Derrett *et al*, 1984). GM is calculated from three characteristic values of the hull and the underwater volume, location of the centre of buoyancy from the bottom of a vessel, the keel, (KB), location of the centre of gravity from the keel (KG) and the distance between the centre of buoyancy and the metacentre (BM) as shown by

$$GM = KB + BM - KG.$$

Further, the distance BM is related to the second moment of area of the waterplane, I_{xx}, and the ship displaced volume, ∇:

$$BM = \frac{I_{xx}}{\nabla}$$

and thus variations in BM due to changes in waterplane area lead to alterations in GM.

So as the GM varies due to the different wave's longitudinal position along the ship, the GM may be considered as a periodic function with period T_e. In the first order approximation this variation may be modelled as a single sinusoidal function in time:

$$GM(t)_{(wave)} = GM_{(still)}(1 + \eta \cos \omega_e t)$$

where η is the fractional variation of GM due to waves and ω_e is the encounter wave frequency (Lee, 2000, Spyrou, 2000b, France *et al*, 2003). The equation of roll motion may be given by:

$$\varphi'' + b(\varphi)\varphi' + \omega_n^2(1 + \eta \cos \omega_e t)\varphi = 0 \qquad (7.2.1)$$

where ω_n represents the natural frequency of roll determined by $(\frac{mgGM_{(still)}}{I+A})^{\frac{1}{2}}$ (I is the moment of inertia and A is the added moment of inertia, as defined in Chapter 5).

Under a suitable substitution, the damped Mathieu equation may be recovered which we have examined in great detail within Chapter 2. It is well known that instability regions occur around the following frequency ratios (Stoker, 1950, Jordan and Smith, 1987):

$$\frac{\omega_e}{\omega_n} \approx \frac{2}{n} \qquad n = 1, 2, 3....$$

In terms of ship dynamics, the susceptibility to resonance or the frequency range for which a resonance is possible, is greater, i.e. frequency range is wider, for the case $n = 1$ than for others. For this reason, much of the bibliography on parametric roll resonance consider the particular case when $\omega_e \approx 2\omega_n$. So with the encounter period half the natural roll period, otherwise known as principal resonance, this the most significant regime that may easily lead to capsize.

It is also noted that a classical quadratic approximation of the damping moment may be considered in (7.2.1) in normalised form,

$$b(\varphi)\varphi' = b_1\varphi' + b_2\varphi'|\varphi'|$$

where b_1 and b_2 are linear and quadratic coefficients respectively and $b(\varphi)$ is an angle dependent roll damping coefficient per unit inertia. The $\varphi'|\varphi'|$ ensures that when φ' changes sign, this term also changes sign so that the damping moment will always oppose the roll motion. The damping damps or dissipates the energy of the motion (Shin *et al*, 2004). Nonlinear damping composed from a linear and cubic model may also be alternatively considered as will be discussed later on.

Earlier Chapters allowed us to study and examine parametric resonance. We mentioned above that in ship dynamics, parametric resonance may be brought upon by parametric excitation due to periodic changes of the coefficients in the rolling equation, where we noted a possible reason of such changes is the restoring arm variation in longitudinal waves. Other causes however for parametric excitation may also be considered such as coupling between roll and heave and between roll and pitch motion.

It has been known from the time of Froude (Froude, 1863), that the coupling between heave and roll may result in unstable ship motion. The phenomenon was investigated, (not in great depth), experimentally and theoretically by Paulling and Rosenberg (Paulling and Rosenberg, 1959) for a ship undergoing forced oscillations in heave with an initial roll angle. The instability is related to the geometrical properties of a ship, the location of center of gravity and the amplitude of the heave motion. This instability in roll is most likely to occur at the heave resonance frequency ω_h, when the heave amplitude is sufficiently large.

Despite evident differences between these sources of parametric excitation, the outcome remains the same; a significant increase in rolling motion in longitudinal or

quartering seas where wave excitation is small. The phenomenon of coupling between roll and pitch or heave, is described by the same rolling equation with a periodic coefficient, such as (7.2.1). The only difference is how to determine the amplitude of the parametric excitation from variation of the GZ curve in longitudinal seas or from coupling between roll and heave or pitch (Liaw *et al*, 1993, Liaw and Bishop, 1995, Belenky and Sevastianov, 2003).

With the growing awareness of the parametric roll phenomenon, there is corresponding growing interest in the use of roll control devices to mitigate parametric roll. Since parametric roll, like all parametric oscillations, has an excitation threshold that must be overcome in order for the phenomenon to exist, a natural way to lessen parametric roll would be to decrease the excitation below the threshold, by creating an opposing roll moment. The opposing roll moment could be generated by anti-rolling fins, water motion in tanks, moving mass systems or rudder deflection.

In the current studies of Belenky *et al* (Belenky, Weems, Paulling, 2003) they consider a large, modern containership fitted with a U-tube anti-rolling tank which appears to have a great deal and promise in the mitigation of the large roll motions caused by parametric roll. We add however, that the optimisation of such a system for maximum benefit at minimum cost will require a fairly sophisticated simulation system coupled to advanced probabilistic methods.

7.3 Determination of Roll Damping coefficients

Prediction of ship roll damping from first principles with satisfactory engineering accuracy still remains beyond reach for contemporary theoretical approaches of ship hydrodynamics (Spyrou, 2004). While there is some hope that modern computational fluid dynamics techniques will soon be able to provide acceptable predictions of roll damping coefficients, in current simulation studies there is still reliance on semi-empirical formulae for the damping components such as frictional, eddy making and lift damping. These are damping components that contribute to the total roll damping formulation. Frictional damping is caused by skin friction stress on the hull surface of the ship as the ship rolls, eddy making damping is caused by pressure variation on the hull due to flow separation at the bottom of the ship and lift damping occurs in roll in the form of a lift moment. But until these novel methods are readily available, researchers rely on roll decay coefficients determined from either forced or free roll decrement experiments.

For the former, forced roll decay experiments, a pure sinusoidal roll moment is applied to a ship model and the resultant steady roll amplitude and phase difference are recorded along with the forcing moment amplitude and frequency. The test is repeated over a range of forcing moment amplitudes so that results are obtained for different roll amplitudes.

Obtaining roll damping coefficients from a free roll decrement experiment is accomplished when a model is given an initial heel angle in calm water, at zero speed, and then allowed to roll freely so that the resulting decaying roll motion is measured. The models roll motion will decay at the damped natural frequency.

Using these model results and taking the assumption that in both cases pure roll

motion has been recorded, that is that roll motion is not coupled with surge, sway, heave, pitch or yaw, the roll damping coefficients may be calculated. Spouge (Spouge, 1988) gives a review of methods that are available for obtaining these coefficients from either free or forced rolling experiments for an uncoupled equation of roll motion.

Parameter Identification Techniques may be used to determine the constant coefficients of the equation of motion and these methods use the complete roll angle response time history. These techniques have been discussed by Roberts, Kountzeris and Gawthrop (Robets *et al*, 1991), Contento, Francescutto and Piciullo (Contento *et al*, 1996) and Francescutto and Contento (Francescutto and Contento, 1999).

The method however that we shall employ to analyse the adopted trimaran experimental data and our own monohull experimental free decay tests is reviewed in the section that follows. Free roll decay was chosen, as opposed to forced roll decay, as this way is more practical and in the case of our experimental monohull investigation, the method was more achievable under the experimental apparatus provided; the reason being that a special rig is required for the forced roll decay whereby the model is fitted to a carriage in a towing tank to conduct experiments at forward speed. As a result, we add that it was beyond the capabilities of the testing facilities at NTUA to perform forced roll decay experiments.

The quadratic damping model is mainly accredited to Froude (Froude, 1863) and this formulation has been widely used and also adopted here within. Haddara (Haddara, 1971) introduced the cubic model to overcome analytical difficulties arising from the use of the quadratic form where the solution to the equation of motion is more complex, see for example Mathisen and Price (Mathisen and Price, 1984). The choice of selecting a suitable damping model is not a simple task. It can be affected

by hull shape, ship speed, the total damping and the portion of the decay history where the analysis is to be performed on.

A literature search shows that the quadratic model was preferred over the cubic by Mathisen and Price (Mathisen and Price, 1984), Roberts (Roberts, 1985), Renyuan (Renyuan,1986) and Spouge (Spouge, 1988). All of them reported a better correlation with their experimental data.

The quadratic and the cubic damping models were both investigated by Chan, Xu and Huang (Chan *et al*, 1995). They showed adequate results using both models when a nonlinear roll restoring moment was employed and large initial roll angle induced.

Francescutto, Nabergoj and Hsiu (Francescutto *et al*, 1991) and Bulian (Bulian, 2005) at the University of Trieste, prefer a cubic damping model based on their research on large amplitude rolling. Cotton and Spyrou (Cotton and Spyrou, 2001) conducted research into ship capsize and model experiments on a prismatic ship section including free decay. They initiated the free decay by releasing the model at the angle of vanishing stability, around 38 degrees. At this large initial heel angle, they found that a cubic damping model provided the best fit to the experimental data. They realised that in looking at their experimental data, a quadratic model would produce an adequate fit to the decay for roll amplitude below 20 degrees.

What we may deduce from this literature review is that at present one model does not serve a better purpose than the other. The quadratic model is the longest established and the most commonly used. It would further seem that it provides a better fit than the cubic model when the roll amplitude is moderate.

7.3.1 Roll damping assessment

The damping coefficients are obtained from free roll decay tests where both the model types of ship, trimaran and monohull, are initially inclined at an angle of heel and then released and let to roll freely under calm water, with no forward speed. The resulting roll angles are to be recorded.

In the case of limited number of cycles of roll decay traces, the energy balance is a traditional approach and explained and adopted within this chapter. The method is based on the idea that the rate of change of the total energy in roll motion is equal to the rate of energy dissipated by the roll damping (Spouge, 1988).

7.4 Relations between equivalent linear damping and nonlinear coefficients

The analysis method makes use of a single degree of freedom equation for roll motion under an external exciting moment in calm water, see Chapter 5 equation (5.2.1) but with H set to zero, so that we are dealing with a symmetric equation of motion.

The equation of motion may be expressed in a normalised form as:

$$\varphi'' + b(\varphi)\varphi' + c(\varphi)\varphi = f(t) \tag{7.4.1}$$

with $c(\varphi)$ equivalent to the roll stiffness coefficient per unit inertia, or otherwise $\frac{mgGZ(\varphi)}{(I+A)\varphi}$, which is similar to Chapter 5 equation (5.2.1), but with differences in the damping terms and symmetry. $f(t)$ is the forcing moment per unit inertia, which is time dependent.

Equation (7.4.1) may also be expressed as an equivalent linear equation of motion by

$$\varphi'' + b_e(\varphi_a)\varphi' + c_e(\varphi_a)\varphi = f(t) \tag{7.4.2}$$

where $b_e(\varphi_a)$ is roll amplitude, φ_a, dependent equivalent linear damping.

Further, an equation of forced motion in normalised form:

$$\varphi'' + b_1\varphi' + b_2\varphi'|\varphi'| + c(\varphi)\varphi = f_a \cos\omega t \tag{7.4.3}$$

which produces the roll motion:

$$\varphi = \varphi_a \cos(\omega t + \epsilon)$$

where φ_a corresponds to the maximum sinusoidal amplitude and ϵ a phase angle, may be expressed in the equivalent linear form:

$$\varphi'' + b_e(\varphi_a)\varphi' + c_e(\varphi_a)\varphi = f_a \cos\omega t \tag{7.4.4}$$

where it is ensured that each term absorbs energy at the same rate in both equations. By definition, the total work done for angular displacement is the area under a torque displacement graph (Kreyszig, 1999), so that,

$$Work \quad Done = \int Torque \quad d\varphi.$$

Hence, the energy absorbed by a moment M in a quarter cycle, so that maximum amplitude φ_a, is an upper limit is

$$Energy = \int_0^{\varphi_a} M \, d\varphi$$

which by change of variable and suitable substitution becomes:

$$Energy = \int_0^{\frac{\pi}{2\omega}} M\varphi' \quad dt.$$

The energy dissipated, $Energy_D$, in a quarter cycle for the quadratic model for the damping term is

$$Energy_D = \int_0^{\varphi_a} (b_1\varphi' + b_2\varphi'|\varphi'|) \, d\varphi$$

and similarly like above and by change of variables,

$$Energy_D = \int_0^{\frac{\pi}{2\omega}} b_1\varphi'^2 + b_2\varphi'^2|\varphi'| \quad dt.$$

Substituting for φ and then integrating with respect to dt gives

$$Energy_D = \frac{\pi}{4}\varphi_a^2\omega b_1 + \frac{2}{3}b_2\varphi_a^3\omega^2. \tag{7.4.5}$$

The energy dissipated by the equivalent linear term at this amplitude is

$$Energy_D = \frac{\pi}{4}\varphi_a^2\omega b_e \tag{7.4.6}$$

and so by equating (7.4.5) and (7.4.6), a relation between the equivalent linear damped and the damping coefficients, b_1 and b_2 is reached:

$$b_e = b_1 + \frac{8}{3\pi}b_2\omega\varphi_a. \tag{7.4.7}$$

Similar analysis may be used to obtain the following expression for the cubic damping model:

$$b_e = b_1 + \frac{3}{4} b_3 \omega^2 \varphi_a^2. \tag{7.4.8}$$

To receive decaying oscillation data from an experiment it is assumed that the forcing moment is, by definition, zero and that the model ship always rolls at its damped natural frequency. The model's restoring properties are assumed to be broadly linear, so that only the successive peak amplitudes need be recorded. One of the most popular methods for analysing free decay experimental data is the *quasi − linear method.*

This is simply a linear analysis of the experimental decay of the peaks of the roll decrement time history used to determine at various points in the decrement. In the quasi-linear method, the damping is measured over half of a roll cycle. The motion of this free decay of the equivalent linear equation of motion, may be expressed as:

$$\varphi(t) = \varphi_s e^{-\frac{b_e t}{2}} \cos(\omega_n t + \epsilon).$$

The peaks (positive and negative) occur at $t = \frac{r\pi - \epsilon}{\omega_n}$, with $r = 0, 1, 2..$, so that the exponentially decaying amplitude of the roll, called the amplitude envelope, is at

$$\varphi_a = \varphi_s e^{-\frac{b_e t}{2}}.$$

We note that throughout this Chapter when referring to successive peaks, we imply that the negative peaks have been reflected in the time axis so as to become positive, so that the successive peaks over half a roll cycle occur at

$$\varphi_r = \varphi_s e^{-\frac{b_e (r\pi - \epsilon)}{2\omega_n}}.$$

The ratio of two successive peaks is the following

$$\frac{\varphi_r}{\varphi_{r+1}} = \frac{\varphi_s e^{(-\frac{b_e r\pi}{2\omega_n} + \frac{b_e \epsilon}{2\omega_n})}}{\varphi_s e^{(-\frac{b_e (r+1)\pi}{2\omega_n} + \frac{b_e \epsilon}{2\omega_n})}}$$

which reduces to,

$$\frac{\varphi_r}{\varphi_{r+1}} = \frac{1}{e^{-\frac{b_e \pi}{2\omega_n}}}$$

which is also equal to

$$\frac{\varphi_r}{\varphi_{r+1}} = e^{\frac{b_e \pi}{2\omega_n}}.$$

Thus producing the logarithmic decrement of free decay

$$ln(\frac{\varphi_r}{\varphi_{r+1}}) = \frac{b_e \pi}{2\omega_n}.$$

Re-arranging,

$$b_e(\varphi_\alpha) = \frac{2\omega_n}{\pi} ln(\frac{\varphi_r}{\varphi_{r+1}}) \tag{7.4.9}$$

for half a roll cycle. φ_r, φ_{r+1} are successive peak amplitudes, ω_n is the damped natural frequency and recalling that b_e is the equivalent linear roll damping term per unit roll inertia and added inertia.

The appropriate amplitude, φ_a is taken as the mean of the two successive peaks, so that

$$\varphi_a = \frac{\varphi_r + \varphi_{r+1}}{2}.$$

A linear least square fit method is usually used to fit the theoretical form for linear and quadratic damping, (7.4.7) at damped natural frequency ω_n, in order to determine the damping coefficients of b_1 and b_2.

7.5 Trimaran Investigation: Roll damping assessment

Current research work is being undertaken at the Naval Architecture and Marine Engineering Research Group of the Mechanical Engineering Department of UCL with the collaboration of QinetiQ, on Trimaran ships (three hulled vessel) with the purpose of investigating the roll motion of these multihull vessels and to develop comprehensive and validated theories for the prediction of trimaran roll damping fitted both with and without appendages. We mention here that the concept of the trimaran ship is based upon a ship with a centre hull, supported by two slender side hulls which provide the necessary stability in roll to keep the ship upright. The three hulls are joined together by a cross-structure that may incorporate one or more internal decks depending on the size of the vessel (see Figure 7.3).

One of the aims of fellow researcher Grafton (Grafton, *preprint PhD Thesis*, 2006) is to understand the nature of roll motion of a trimaran at zero speed in calm water through simulations and model experiments focusing on determining if roll couples with heave. Parts of his research investigated two sets of roll decay experiments conducted on a trimaran model from which roll decay coefficients were obtained. These coefficients were derived making an assumption that a single degree of freedom uncoupled roll equation with constant coefficients adequately defines the motion.

Collaboration and access was granted by the department of Mechanical Engineering and QinetiQ to conduct our own analysis on one of the sets of experimental data in order to compare and verify their own findings and for this permission we are grateful. In addition though, the data has also been used previously by the authors Grafton, Zhang and Rusling (Grafton *et al*, 2004) for roll analysis work.

The model represents a 22.4:1 scale trimaran frigate and the particulars of the model are shown below in Table 7.1 for the set of experiment that was provided to us. Moreover, the model experiments of this trimaran model were conducted in the Ocean Basin at QinetiQ's Haslar facilities in Gosport, U.K.

	Trimaran	Model
Length Overall (m)	160.20	7.15
Beam(m)	30.4	1.36
Draught (m)	5.20	0.23
Mass	4893.84(tonnes)	424 kg
GM	3.14 m	0.14 m
Natural Roll Period (secs)	10.65	2.21
Natural Roll Frequency	0.59 $rads^{-1}$	2.84 $rads^{-1}$
Side Hull Mass	161.03 kg	13.95 kg
Centre Hull Mass	4571.78 (tonnes)	396.10 kg

Table 7.1: *Particulars of the Trimaran model.*

Figure 7.3 consists firstly of an example of a trimaran vessel, Research Vessel Triton, taken from *www.naval – technology.com/projects/trimaran*, in order to show the structure and to aid visually in the definitions of parts of the multihull.

Below is a typical GZ curve for a trimaran vessel. Looking at the typical stability curve, one side hull comes out of the water at around 10^o, (labelled A), with the cross-structure entering the water at 25^o (at B). GZ increases until the upper deck is immersed at around 50^o (indicated by point C).

For a trimaran, the shape of the GZ curve is significant most importantly when the

heel angle is enough for one side hull to come out of the water. To avoid sudden flattening of the GZ curve when one side hull emerges, extra volume is generally placed above the waterline and this is done so in the form of flare on the inboard face of the side hulls, known as haunches (see Figure 7.3).

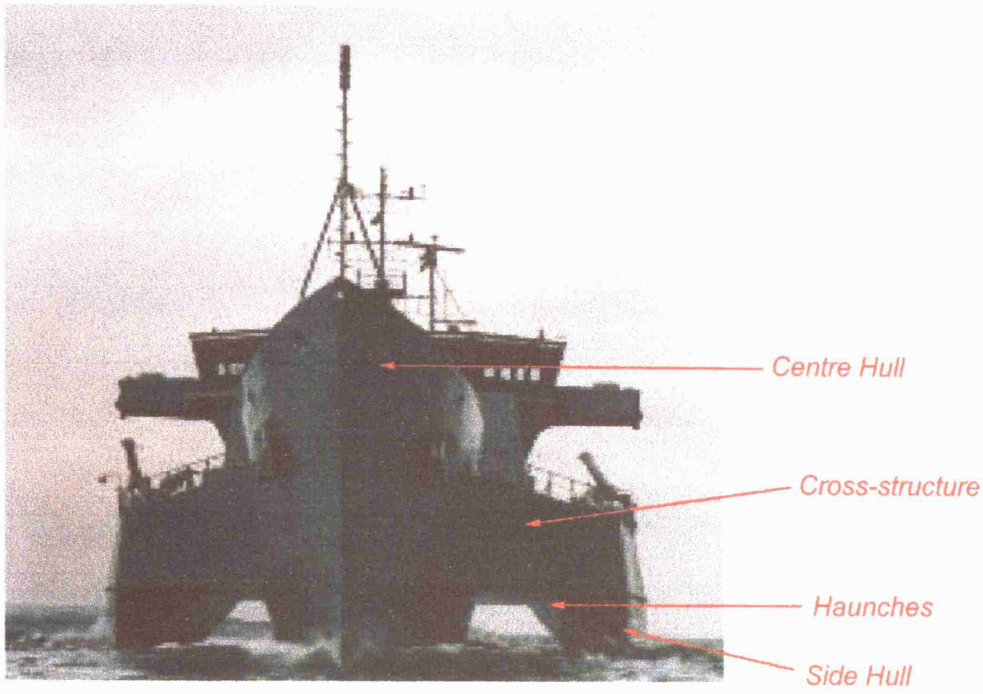

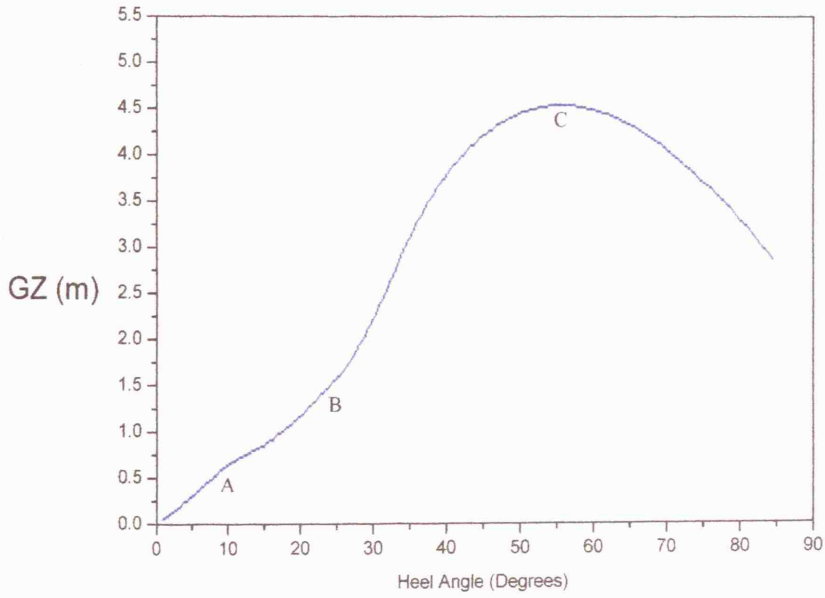

Figure 7.3: *Trimaran vessel R. V. Triton taken from www.naval – technology.com/projects/trimaran. Below a typical GZ curve for a trimaran.*

7.6 Trimaran model roll decay

We represent as Figure 7.4 a plot of the adopted experimental roll decay data in calm water, indicated by black colour. The model was released at an angle of heel about 10^o and the resulting data was recorded using similar techniques with those employed in the NTUA tank (which are described in greater detail later on for our own experimental testing on a monohull model).

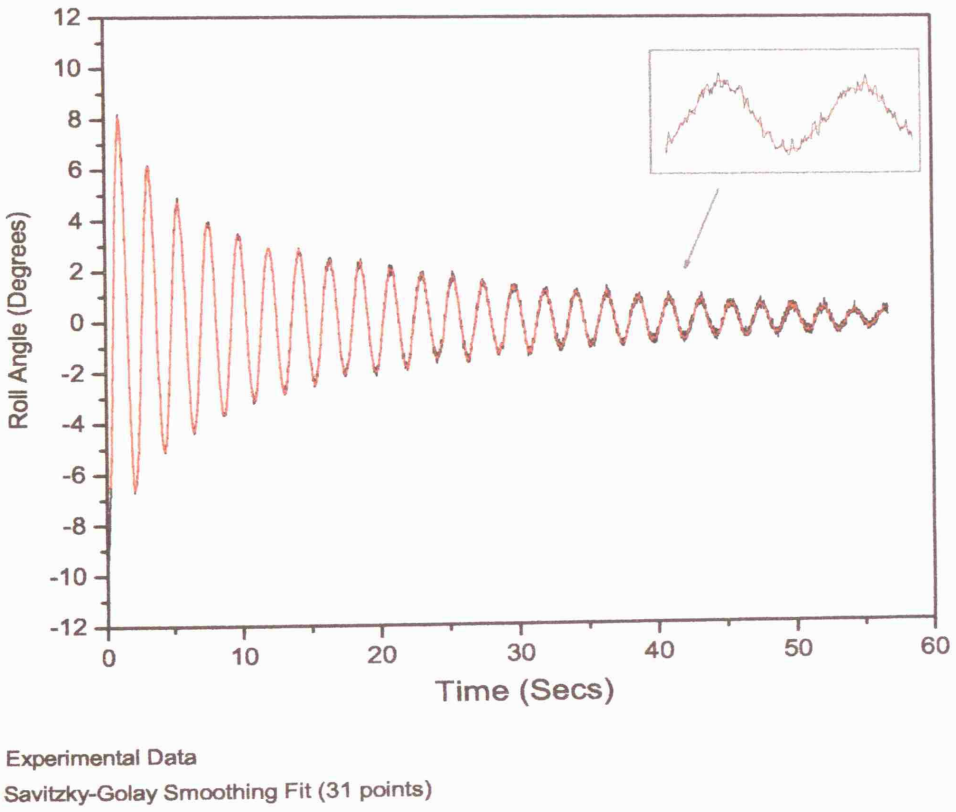

Figure 7.4: *Experimental Data for trimaran roll decay shown in black and a Savitzky-Golay smoothing curve fit shown in red. The rectangular inset is a focus of two consecutive peaks.*

From the above experimental data we notice that the resulting motion appears to be rather irregular. By this we mean that during the decay extra multi-peaks occur upon each peak. The rectangular inset shows for clarity a focus of two consecutive peaks where this behaviour may evidently be seen. Deakin (Deakin, 2003) agrees that the trimaran roll motion is truly complex since the motion of each hull propagates waves to which the other hull responds.

Forcing a mathematical fit to the data may remove effects caused by coupling of roll motion with heave or pitch motion. To avoid this a fitting method must be obtained to produce a smoother line through the experimental data. Different fitting tools provided by *Origin Scientific Graphing and Analysis Software* were tried and examined but we found that a Savitzky-Golay smoothing filter gave a more achievable and appropriate fit than others.

Savitzky-Golay filters are normally used to smooth out a noisy signal. The method works by fitting a polynomial to a small part of the signal of a chosen window size using a least squares method. It then moves on stepping through the signal in steps equal in size to the chosen window. The complete signal is then the summation of these individual least square fits.

For the results of the decay experiment, a fourth order polynomial was fitted to a length of the decay containing 31 data points. This was found after trying other lower order polynomials and seeing that the fourth order polynomial provided a better fit to the experimental decay. This fit is shown in red colour in Figure 7.4 noticing that the peaks of the decay are now much smoother hence making our analysis of the decay data clearer and simpler.

Figure 7.5 shows the decrement of the peaks considering both positive and negative peaks. The negative peaks have been treated as positive so that the absolute value

of the decay history is taken with all troughs at negative roll angles been reflected to become positive peaks.

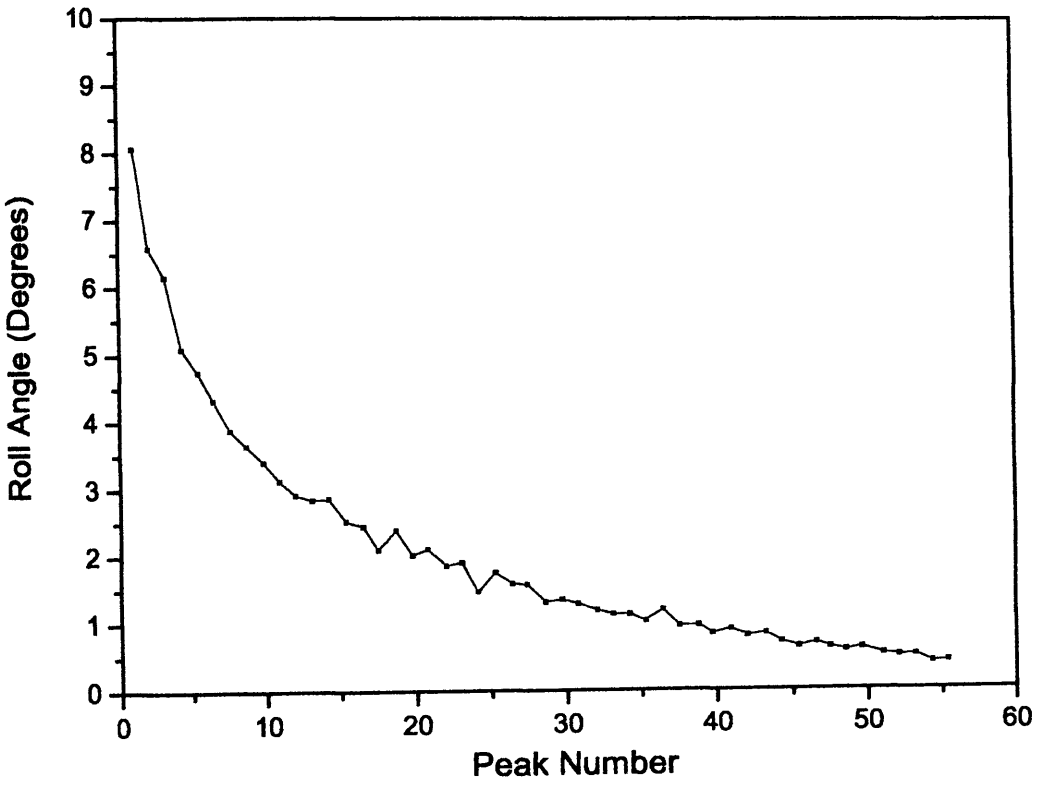

Figure 7.5: *Decay of peak roll amplitudes for trimaran model (absolute values taken, so both positive and negative roll angles may be considered.*

At about the 16^{th} peak number, there is evidence of fluctuation, which comes about due to the fact that in the roll decay time series, one roll peak is greater in magnitude than the previous one.

A relationship between the equivalent linear damping calculated over each half roll

cycle and the assumed roll damping model may now be investigated. Using the peak decrement (the quasi-linear method) and the energy balance approach, theoretically described earlier, the equivalent linear roll damping term, b_e, may be calculated between two successive peaks in the decrement, recalling equation (7.4.9):

$$b_e = \frac{2\omega_n}{\pi} ln(\frac{\varphi_r}{\varphi_{r+1}})$$

so that a value of b_e is obtained for every half cycle of the decay. Figure 7.6 represents these values plotted against the mean of the amplitudes used in the calculation for b_e as red points. We remind ourselves here that these b_e values are calculated assuming roll stiffness, inertia and added inertia remain constant throughout the decay.

The blue line represents the line of best fit of the data used to obtain linear and quadratic damping coefficients for the quadratic model. The intercept of this line gives the linear damping coefficient, b_1 whilst the gradient represents the quadratic damping coefficient, b_2.

Choosing a cubic damping model is no better than when a quadratic damping model is used (Grafton, *preprint PhD Thesis*, 2006). Similarly to the findings of the Naval Architecture and Marine Engineering Research Group, there is a large variation of the data points around the line of best fit shown by the solid black line connecting the b_e points especially at low roll amplitudes and moreover, some of the values of the equivalent linear damping are negative. This can be explained when one peak in the decrement is higher than the previous one.

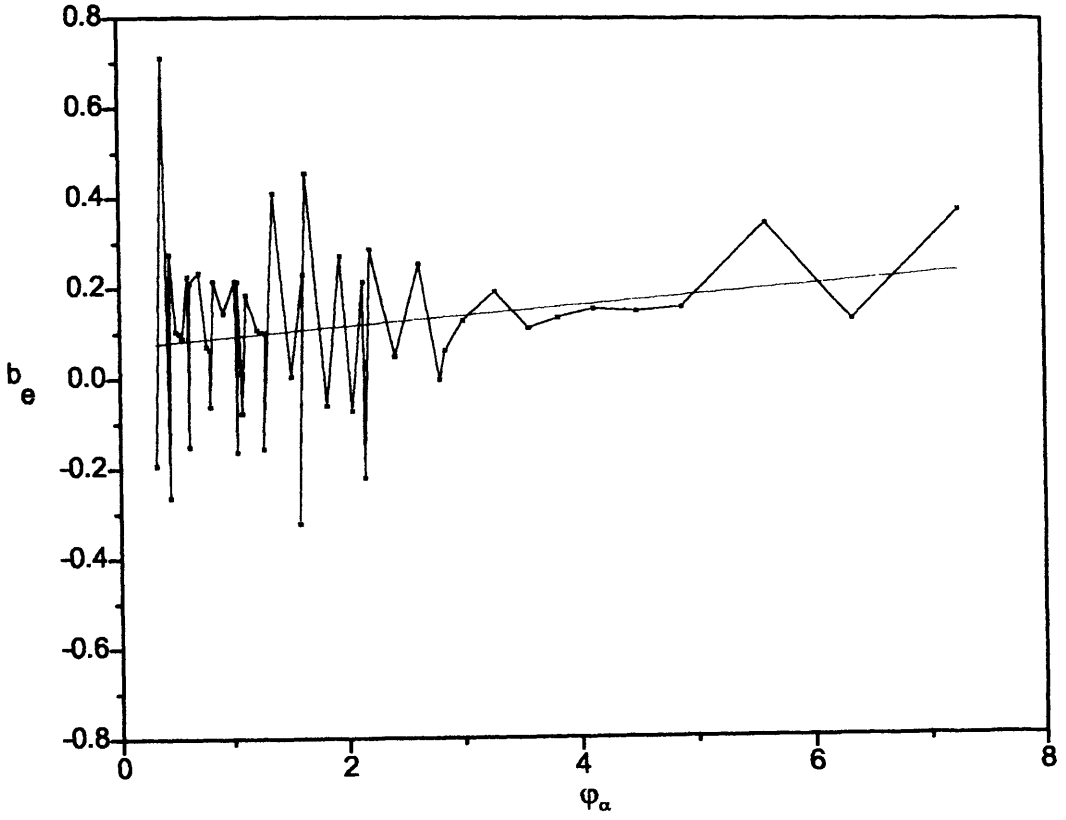

Figure 7.6: *Equivalent linear roll damping, b_e, plotted against mean roll angle between two successive peaks (red points) for the trimaran model. The black line shows the b_e variation. The blue line is a line of best fit to the data used to obtain linear and quadratic damping coefficients, b_1 and b_2.*

The linear and quadratic damping coefficients derived using the quasi-linear method from this set of experiments are:

	b_1	b_2	ω_n
10° Heel	0.0686	0.559	2.837

Table 7.2: *Linear and quadratic damping coefficients and natural roll frequency.*

These linear and quadratic damping coefficients obtained from our own analysis of experimental data are similar to the series of results found by Grafton (Grafton, *preprint PhD Thesis*, 2006) for both sets of roll experiments that he examined. The small difference in the coefficients may be tolerated as the roll response has a slightly different damped natural frequency. Probably due to our different approach of smooth fitting to the experimental data and the different instances of truncating the roll experimental decay for analysis.

Since there is so much scatter in our equivalent linear roll damping plot especially at low angles of roll, neither accurate nor stable roll damping coefficients may be obtained for the trimaran under investigation using an uncoupled equation of roll motion with constant coefficients. Due to this spread, damping coefficients cannot be determined from the set of experimental decay with any degree of certainty.

We mention that applying the techniques reviewed above for the set of roll exper-

imental decay commencing at an initial heel on the other side of the trimaran, (so from the port side), still leads us to the same scattering effect of b_e data. Grafton (Grafton, *preprint PhD Thesis*, 2006) notes also that the linear and quadratic damping coefficients still differ between the equivalent linear damping analysis for the port and starboard case and this would only be the case if the model was asymmetrical. However, discussions with our fellow collaborators lead to the assumption that the trimaran model was symmetrical after careful calibration, so this result is hence unexpected.

For low angles of roll, we see here as well that roll damping coefficients for the trimaran model may not be determined with confidence under the assumption that roll decay can be adequately modelled by a single degree of freedom uncoupled roll equation with constant coefficients. Furthermore, under this assumption, with damping measured over half a roll cycle, between successive peaks in the decay, instances of negative damping occur suggesting an indication of changes in inertia, added inertia or stiffness in the equation of motion.

With this in mind, re-analysis of roll decay results in more than more degree of freedom must be considered in order to establish if there is truly any coupling with other motions that may cause alteration in the roll and added roll inertia or roll stiffness. The difficulty with this approach is that cross coupling terms may not be easily measured in model testing.

7.7 Simulation of Coupled Roll and Heave Free Decay using a single degree of freedom equation of motion for the trimaran model

For a monohull vessel in beam seas, researchers such as Blocki (Blocki, 1980), Liaw and Bishop (Liaw and Bishop, 1995) and Sanchez and Nayfeh (Sanchez and Nayfeh, 1997) suggest that the most likely coupling between the six types of motion of a ship, is the roll and heave coupling. Grafton (Grafton, *preprint PhD Thesis*, 2006) also suggests that the most likely coupling mechanisms for a trimaran fitted with haunches on the side hulls will be between roll and heave, whereby during roll motion, the haunches will continually immerse and emerge from the water. The flare on the inboard side of the side hulls of the trimaran model form the haunches that start at the design waterline and during roll motion, there is an increase in buoyancy due to the side hulls causing the model to heave (see also Figure 7.3). This forced heave motion is suggested to occur at the frequency of rolling.

In addition, the initial heel angle that initiated the roll decay trimaran experiment was induced by applying a force to the side hulls which was then removed. This has the effect of instigating the decay. This will also induce a heave motion that decays at the heave damped natural frequency, say ω_h. This heave motion will most likely be heavily damped. Free heave decay experiments were performed on monohull vessels by Crossland, Wilson, Bradburn (Crossland *et al*, 1993) and their results showed heave motion decaying away in just two to three cycles.

So, if the trimaran model was undergoing coupled roll and heave motion the roll stiffness would vary with time as the waterplane area changes during heave. This is in essence the idea that the trimaran researchers at UCL have adopted in order

to maintain a single degree of freedom equation of motion but at the same time incorporate heave motion modelled only by the effect it has on the roll stiffness. Hence their coupled heave and roll decay model was considered as the sum of the heave motion induced by the removal of the inclining force induced to initiate roll decay, decaying at the natural heave frequency, roll motion without heave decaying at the natural roll frequency around a fixed waterplane and heave motion induced by the additional buoyancy of the haunches as they are immersed during roll motion, where this latter motion decays at the roll natural frequency.

The final proposed equation of motion undertaken in order to imitate the behaviour of the trimaran model under a single degree of freedom roll equation conducted at model scale, is of the form:

$$\varphi'' + b_1\varphi' + b_2\varphi'|\varphi'| + \omega_n^2(1 + e^{\mu t}(\alpha_1 \cos\omega_n t + \alpha_2 \cos\omega_h t))\varphi = 0. \qquad (7.7.1)$$

Paramarine software (www.gre-ltd.co.uk) was used to assess changes in GM due to the heel about the fixed waterline, the GM variation due to heaving as the haunches are immersed (α_1) and the GM variation due to heaving induced by the removal of the inclining force (α_2). The actual formation of α_1 and α_2 using this software does not interest us here, but merely mentioned and added so that we may gain an idea of what their actual values might be and represent. ω_n and ω_h are the natural roll and heave frequencies respectively. μ represents heave damping and b_1 and b_2 the linear and quadratic damping coefficients per unit inertia.

We note that (7.7.1) is similar to our double parametrically excited pendulum system examined in Chapter 6 with the main difference lying in the presence of the exponential heave damping component. For equality to hold $\mu = 0$.

Using our own analysis undertaken in the previous section from the trimaran experimental data provided, we incorporate our own set of damping coefficients, $b_1 = 0.0686$ and $b_2 = 0.559$ and based on the period of decay, we choose the natural roll frequency to be $\omega_n = 2.837$ radians per second. We employ our chosen values deduced from the experiments to draw our own conclusions and produce extensions to the hypothesis of the researchers in the Naval Architecture and Marine Engineering Research Group; that roll and heave are coupled due in part to the immersion and emergence of the haunches on the side hulls during rolling, thus modifying the form of the typical single degree of freedom equation of roll motion.

When α_1 and α_2 are set to zero in (7.7.1) we expect that the equivalent linear roll damping, b_e, plotted against the mean roll amplitude between successive peaks would show no noticeable changes in the equivalent linear damping values with all the b_e points lying in a straight line. This is a valid expectation where the equivalent linear damping results should not spread away from the line of best fit.

We now examine the effects of adding the two sinusoidal variations in stiffness term by firstly varying the heave frequency whilst the roll frequency is set to $\omega_n = 2.837$ rad/s, $b_1 = 0.0686$ and $b_2 = 0.559$ for the rest of the simulations. We emphasise that these values were deduced from the experimental analysis of roll decrement testing. We initially consider the ratio of $\frac{\omega_h}{\omega_n} = 0.9$ where heave frequency here is $\omega_h = 2.598$ for different heave damping conditions, $\mu = 0, -0.02, -0.03$ (see top set of Figure 7.7). These non-fixed values are not specific, just typical numbers which we will vary.

Since only one set of experimental data was available, we find ourselves assuming and adopting the values $\alpha_1 = 0.04m$ and $\alpha_2 = 0.03m$ provided with the help of the Paramarine software from investigations by Grafton (Grafton, *preprint PhD*

Thesis, 2006). It is worth mentioning here that higher values of α_1 and α_2 might cause the roll to grow instead of decay and care must be taken to make sure that at these values such phenomenon does not occur. Whilst there is no evidence of this occurring in the free decay model experiments with the trimaran model, it could pose a problem in a seaway where heave motion will be propagated by the waves as well as by roll motions.

The red points in both diagrams that follow in Figure 7.7 and 7.8, represent equivalent linear roll damping values from simulated decay and the black line that connects each point is the b_e variation. In the cases when heave damping is absent, so with $\mu = 0$, at the different heave frequencies we realise that few negative b_e values are present. Only when μ exists do variations in negative linear damping values occur especially at low roll amplitude, as was the case for the trimaran's experimental analysis.

During the cases when $\mu = -0.02$, $\mu = -0.03$ and the frequency ratio is equal to 1 so that heave and roll frequencies are equal, but also when the heave frequency is close to the value of the roll frequency, the response in all plots is a scattering effect of b_e values, however not in a manner that resembles that of Figure 7.6. Taking μ as positive will have the opposite effects. The scatter will be greater at high angles of roll instead of the lower angles of roll that characterise the experimental behaviour.

Looking further into other frequency ratios and more specifically when the heave frequency is near the value 2, $\omega_h \approx 2$ (see third set of figures in Figure 7.7 and Figure 7.8), we discover that the simulated equivalent linear damping plotted against the mean roll amplitude between successive peaks responds similarly to the experimental damping data, allowing us to suggest that within this range of heave frequency, more realistic outcomes are obtained.

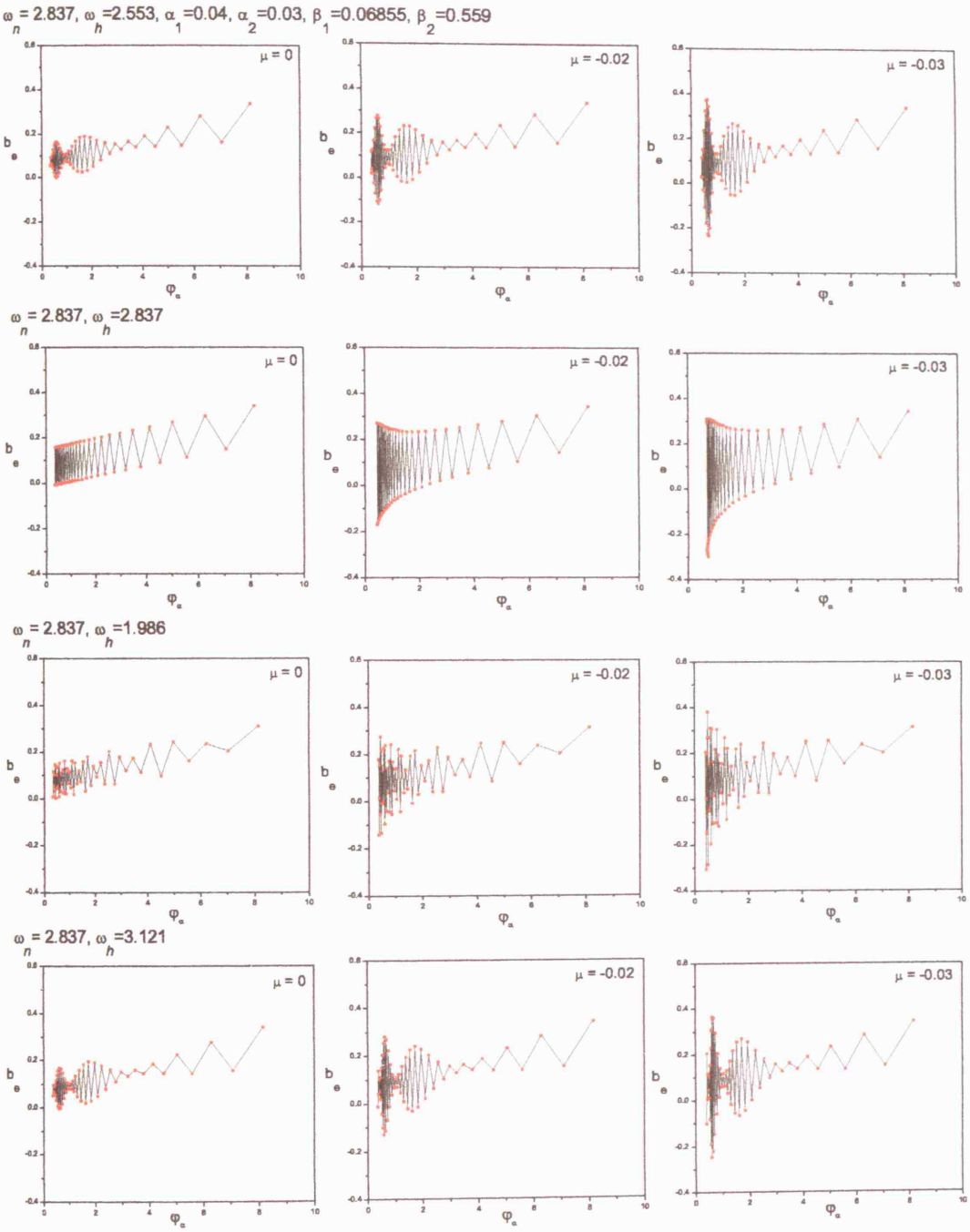

Figure 7.7: *Simulated equivalent linear roll damping, b_e, plotted against mean roll angle between two successive peaks (red points) for the trimaran model under the stated conditions. The black line shows the b_e variation.*

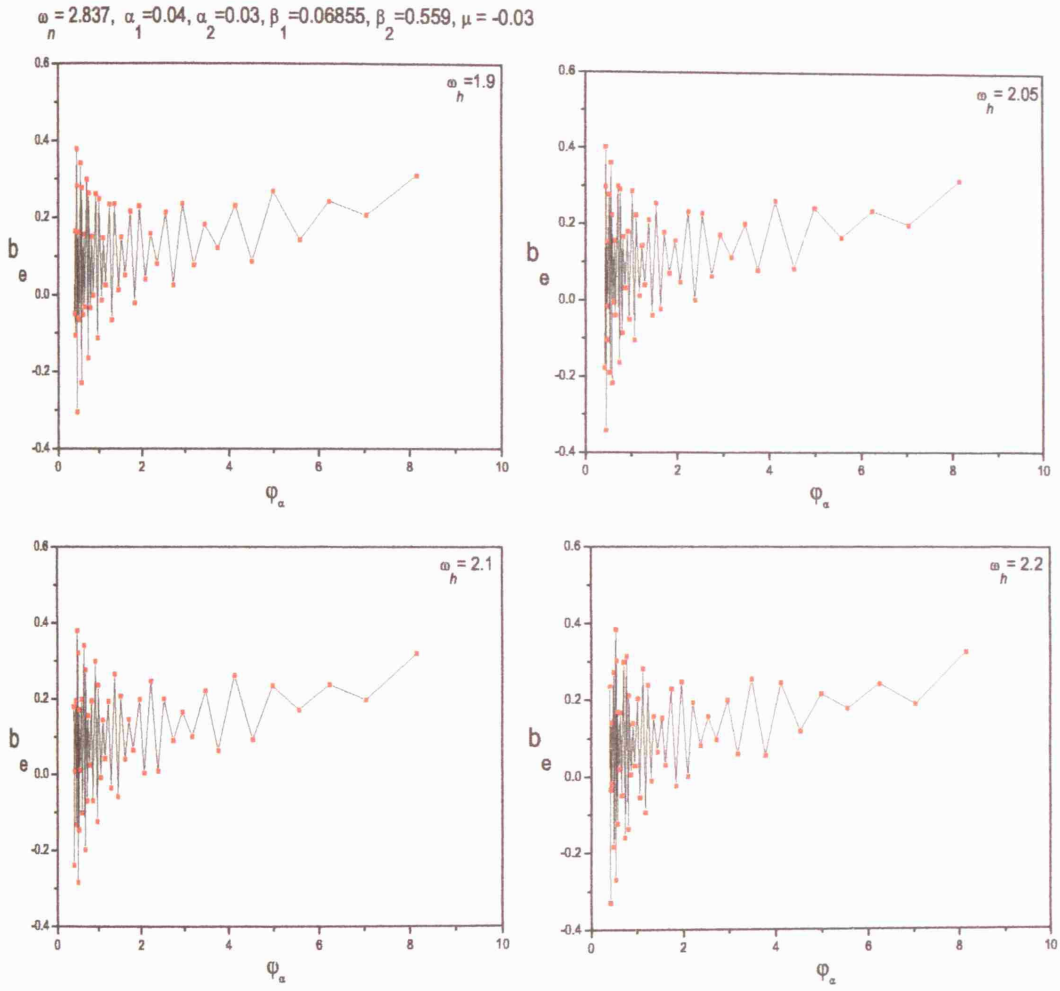

Figure 7.8: *Simulated equivalent linear roll damping, b_e, plotted against mean roll angle between two successive peaks (red points) for the trimaran model under the stated conditions. The black line shows the b_e variation.*

This analysis of simulation has shown that to get a large spread in the equivalent linear damping data, especially at low angles of roll, and a better representation to that of the experimental damping data whilst the natural roll frequency $\omega_n = 2.837\ rad/s$, the heave natural frequency must lie near the value of 2 radians per second and the heave damping may be zero or negative, so that some form of heave excitation may be present.

The first result raised here deduced from our simulation analysis is more strict and clearer than the current findings of the research trimaran group at UCL. Research to date comments that when the roll and heave frequencies are co-incident or very close to one another (remaining coherent with our terminology, this means that the ratio of frequencies is close to 1), this is when a large spread in the equivalent linear damping data occurs. From our investigations, we are also in agreement here but we further discuss and add that during this ratio range, the b_e against φ_α plot does not resemble precisely the manner at which the scattering and the b_e variation occur in the testing data.

We exemplify that a better presentation is achieved, both visibly and numerically, when the heave frequency is near the vicinity of value 2 radians per second.

Having developed this hypothesis that roll motion couples with heave motion we add as Figure 7.9 (taken from Grafton, *preprint PhD Thesis*, 2006) a plot of the resulting heave displacement time history during the roll decay and a diagram of the absolute heave displacement Fast Fourier Transform where frequencies below ≈ 1.25 *rad/s* have been filtered. Actual heave data was not provided to us and so we must be satisfied with referring to this imported Figure.

The heave displacement decays during the initial five seconds after which there is

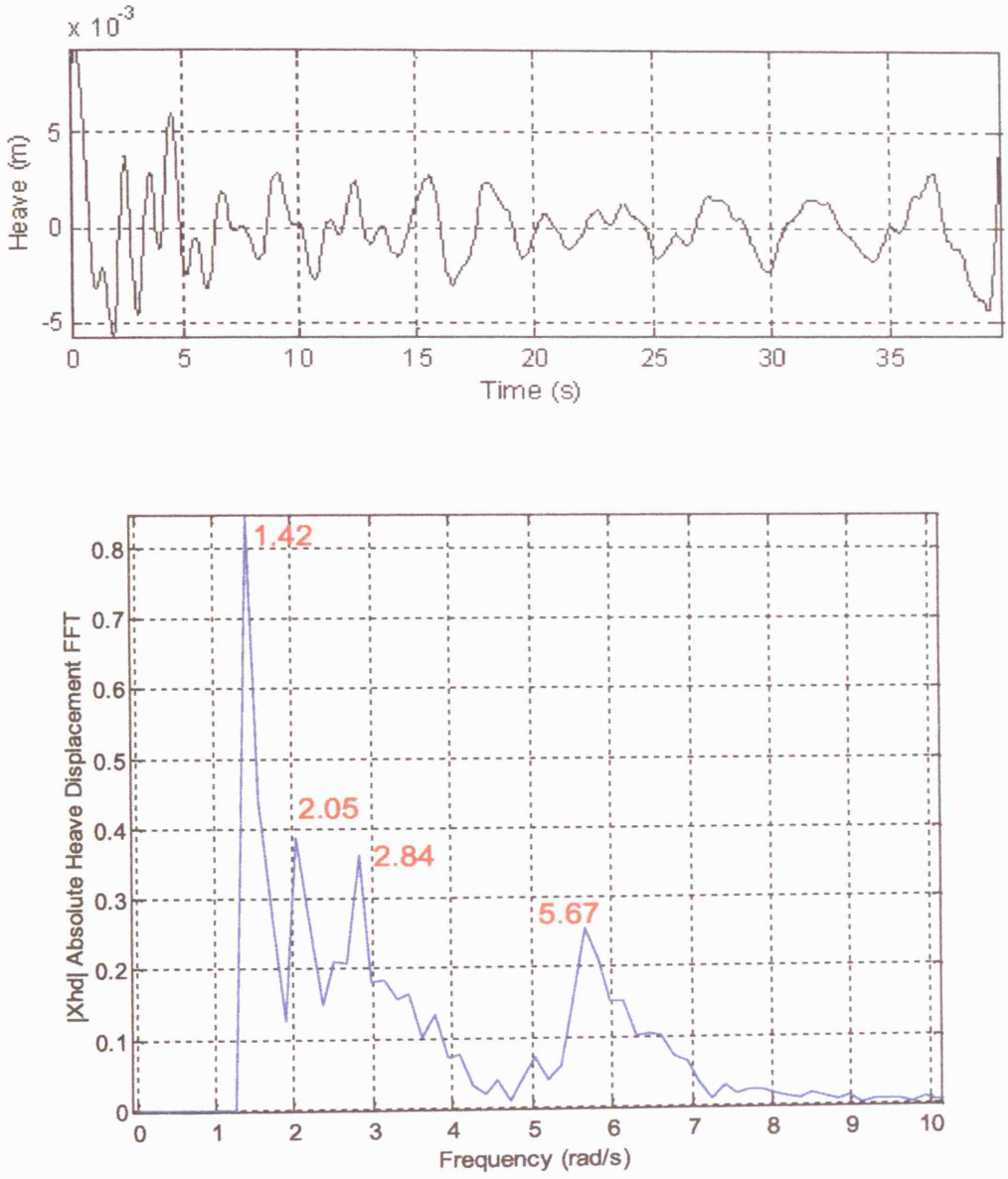

Figure 7.9: *Heave displacement time history for the roll decay and a diagram of the absolute heave displacement Fast Fourier Transform where frequencies below* ≈ 1.25 *rad/s have been filtered. Peaks occur at* $1.42, 2.05, 2.84$ *and* 5.67 *rad/s (taken from Grafton, PhD Thesis, 2006).*

no evidence of any signs of decay. The heave motion appears to be made up of more than one frequency component which supports the simulation work where we agree with fellow researchers at UCL that there would be heave components at both the heave and roll natural frequencies.

The breakdown of the frequency components is investigated by the Fast Fourier Transform where the lower diagram exhibits four distinct peaks. These peaks represent the dominant frequency components of the heave time history. The peaks are shown to occur at approximately $1.42, 2.05, 2.84$ and 5.67 rad/s.

Figure 7.10, shows our computation version of the absolute roll displacement FFT for the Savitzky-Golay filter curve of the experimental roll decay, showing a major peak occurring at frequency 0.452 Hz which coincides with 2.84 rad/s, giving an excellent agreement. Hence we may conclude that the third peak occurring in Figure 7.9 may be presumed to be the roll damped natural frequency. The other two peaks occur at both half this frequency and twice this frequency.

The remaining peak frequency, at 2.05 rad/s is most likely to be related to the heave frequency where we notice that it satisfies our results from our simulated investigations. It is a value of heave natural frequency close to ≈ 2 which we deduced would provide together with $\omega_n = 2.837$ of the model, a more appropriate and good representation of the scatter of the equivalent linear damping points.

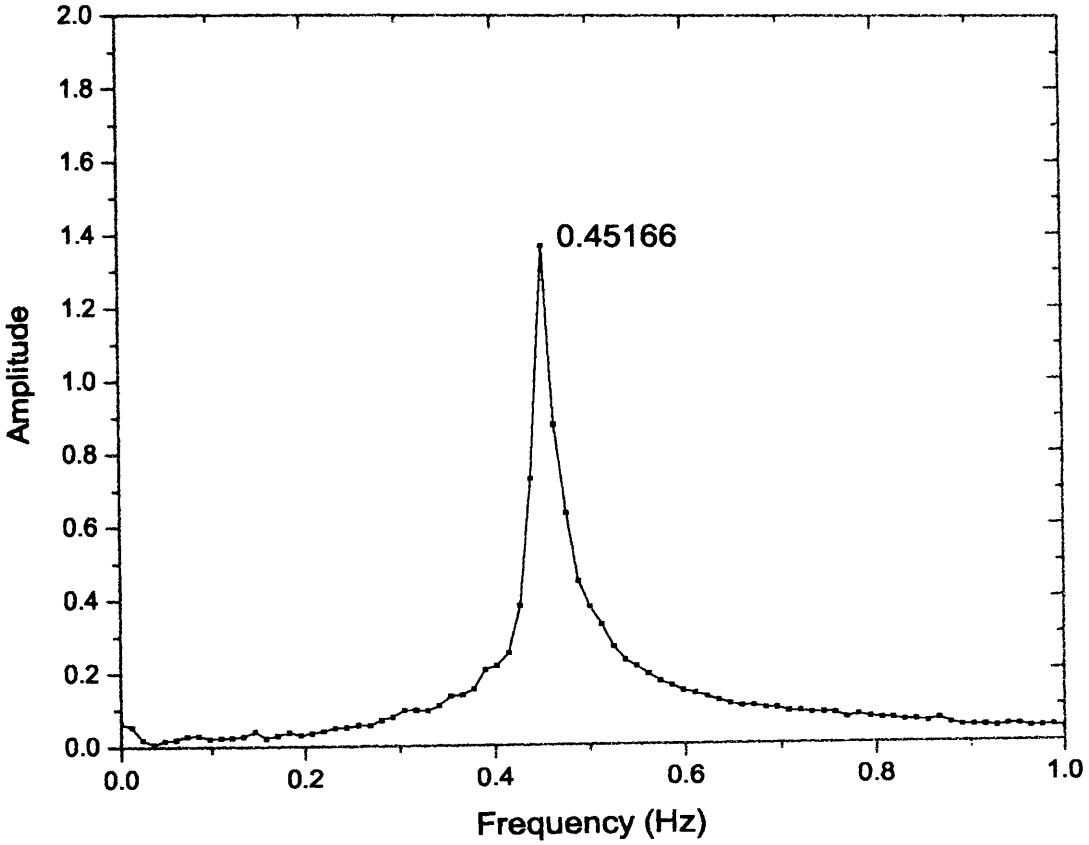

Figure 7.10: *Our computational version of the absolute roll displacement FFT for the Savitzky-Golay filter curve of the experimental roll decay. Peak occurs at frequency* 0.45166 Hz *or* 2.84 rad/s.

In order to show further that our numerical simulations fairly match the experimental results with the implementation of coupling heave and roll under a single degree of freedom equation, we need to ascertain that the value of heave damping used and that we varied during simulations was of feasible magnitude. From the heave displacement time history diagram of Figure 7.9, we may extract from the first $\approx 4\frac{1}{2}$ seconds, the rough maximum heave values, in order to calculate an approximate heave damping, μ.

Figure 7.11 shows as black points the maximum positive heave displacement values of the initial decay. These points are joined together via straight lines to form the black curve. The red curve is an exponential curve fit of the form $y = d_h e^{\mu_h t}$, where $d_h \approx 9.599$ and $\mu_h \approx -0.306$. This approximate curve fit, was configured with the aid of Origin Software. Since the value of the square of the correlation between the response values and the predicted ones, $R^2 = 0.9938$, is close to one, then it remains to be said that the red curve serves a good approximation to the actual heave decay.

From equation (7.7.1), the maximum possible heave displacement is

$$\omega_n^2(e^{\mu t}(a_1 \cos \omega_n t + a_2 \cos \omega_h t)) \approx \omega_n^2(a_1 + a_2)e^{\mu t}.$$

This means that the following expressions are proportional thus allowing us to deduce the heave damping term, μ.

$$\omega_n^2(a_1 + a_2) \propto d_h.$$

$$\text{and} \quad e^{\mu t} \propto e^{\mu_h t}.$$

Replacing the values of $\omega_n = 2.837 rad/s$, $a_1 = 0.04$ and $a_2 = 0.03$ derived from the experimental testing, and the parameter values of the exponential curve fit, we may

deduce that $\mu \approx -0.02$. This is in the vicinity of the heave damping values employed during simulations and around the proposed magnitude of heave damping that we suggested may contribute to the accurate scattering behaviour of the equivalent linear roll damping plot against the mean roll amplitude between successive peaks.

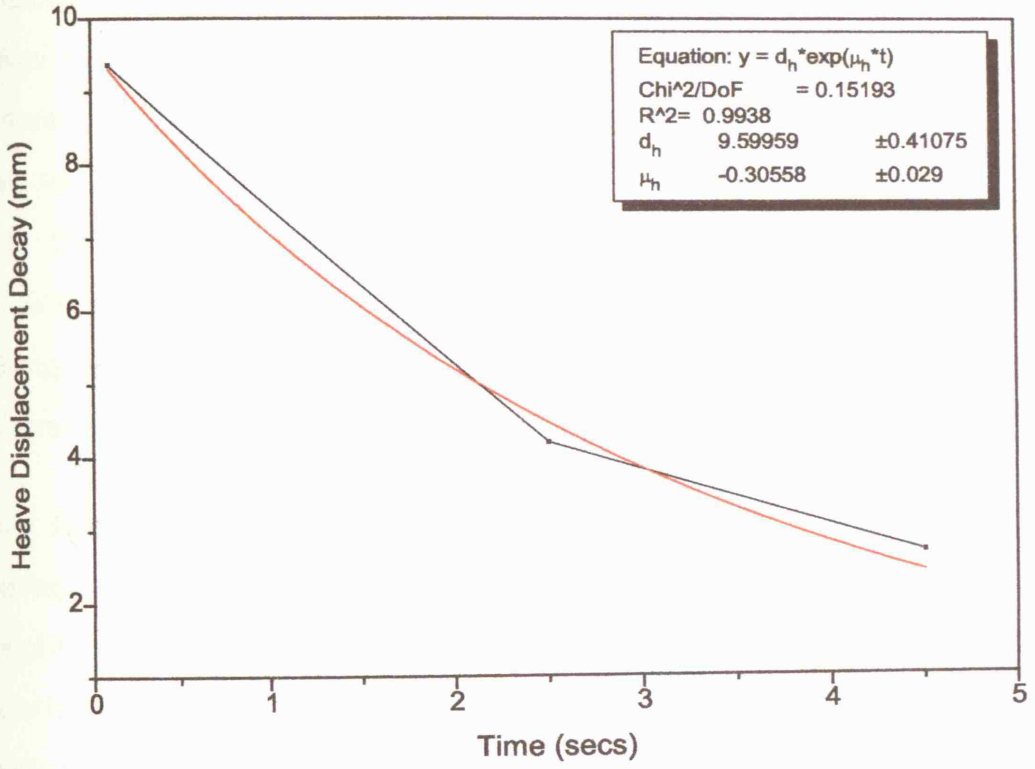

Figure 7.11: *Heave Displacement Decay. Black represents actual decay and the red curve is an exponential curve fit to the response values.*

Consequently, from this analysis it appears very likely that the haunches on the side hulls do induce heave motion whilst the model rolls in free decay. We note as an addition that the heave natural frequency is around $\frac{2.05}{2.837} = 72.3\%$ of the roll natural frequency and once heave motion is induced it may lead to resonance.

7.8 Monohull Experimental Investigation undertaken at NTUA

The experimental free decay test in calm water examined within the previous section for the trimaran case, led us to question the assumption that the motion of the multihull model undergoing free decay could be modelled by a single degree of freedom uncoupled roll equation with constant coefficients. We therefore adopted a proposed equation of motion with two decaying time varying sinusoidal stiffness terms, where the coupled heave and roll can be considered as the sum of the three effects: the heave motion induced by the removal of the inclining force instigating the heel angle, pure rolling around a fixed waterplane induced by the removal of the inclining force and the extra heave motion induced by the additional buoyancy of the haunches as they are immersed during roll motion.

Taking these effects into consideration, simulations based upon the experimental damping coefficients and natural roll frequency were selected based upon the results of the quasi-linear analysis of the roll decrement. The major outcome of the simulations was a spread in the equivalent linear roll damping for every half cycle, mimicking the version with the experimental data.

At this point in our research we were intrigued to find out if similar behaviour may be found in roll damping assessment of a monohull model. That is, is the heave motion damped out quickly for a monohull. Hence, the second investigatory section of this Chapter consists of the experimental tests that took place in the National Technical University of Athens, Greece, at the Ship and Marine Hydrodynamics Laboratory's towing tank, using a newly designed and constructed monohull model. The model is based upon the design of a passenger ferry which still cruises to date in the Mediterranean Sea but whose name remains undisclosed for confidentiality

reasons. In Naval Architecture, once a ship has been designed, model experiments must be performed to determine the total roll damping accounting for both viscous and non-viscous effects.

The particulars and specifications of the ship and monohull model are given in Table 7.3 below, where the scale ratio of ship to model is 25:1.

	Ship	Model
Length Overall (m)	84	3.36
Length between perps (m)	74.2	2.97
Beam(m)	14.4	0.58
Depth to main deck (m)	6	0.24
Draught (m)	4.023	0.16
Mass	2357 (tonnes)	150.9 kg
GM	1.21 m	0.0484 m
Natural Roll Period (secs)	10.5	2.313
Natural Roll Frequency	0.598 $rads^{-1}$	2.717 $rads^{-1}$

Table 7.3: *Particulars of the ship and monohull model.*

A photo of the model employed may be viewed in Figure 7.12, where it hangs safely before being launched in the water. The experiments were conducted in a wave tank of length $100m$, width $4.57m$ and a water depth of $3m$, with a vertical paddle wave maker (see Figure 7.13).

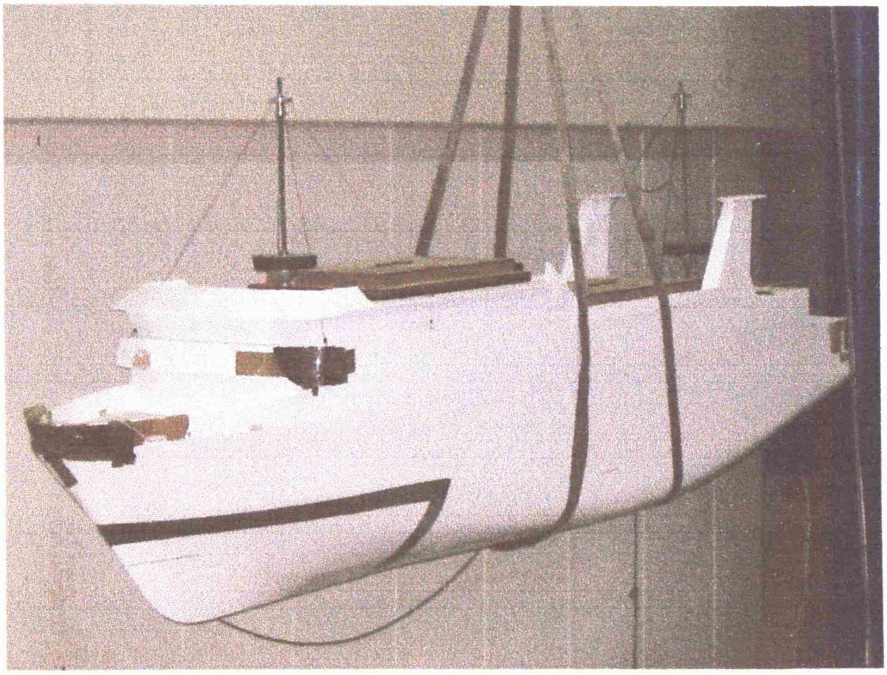

Figure 7.12: *Photo of the monohull model.*

The model was released from a number of different angles, $10, 20, 30$ degrees of roll. This was achieved by applying a force on the starboard side of the model, around its midsection or otherwise referred to as near midship, until the specific angle was reached, and then released. Care was taken so that no extra force was imposed, or unnecessary roll was induced. The time counting begun at the instant the angle was achieved and the free roll decay initialised. The process was repeated for a range of initial angles, making sure that after each run, the model returns to its upright position, and the water has reached its calm and still state. The general elapsed time for our decay tests was about a minute.

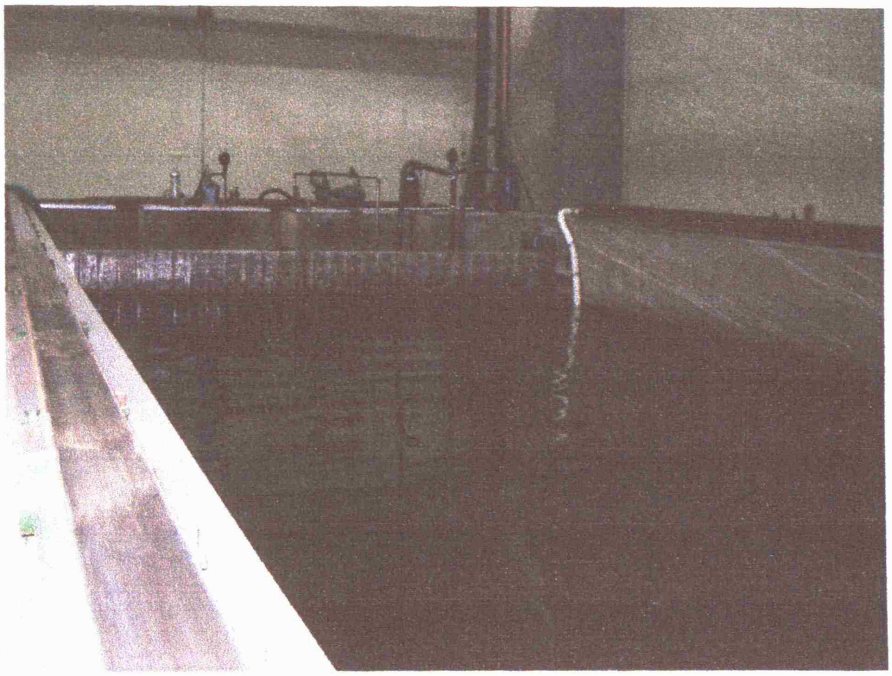

Figure 7.13: *Photo of the towing tank at the NTUA.*

Roll motion was measured using an onboard Gyro Enhanced Orientation Sensor or for short a gyroscope, with the data from this fed into a computer using an umbilical connecting cable. The gyroscope was zeroed before every test. A sampling rate of 100 Hz was used. Readings were taken every 0.01 to 0.03 seconds. Records were checked after each test and inconclusive or bad runs were repeated. The recorded data provided information on roll, pitch, yaw with respect to time in seconds. By bad runs we mean that if too much force was applied to initially commence the roll oscillation, and this was detected by the immediate readings from the pitch and yaw readings, the run was neglected and re-attempted.

7.8.1 Analysis of experimental data

The first assumption that is made in a roll decay experiment is that pure roll motion is measured, that is, there is no surge, sway, heave, pitch or yaw motions, hence the recorded roll decay data should not be influenced by these other motions. The second major assumption is that there is no forcing from waves. This means that the water remains calm at all times and there is no reflection of waves radiated from the hull during the roll decay.

Just like in the trimaran experimental tests, the decay is initiated by pushing down on one side of the model and releasing it. This may induce a small amount of heave motion and possible pitch and sway motion and these motions are assumed to decay away rapidly. However, as pointed out by Spouge (Spouge, 1988) this may lead to some uncertainty in the roll decay. This shall be examined in detail later on during our simulation analysis.

Figure 7.14 shows the roll decay history, initial roll to starboard, of roll amplitude in degrees against time in seconds for our monohull model released from an initial angle of 10^o, thus remaining consistent with our previous trimaran investigation.

Evidently the decay appears to be smooth as there are no signs of rough edges. Hence, a Savitzky-Golay smoothing curve fit is not necessary in this case. After about 65 seconds the model oscillates towards one degree in both directions, where we felt adequate analysis can be made and the model allowed to decay no further.

Figure 7.15 shows the decrement of the peaks of the decay considering both positive and negative peaks. The negative peaks have been treated as positive so that the absolute value of the decay history is taken with all troughs at negative roll angles been reflected to become positive peaks. In this figure, initially the decrement

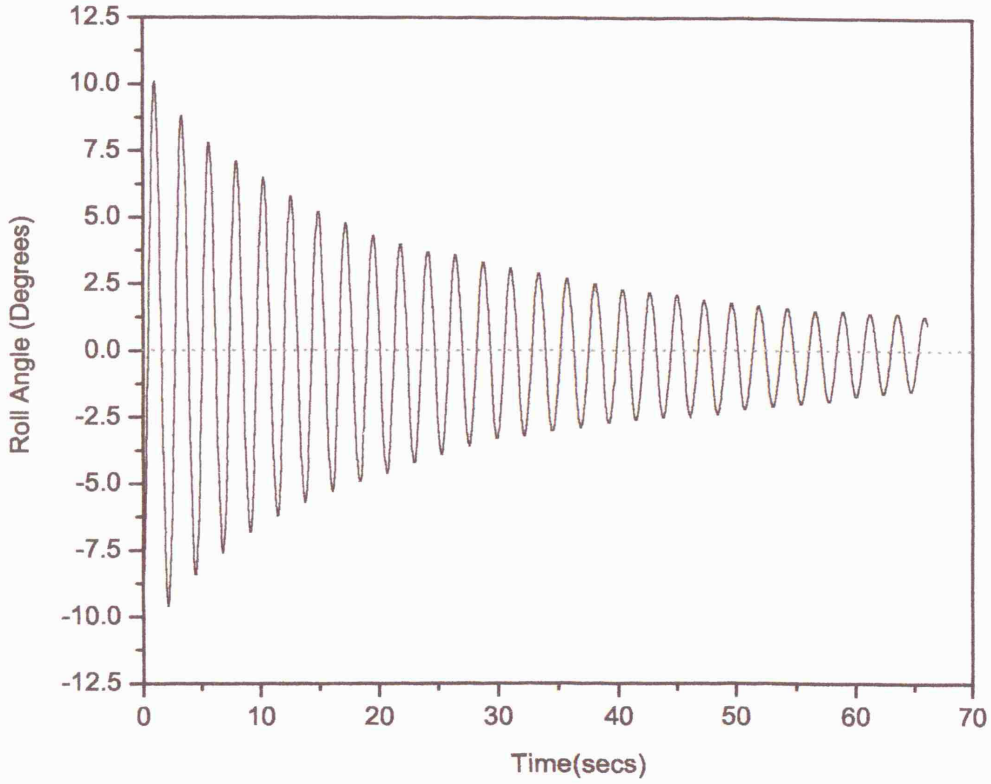

Figure 7.14: *Experimental roll decay for monohull model, initial roll to starboard, released at an initial angle of* 10^o.

appears smooth but a "sawtooth" effect appears at about the 15^{th} peak number, something which might not have been expected just from visual examination of Figure 7.14.

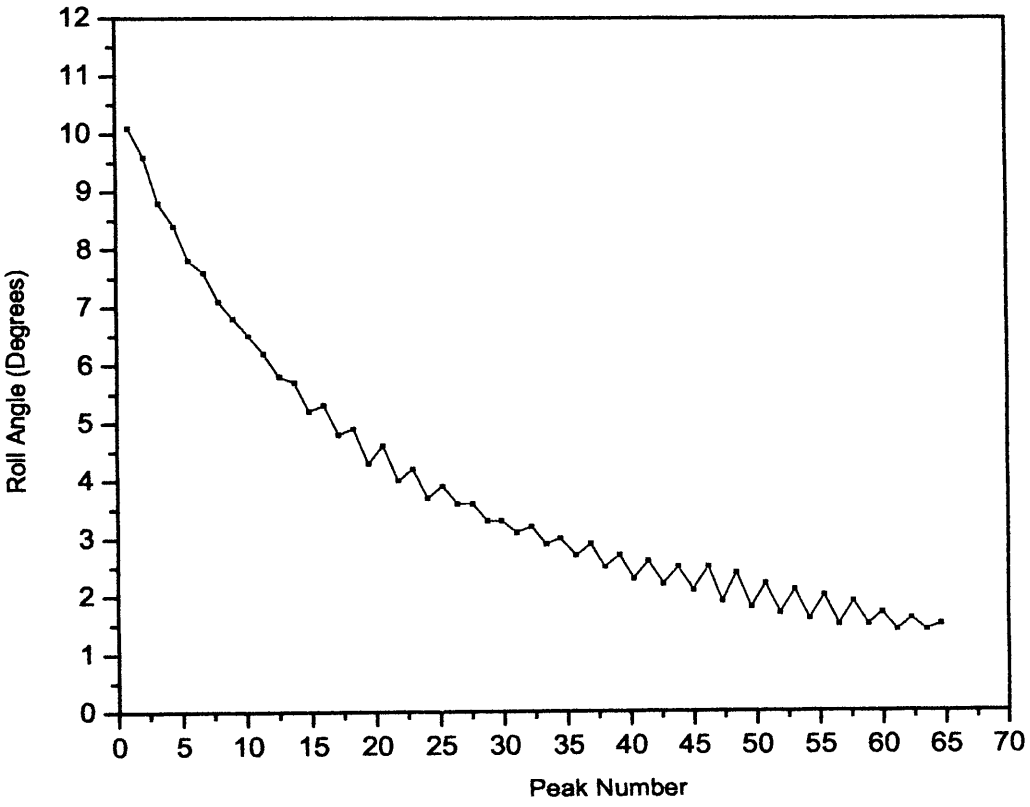

Figure 7.15: *Decay of peak roll amplitudes for monohull model (absolute values taken so both positive and negative roll angles may be considered).*

As in the trimaran peak roll amplitude decay, the fluctuations show that at some points during the decay, one roll peak is greater in magnitude than the previous one. These fluctuations are not uncommon in roll decay analysis. Spouge (Spouge, 1988) presents a decrement exhibiting this behaviour for the Fishery Protection

Vessel Sulisker. Mathisen and Price (Mathisen *et al*, 1984) and Renyuan (Renyuan, 1986) also show this on their analysis of the same roll decay data for the Sulisker Monohull. Spouge smoothed out these anomalies by fitting a mean line through the peak decrement data. The problem with doing this though is that other effects such as variations in roll stiffness or inertia during the decay could be removed and so this approach is not adopted here since we want to fully understand the damping mechanism.

We also mention that these fluctuations might be due to a bias being present in the model set up. Before any roll decay tests were conducted a calibration of the model was performed at calm water where an average steady angle of 0.8^o was exhibited inclining towards the port side of the ship. This bias was removed from the experimental decay data before further analysis was undergone, diminishing the chances that a bias might be a major reason for the sawtooth effects.

Moreover, the fact that this phenomenon is not consistent throughout the decay of peak roll amplitudes implies that other reasons must be considered, such as coupling with other types of motion. For the sake of investigating if roll is coupling with motions such as heave, pitch and yaw, it is necessary that these sawtooth effects must not be smoothed out by adopting a fitting curve and hence must be included in our roll decrement analysis.

As mentioned previously, the gyroscope measures pitch, yaw and roll and for this experiment, the pitch and yaw recorded data seemed to show no sudden increases or decreases to encourage the assumption that roll is coupling at this instance with these types of motion. Unfortunately, the experimental apparatus did not allow for heave motion to be measured, leaving this degree of freedom as the most likely one to contribute to coupling. As we were borrowing the facilities, we could not alter

the set up.

Using the quasi-linear method of roll decrement described earlier, (7.4.9), the equivalent linear roll damping term, b_e, is calculated between the two successive peaks in the decay. Recalling here that by successive peaks we mean that the negative peaks have become positive so that a value of b_e is obtained for every half cycle of the decay.

These values are plotted against the mean of the amplitudes of the two peaks, $\varphi_a = \frac{\varphi_r + \varphi_{r+1}}{2}$, and coloured as red points in Figure 7.16. As before, these b_e values are calculated assuming the roll stiffness, inertia and added inertia remain constant throughout the decay. The variation in b_e is shown by the black line joining these points together. If a quadratic damping model is assumed then the variation in equivalent linear damping is described by equation (7.4.7) where φ_a is the mean of the amplitudes of the two peaks used in the calculation for b_e.

Applying this quadratic model of damping, a line of best fit is calculated, coloured in blue in Figure 7.16. The gradient of this line represents the quadratic damping coefficient, b_2, whilst the intercept gives the linear damping coefficient, b_1. Hence, we finally reach the result that $b_1 = 0.024$ and $b_2 = 0.2335$.

We notice that there is a large variation of the data points around this line of best fit, especially at low amplitudes. This is same behaviour to what we noticed in the examination of the equivalent linear roll damping of the trimaran. Similarly, some of the values of the equivalent linear damping are negative, implying that one peak in the decrement is higher than the previous one. We note that time is running from left to right.

We also include as Figure 7.17 and Figure 7.18, roll decay tests initially inclined at 20^o and 30^o respectively for the sake of experimental repetitiveness. The initial offset of the model was extracted and quasi linear analysis of roll decrements was used to determine the corresponding damping coefficients of both sets.

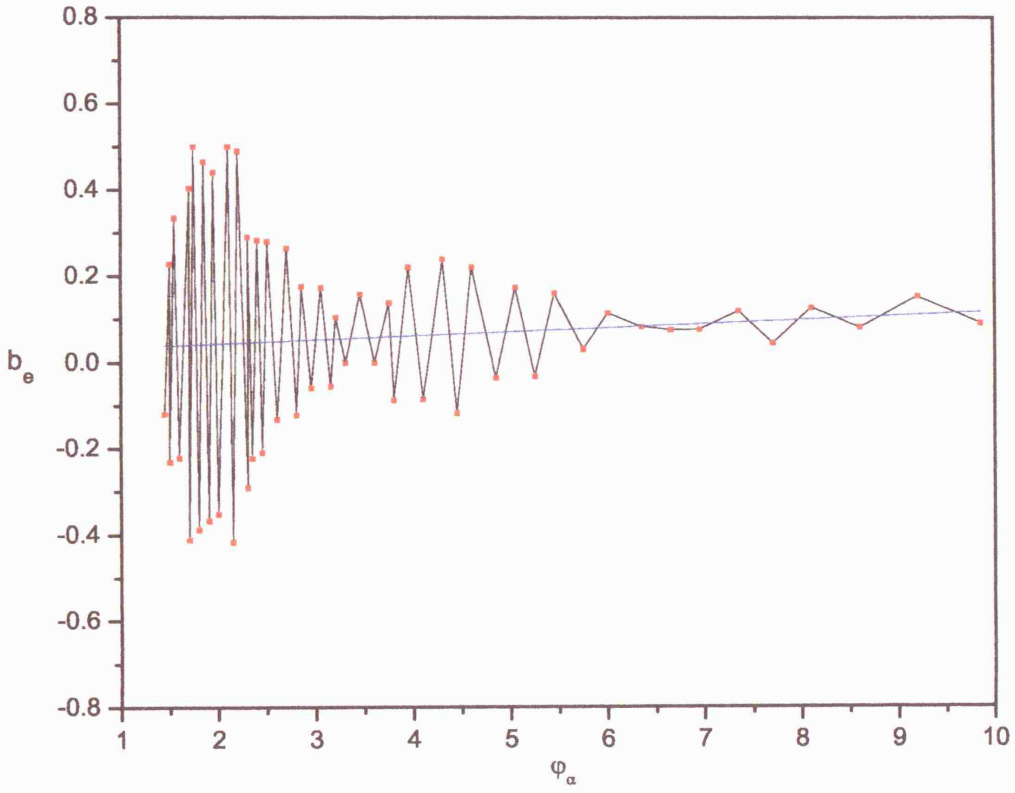

Figure 7.16: *Equivalent linear roll damping, b_e, plotted against mean roll angle between two successive peaks for monohull (red points). The black line shows the b_e variation. The blue line is a line of best fit to obtain linear and quadratic damping coefficients, b_1 and b_2.*

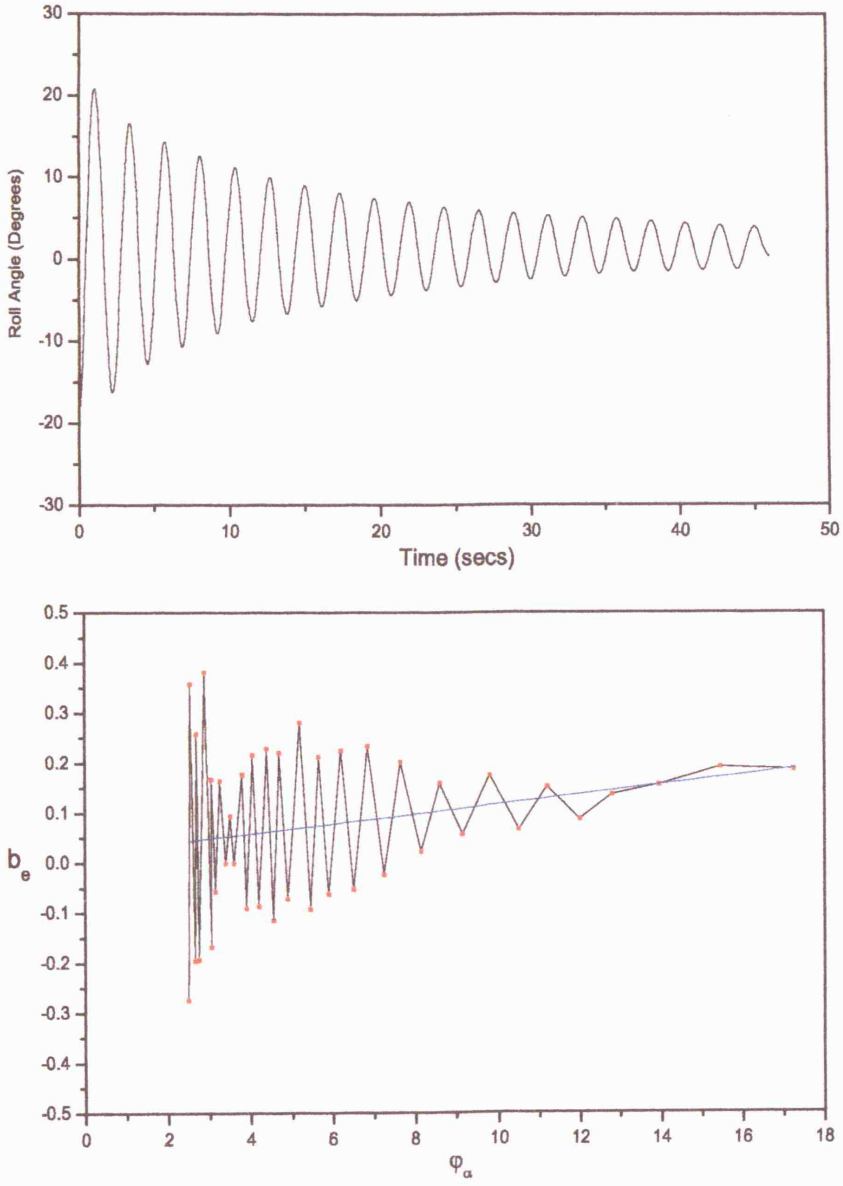

Figure 7.17: *Experimental roll decay for monohull model, initial roll to starboard, released at an initial angle of* 20°. *Equivalent linear roll damping,* b_e, *plotted against mean roll angle between two successive peaks (red points). The black line shows the* b_e *variation. The blue line is a line of best fit to obtain linear and quadratic damping coefficients,* b_1 *and* b_2.

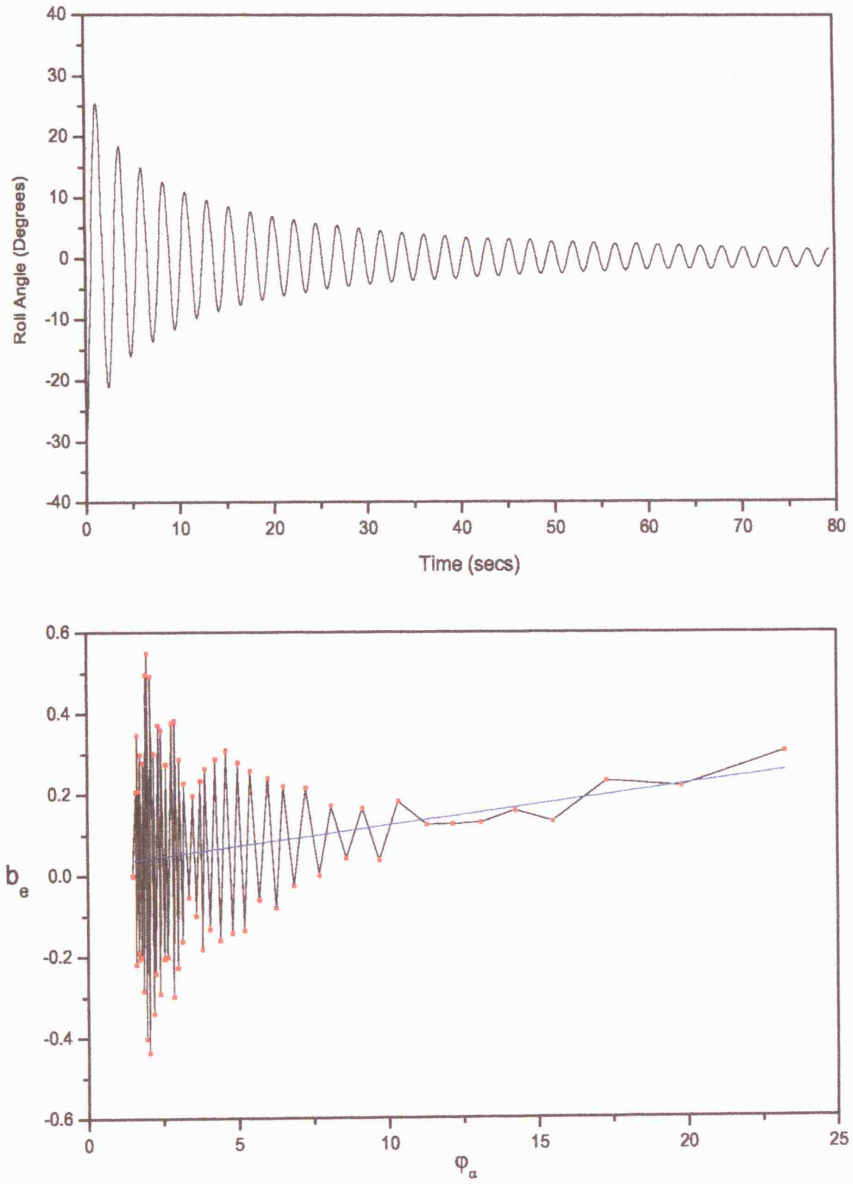

Figure 7.18: *Experimental roll decay for monohull model, initial roll to starboard, released at an initial angle of* 30°. *Equivalent linear roll damping,* b_e, *plotted against mean roll angle between two successive peaks (red points). The black line shows the* b_e *variation. The blue line is a line of best fit to obtain linear and quadratic damping coefficients,* b_1 *and* b_2.

As before, there is a large variation of the data points around the lines of best fit, especially at low roll amplitudes. Under these conditions, the following details were gathered:

	b_1	b_2	ω_n
10° Heel	0.024	0.234	2.72
20° Heel	0.0019	0.243	2.73
30° Heel	0.022	0.250	2.74

Table 7.4: *Linear and quadratic damping coefficients and natural damped frequency for each set of experiment.*

showing that the damping coefficients from the three different sets of experiments do not vary too much in magnitude hence providing validated approximations for when choosing b_1 and b_2 during numerical simulations.

Due to the considerable spread of the equivalent linear damping values, the line of best fit of the quadratic damping model is expected to vary for different runs. This means that it might not be possible to obtain stable damping coefficients from one run to the next using the quasi-linear method. Klaka (Klaka, 2001), reported problems with the stability of results from this type of analysis for his work on the roll motion of a circular cylinder with large appendages representing the keels of yachts. He attributed the variation in linear and quadratic damping coefficients to

different initial heel angles at the beginning of each experimental run.

In our experimental results changes in initial heeling angles do not verify Klaka's observation since the linear and quadratic damping coefficients do not vary too much between them. Hence our experiments may be considered as repeatable, providing similar damping coefficients but still leaving the issue of considerable spread of the damping data around the assumed quadratic model undetermined.

During the model experiments a number of interesting observations were noted. The roll motion never completely decayed away but the model would continue to roll at small amplitudes (typically less than one degrees) for quite a long period of time. The data logger was generally switched off after about one minute. For analysis, the recorded decrement was usually truncated once the roll angle reached this state.

The reason for the large spread of equivalent linear damping values, b_e, must be understood. Due to this spread damping coefficients may not be determined from any of the set of the decay experiments with any degree of certainty.

7.9 Coupled roll-heave free decay using a single degree of freedom equation of motion

It is clear from earlier discussions that the roll damping of the monohull model used in NTUA, may not be accurately determined with the assumption that roll decay can be adequately modelled as a single degree of freedom uncoupled roll motion with constant coefficients. Furthermore, with this assumption, measuring damping over one half a roll cycle instances of negative damping occur as we determined in the trimaran case as well. Realistically it is changes within inertia, added inertia or stiffness in the equation of motion that may cause the negativeness.

In response to this, it would seem wise to analyse the roll decay results in more than one degree of freedom, to establish if there are other types of motion that might cause changes in roll inertia, added roll inertia or roll stiffness. The challenge with this approach however, is that cross coupled terms have to be determined and these can not easily be measured in model experiments. As mentioned earlier from the recorded data of pitch and yaw, no signs of irregularity was present implying that these motions did not affect the roll decay of the model. Heave and the rest of the degrees of freedom were not accessible since the gyroscope used did not allow for their measurement. In any case, further experimentation was not possible and we feel it is necessary to consider other ways to examine and introduce changes in roll inertia, added inertia and stiffness into a single degree of freedom equation of motion using a simple manner.

During the roll decay experiments, the initial heel angle was induced by applying a force to the starboard side of the model which was then removed to instigate the decay. This in itself will induce a heave motion that decays at the heave natural frequency, say ω_h. If the model were undergoing coupled roll and heave motion,

the roll stiffness would vary with time as the waterplane area changes during heave. Thus coupled heave and roll free decay at zero speed may be modelled here using a single degree of freedom equation of motion.

More specifically, the coupling of heave and roll may be thought of as the sum of two effects. Pure heave motion induced by the removal of the force producing the heel angle (without roll motion) decaying at the heave natural frequency and roll motion (without induced heave) decaying at the roll natural frequency, ω_n. In other words, rolling around a fixed waterplane.

To maintain a single degree of freedom equation of motion, the heave motion is modelled only by the effect it has on the roll stiffness. Whilst the model heaves, the waterplane area changes which in turn causes the GM to change (as discussed in the early sections of this Chapter). Coupling heave and roll may be modelled in a simplistic way by modifying the roll stiffness term. These alterations in roll stiffness will be time varying with the equation of motion simulated in the time domain.

For clarity purposes, we note that for our monohull roll decay simulation, our adoption of coupled heave and roll as a single degree of freedom equation includes only the first two effects of the trimaran simulation mentioned in the first section of investigation of this Chapter, since evidently the extra hulls, sidehulls, do not exist in a monohull vessel.

We also note that cyclic variations in roll stiffness may cause parametric roll motion, but there was no evidence of this occurring in the free decay model experiments with our monohull. In real life instances, this may cause a problem in a seaway where heave motion will be induced by the waves as well as by roll motions and result in augmented roll amplitude motions.

7.9.1 Simulation with a single time varying sinusoidal stiffness term

Taking into consideration suggestions of the earlier section, the equation of simulated motion may be assumed to be of the following form;

$$\varphi'' + b_1\varphi' + b_2\varphi'|\varphi'| + \omega_n^2(1 + \alpha e^{\mu t}\cos\omega_h t)\varphi = 0 \qquad (7.9.1)$$

where α is a constant term representing the ratio of the amplitude of the variation in GM (due to the removal of the inclining force) over GM. Similarly as for the trimaran simulation, μ is a measure of the heave damping. Earlier reference to heave motion decaying after a couple of cycles, allows us to approximate this quick decay exponentially and with a sinusoidal function of natural heave frequency ω_h. The damping coefficients b_1, b_2 and the roll natural frequency ω_n were selected based upon the results of the quasi-linear analysis of the roll decrement (with 10^o heel) at calm water. In other words, $b_1 = 0.024$, $b_2 = 0.234$ and $\omega_n = 2.717\ rad/s$. α, ω_h and μ are allowed to vary.

Initially however, we introduce Figure 7.19, the equivalent linear roll damping plot against mean roll angle between two successive peaks, for the case with only linear damping considered, so that $b_2 = 0$ and also $\alpha = 0$, $\omega_h = 0$ and $\mu = 0$ in equation (7.9.1). The intercept is the actual value of b_1 derived from the roll decrement experiment with 10^o heel. We notice that since the system is linear, there is no scatter in the data points, reassuring that the fact that we are calculating the equivalent linear roll damping values over half a roll cycle does not influence or encourage the scatter. One might consider that the scatter in (φ_α, b_e) space may arise due to the reflection of the negative peaks into positive of the quasi-linear method, but using

the same method for this linear system, we confirm no variation in equivalent linear damping points.

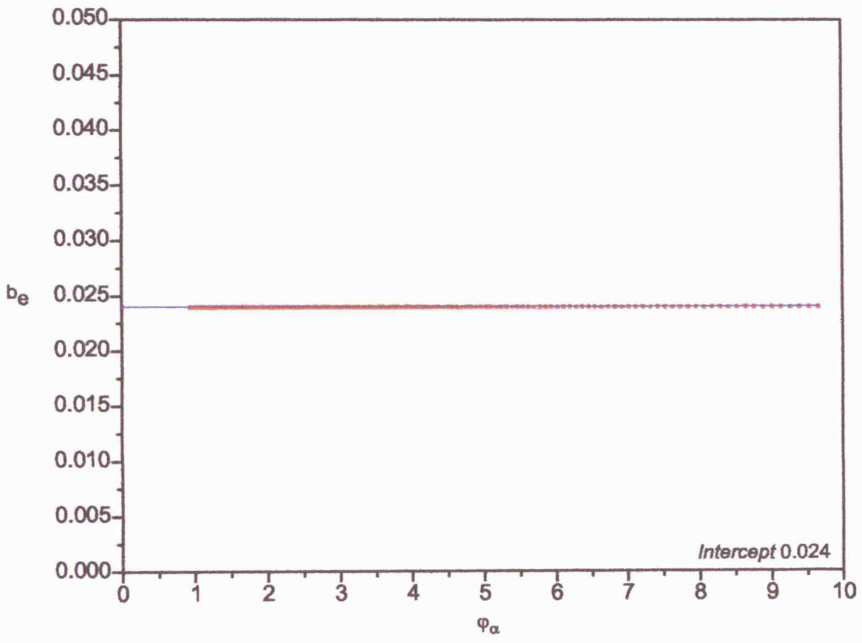

Figure 7.19: *Equivalent linear roll damping, b_e, plotted against φ_α for the case of linear damping. So $b_1 = 0.024$, $b_2 = 0$, $\alpha = 0$, $\omega_n = 2.717$, $\omega_h = 0$ and $\mu = 0$. The black line shows b_e variation. Blue line is a line of best fit.*

Figure 7.20 shows three different sets of plots of free roll decay and equivalent linear roll damping under various conditions. The first set is a time history response and a plot of the equivalent linear roll damping points calculated over half a roll period (in red), including also the b_e variation (in black) and a line of best fit (in blue) for the case without stiffness variation ($\omega_h = 0, \alpha = 0, \mu = 0$).

As expected, without stiffness variation, the equivalent linear damping calculated

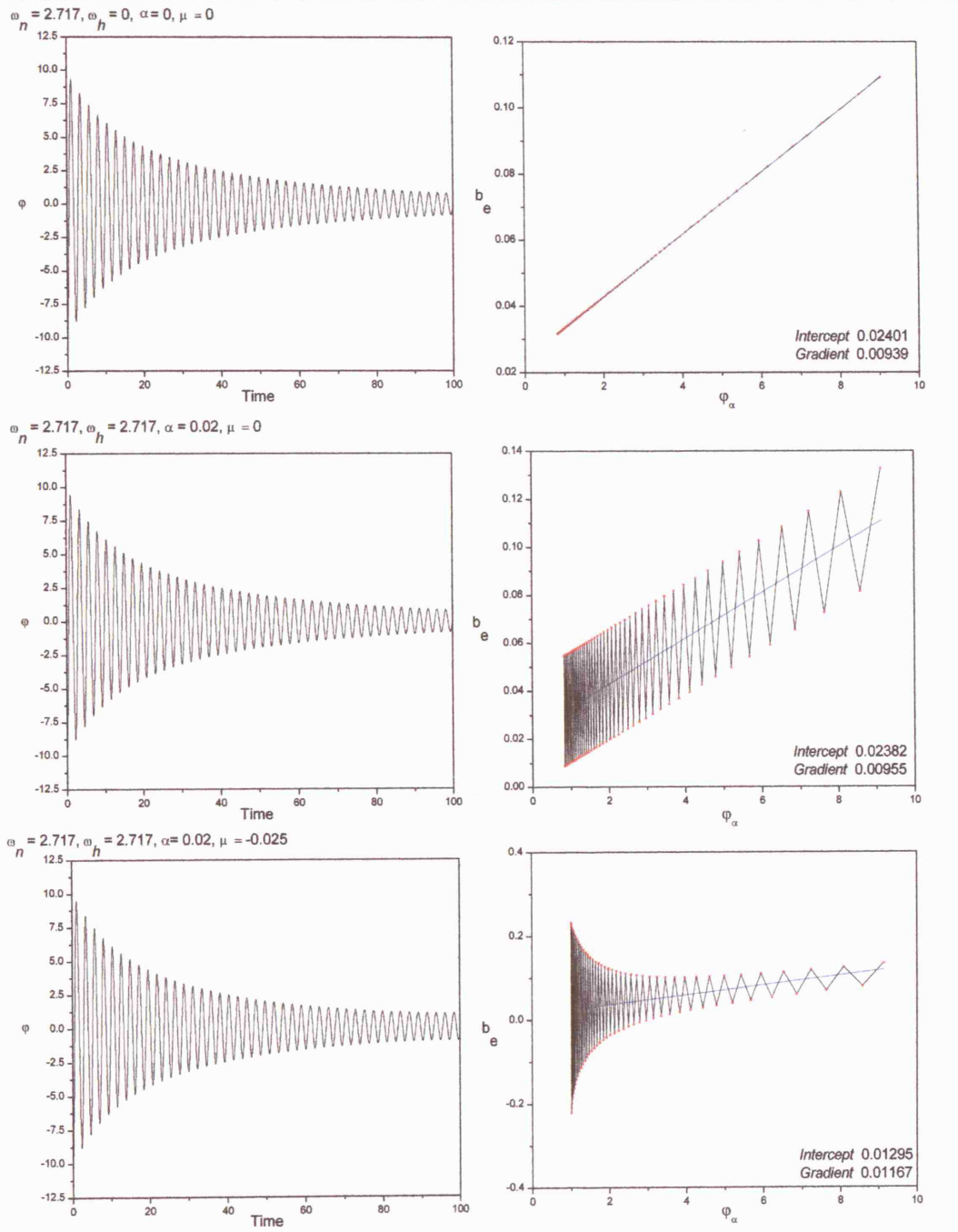

Figure 7.20: *Simulated roll decay data for the conditions stated within each time history plot. Equivalent linear roll damping, b_e, plotted against φ_α (red points). The black line shows b_e variation. Blue line is a line of best fit.*

from the peaks of the simulated decay match the damping model used in simulation. The middle set includes stiffness variation, but with heave natural frequency ω_h equal to the roll natural frequency ω_n, $\alpha = 0.02$ and there is no heave damping, $\mu = 0$. The set incorporates the simulated roll decay history and the corresponding b_e against φ_α plot. The variation of the equivalent linear damping is shown as black lines joining the red b_e points showing a significant spread in the equivalent linear damping values somewhat similar to the results from the experimental damping analysis. But yet the variation seems to be constant, unlike Figure 7.16.

In the third set the heave natural frequency is still equal to the roll natural frequency and $\alpha = 0.02$ but we have added heave damping to be of value $\mu = -0.025$ in order to see the effects of this inclusion. We notice that in the b_e against φ_α plot these conditions do not aid to mimic precisely the experimental Figure 7.16, even though at small roll angles there is a relatively high spread where the red points tend to a convex route. With μ positive, the points do not decay towards the blue line, the line of best fit, at high roll amplitudes, but react in an opposite manner, expanding away.

Figure 7.21 and 7.22 show sets of similar diagrams but when the natural roll frequency and the heave natural frequency no longer remain equal. The frequency ratio is $\frac{\omega_h}{\omega_n} = \frac{2.445}{2.717} \approx 0.9$, $\alpha = 0.03$ and the heave damping, μ, begins at zero (Figure 7.21) and then varies as stated in each plot of Figure 7.22.

Figure 7.21 portrays the scattering of b_e data points analogous to the experimental equivalent linear damping case but the dispersion magnitude does not seem to increase at small angles, as in Figure 7.16. Moreover negative damping is not evident hence not fully providing an adequate representation.

In Figure 7.22 we notice that each b_e against φ_α plot is initially similar at large

angles with differences remaining at smaller roll angles, where the spread of the equivalent linear damping results is greater as μ decreases.

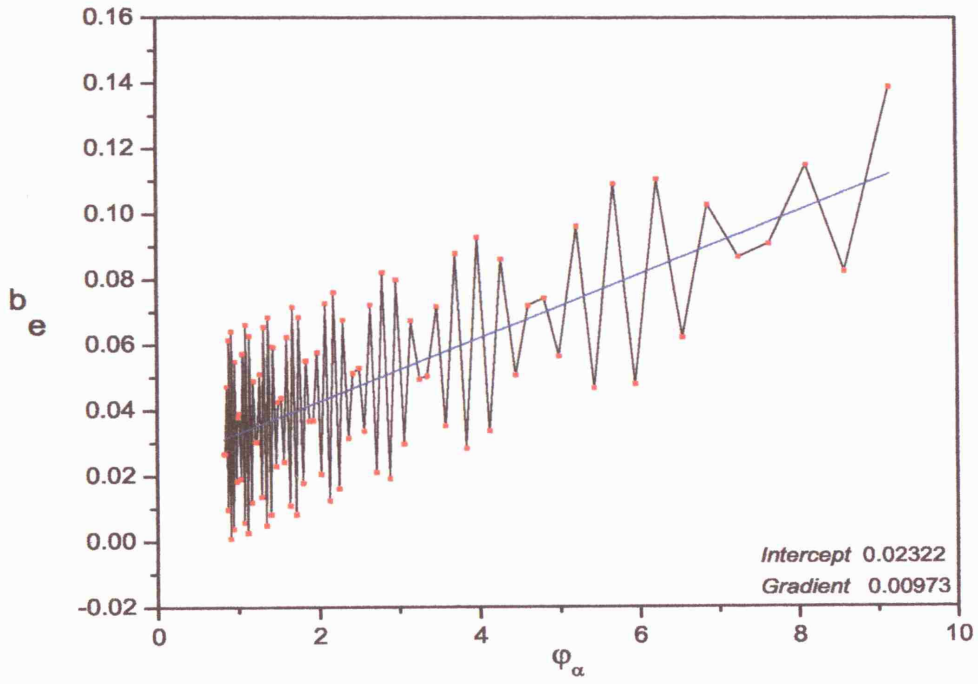

Figure 7.21: *Simulated equivalent linear roll damping, b_e, plotted against φ_α (red points) for the simulated equation of motion. The black line shows b_e variation. Blue line is a line of best fit. The frequency ratio is* $\frac{\omega_h}{\omega_n} = \frac{2.445}{2.717} \approx 0.9$.

When the ratio is approximately $\frac{\omega_h}{\omega_n} = \frac{2.9887}{2.717} \approx 1.1$, similar roll decay tests were computed with the corresponding b_e against φ_α plots at the various heave damping values to form Figure 7.23.

Hence, we may conclude that our simulations show that the heave damping frequency

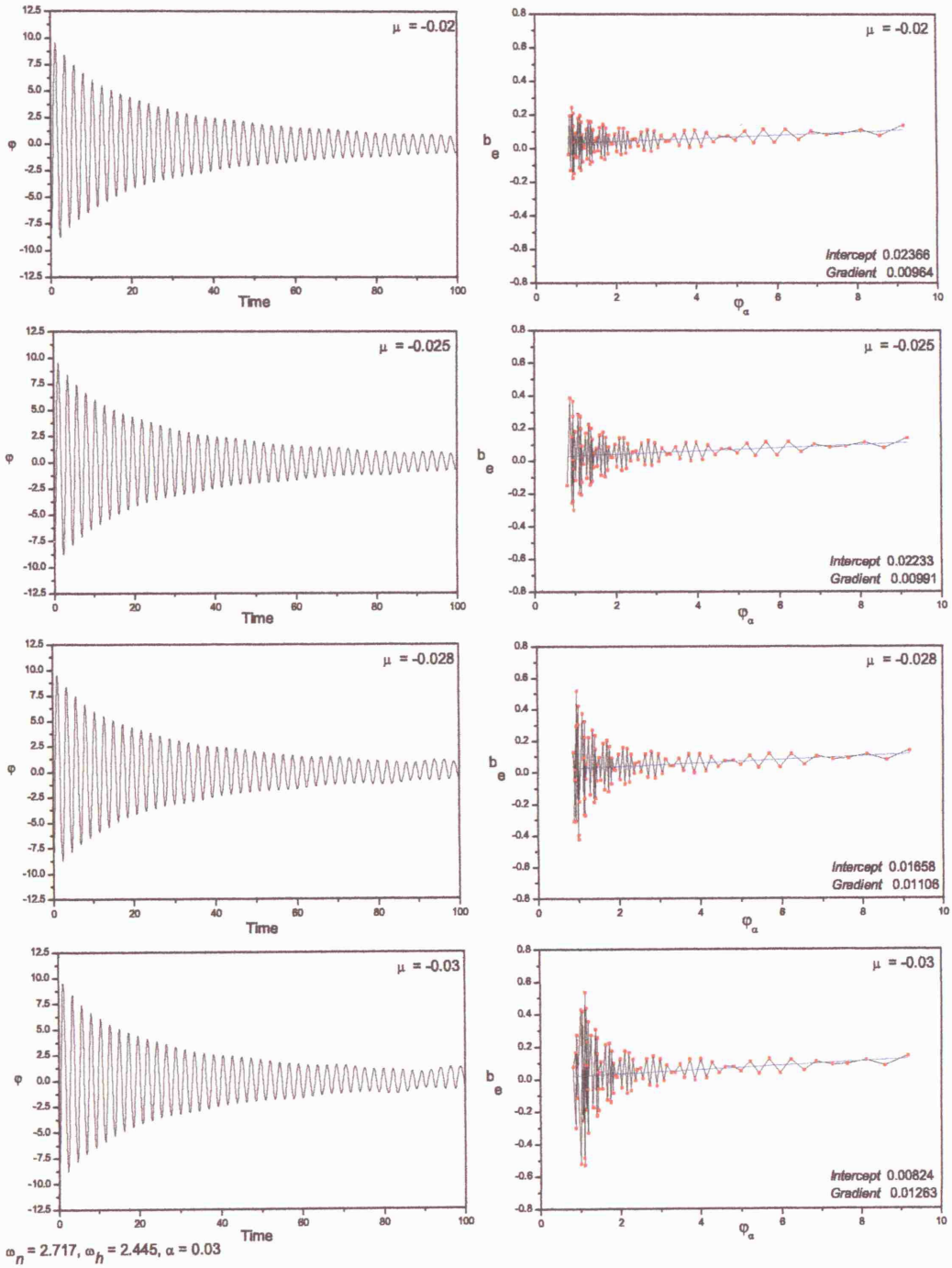

Figure 7.22: *Simulated roll decay histories and corresponding equivalent linear roll damping, b_e, plotted against φ_α (red points). The frequency ratio is $\frac{\omega_h}{\omega_n} = \frac{2.445}{2.717} \approx 0.9$ and heave damping varies.*

has a significant effect on the spread of the equivalent linear roll damping calculated for every half roll period. There exists a spread of equivalent linear damping points when the heave and roll frequencies coincide, however at this instant, no incidences of negative damping appear in the simulation. This phenomenon appears to occur once the frequencies differ and as heave damping decreases, μ, the negative and positive b_e values reach greater peaks (see case $\mu = -0.03$, where $b_e \approx 0.8$ and -0.6 at $\varphi_a = 1^o$).

So, a spread in the equivalent linear roll damping measured using the quasi-linear method for every half roll cycle is possible if there are sinusoidal variations in the stiffness term. The magnitude of this spread across the decay is affected by the ratio of the heave and roll frequencies. Heave damping will cause the spread to reduce or increase accordingly towards the end of the decay when the roll amplitudes are small.

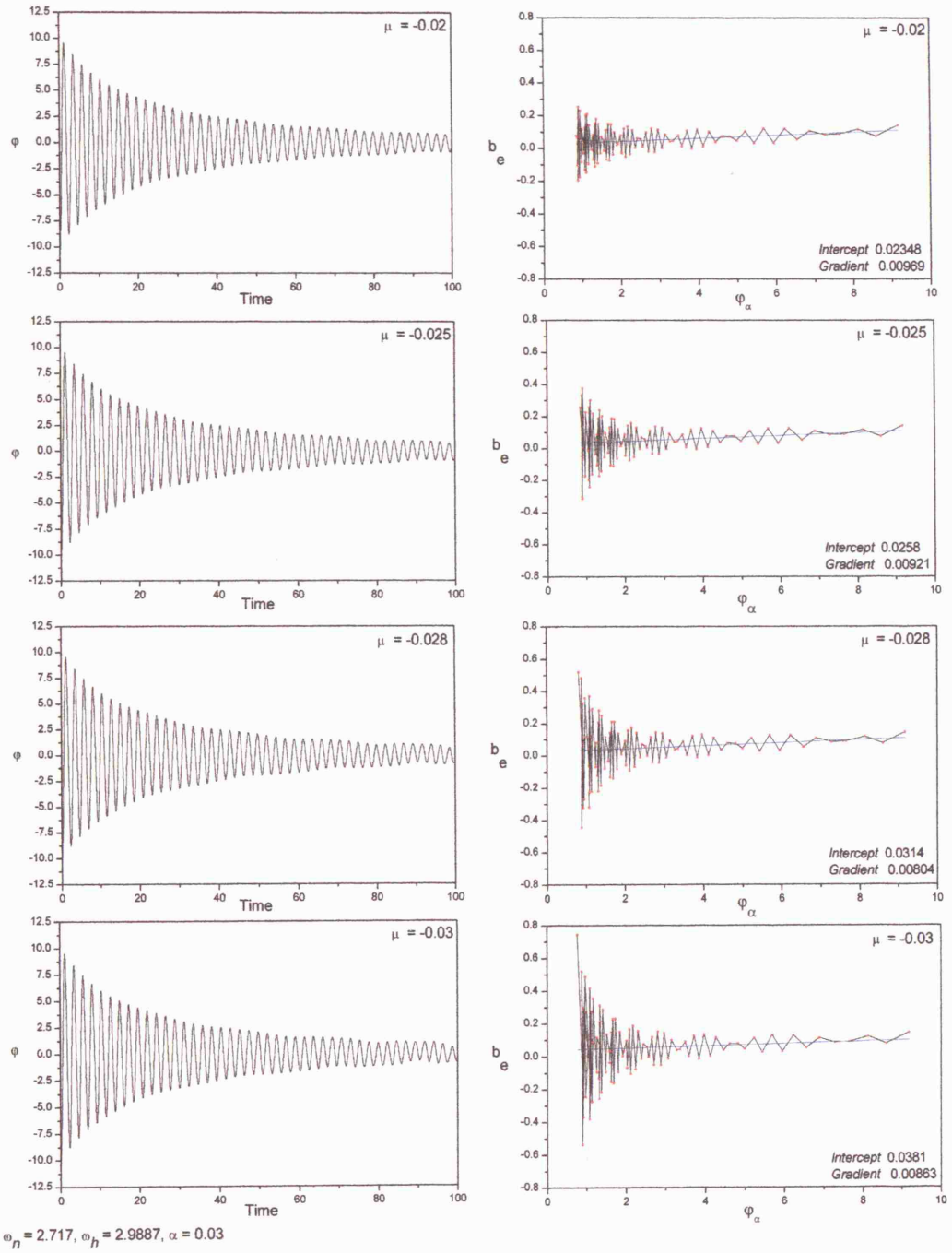

Figure 7.23: *Simulated roll decay histories and corresponding equivalent linear roll damping, b_e, plotted against φ_α (red points). The frequency ratio is $\frac{\omega_h}{\omega_n} = \frac{2.9887}{2.717} \approx 1.1$ and heave damping varies.*

7.9.2 Conclusion of roll decay tests for monohull

The analysis of experimental roll decay tests showed a spread in the equivalent linear damping when calculated for each half roll period. This spread was at greatest at low roll amplitudes where some values were negative implying an input of energy. Using a line of best fit linear and quadratic damping coefficients were determined.

From our numerical simulations this indicates that there was some heave amplification. To obtain incidences of negative damping in the simulation with the heave and roll natural frequencies set equal to one another, the heave damping term, μ, had to be negative. When the frequency ratio was also less than or more than one, negative values of b_e were present with a spread mimicking more successfully the version of the experimental b_e against φ_α plot.

Our simulation of a single degree of freedom roll equation with a quadratic damping model and a time varying sinusoidal variation in GM equivalent to a sinusoidal variation in stiffness causes a spread in equivalent linear damping values when calculated between two successive peaks of the roll decrement.

The system of proposed equation reminds us of the parametrically excited pendulum system studied in detail within earlier parts of the thesis but where the heave amplification was constant and the damping term was linear with no consideration of quadratic damping components.

The spread is at its maximum when the frequency of the GM variations is equal to the natural roll frequency and reduces in magnitude as the two frequencies become ratios of each other, causing uneven spread, better describing the experimental equivalent linear roll damping plot. In addition, incorporating an exponential damping term in the variation causes the overall spread at low angles towards the end

of the decay to reduce whilst heave damping is increasing. Hence we have managed to show that our simulations of our proposed coupled heave and roll motion under a single degree of freedom equation, for the monohull model, do match the experimental equivalent linear roll damping output.

These simulations and theoretical results might indicate that in the model experiment some form of heave excitation was present and must be considered if more precise roll decrement results are to be examined to produce appropriate damping coefficients of a model in the future. Since our onboard gyroscope did not provide us with heave data during our experimental work, as this type of motion could not be measured using this Institutions gyroscope, further verification and analysis is no longer possible to be able to support fully our simulation and hypothetical approach of free roll decay. Hence investigations of how heave varies during roll decay are also required before any further conclusions can be drawn form this analysis. We have to leave this as a future aim for further investigation.

7.10 Transient Capsize tests

This final section of this Chapter comprises of a continuation in our experimental work at NTUA but tackling a different issue, that of capsize. In order to produce and complete a comprehensive experimental application of the escape phenomenon, examined both analytically and numerically for the case of the parametrically excited pendulum model within Chapter 2 and 3, as well as associate the theoretical findings of Chapter 5 to corresponding practical investigation, we conducted transient capsize tests on the monohull provided. We examine transient capsize due to the danger of damaging expensive equipment, and since actual physical capsize of the model was not permitted. Therefore, the intention is to analyse the transient roll motion (instead of the steady state roll) with the view of predicting capsize.

Since escape from the potential well of the parametrically excited pendulum system has been our major analytical and numerical concern of danger within a mechanical system, as seen in earlier parts of the thesis, it only seems fair to accomplish a link of this phenomenon with that to the analogous case of capsize in the field of ship dynamics.

From a naval architecture perspective, capsize is considered to occur via four basic mechanisms. These are typically referred to as pure loss of stability, broaching, parametric resonance and beam sea capsize.

Pure loss of stability occurs when buoyancy is lost as a ship sits on the crest of a wave-the upright position can lose stability in this way. The second capsizing mode is surf-riding and consequent broaching. Large following waves acting on the ship can force her to move with the same speed so that the ship begins to move with the wave simultaneously. This is called surf-riding and the majority of ships are directionally

unstable during surf-riding so that the ship can experience an unsteered turn to a beam position relative to the waves. It is the dramatic turning and heeling that may lead to capsize (Spyrou, 2000). Parametric resonance, is the case we have described in detail at the beginning of this Chapter where longitudinal waves excite the vessel at twice the natural roll frequency thus leading to large resonant roll amplitudes and possibly capsize. Beam sea capsize is caused by waves arriving from the side of the vessel directly exciting large angle roll motions (recall Chapter 5).

In recent years there have been considerable advances in the nonlinear modelling of ship capsize. There remains though still, a lack of experimental work in this field (Contento *et al*, 1996). Whilst the modelling of the above mechanisms has often taken a multi degree of freedom approach (Kan, Saruta and Taguchi, 1991, Kan and Taguchi, 1993, Chen, Shaw and Troesch, 1999), the ultimate precursor of capsize must be large angle roll motion. For this reason we focus here on the problem of beam sea roll. Another reason for considering this experimental model of capsize instead of, for example the influence of parametric resonance, is because of the experimental configuration. During the period of our stay at the NTUA, the experimental arrangement provided to us only made it possible to examine beam sea rolling. A series of experiments was therefore performed to test our theoretical predictions for the monohull model at the NTUA laboratory's wavetank.

Before we embark on the description of the experimental arrangements, we ask ourselves, why can ships capsize at all and why are they not built is such a way that capsizing may just be impossible. Clearly the answer lies on the fact that in ship design a compromise must be reached between many requirements, some of which conflict with ship stability. The vertical position of the centre of gravity is a typical case. A vessel can be built with such a low centre of gravity that the only stable floating position is upright, so that no matter how large the disturbance such vessel

experiences, it will always return to its original position.

Unfortunately however, such flexibility in positioning the centre of gravity of a vessel is not available when designing most merchant, naval or work vessels. The final position of the centre of gravity is the result of a large number of factors involved in the ship's layout. As a result, there exist indeed other stable floating positions apart from the desirable one, the upright state. The vessel is drawn towards these positions and therefore towards capsize, by unacceptably large amplitude motions. This stresses our interest in turning our attention to the production of large amplitude motions, particularly roll motion.

7.10.1 Experimental Details

A wire mesh is placed infront of the paddle to damp out high frequency "ripples" on the wave surface. The throw, being the amplitude of paddle motion, controls the height of the wave and the wave frequency is controlled by varying the paddle oscillation frequency (recall Figure 7.13).

In order to measure the actual height and frequency of the mono-chromatic wave, a wave probe is inserted within the towing tank and connected to a computer for data acquisition, at a sampling rate of 10 Hz. Labview data acquisition software was used to both acquire and manage the data. The wave probe was positioned at approximately 10 m from the wave maker and 0.5 m behind the model. The model was free to drift slightly but restricted from excessive motions in the other degrees of freedom, so that emphasis may be placed on our concern of roll motion. The restriction was imposed by using loose pieces of string that were tied at the bow and stern of the model and controlled from the sides of the tank. This also prevented the model from undergoing unnecessary yaw motions so as to avoid hitting the sides of the tank.

Some limitation in the apparatus did exist in the generation of large amplitude, long period waves. The roll angle was measured using the gyroscope situated securely on the deck of the model attached by an umbilical cable which was held loosely above the model to minimise any effect on the rolling. Data was recorded via the cable onto a computer, providing information on roll amplitude, pitch, yaw with respect to time (in seconds).

In order to diminish the mirroring effects of the waves, at the opposite end of the tank, away from the paddle, irregular concrete blocks with a porous foam cover were installed. These are referred as "beaches" and are used to minimise the interference

of the reflected waves by absorbing energy of the waves. The effect of reflections is to cause modulations in the wave amplitude once a steady state is reached. These modulations were, however, quite small compared to the wave amplitude.

Most importantly we also note that the transient capsize tests were performed at a later stage compared with the roll decay tests. The same monohull model was used but due to a change in position of the magnetic masses within the model or change in the position of the gyroscope, the set up was not identical thus having an effect on the natural roll frequency. For these transient capsize tests, $\omega_n = 2.992\ rad/s$ as opposed to the value of $\omega_n = 2.717\ rad/s$ derived from the monohull roll decay tests.

Before switching on the wavemaker, any oscillations were allowed to die away. For each amplitude of paddle motion and wave frequency, the monohull was allowed to roll and wave data recorded. As actual physical capsize of the model was not permitted we are allowed to assume that capsize may be considered and represented when a maximum roll angle of $\varphi = 20^o$ is reached and exceeded.

The table that follows, Table 7.5, consists of columns identifying: specific ratio of wave frequency to natural frequency, $\Omega = \frac{\omega_f}{\omega_n}$ (in radians per second), frequency of the generated waves in Hertz and different wave amplitudes (A) in centimetres. To calculate Ω, the wave frequency is converted into radians per second by multiplying by the frequency value in Hertz by 2π. Not all conditions were attainable in the NTUA towing tank especially those where $\Omega < 0.85$.

$\Omega = \omega_f/\omega_n$	Frequency (Hz)	Amplitude (cm)						
0.85	0.405	5.956	6.807	7.942	9.530	11.912	15.883	23.825
0.9	0.429	5.313	6.072	7.084	8.500	10.626	14.167	21.251
0.95	0.452	4.768	5.449	6.358	7.629	9.537	12.715	19.073
1.00	0.476	4.303	4.918	5.738	6.885	8.607	11.476	17.213
1.05	0.500	3.903	4.461	5.204	6.245	7.807	10.409	15.613
1.10	0.524	3.556	4.065	4.742	5.690	7.113	9.484	14.226
1.20	0.571	2.988	3.415	3.985	4.782	5.977	7.969	11.954

Table 7.5: *Particulars of the wave frequency and amplitude.*

Some examples of time history responses of the monohull model under the specified forced wave conditions may be seen in Figure 7.24. When the amplitude of the transient roll motion exceeds $\varphi \approx 20^o$, then we consider that the model has capsized otherwise the model performs roll oscillations. The top row represents transient noncapsize motions whereas the bottom row the transient capsize motions where the roll amplitude exceeds the capsize criteria are clarified by the dotted red lines.

Following our discussions within Chapter 3 and 4, we note that these roll oscillations still may not be presumed as safe since any type of induced oscillation, especially with large angular displacement, may be considered as dangerous with disastrous outcomes.

For the time history of wave frequency $0.452Hz$ and $A = 7.629cm$ in Figure 7.24 we notice that the steady state is safe but initial transient leads to capsize. This is a significant finding. In this case, if we were considering the steady state response to configure the capsize boundary, then the effect would be a shift upwards delaying the escape phenomenon.

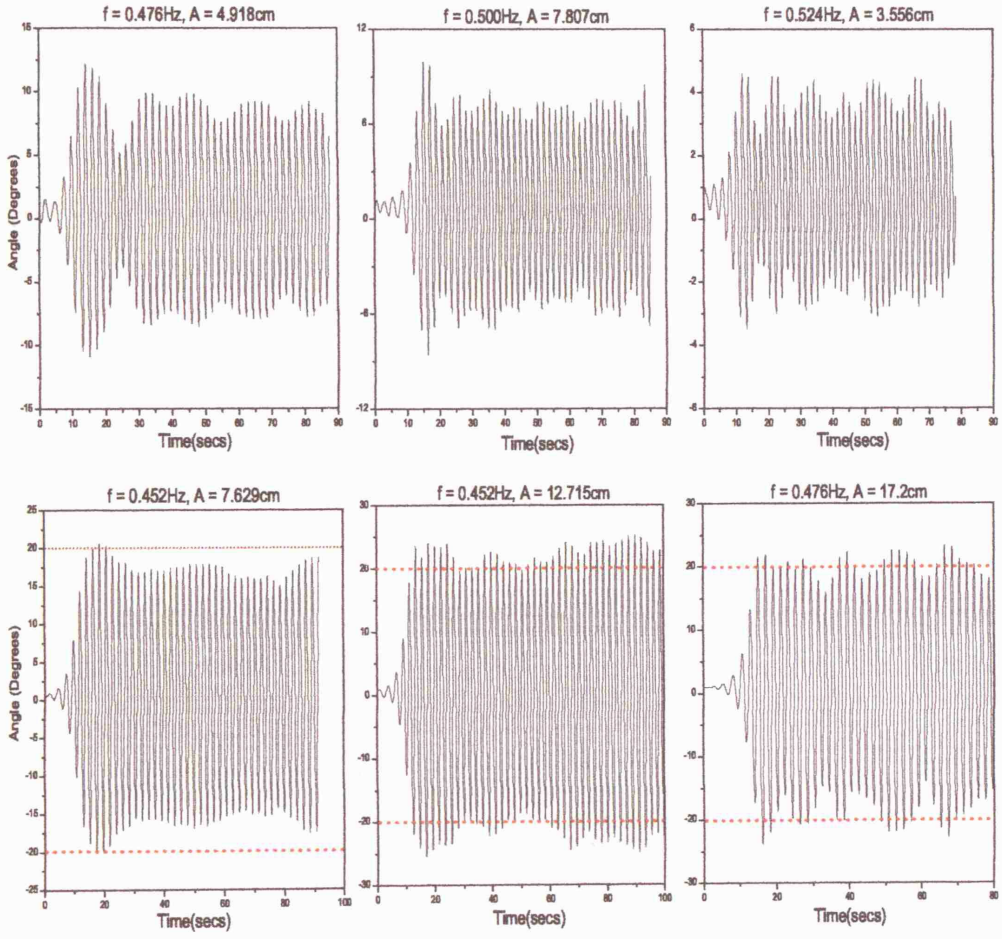

Figure 7.24: *Transient roll motion identifying noncapsize and capsize incidences.*

In the continually changing conditions of the ocean however, a ship will only rarely operate in a steady condition, hence understanding and incorporating transient motion is very important.

With the aid of this time series in Figure 7.24, we propose that the level of excitation required for system escape during a transient is lower than that of the steady state and thus safety margin predictions based on steady states could overestimate the true safety margin. Moreover, we emphasise that naval architects should pay more attention to capsize under transient, rather than steady state conditions.

Collecting the outcomes of capsize and noncapsize transient motion from our experimental testing we are able to produce a Transient Capsize diagram as seen in Figure 7.25 of wave height A against Ω. The figure shows runs coloured in black where noncapsize experimental tests were achieved under the specific wave frequency and wave amplitude input. Red boxes represent transient capsize motion where a certain maximum wave amplitude and frequency produced a transient roll response that exceeded the capsize criteria.

For comparison, the diagram also includes a numerically determined capsize curve based on steady state responses, for an unbiased linear roll equation of motion in beam seas (linear form of (7.4.1)) calculated by Cotton and Spyrou (Cotton *et al*, 2001) based upon a smaller model hull. Of course, since the curve was based upon the dimensions of their experimental model hull, their model's moulded depth registered $0.097m$, the beam or breadth $0.18m$ and the model's length was $0.57m$, we do not expect an excellent fit but merely an indication that the dangerous regions are close.

The purpose of including the blue curve in Figure 7.25 is to compare our results with other similar tests. Encouragingly, the predicted capsize boundary, is close

to that found in the tests. These differences in model size will effect the natural frequency of roll for the models, hence a perfect match in capsize boundaries is not anticipated. We also remember that we do not expect the steady state capsize line to give a particularly good fit to the data since our experimental capsize tests were essentially transient however in fact the fit is reasonable.

We may also speculate here that since the model by Cotton and Spyrou (Cotton *et al*, 2001) has a lower freeboard, the vertical distance between the waterline and the upper deck, than our passenger ferry model, changes in the stability curves are inevitable. Hence a quicker or slower route to capsize is awaited.

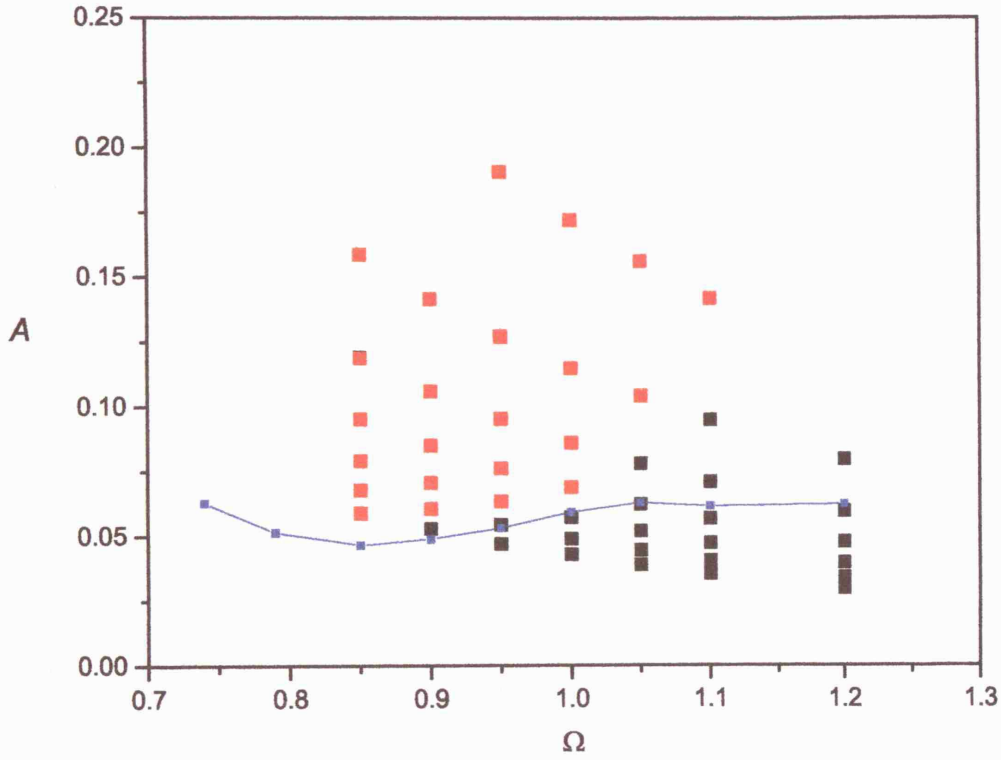

Figure 7.25: *Transient Capsize diagram. Red boxes indicate transient capsize, black boxes noncapsize conditions in the NTUA wavetank. The blue line is a numerically generated steady state capsize line for an unbiased roll equation of motion calculated by Cotton and Spyrou (Cotton et al, 2001).*

One of the key features of nonlinear systems is the sensitivity to initial conditions. If time was not a hindrance during our research visit to NTUA, more experiments could have been performed taking this comment into consideration. This could be achieved by starting the wavemaker paddle from different positions so that the wave build up can be varied thus varying the initial conditions of the system. In other words examining if the wave build up is initiated by a trough or a crest. The effect of this upon capsize could be observed. The importance of such initial conditions in determining the outcome of transient roll may be considerable for the experimental testing of new designs.

Another issue that we raise for future experimental advances is the existence of bias and its implications for modelling capsize. Our knowledge and analysis of numerical and analytical work within Chapters 4 and 5 show that asymmetry causes dramatic drops in the boundary of safe operational region. Experimental verification would form a strong case and shed new insights on the issue of asymmetry within vessels and results of new transient capsize tests could then be compared to theoretical and numerical simulations.

7.11 Final Remarks

In this Chapter the roll decay of a monohull model and of a trimaran with haunches was investigated. The monohull experimental testing was performed at the NTUA, whereas for the trimaran comparison, we found it necessary to adopt roll decay experimental data from recent research undertaken at Qinetiq in collaboration with UCL.

In both cases, it has been shown that it is not possible to extract roll damping coefficients from model experimental data if analysis is performed on a single degree of freedom roll equation with constant coefficients.

For the monohull case, it is deduced that the reason for this could be because of the heave motion induced once the force applied to create the initial heel for free roll is removed. In the trimaran scenario, an extra form of heave motion is suggested to be induced by the roll motion due to the haunches on the side hulls and these must be properly accounted for in the equations of motion.

Analysis of the experimental data was conducted for both model vessel types, using a quadratic damping model. The equivalent linear damping was calculated for each half roll cycle and at low roll amplitudes negative damping values were presented.

To support the idea that roll and heave are coupled during the roll decay, simulations were performed in the time domain using a single degree of freedom roll equation with a single time varying sinusoidal function for the monohull and a double time varying sinusoidal function for the trimaran model, describing the roll stiffness. These equations of motion were also referred to relate to the equation of motion of the parametrically excited pendulum and the double parametrically forced pendulum equation, both examined and discussed in detail in earlier chapters.

This allows the coupling between heave and roll to be modelled in a simplistic manner. Using these equations, a spread of equivalent linear damping data was obtained which was similar to those observed in the model experiments.

For the monohull roll decay equation of motion the stiffness variation comprised of the heave motion stimulated by the removal of the inclining force and this term occurred at the heave natural frequency. For the trimaran roll decay equation of motion, the above term was incorporated as well as a second heave component induced by the submergence and emergence of the haunches within the water during roll motion. This latter term occurs at the roll natural frequency.

During the monohull experimental testing heave response was not measured due to lack of experimental capabilities and time limitation created an obstacle for further investigations. So, in order to create a strong case for the hypothesis, we found it necessary to employ not only roll but heave data time histories for the same trimaran model provided to us by the current Naval Architecture and Marine Engineering Research team at the Mechanical Engineering Department at UCL. With this in hand we were able to show the existence of heave motion occurring at a range of individual frequencies which are suggested to be related to the roll and heave natural frequency.

In this series of monohull tests, we also added the experimental evidence of transient capsize. This involved considering the capsize of the monohull model given the onset of a wave of a certain amplitude and frequency. Our experimental transient capsize points were also compared with a previously studied numerical steady state capsize boundary computed by Cotton and Spyrou (Cotton *et al*, 2001) but for a different monohull model still though, providing a reasonable fit. The significance of transient capsize as opposed to steady state capsize was also noted.

Finally, the transient capsize tests managed to produce an experimental application of the escape phenomenon examined both analytically and numerically for the case of the parametrically excited pendulum model within Chapters 2 and 3. Moreover, we linked the theoretical findings of Chapter 5 to the practical investigation under consideration.

Chapter 8

Conclusions

In this thesis we have attempted to improve our ability to use nonlinear dynamics in the parametrically excited pendulum system with a view to generating new extensions to existing research and further endeavour to propose fresh applications of the model to the area of ship dynamics with the aspiration of developing alternative approaches to roll damping assessment.

We have explored a number of different areas whilst always aiming to focus on obtaining a better understanding of the involved nonlinear dynamics. Furthermore, we have accompanied these studies with experimental support showing the significance of nonlinear dynamics within this field.

The first part of this thesis is a review of the background to this work, highlighting our aims and motivation for this research.

We continue by configuring the equation of motion for the vertically driven pendulum whilst relating the system's behaviour to the Mathieu equation. Analytical techniques are employed to distinguish and determine the stability boundaries for the resonance zones over a certain parameter range for both systems, showing their

inter-linkage.

Two approximate analytical methods are applied to envisage the parameter region where no major stable non-rotating orbits exist for the parametrically excited pendulum termed as escape. This allowed much of the bifurcational behaviour to be predicted. Our adopted analytical procedures were compared with each other as well as with current literature results in order to show adequacy in the approximations of the escape zone. Both methods offered reasonable and fairly good representations to the escape zone, especially at higher frequencies.

Particular attention to the dynamics in the lower resonance zones has also been paid, since previous researchers have overlooked these regions. The effect is producing a detailed bifurcational study of the major and minor tongues generating a more complete picture of the phenomena undergone and that characterise the control parameter space.

Numerical work aided to exemplify that the symmetry-breaking, pitchfork bifurcation takes place when one eigenvalue of the solution reaches 1. From an additional perspective, the mechanism of the symmetry-breaking, pitchfork bifurcation has been characterised by a pinched cylinder and compared geometrically with another type of bifurcation, that of period doubling.

The experimental importance of the symmetry-breaking phenomenon undergone by the oscillatory symmetric solution of the model is also discussed whereby a reduction in amplitude swing can act as a precursor of the bifurcations that will soon follow and more specifically of the escape boundary.

We give a major emphasis on the nonlinearity of this model and its application extended to engineering problems. The system's nonlinearity means that possibly

all frequencies below the largest resonance zone in the control space have potential dangers and we suggest that engineers should always aim to operate at larger than $\omega > 2$ values. The need to understand more about the different types of oscillatory solutions was motivated by the fact that in some applications of the parametrically excited pendulum, the main interest is in achieving periodic solutions that do not exceed $\theta = \pm\pi$ as this might correspond to some failure in operation in some sense.

A major part of this thesis is concerned with breaking the initial symmetry of the parametrically excited pendulum model. We are of the opinion that perfect symmetry assumed in any physical representation of a mathematical model can never quite be achieved, even with thorough and detailed experimental arrangements. Hence we believe it is necessary to gain a deeper understanding on how breaking the symmetry of a system can affect its bifurcational behaviour so that to present a better physical realisation of the problem and create more feasible and strict boundaries for the safe operation of systems. With this in mind, we embarked on an investigation, using two different ways, on breaking the symmetry of the parametrically driven pendulum. Firstly by an inclusion of a bias term in the symmetric equation of motion and secondly by inclining the corresponding inverted case by an angle.

We are of the opinion that imperfections and unforeseen uncertainties in experimental testing may make it difficult to yield accurate results and may also cause significant discrepancies between experimental data and analytical expectations. So here, we sought to examine the origin of such deviations by considering these two mathematically asymmetric modelled cases.

For the first non-symmetric problem using the bias term inclusion, a harmonic balance approach was implemented to evaluate an approximation of the boundary of the escape region as the symmetry breaking term is varied. The simple asymmetric

system exhibited various nonlinear phenomena, such as cascades of period doubling bifurcations.

Emphasis was given to the disappearance of the symmetry-breaking, pitchfork bifurcation, that is present in the symmetric counterpart, due to the addition of imperfection term. The drop in the positive amplitude response side experienced by the oscillatory solution, has a significant experimental result, whereby a visible decline in the swing angle can predict that something will 'soon' happen as parameters are varied which will be of rotational nature. The asymmetric perturbation produced a qualitative change in the behaviour of the system, which is also apparent for the inverted tilted driven pendulum case.

Due to the asymmetry, it is also confirmed that an appearance of the first period doubling in its sequence leading to cascade triggers escape from the potential well and we recommend that this bifurcation may also be regarded as a precursor of the imminent danger and difficult operation of a practical system.

One of the major new features of this thesis is a construction and determination of a safe zone in terms of the (γ, p) control space, with the aid of numerically computed bifurcation diagrams during a variation of γ. The significance of the region within the boundary points was noted and the dramatic drop in safe oscillatory motion was embodied. Basins of attraction were also studied and compared for the symmetric and asymmetric counterpart, to show the reduction in basin of the oscillatory solutions as the bias term increases.

In order to compare the results derived from breaking the initial symmetry of the model by a bias term, we considered breaking the symmetry of the inverted parametrically excited pendulum by tilting the model by an angle. Numerical investigations were undertaken for the tilted inverted system and compared with its symmetric

counterpart. Another aim was to examine the origin of how the subcritical pitchfork bifurcation experienced in a symmetric system is replaced in the asymmetric case by disconnected branches, one of which undergoes a saddle node bifurcation. Analytical techniques using the method of multiple scales allowed us to verify the above behaviour of the inverted solution of the vertically tilted parametrically excited pendulum model.

In this thesis we also moved our attention away from the actual parametrically excited model and concentrated on the effects of symmetry breaking to the field of our growing interest, ship dynamics. This deviation in systems allowed us to examine actual practical characteristics that induce asymmetry that may occur under real circumstances, such as shifting in cargo or added mass within a vessel, and we studied their effects with respect to a specific ships stability in calm water. Examples such as these are what we presume an imperfection term may represent in a single degree of freedom roll equation and our general result showed that the farther towards the port or starboard side of a ship an external added mass is placed from her original centre of gravity, the smaller heeling angle is needed to capsize her since the range of stability will decrease.

We further investigated this mathematical representation for a ship in beam seas, to be able to confirm the oscillatory safe zone we computed for the parametrically excited pendulum case. We undertook beam waves as the external forcing because these types of seas are considered to be the most dangerous that provoke large amplitudes that lead to the capsize problem.

We produced basins of attraction for rising bias and we quantified the basin erosion of non-capsizing regions, providing a safety index as the value of bias increases. We showed an agreement between our two investigatory systems, identifying similarly

evidence of drop in safe operating regions. We enforced the sensitivity to bias and its significance for ship criteria and capsize testing. We demonstrated here that small biasing from symmetry can lead to a sudden reduction in the domain of capsize. In reality there will always be some bias in a ship and so we advise that these effects must be considered by naval architects especially during their design process.

Moreover this thesis includes an extension to the parametrically excited pendulum system where now we progressed to oscillations which are acted on by a combination of two parametric forces. We considered therefore what happens to the parametrically excited pendulum model when subject to a two frequency combined parametric excitation.

To provide an outline and understanding of the stability regions of our two forcing system, we considered briefly the undamped linear extended version of the Mathieu equation producing our own version of the stability diagrams as the control parameters vary. The effect of this forcing type was a modification on the shape of the parametric stability regions. From the diagrams evidence of an increase then a decrease in area of stable region as one of the control parameters increases is evident, remaining in agreement with current research studies performed on this version of the Mathieu equation.

The key to determining the anticipated form of response of our proposed double parametric forcing with nonlinear damping is whether the frequencies are commensurate or not. As a result, we initially considered a rational multiple between the forcing frequencies and produced a three dimensional plot portraying a combination of bifurcation diagrams computed over the variation of one forcing amplitude at specific frequency ratios. The nature of the bifurcation diagrams and the route to chaos were not always as expected.

Phase portraits and time series were included to justify the oscillatory response at the certain parameter values. The phenomenon of double nodding was also numerically exhibited for specific parameter conditions using time series and phase portraits.

At a certain ratio of forcing frequency and amplitude, a bifurcation diagram was constructed that showed correspondence to the cross-over of the stability tongue in the Mathieu extended version.

The case of incommensurate frequencies was also assessed but not in great depth due to time restrictions. It was necessary to look into this situation since often two or more external forces may act on systems or even an external force may consist of more than one frequency itself. Poincaré mapping and Fast Fourier Transforms were utilised to show quasiperiodicity and the route to chaos under such model was discussed. The scenario of intermittency was incorporated and demonstrated via a simple three dimensional combination plot of time history and phase space under specific parameter conditions.

The results within this section of the thesis even though are prone and eligible to further and deeper investigation provide unique findings, since to the best of our knowledge the study of the double parametrically forced pendulum model has not yet been examined by researchers. It is interesting to see the different nonlinear behaviour been exhibited.

A frequent criticism of the use of simple single degree of freedom models is the uncertainty in how far the observed behaviour conforms to that of the real system. In the final part of this thesis we conducted a series of roll damping and capsize experiments. We initially investigated the roll decay of a trimaran model with haunches and of a monohull model. The monohull experimental testing was performed at the NTUA, whereas for the trimaran comparison, we were approached by the Naval Ar-

chitecture and Marine Engineering Research Group of the Mechanical Engineering Department of UCL, to provide numerical vindication to their ideas on roll damping assessment. It was therefore necessary to adopt roll decay experimental data from one of their recent testing and perform our own experimental analysis and numerical simulations.

In both cases, we show that it is not possible to extract roll damping coefficients with certainty from model experimental data if analysis is performed on a single degree of freedom roll equation with constant coefficients. For the monohull case, we suggest that the reason for this could be due to the heave motion induced once the force applied to create the initial heel for free roll is released. In the trimaran scenario, an extra form of heave motion is assumed to be induced by the roll motion due to the haunches on the side hulls and these must be properly accounted for in the equations of motion.

Analysis of the experimental data was conducted for both model vessel types, using a quadratic damping model. The equivalent linear damping was calculated for each half roll cycle and at low roll amplitudes negative damping values were presented and a lot of scattering effects. This was an unexpected result since at low angles of roll you usually assume that the decay will settle down, instead of invoking heave coupling.

To support the idea that roll and heave are coupled during the roll decay, simulations were performed in the time domain using a single degree of freedom roll equation with a single time varying sinusoidal function for the monohull and a double time varying sinusoidal function for the trimaran model, describing the roll stiffness. These equations of motion were also referred to relate to the equation of motion of the parametrically excited pendulum and the double parametrically forced pendulum

equation, both examined and discussed in detail in earlier within the thesis.

This allows the coupling between heave and roll to be modelled in a simplistic manner. Using these equations, a spread of equivalent linear damping data was obtained which was similar to those observed in the model experiments.

For the monohull roll decay equation of motion the stiffness variation comprised of the heave motion stimulated by the removal of the inclining force and this term is taken to occur at the heave natural frequency. For the trimaran roll decay equation of motion, the above term was incorporated as well as a second heave component induced by the submergence and emergence of the haunches within the water during roll motion. This latter term occurs at the roll natural frequency.

During the monohull experimental testing heave response was not measured due to lack of experimental capabilities and time limitation created an obstacle for further investigations. So, in order to create a strong case for the hypothesis, we found it necessary to employ not only roll but heave data time histories for the same trimaran model provided to us by the current Naval Architecture and Marine Research team at Mechanical Engineering Department at UCL. With this in hand we were able to show the existence of heave motion occurring at a range of individual frequencies which are suggested to be related to the roll and heave natural frequency. Moreover, we also managed to extract a heave damping approximation from the recorded experimental heave data, which we correlated with the assumed heave damping value used in our numerical simulations that would help to mimic the scatter behaviour in the equivalent linear damping plot. Overall, the match of the experimental and numerical simulations was in fact quite good and reasonable, both for the trimaran and monohull models.

In this series of tests, we also added the experimental evidence of transient capsize.

This involved considering the capsize of the monohull model given the onset of a wave of a certain amplitude and frequency. Our experimental transient capsize points were also compared with a previously studied numerical steady state capsize boundary computed by Cotton and Spyrou (Cotton *et al*, 2001) but for a different monohull model still though, providing a reasonable fit. The significance of transient capsize as opposed to steady state capsize was also noted.

Finally, the transient capsize tests managed to produce an experimental application of the escape phenomenon examined both analytically and numerically for the case of the parametrically excited pendulum model. We linked the theoretical findings of the beam sea equation of roll motion to the practical investigation under consideration.

To summarise, the aim of this work is not to supplant the current approaches but to compliment them with a better understanding of the underlying equations.

8.1 Future Work

Throughout this thesis we have emphasised that any type of non-oscillatory behaviour by the pendulum is considered as not safe, but we suggest here a positive influence of rotational behaviour undergone in the parametrically excited pendulum system. For instance, consider the extraction of energy from sea waves using the rotational motion of the pendulum system. Actually, during the early stages of our research project, another organised research trip to the University of Strathclyde lead us to observe and inspect first hand current experimental research where such an advancement is being undertaken where the researchers purpose and scopes are to generate electrical power.

This new concept is based on the conversion of vertical motion to rotational motion by means of a parametrically excited pendulum operating in rotational mode. As a contribution to their research and for future advances, we propose considering also a group of pendula systems all positioned on a sea platform for example, and converting the combined energy from rotational motions induced by the sea waves to electrical power.

The results of this thesis leave other room for possible future work. In conclusion, the following future research directions are also suggested:

(i) Investigation into nonlinear damping in the parametrically driven pendulum model.

(ii) More work is needed on quasiperiodic behaviour for the double parametrically forced pendulum model.

(iii) Experimental investigation into ship capsize but with an unbiased model. This would accompany very well and complete the study of asymmetric systems within this thesis.

Appendices

Appendix A

Here is the derivation of the equation of motion for the parametrically excited pendulum system. It uses the Lagrangian formulation of mechanics. With a view of Figure 2.1, the rectangular coordinates of the pendulum bob are

$$x = l\sin\theta \qquad \text{and} \qquad y = -(z(\tau) + l\cos\theta),$$

where $z(\tau)$ is a function of time and l is a constant. Noting that displacement below the pivot point is taken as negative. The kinetic and potential energies are given by

$$T = \tfrac{1}{2}m(\dot{x}^2 + \dot{y}^2) \qquad \text{and} \qquad V = mgy$$

respectively, where m is the mass of the pendulum bob and g is the gravitational acceleration. The Lagrangian, $\mathcal{L}$, is

$$\mathcal{L} = T - V$$

and substituting the above gives

$$\mathcal{L} = \tfrac{m}{2}(l^2\dot{\theta}^2 + \dot{z}^2 - 2l\dot{z}\dot{\theta}\sin\theta) + mg(z + l\cos\theta).$$

The Euler-Lagrange equation of motion for the coordinate θ is

$$\frac{d}{d\tau}\frac{\partial \mathcal{L}}{\partial \dot{\theta}} - \frac{\partial \mathcal{L}}{\partial \theta} = 0$$

Substituting again and taking the partial derivatives of $\mathcal{L}$ with respect to $\dot{\theta}$ and θ, we find,

$$\frac{d}{d\tau}[\tfrac{m}{2}(2l^2\dot{\theta} - 2l\dot{z}\sin\theta)] + ml\dot{z}\dot{\theta}\cos\theta + mgl\sin\theta = 0.$$

After differentiating, with respect to τ we reach

$$\ddot{\theta} + \tfrac{g}{l}(1 - \tfrac{\ddot{z}}{g})\sin\theta = 0.$$

Allowing $z(\tau)$ to be of cosinusoidal form:

$$z(\tau) = Z\cos\Omega\tau$$

we substitute in to get

$$\ddot{\theta} + \tfrac{g}{l}(1 + \tfrac{Z\Omega^2}{g}\cos\Omega\tau)\sin\theta = 0.$$

Scaling time and using the following notation,

$$\omega_0 = \sqrt{(\tfrac{g}{l})} \qquad t = \omega_0\tau,$$

where ω_0 represents the natural frequency of the pendulum and Ω the frequency of the cosinusoidal time-history displacement then the above equation reduces to,

$$\theta'' + (1 + p\cos\omega t)\sin\theta = 0$$

with $p = \frac{Z\Omega^2}{g}$ and $\omega = \frac{\Omega}{\omega_0}$. This is equivalent to the undamped version of the parametrically excited pendulum motion in Chapter 2 equation (2.2.2).

Appendix B

Here is the derivation of the equation of motion for the tilted inverted parametrically driven pendulum system. Lagrangian mechanics are again employed. The rectangular coordinates of the pendulum bob are

$$x = l\sin\theta + z(\tau)\sin\phi \qquad \text{and} \qquad y = z(\tau)\cos\phi + l\cos\theta.$$

We note that displacement below the pivot point is taken as negative so that for the inverted case, the y coordinates are now taken as positive. The kinetic and potential energies are given by

$$T = \tfrac{1}{2}m[l^2\dot{\theta}^2 + \dot{z}^2 - 2l\dot{\theta}\dot{z}\sin(\theta - \phi)]$$

$$V = mg(z\cos\phi + l\cos\theta)$$

respectively. The Lagrangian, $\mathcal{L}$, is

$$\mathcal{L} = \tfrac{1}{2}m[l^2\dot{\theta}^2 + \dot{z}^2 - 2l\dot{\theta}\dot{z}\sin(\theta - \phi)] - mgz\cos\phi - mgl\cos\theta.$$

Substituting into the Euler-Lagrange formula, taking the partial derivatives of $\mathcal{L}$ with respect to $\dot{\theta}$ and θ and differentiating with repect to τ, we find,

$$\ddot{\theta} - \tfrac{g}{l}\sin\theta - \tfrac{\ddot{z}}{l}\sin(\theta - \phi) = 0.$$

Allowing $z(\tau)$ to be, this time of negative cosinusoidal form since we are dealing with the inverted case:

$$z(\tau) = -Z\cos\Omega\tau,$$

then substituting in we get

$$\ddot{\theta} - \tfrac{g}{l}\sin\theta - \tfrac{Z\Omega^2}{l}\cos\Omega\tau\sin(\theta-\phi) = 0.$$

Scaling time and using the usual following notation:

$$\omega_0 = \sqrt{(\tfrac{g}{l})} \qquad t = \omega_0\tau$$

the above equation finally reduces to,

$$\theta'' - \sin\theta - p\cos\omega t\sin(\theta-\phi) = 0$$

with $p = \frac{Z\Omega^2}{g}$ and $\omega = \frac{\Omega}{\omega_0}$. This is equivalent to the undamped version of the tilted inverted parametrically driven pendulum motion in Chapter 4 equation (4.7.2).

Appendix C

At a large angle of heel the buoyancy force can no longer be considered to act vertically upwards through the initial Metacentre (M). This is shown below in Figure A.1, where the ship is heeled to an angle ϕ of more than 15 degrees. The centre of buoyancy has moved further out to B_1 which is not on the same horizontal level as the initial B. The vertical through B_1 no longer passes through M. The righting lever, GZ, is once again the perpendicular distance between the vertical through G and the vertical through B_1, so that the moment of statical stability is equal to $weight \times GZ$.

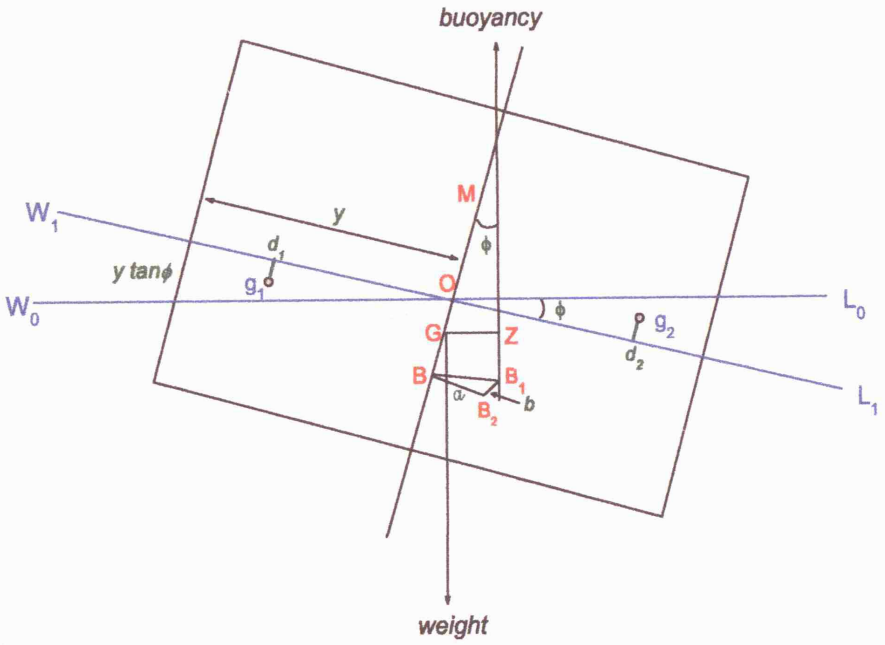

Figure C.1: *The moment of statical stability at a large angle of heel.*

But GZ is no longer equal to $GM \sin\phi$ and up to the angle at which deck edge is immersed, it may be found using a formula known as the "Wall-sided formula".

$$GZ = (GM + \tfrac{1}{2}BM \tan^2\phi) \sin\phi.$$

Referring to Figure C.1, with the ship is inclined, the wedge W_0OW_1 is transferred to L_0OL_1 such that the centre of gravity shifts from g_1 to g_2. This causes the centre of buoyancy to also shift from B to B_1. The horizontal components of these shifts are d_1d_2 and BB_2 respectively. The vertical components are $(g_1d_1 + g_2d_2)$ and B_1B_2 respectively. We label BB_2 to be α units and B_1B_2 to be b units.

The derivation of the above formula consists of the following steps. The area of the wedge L_0OL_1 is:

$$Area = \tfrac{1}{2}y^2 \tan\phi.$$

We now consider an elementary strip longitudinally of length dx as in Figure C.2(b). The Volume is given as:

$$Volume = \tfrac{1}{2}y^2 \tan\phi dx.$$

Using the mathematical fact that the centroid of a triangle is at $\frac{2}{3}$ of the median from the apex, then the total horizontal shift of the wedge, d_1d_2, is $\frac{2}{3} \times 2y$. Therefore the Moment of shifting this wedge is:

$$\tfrac{2}{3} \times 2y \times \tfrac{1}{2}y^2 \tan\phi dx = \tfrac{2}{3}y^3 \tan\phi dx.$$

The sum of the moment of all such wedges is:

$$\int_0^{L_0} \frac{2}{3} y^3 \tan\phi dx$$
$$= \tan\phi \int_0^{L_0} \frac{2}{3} y^3 dx.$$

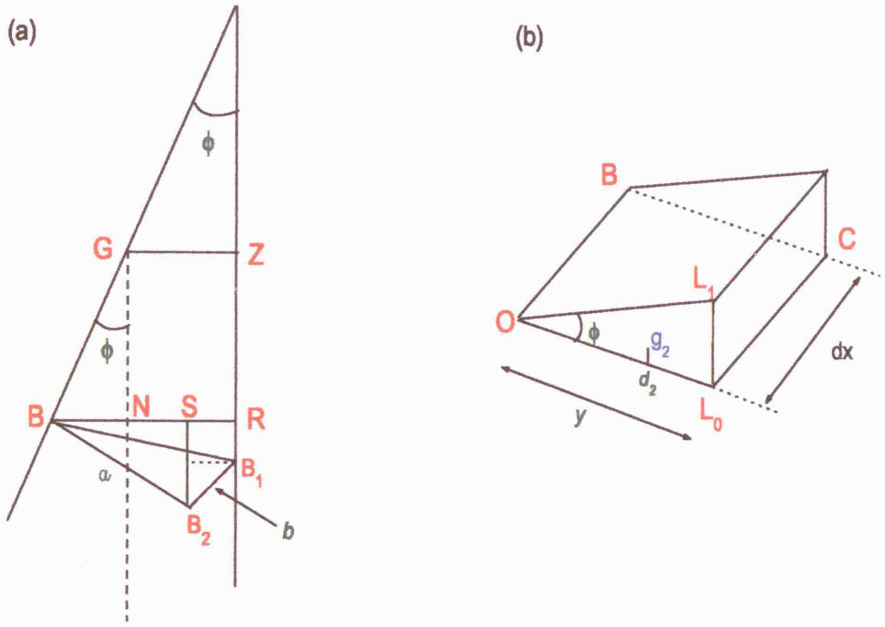

Figure C.2: *(a) Focus of Figure C.1. (b) Wedge* L_0OL_1.

But the second moment of the waterplane area about the center-line is $I_{xx} = \int_0^{L_0} \frac{2}{3} y^3 dx$. This is a result deducted from the Theorem of Parallel Axes. The second moment of an area about an axis through the centroid is equal to the second moment about any other axis parallel to the first reduced by the product of the area

and the square of the perpendicular distance between the two axes. Hence the sum of the moment of all such wedges is:

$$= I_{xx} \tan \phi.$$

But the sum of the moments of the wedges $= v \times d_1 d_2$ where v is the volume of the immersed or emerged wedge. Now:

$$BB_2 = \frac{v \times d_1 d_2}{V}$$

where V is the ship's volume of displacement. Therefore,

$$V \times BB_2 = I_{xx} \tan \phi$$
$$BB_2 = \frac{I_{xx} \tan \phi}{V}$$

By ship theory (Derrett *et al*, 1964), the transverse BM is the height of the transverse metacentre above the centre of buoyancy and is found using the formula:

$$BM = \frac{I_{xx}}{V}$$

where I_{xx} = The second moment of the waterplane area about the centre line. So, by this definition,

$$BB_2 = BM \tan \phi = \alpha.$$

The vertical shift of the wedge $= d_1g_1 + d_2g_2 = 2d_1g_1$. The vertical moment of the shift $= v \times 2d_1g_1$. In Figure C.2(b),

$$OL_0 = y \qquad Od_2 = \tfrac{2}{3}y.$$

But, $L_0L_1 = y\tan\phi$. Therefore $g_2d_2 = \frac{1}{3}y\tan\phi$. The volume of the wedge is:

$$\tfrac{1}{2}y^2\tan\phi dx.$$

The moment of the vertical shift is

$$= \tfrac{1}{2}y^2\tan\phi dx \times \tfrac{2}{3}y\tan\phi = \tfrac{1}{3}y^3\tan^2\phi dx.$$

The vertical moment of all such wedges $= \int_0^{L_0} \frac{1}{3}y^3\tan^2\phi dx$. Similarly, this is equal to $\frac{1}{2}I_{xx}\tan^2\phi$ which is the moment of the vertical shift. Also,

$$B_1B_2 = \tfrac{v\times 2g_1d_1}{V} = b.$$

But $2vg_1d_1$ is the vertical moment of the shift and so $V \times b = \frac{1}{2}I_{xx}\tan^2\phi$ or equally,

$$B_1B_2 = \tfrac{BM\tan^2\phi}{2} = b$$

Referring now to Figure C.2(a) and with the help of geometric manipulation:

$$\begin{aligned} GZ &= NR \\ &= BR - BN \\ &= (BS + SR) - BN \\ &= \alpha \cos\phi + b \sin\phi - BG \sin\phi. \end{aligned}$$

From α and b,

$$\begin{aligned} GZ &= BM \tan\phi \cos\phi + \frac{1}{2} \tan^2\phi \sin\phi - BG \sin\phi \\ &= BM \sin\phi + \frac{1}{2} \tan^2\phi \sin\phi - BG \sin\phi \\ &= \sin\phi (BM + \frac{1}{2} \tan^2\phi - BG) \end{aligned}$$

and since $GM = BM - BG$, we finally reach the result:

$$GZ = \sin\phi (GM + \tfrac{1}{2} \tan^2\phi).$$

This formula may be used to obtain the GZ at any angle of heel, and for small angles of heel, the term $\frac{1}{2} \tan^2\phi$ may be neglected. This derivation of the Wall-sided formula may also be found in Derrett (Derrett *et al*, 1964) but re-derived here for fullness and completeness to our section of study on the Static Stability Curve.

References

Acheson, D. J. (1993). "A Pendulum Theorem," *Proceedings: Mathematical and Physical Sciences*, Vol. **443**, No. **1917**, pp 239-245.

Acheson, D. J. (1995). "Multiple-nodding oscillations of a driven inverted pendulum," *Proceedings: Mathematical and Physical Sciences*, Vol. **448**, No. **1932**, pp 89-95.

Alexander, N. A. (1989). "Production of computational portraits of bounded invariant manifolds," *Journal of Sound and Vibration*, Vol. **135**, No. **63-77**, pp 707-716.

Alexander, N. A. (1998a). "Evaluating the global characteristic of a nonlinear dynamical system with Recursive Boundary Enhancement," *Advances in Engineering Software*, Vol. **29**, No. **7-9**, pp 707-716.

Alexander, N. A. (1998b). "Evaluating basins of attraction in non-linear dynamical systems using an improved Recursive Boundary Enhancement (RBE)," *Journal of Sound and Vibration*, Vol. **209**, No. **3**, pp 443-472.

Arnol'd, V. I. (1991). *Ordinary Differential Equations*, Springer-Verlag Berlin Heidelberg.

Arrowsmith, D. K. and Place, C. M. (1990). *An Introduction to Dynamical Systems,* Cambridge University Press, Cambridge.

Arrowsmith, D. K. and Place, C. M. (1992). *Dynamical Systems: Differential Equations, maps and chaotic behaviour,* Chapman and Hall, USA.

Arrowsmith, D. K. and Mondragón, R. J. (1999). "Stability Region Control for a Parametrically Forced Mathieu Equation," *Meccanica*, Vol. **34**, pp 401-410.

Aston, P. J. (1996). *Nonlinear Mathematics and its Applications,* Cambridge University Press, Cambridge.

Banning, E. J. (1998). *On the dynamics of two coupled parametrically driven pendulums: Mode competition and transition to chaos,* PhD Thesis, University of Eindhoven, ISBN: 90-3650933-5.

Bartucceli, M. V., Gentile, G. and Georgiou. K. V. (2001). "On the dynamics of a vertically driven damped planar pendulum," *Proc. R. Soc. Lond. A*, Vol. **457**, pp 3007-3022.

Belenky, V. L. and Sevastianov, N. B. (2003). *Stability and Safety Of Ships, Volume II: Risk of Capsizing,* Elsevier Ocean Engineering Book Series, Volume **10**, Oxford, England.

Belenky, V. L., Weems, K. M. and Paulling, J. R. (2003). "Probabilistic Analysis of Roll Parametric Resonance in Head Seas," *Proc. of STAB 2003, Madrid*, pp 325-340.

Belhaq, M. and Houssni, M. (1999). "Quasi-Periodic Oscillations, Chaos and Suppression of Chaos in a Nonlinear Oscillator Driven by Parametric and External Excitations," *Nonlinear Dynamics*, Vol. **18**, pp 1-24.

Belhaq, M. and Houssni, M. (2000). "Suppression of chaos in averaged oscillator driven by external and parametric excitations," *Chaos, Solitons and Fractals*, Vol. **11**, pp 1237-1246.

Belhaq, M. Guennoun, K. and Houssni, M. (2002). "Asymptotic solutions for a damped non-linear quasi-periodic Mathieu equation," *International Journal of Non-Linear Mechanics*, Vol. **37**, pp 445-460.

Berkemeier, M. D. (1995). "Coupled oscillators in a platform with four springy legs and feedback," *Proc. 34th IEEE Conf. Decision and Control*, Vol. **3**, pp 2847-2852.

Bergé, P., Pomeau, Y. and Vidal, C. (1984). *Order within Chaos: Towards a Deterministic Approach to Turbulence,* Wiley, New York.

Bikdash, M. Balachandran, B. and Nayfeh, A. (1994). "Melnikov Analysis for a Ship with a General Roll-Damping Model," *Nonlinear Dynamics*, Vol. **6**, pp 101-124.

Bishop, S. R. (2000). "The Use of Low Dimensional Models of Engineering Dynamical Systems," *Nonlinear Phenomena in Complex Systems*, Vol. **3**, No. **1**, pp 71-80.

Bishop, S. R. and Clifford, M. J. (1994a). "Non rotating periodic orbits in the parametrically excited pendulum," *Eur. J. Mech., A/Solids*, Vol. **13**, No. **4**, pp 581-587.

Bishop, S. R. and Clifford, M. J. (1994b). "Zones of chaotic behaviour in the parametrically excited pendulum," *Journal of Sound and Vibration*, Vol. **189**, No. **1**, pp 142-147.

Bishop, S. R., Sofroniou, A. and Shi, P. (2005). "Symmetry-breaking in the response of the parametrically excited pendulum model," *Chaos, Solitons and Fractals*, Vol. **25**, pp 257-264.

Bishop, S. R. and Sudor, D. J. (1999). "The "Not Quite" Inverted Pendulum," *International Journal of Bifurcation and Chaos*, Vol. **9**, No. **1**, pp 273-285.

Bishop, S. R., Virgin, L. N. and Leung, D. L. M. (1988). "On the computation of domains of attraction during the dynamic modelling of oscillating systems," *Appl. Math. Modelling*, Vol. **12**, pp 503-516.

Bishop, S. R., Xu, D. L. and Clifford, M. J. (1996). "Flexible control of the parametrically excited pendulum," *Proc. R. Soc. London. A*, Vol. **452**, pp 1789-1806.

Blackburn, J. A., Smith, H. J. T. and Gronbech-Jensen, N. (1992). "Stability and Hopf bifurcations in an inverted pendulum," *Am. J. Phys.*, Vol. **60**, No. **10**, pp 903-908.

Blocki, W. (1980). "Ship Safety in connection with parametric resonance of the roll," *International Shipbuilding Progress*, No. **306**, pp 263-267.

Bountis, T. and Van Der Welle, J. P. (1999). "Subharmonic Bifurcations and Melnikov's Theory in a System of Parametrically Driven Pendulums," *Nonlinear Phenomena in Complex Systems*, Vol. **2**, No. **3**, pp 1-13.

Bryant, P. J. and Miles, J. W. (1990a). "On a periodically forced, weakly damped pendulum. Part 1: Applied Torque," *J. Austral. Math. Soc. Ser B*, Vol. **32**, pp 1-22.

Bryant, P. J. and Miles, J. W. (1990b). "On a periodically forced, weakly damped pendulum. Part 2: Horizontal Forcing," *J. Austral. Math. Soc. Ser B*, Vol. **32**, pp 23-41.

Bryant, P. J. and Miles, J. W. (1990c). "On a periodically forced, weakly damped pendulum. Part 3: Vertical Forcing," *J. Austral. Math. Soc. Ser B*, Vol. **32**, pp 42-60.

Bulian, G. (2005). "Nonlinear parametric rolling in regular waves - a general procedure for the analytical approximation of the GZ curve and its use in time domain simulations," *Ocean Engineering*, Vol. **32**, pp 309-330.

Butikov, E. (1999). "The rigid pendulum - an antique but evergreen physical model," *Eur. J. Phys.*, Vol. **20**, pp 429-441.

Butikov, E. (2001). "On the dynamic stabilization of an inverted pendulum," *Am. J. Phys.*, Vol. **69**, No. **7**, pp 755-768.

Capecchi, D. and Bishop, S. R. (1994). "Periodic oscillations and attracting basins for a parametrically excited pendulum," *Dynamics and Stability of Systems*, Vol. **9**, No. **2**, pp 123-143.

Chacón, R., Balibrea, F. and López, M. A. (1997). "Role of parametric resonance in the inhibition of chaotic escape from a potential well," *Phys. Lett.*, **A235**, pp 153-158.

Chan, H. S., Xu, Z. and Huang, W. L. (1995). "Estimation of nonlinear damping coefficients from large-amplitude ship rolling motions," *Applied Ocean Res.*, Vol. **17**, No. **4**, pp 217.

Chastell, P. R., Glendinning, P. A. and Stark, J. (1995). "Determining the Locations of Bifurcations in Quasiperiodic Systems," *Phys. Lett. A.*, Vol. **200**, pp 17-26.

Chen, S. L., Shaw, S. W. and Troesch, A. W. (1999). "A systematic approach to modelling nonlinear multi-degree of freedom ship motions in regular seas," *Journal of Ship Research*, Vol. **43**, No. **1**, pp 25-37.

Clifford, M. J. (1994). *The Parametrically Excited Pendulum: a Paradigm of Nonlinear Systems,* PhD Thesis, Centre for Nonlinear Dynamics and its Apllications, University College London, England.

Clifford, M. J. and Bishop, S. R. (1993). "Generic features of escape from a potential well under parametric excitation," *Physics Letters A*, Vol. **184**, pp 57-63.

Clifford, M. J. and Bishop, S. R. (1994a). "Approximating the escape zone for the parametrically excited pendulum," *Journal of Sound and Vibration*, Vol. **172**, No. **4**, pp 572-576.

Clifford, M. J. and Bishop, S. R. (1994b). "Inverted oscillations of a driven pendulum," *Proc. R. Soc. London. A*, Vol. **454**, pp 2811-2817.

Clifford, M. J. and Bishop, S. R. (1996). "Locating oscillatory orbits of the parametrically excited pendulum," *J. Austral. Math. Soc. Ser B*, Vol. **37**, pp 309-319.

Contento, G., Francescutto. A. and Piciullo, M. (1996). "On the effectiveness of constant coefficients roll motion equation," *Ocean Engineering*, Vol. **23**, No. **7**, pp 597-618.

Cotton, B. and Spyrou, K. J. (2001). "An experimental study of nonlinear behaviour in roll and capsize," *Int. Shipbuild. Progr.*, Vol. **48**, No. **1**, pp 5-18.

Crossland, P., Wilson, P. A. and Bradburn, J. C. (1993). "The free decay of coupled heave and pitch motions of a model frigate," *RINA Trans. Part A.*, Vol. **135**, pp 121.

Cusumano, J. P. and Kimble, B. (1995). "A stochastic interrogation method for experimental measurements of global dynamics and basin evolution: Application to a two-well oscillator," *Nonlinear Dynamics* Vol. **8**, pp 213-235.

Davis, S. H. and Rosenblat, R. (1980). "A Quasiperiodic Mathieu-Hill Equation," *Journal of Appl. Math.*, Vol. **38**, No. **1**, pp 139-155.

Deakin, B. (2003). "Model tests to study Capsize and stability of sailing multihulls," *International Journal of Small Craft Technology, RINA*, pp 619-639.

Derrett, D. R. and Barrass, C. B. (1964). *"Ship Stability: For Masters and Mates,"* Stanford Maritime Ltd.

Doedel, E. J. (1986). *AUTO - Software for continuation and bifurcation problems in ordinary differential equations,* California Institute of Technology.

Erdos, G. and Singh, T. (1996). "Stability of a parametrically excited damped inverted pendulum," *Journal of Sound and Vibration*, Vol. **198**, No. **5**, pp 643-650.

Falzarano, J., Shaw. S. and Troesch, A. W. (1992). "Application of Global Methods for Analysing Dynamical Systems to Ship Rolling Motion and Capsizing," *International Journal of Bifurcation and Chaos*, Vol. **2**, No. **1**, pp 101-115.

Féat, G. and Jones. D. (1981). "Parametric Excitation and the Stability of a Ship Subjected to a Steady Heeling Moment," *International Shipbuilding Progress*, Vol. **2**, pp 263-267.

Foale, S. and Thompson, J. M. T. (1991). "Geometric concepts and computational techniques of nonlinear dynamics," *Computer Methods in Applied Mechanics and Engineering*, Vol. **89**, pp 381-394.

France, W. N., Levadou, M., Treakle, T. W., Paulling, R., Keith Michel, R. and Moore, C. (2003). "An Investigation of Head-Sea Parametric Rolling and its Influence on Container Lashing Systems," *Marine Technology*, Vol. **40**, No. *1*, pp 1-19.

Francescutto, A. (2001). "On the Roll Motion of a Trimaran in Beam Seas," *Proceedings of the Eleventh (2001) International Offshore and Polar Engineering Conference*, Stavanger, Norway, June 17-22, 2001.

Francescutto, A. and Contento, G. (1999). "Bifurcations in ship rolling: experimental results and parameter identification technique," *Ocean Engineering*, Vol. **26**, pp 1095-1123.

Francescutto, A., Nabergoj, R. and Hsiu, T. C (1991). "Nonlinear ship rolling: identification of damping model," *Tecnica Italiana*, Vol. **3**, pp 151.

Froude, W. (1863). "On the Rolling of Ships," *Institution of Naval Architects*, March 1, 1986.

Garira, W. and Bishop, S. R. (2003). "Oscillatory Orbits of the parametrically excited pendulum," *International Journal of Bifurcation and Chaos*, Vol. **13**, No. **10**, pp 2949-2958.

Garira, W. and Bishop, S. R. (2003). "Rotating solutions of the parametrically excited pendulum," *Journal of Sound and Vibration*, Vol. **263**, pp 233-239.

Glendinning, P. (1994). *Stability, Instability and Chaos: an introduction to the theory of nonlinear differential equations,* Cambridge University Press, Cambrigde.

Golubitsky, M. and Shaeffer, D. G. (1986). *Singularities and Groups in Bifurcation Theory,* Springer-Verlag, New York.

Grafton, T. J. (2006). *Towards Validated Theory for the Prediction of Roll Motion and Roll Damping of Trimaran Ships,* preprint, PhD Thesis, Mechanical Engineering, University College London, England.

Grafton, T. J., Zhang, J. and Rusling, W. J. (2004). "Theoretical Roll Motion Predictions for a Trimaran Fitted with Roll Damping Appendages," *NARG Report* No. **1055/04**, Department of Mechanical Engineering, UCL, December 2004.

Grafton, T. J., Zhang, J. and Van Griethuysen, W. J. (2003). "Roll Decay Experiments on a Trimaran Model with Various Fixed Roll Damping Appendages," *NARG Report* No. **1052/03**, Department of Mechanical Engineering, UCL, January 2003.

Grebogi, C., Ott, E., Pelikan, S. and Yorke, J. A. (1984). "Strange attractors that are not chaotic," *Physica D*, Vol. **13**, pp 216-268.

Grimshaw, R. (1993). *Nonlinear Ordinary Differential Equations,* CRC Press, USA.

Guckenheimer, J. and Holmes, P. (1983). *Nonlinear Oscillations, Dynamical Systems, and Bifurcations of Vector Fields,* Springer-Verlag, New York, USA.

Guckenheimer, J. and Worfolk, P. (1993). *Dynamical Systems: Some computational problems,* In Bifurcations and Periodic Orbits of Vector Fields, Kluwer.

Guennoun, M., Houssni, M. and Belhaq, M. (2002). "Quasi-Periodic Solutions and Stability for a Weakly Damped Nonlinear Quasi-Periodic Mathieu Equation," *Nonlinear Dynamics*, Vol. **27**, pp 211-236.

Hayashi, C. (1985). *Nonlinear Oscillations in Physical Systems,* Princeton University Press, USA.

Helmholtz, H. L. (1863). "On the Sensations of Tone as a Physiological Basis for the Theory of Music," *Translation of the 1877 Edition*, Dover, 1954.

Housner, G. W. (1963). "The behaviour of inverted pendulum structures during earthquakes," *Bull. Seism. Soc. Am.*, Vol. **53**, pp 403-417.

Hsu, C. S. (1987). *Cell to Cell Mapping: A Method of Global Analysis for Nonlinear Systems,* Springer-Verlag, New York.

Jiang, C., Troesch, A. W. and Shaw, S. W. (1996). "Highly Nonlinear Rolling Motion of Biased Ships in Random Beam Seas," *Journal of Ship Research*, Vol. **40**, No. **2**, pp 125-135.

Jiang, C., Troesch, A. W. and Shaw, S. W. (2000). "Capsize Criteria for ship models with memory-dependent hydrodynamics and random excitation," *Phil. Trans. R. Soc. London A*, Vol. **358**, pp 1761-1791.

Jordan, D. W. and Smith, P. (1987). *Nonlinear Ordinary Differential Equaitons,* Oxford Applied Mathematics and Computing Science Series, Clarendon Press, Oxford, England.

Kalmus, H. P. (1970). "The Inverted Pendulum," *American Journal of Physics*, Vol. **38**, No. **7**, pp 874-878.

Kan, M., Saruta, T. and Taguchi, H. (1990). "Capsizing of a Ship in Quartering Waves," *Naval Architecture and Ocean Engineering*, Vol. **29**.

Kan, M. and Taguchi, H. (1991). "Chaos and Fractals in Asymmetric Capsize Equation," *Naval Architecture and Ocean Engineering*, Vol. **30**.

Kan, M. and Taguchi, H. (1993). "Chaos and Fractals in Nonlinear Roll and Capsize of a Damaged Ship," *International Workshop on Physical and Mathematical Modelling of Vessel's Stability in a Seaway*, Russia, 17-21 May, 1993.

Kapitaniak, T. (1992). *Chaotic Oscillations: Theory and Applications,* World Scientific Publishing Co. Pte. Ltd.

Kapitza, P. L. (1951). "Dynamic stability of the pendulum with vibrating suspension point," *Collected Papers of P.L. Kapitza, edited by D. Ter Haar (Pergamon, London, 1965)* Vol. **2**, pp 714-726.

Kern, A. and Stoop, R. (2003). "Nonlinear Dynamics of Cochlear Information Processing," *Phys. Rev. Lett*, Vol. **91**.

Kerwin, J. E. (1955). "Notes on Rolling in Longitudinal Waves," *International Shipbuilding Progress*, No. **16**.

Kim, S. Y. and Hu, B. (1998). "Bifurcations and transitions to chaos in an inverted pendulum," *Physical Review E*, Vol. **58**, No. **3**, pp 3028-3035.

Klaka, K. P. (2001). "Model tests on a circular cylinder with appendages," *Centre for Marine Science and Technology Interim Report*, Australia.

Koch, B. P. and Leven, R. W. (1985). "Subharmonic and Homoclinic bifurcations in a parametrically forced pendulum," *Physica 16D*, pp 1-13.

Koplow, M. A. and Mann, B. (2005). "Bifurcations of a planar pendulum driven at a tilted angle," *Proceedings of IDETC 2005, ASME Design Engineering Technical Conference*, September 24-28, 2005, Long Beach, C. A, USA.

Kreyszig, E. (1999). *Advanced Engineering Mathematics,* John Wiley and Sons, Inc.

Lee, S. K. (2000). "Stability Analysis of an Initially Inclined Ship in Following Sea," *Journal of Applied Mechanics*, Vol. **67**, pp 717-719.

Leven, R. W. and Koch, B. P. (1981). "Chaotic Behaviour of a Parametrically Excited Damped Pendulum," *Physics Letters*, Vol. **86A**, No. **2**, pp 71-73.

Liaw, C. Y., Bishop, S. R. (1995). "Nonlinear Heave-Roll Coupling and Ship Rolling," *Nonlinear Dynamics*, Vol. **8**, pp 197-211.

Liaw, C. Y., Bishop, S. R. and Thompson, J. M. T. (1993). "Heave-Excited Rolling Motion of a Rectangular Vessel in Head Seas," *International Journal of Offshore and Polar Engineering*, Vol. **3**, No. **1**, pp 26-31.

Lsu, S. L., Cheung, Y. K. and Wu, S. Y. (1982). "A variable parameter incrementation method for dynamic instability of linear and nonlinear elastic systems," *Journal of Applied Mechanics*, Vol. **49**, pp 849-853.

Mathieu, É. (1868). "Mémoire sur le mouvement vibratoire d'une membrane de forme elliptique," *Journal Math. Pure. Appl.*, Vol. **13**, pp 137-203.

Mathisen, J. B. and Price, W. G. (1984). " Estimation of Ship Roll Damping Coefficients," *Transactions of the Royal Institution of Naval Architects.*, Vol. **127**, pp 295-307.

Matlab. (1989). *Users Guide, Technical Report, The Math Works*, www.mathworks.com.

McLachlan, N. W. (1947). *Theory and Application of Mathieu Functions,* Clarendon Press, Oxford, England.

Melnikov, V. K. (1963). "On the stability of the center for time periodic perturbations," *Trans. Moscow Math. Soc.*, Vol. **12**, pp 3-56.

Michaelis, M. M. (1985). "Stroboscopic study of the inverted pendulum," *Am. J. Phys.*, Vol. **53**, No. **11**, pp 1079-1083.

Miles, J. (1989). "The Pendulum from Huygens' Horologium to symmetry breaking and chaos," *Theoretical and Applied Mechanics*, edited by P. Germain, M. Piau and D. Caillerie. Elsevier Science, North Holland: pp 193-215.

Miles, J. and Bryant, P. J. (1989). "Resonance and Symmetry Breaking for a Duffing Oscillator," *SIAM Journal on Applied Mathematics*, Vol. **49**, Issue. **3**, pp 968-981.

Miles, J. and Zou, Q. P. (1993). "Parametric Excitation of a detuned Spherical Pendulum," *Journal of Sound and Vibration*, Vol. **164**, Issue. **2**, pp 237-250.

Moon, F. C. (1987). *Chaotic Vibrations: An Introduction for Applied Scientists and Engineers,* John Wiley and Sons, USA.

Mullin, T. (1993). *The Nature of Chaos,* Oxford University Press, Oxford, England.

Nayfeh, A. H. (1993). *Introduction to Perturbation Techniques,* John Wiley and Sons, USA.

Nayfeh, A. H. and Balachandran, B. (1995). *Applied Nonlinear Dynamics,* John Wiley and Sons, USA.

Nayfeh, A. H. and Mook, D. T. (1979). *Nonlinear Oscillations,* New York, Wiley.

Nayfeh, A. H. and Sanchez, N. E. (1988). "Chaos and dynamics instability in the rolling motion of ships," *Proceedings of the 17th O. N. R. Naval Hydrodynamics Symposium*, The Hague.

Nayfeh, A. H. and Sanchez, N. E. (1990). "Stability and compicated rolling response of ships in regular beam seas," *International Shipbuilding Progress*, Vol. **37**, No. **412**, pp 331-352.

Nelson, R. A. and Olsson, M. G. (1986). "The Pendulum - Rich physics from a simple system," *Am, J. Phys.*, Vol. **54**, No. **2**.

Nusse, H. E. and Yorke, J. A. (1994). *Dynamics: Numerical Explorations,* Springer-Verlag New York.

Ott, E. (1993). *Chaos in Dynamical Systems,* Cambridge University Press, Cambridge, England.

Parker, T. S. and Chua, L. O. (1989). *Practical Numerical Algorithms for Chaotic Systems,* Springer-Verlag New York.

Pattison, D. R. and Zhang, J. W. (1994). "Trimaran Ships," *The Royal Institution of Naval Architects*, April 27, 1994.

Paulling, J. R. and Rosenberg, R. M. (1959). "On unstable Ship Motions Resulting from Nonlinear Coupling," *Journal of Ship Research*, Vol. **3**, No. **1**.

Phelps, F. M. and Hunter, J. H. (1965). "An analytical solution of the Inverted Pendulum," *Am. J. Phys*, Vol. **33**, pp 285-295.

Plaut, R. H., HaQuang, N. and Mook, D. T. (1986). "Simultaneous resonances in the non-linear structural vibrations under two-frequency excitation," *Journal of Sound and Vibration*, Vol. **106**, pp 361-376.

Plaut, R. H., Gentry, J. J. and Mook, D. T. (1990). "Resonances in the non-linear structural vibrations involving two external excitations," *Journal of Sound and Vibration*, Vol. **140**, pp 371-379.

Rainey, R. C. T. and Thompson, J. M. T. (1991). "The Transient Capsize Diagram - A New Method of Quantifying Stability in Waves," *Journal of Ship Research*, Vol. **35**, No. **1**, pp 58-62.

Rand, R. and Hastings, R. (1995). "A Quasiperiodic Mathieu Equation," *DE-Vol. 84-1, 1995 Design Engineering Technical Conferences*, Vol. **3** - Part A ASME, pp 747-758.

Rawson, K. J. and Tupper, E. C. (1968a). *Basic Ship Stability: Volume 1,* John Wiley and Sons, USA.

Rawson, K. J. and Tupper, E. C. (1968b). *Basic Ship Stability: Volume 2,* John Wiley and Sons, USA.

Rayleigh, J. W. S. (1945). *The Theory of Sound,* 2nd Edition, New York: Dover.

Renyuan, D. (1986). "An improvement in the Analysis of Roll Decay tests," *Selected Papers of the Chinese Society of Naval Architecture and Marine Engineering*, No. **2**.

Ribeiro e Silva, S., Santos, T. A. and Soares, C. G. (2005). "Parametrically excited roll in regular and irregular head seas," *Int. Shipbuilding. Progr.*, Vol. **52**, No. **1**, pp 29-56.

Roberts, J. B. (1985). "Estimation of Nonlinear Ship Roll Damping from Free-Decay Data," *Journal of Ship Research*, Vol. **29**, No. **2**, pp 127-138.

Roberts, J. B., Kountzeris, A. and Gawthrop (1991). "Parametric identification techniques for roll decrement data," *Intl. Shipbuilding Progress*, Vol. **38**, No. **415**, pp 217.

Robertson, J. (1996). *Engineering Mathematics with Maple,* McGraw-Hill.

Sanchez, N. E. and Nayfeh. A. H. (1997). "Global behaviour of a biased non-linear oscillator under external and parametric excitations," *Journal of Sound and Vibration*, Vol. **207**, No. **2**, pp 137-149.

Sanjuán, M. A. (1999). "The effect of nonlinear damping on the universal escape oscillator," *International Journal of Bifurcation and Chaos*, Vol. **9**, No. **4**, pp 735-744.

Schmitt, J. M. and Bayly, P. V. (1998). "Bifurcations in the Mean Angle of a Horizontally Shaken Pendulum: Analysis and Experiment," *Nonlinear Dynamics*, Vol. **15**, pp 1-14.

Seydel, R. (1991). *Practical Bifurcation and Stability Analysis: From Equilibrium to Choas,* Springer-Verlag New York.

Shenker, S. J. (1982). "Scaling behaviour in a map of a circle onto itself," *Physica D*, Vol. **5**, pp 405-411.

Shin, Y. S., Belenky, V. L., Paulling, J. R., Weems, K. M. and Lin, W. M. (2004). "Criteria for Parametric Roll of Large Containerships in Longitudinal Seas," *ABS Technical Papers: The Society of Naval Architects and Marine Engineers.*

Sofroniou, A. and Bishop, S. R. (2006). "Breaking the symmetry of the parametrically excited pendulum," *Chaos, Solitons and Fractals*, Vol. **28**, Issue. **3**, pp 673-681.

Soliman, M. (1996). "Jump phenomena resulting in unpredictable dynamics in the driven damped pendulum," *Int. J. Non-Linear Mechanics*, Vol. **31**, No. **2**, pp 167-174.

Soliman, M. and Thompson, J. M. T. (1989). "Integrity Measures quantifying the Erosion of Smooth and Fractal Basins of Attraction," *Journal of Sound and Vibration*, Vol. **135**, No. **3**, pp 453-475.

Soliman, M. and Thompson, J. M. T. (1992). "Global dynamics underlying sharp basin erosion in nonlinear driven oscillators," *Phys. Rev. A.*, Vol. **45**, pp 3425-3431.

Spyrou, K. J. (2000a). "Designing against parametric instability in following seas," *Ocean Engineering*, Vol. **27**, pp 625-653.

Spyrou, K. J. (2000b). "On the parametric rolling of ships in a following sea under simultaneous nonlinear periodic surging," *Phil. Trans. R. Soc. London. A*, Vol. **358**, pp 1813-1834.

Spyrou, K. J. (2002). "A basis for developing a rational alternative to the weather criterion: Problems and Capabilities," *Proceedings of the 6th International Ship Stability Workshop, Webb Institute*, New York, October 13-16, 2002.

Spyrou, K. J. (2004). "Nonlinear damping coefficients from an asymmetric roll decay time series: an analytical method," *Proc. Instn Mech. Engrs*, Vol. **218**, pp 11-22.

Spyrou, K. J. and Thompson, J. M. T. (2000). "The nonlinear dynamics of ship motions: a field overview and some recent advances," *Phil. Trans. R. Soc. London. A*, Vol. **358**, pp 1735-1760.

Spyrou, K. J., Cotton, B. and Gurd, B. (2002). "Analytical Expressions of Capsize Boundary for a Ship with Roll in Beam Waves," *Journal of Ship Research*, Vol. **46**, No. **3**, pp 167-174.

Spouge, J. R. (1988). "Nonlinear Analysis of Large Amplitude Rolling Experiments," *Int. Shipbuild. Progr.*, Vol. **35**, No. **403**, pp 271-320.

Stephenson, A. (1908). "On a new type of dynamics stability," *Mem. Proc. Manch. Lit. Phil. Soc*, Vol. **52**, pp 1-10.

Stewart, I. W. and Faulkner, T. R. (2000). "Estimating the escape zone for a paramterically excited pendulum-type equation," *Physical Review E*, Vol. **62**, No. **4**, pp 4856-4861.

Stoker, J. J. (1950). *Nonlinear Vibrations,* InterScience Publishers, Inc.

Sudor, D. and Bishop, S. R. (1999). "Inverted dynamics of a tilted paramteric pendulum," *Eur. J. Mech. A/Solids*, Vol. **18**, pp 517-526.

Szabelski, K. and Warmiński, J. (1995). "Self-Excited System Vibrations with Parametric and External Excitations," *Journal of Sound and Vibration*, Vol. **187**, No. **4**, pp 595-607.

Szemplińska-Stupnicka, W. and Rudowski, J. (1995). "On minimum safe impulsive velocity in the driven escape oscillator," *Int. J. Non-Linear Mechanics*, Vol. **31**, No. **3**, pp 255-266.

Szemplińska-Stupnicka, W., Tyrkiel, E. and Zubrzycki, A. (2000). "The global bifurcations that lead to transient tumbling chaos in a parametrically driven pendulum," *International Journal of Bifurcation and Chaos*, Vol. **10**, No. **9**, pp 2161-2175.

Taylan, M. (2000). "The effect of nonlinear damping and restoring in ship rolling," *Ocean Engineering*, Vol. **27**, pp 921-932.

Thompson, J. M. T. (1989). "Chaotic phenomena trigerring the escape from a potential well," *Proc. R. Soc. London. A*, Vol. **421**, pp 195-225.

Thompson, J. M. T. and Bishop, S. R. (1994). *Nonlinearity and Chaos in Engineering Dynamics,* John Wiley and Sons Ltd.

Thompson, J. M. T, Bishop, S. R. and Leung, L. M. (1987). "Fractal basins and chaotic bifurcations prior to escape from a potential well," *Physics Letters A*, Vol. **121**, Issue. **3**, pp 116-120.

Thompson, J. M. T., Rainey, R. C. T. and Soliman, M. S. (1990). "Ship stability criteria on chaotic transients from incursive fractals," *Phil. Trans. R. Soc. London. A*, Vol. **332**, pp 149-167.

Thompson, J. M. T., Rainey, R. C. T. and Soliman, M. S. (1992). "Mechanics of ship capsize under direct and parametric wave excitation," *Phil. Trans. R. Soc. London. A*, Vol. **338**, pp 471-490.

Thompson, J. M. T. and Stewart, H. B. (1986). *Nonlinear Dynamics and Chaos,* Chichester: Wiley.

Trueba, J. L., Baltanás, J. P. and Sanjuán, M. A. F. (2003). "A generalized perturbed pendulum," *Chaos, Solitons and Fractals*, Vol. **15**, pp 911-924.

Tritton, D. J. (1986). "Ordered and chaotic motion of a forced spherical pendulum," *Eur, J. Phys*, Vol. **7**, pp 162-169.

Turyn, L. (1993). "The Damped Mathieu Equation," *Quarterly of Applied Mathematics*, Vol. **LI**, No. **2**, pp 389-398.

Van Dooren, R. (1996). "Chaos in a Pendulum with Forced Horizontal Support Motion: a Tutorial," *Chaos, Solitons and Fractals*, Vol. **7**, No. **1**, pp 77-90.

Venkatesan, A. and Lakshmanan, M. (1998). "Different routes to chaos via strange nonchaotic attractors in a quasiperiodically forced system," *Physical Review E*, Vol. **58**, No. **3**, pp 3008-3015.

Virgin, L. N. (1987). "The nonlinear rolling response of a vessel including chaotic motions leading to capsize in regular seas," *Applied Ocean Research*, Vol. **9**, No. **2**, pp 89-95.

Wolfram, S. (1996). *The Mathematica Book,* Cambridge University Press, Cambridge.

Wong, C. W., Zhang, W. S. and Lau, S. L. (1991). "Periodic forced vibration of unsymmetrical piecewise linear systems by incremental harmonic balance method,"

Journal of Sound and Vibration, Vol. **149**, pp 91-105.

Wright, J. H. and Marshfield. W. B. (1980). "Ship roll response and capsize behaviour in beam seas," *Trans. R. Inst. Naval Architects*, Vol. **122**, pp 129-148.

Wu, X., Tao, L. and Li, Y. (2004). "The Safe Basin Erosion of a Ship in Waves with Single Degree of Freedom," *15th Australasian Fluid Lechanics Conference*, The University of Sydney, Australia, 13-17 December, 2004.

Xu Xu, Wiercigroch, M. and Cartmell, M. P. (2005). "Rotating orbits of a parametrically excited pendulum," *Chaos, Solitons and Fractals*, Vol. **23**, pp 1537-1548.

Yabuno, H., Miura, M. and Aoshima, N. (2004). "Bifurcation in an inverted pendulum with tilted high-frequency excitation: analytical and experimental investigations on the symmetry-breaking of the bifurcation," *Journal of Sound and Vibration*, Vol. **273**, pp 493-513.

Yagasaki, K., Sakata, M. and Kimura, K. (1990). "Dynamics of a weakly nonlinear system subjected to combined parametric and external excitation," *Journal of Applied Mechanics*, Vol. **57**, pp 209-217.

Yalcinkaya, T. and Lai, Y. (1996). "Blowout Bifurcation Route to Strange Nonchaotic Attractors," *Physical Review Letters*, Vol. **77**, No. **25**, pp 5039-5042.

Zhang, J. W. and Andrews, D. J. (1999). "Roll Damping Characteristics of a Trimaran Displacement Ship," *Int. Shipbuild. Progr.*, Vol. **46**, No. **448**, pp 445-472.

Zounes, R. S. and Rand, H. R. (1996). "Transition Curves in the Quasiperiodic Mathieu Equation," *SIAM J. Appl. Math*, Vol. **58**, No. **4**, pp 1094-1115.